π^- PHOTOPRODUCTION FROM DEUTERIUM AND A PARTIAL WAVE ANALYSIS OF π^+ AND π^- PHOTOPRODUCTION IN THE ENERGY REGION 500 to 1250 MeV

Thesis by

Paul E. Scheffler

In Partial Fulfillment of the Requirements

For the Degree of

Doctor of Philosophy

California Institute of Technology

Pasadena, California

1972

(Submitted January 24, 1972)

ACKNOWLEDGMENTS

I appreciate the help and encouragement of Professor Robert L. Walker in the conception and execution of most aspects of this experiment, and especially his suggestions for the partial wave analysis of the data.

The experiment would have been impossible without the help provided by the synchrotron crew and operators, especially by Earl Emery and by Al Neubieser.

Assisting in the setup for data runs and in recording data were Craig Maxwell, Chip Smith, Gary Murata, and William Metcalf.

I appreciate the advance results of the π^- polarization experiment done by William Metcalf.

Finally, most helpful of all was Patrick Walden, my partner in this experiment. Mr. Walden was responsible for most of the data reduction and cross section corrections, relieving me of much tedious work. I am grateful for his many suggestions and explanations.

ABSTRACT

Single π^+ and π^- photoproduction rates from deuterium have been measured at the Caltech 1.5 GeV electron synchrotron at 32 photon energies between 585 and 1250 MeV and for 13 CM pion angles between 6 and 160° at each energy. The cross section for the reaction $\gamma n \to \pi^- p$ has been calculated via the π^-/π^+ ratio from deuterium and via the spectator model for the deuteron.

A partial wave analysis has been done on the reactions $\gamma p \to \pi^+ n$ and $\gamma n \to \pi^- p$ in the region of the second and third photoproduction resonances using the model of R. L. Walker. The results show some disagreements with recent quark theories. A case is made for the possibility that the $S_{11}(1535)$ is excited by isoscalar photons, in agreement with some results of η photoproduction experiments, and in disagreement with quark theory. Finally, the helicity 3/2 component of the $F_{15}(1688)$ resonance in π^- photoproduction is seen to be small, but not zero as predicted by the quark model.

TABLE OF CONTENTS

TABLE OF CONTENTS (continued)

LIST OF FIGURES

LIST OF FIGURES (continued)

LIST OF FIGURES (continued)

LIST OF TABLES

PART I

INTRODUCTION

Low energy pion photoproduction data ($k_\gamma^{lab} < 1.5$ GeV) have been used to locate and identify some of the more prominent pion-nucleon resonances without extensive partial wave analysis. The total cross-section for single positive pion photoproduction off protons (Figure 1) clearly shows the presence of the "1st", "2nd", and "3rd" photoproduction resonances which have been identified as the $P_{33}(1236)$, $D_{13}(1520)$, and (partially) the $F_{15}(1688)$ respectively. From phase shift analyses of pion-nucleon scattering data, several other resonances are known or believed to exist in this energy region, namely the $P_{11}(1470)$, $S_{11}(1535)$, $D_{15}(1670)$, $S_{11}(1700)$, $S_{31}(1650)$, $D_{33}(1670)$, and perhaps the $P_{11}(1780)$.

Recent quark model schemes have made predictions for the amplitudes of these resonances for the photoproduction of pions off of both proton and neutron targets.[1,2,21] In order for one to be able to confirm or deny such predictions, it would be helpful if the photoproduction data were sufficiently precise in this energy region for partial wave analysis.

It is desirable to have precise data for both proton and neutron targets, not only to confirm or deny quark model schemes, but in order to pin down the isospin character of

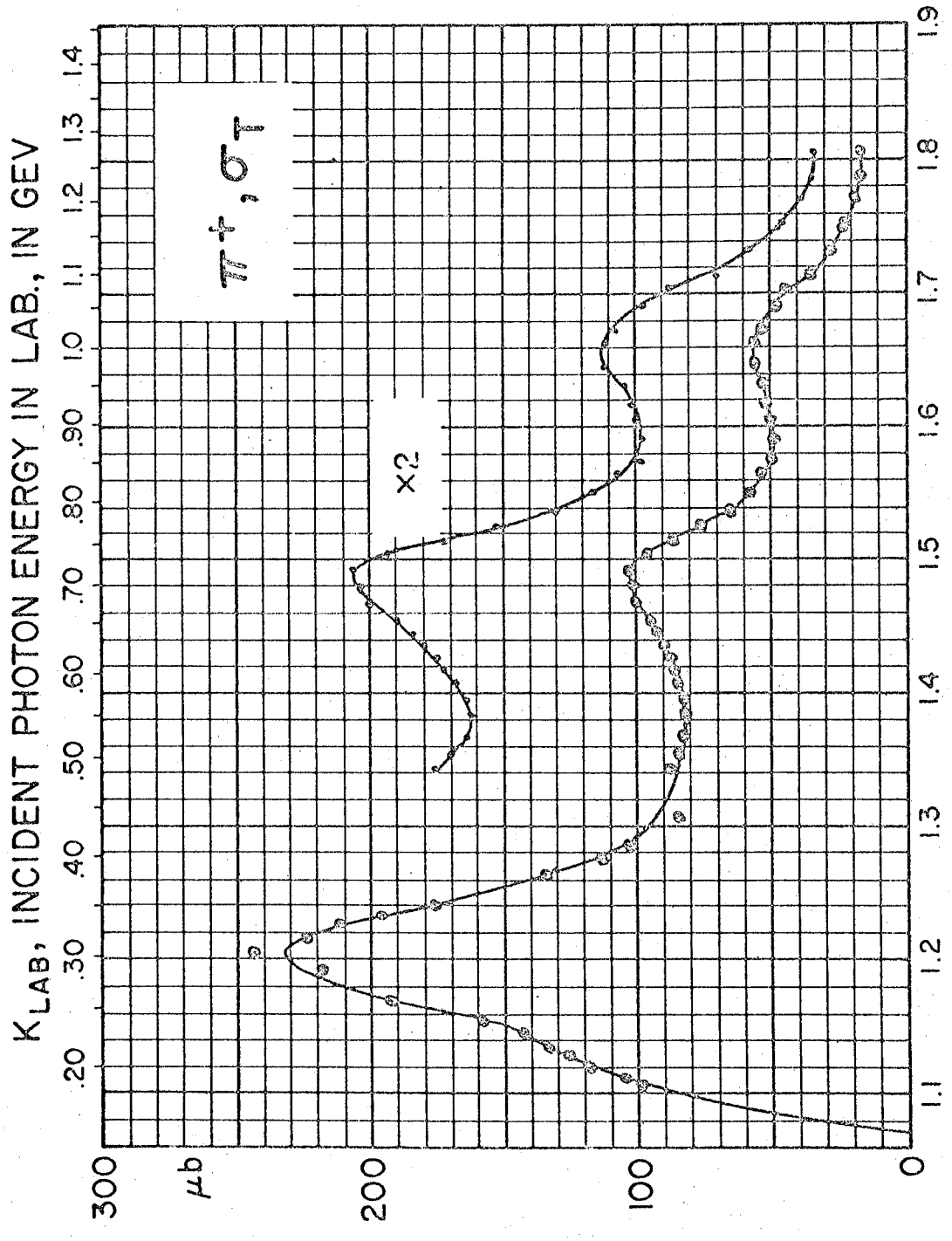
K_{LAB}, INCIDENT PHOTON ENERGY IN LAB., IN GEV
.20
.30
.40
.50
.60
.70
.80
.90
1.0
1.1
1.2
1.3
1.4
W, TOTAL ENERGY IN CM SYSTEM, IN GEV
1.1
1.2
1.3
1.4
1.5
1.6
1.7
1.8
1.9
μb
300
200
100
0
π^+, σ_T
x2

FIGURE 1

the electromagnetic interaction, which has always been an interesting question. This point is clearly illustrated by writing down the amplitudes for the four single pion photoproduction reactions in terms of the isoscalar and isovector amplitudes A^S and A^V as follows:

$$\begin{aligned}
A(\gamma p \to \pi^+ n) &= A^+ = (\sqrt{1/3})A^{V3} - (\sqrt{2/3})(A^{V1} - A^S) \\
A(\gamma p \to \pi^o p) &= A^o = (\sqrt{2/3})A^{V3} + (\sqrt{1/3})(A^{V1} - A^S) \\
A(\gamma n \to \pi^- p) &= A^- = (\sqrt{1/3})A^{V3} - (\sqrt{2/3})(A^{V1} + A^S) \\
A(\gamma n \to \pi^o n) &= A^{no} = (\sqrt{2/3})A^{V3} + (\sqrt{1/3})(A^{V1} + A^S)
\end{aligned} \tag{I.1}$$

The vector part of the interaction gives possible final states of isospin 3/2 and 1/2 with amplitudes A^{V3} and A^{V1} respectively. The scalar part gives final states of isospin 1/2 with amplitude A^S. The above form of the equations, taken from Walker[3], assumes no isotensor interaction. The isoscalar and isovector amplitudes may be calculated if at least three of the photoproduction amplitudes (including at least one with neutron target) are known. The isoscalar and isovector character of a spin 1/2 resonance may be determined if (eg.) A^+ and A^- are known since $A^{V3} = 0$ and the difference of A^{V1} and A^S is taken for proton targets while the sum is taken for neutron targets.

Finally, photoproduction data and associated partial wave analyses can be used in the application of low energy sum rules and in comparison with dispersion relations predictions.

A. Previous data - or lack thereof.

In the past few years, comprehensive differential cross section measurements of both π^+ and π^o photoproduction off protons in the energy region $k_\gamma^{lab} < 1.5$ GeV have been made by Fischer et al.(4), Betourne et al.(5), Ecklund et al.(6), Thiessen(7), Fischer et al.(8), and Wolverton(9). Further measurements at selected energies and angles have been made by many groups(10,11,12,13,14,15,16,17,49,55). Also, several recent experiments have measured recoil nucleon polarizations and polarized beam asymmetries for the π^+ and π^o reactions(18, 19,20,22,23,24,25,26,27). Finally a recent experiment has measured the π^+ cross section at 40^o using a polarized target (28). (A compilation of experiments done before 1967 may be found in the report by Beale et al.(29).)

Several groups(3,30,31,32,33) have attempted partial wave analyses of these data, using various constraints and models to overcome the difficulty of fitting twice as many amplitudes as in pion-nucleon scattering analyses. Of special interest to

me is the comprehensive analysis of low energy photoproduction data carried out by R.L. Walker(3). A discussion of my work with Walker's model appears in Part V.

The data for photoproduction off neutrons have been relatively sparse due to the difficulties associated with neutron targets. Since fixed targets of free neutrons are impossible to maintain, compound (eg. deuterium) targets must be used; or measurements of the inverse reaction might be made. In both cases, the γn cross section must be calculated under certain assumptions, ie. the spectator model for deuterium or time reversal invariance for the inverse reaction.

Up until 1968, when our experiment was started, the main body of π^- photoproduction data below $k_\gamma^{lab} = 1.5$ GeV had been collected in experiments with deuterium targets by Sands et al.(34), Beneventano et al.(35), and Neugebauer et al.(36), totalling about 100 data points (all below $k_\gamma^{lab} = 1.0$ GeV). It was our desire to augment the above by measureing detailed angular distributions (every 10 to 15 degrees) for many lab photon energies between 575 and 1250 MeV and to improve upon the energy resolution and statistics as much as possible.

Since the start of this experiment, several other groups have published π^- data. Among these are two bubble chamber experiments: Lodi-Rizzini et al.(37) and Hilpert et al.(38). A counter experiment at 90° has been done by Beneventano et al. (39).

Also, a counter measurement of π^+ and π^- photoproduction at 180° using bremsstrahlung subtraction to improve the energy resolution has been made by Fujii et al.(11). Finally, a measurement of the π^-/π^+ ratio from deuterium at 0° has been made by Ito et al.(40). All of the above experiments were done with a deuterium target. Comparison of these experiments with the results of our experiment is given in Part IV.

One further measurement of the π^- cross section has been made via the inverse reaction $p\pi^- \rightarrow n\gamma$ (41). The results of this experiment in the energy region $k_\gamma^{lab} = 500$ to 1000 MeV are not yet available for comparison.

Finally, there have been several new measurements of polarized beam asymmetry and recoil proton polarization for the π^- reaction(20,42,43,53). I have tried to incorporate some of these in a reanalysis of the π^- reaction using Walker's model (see Part V).

B. Preparation of the experimental apparatus.

For our experiment, it was desired to use the existing experimental setup in the south beam of the Caltech 1.5 GeV electron synchrotron with as little modification as possible. The synchrotron - now defunct - produced an external bremsstrahlung photon beam with cutoff energy at the endpoint of

the circulating internal electron beam. The bremsstrahlung beam was then collimated, swept of charged particles, and allowed to strike the (3 inch diameter) liquid deuterium or liquid hydrogen target in the experimental area. A schematic diagram of the beam line and experimental area is shown in Figure 2.

The particle detection apparatus consisted of two magnetic spectrometers: one for low momentum (< 600 MeV/c) and the other for high momentum (600 - 1650 MeV/c) charged particle detection. The low energy magnet (LEM) had seven momentum channels with a total momentum range $\Delta P/P_o \simeq 10\%$ while the high energy magnet (HEMA) had four channels with the same total momentum spread. The two spectrometers had been used in a number of previous experiments, most recently by S.D. Ecklund, H.A. Thiessen, and F.B. Wolverton in measurements of π^+ and π^o photoproduction from hydrogen. In addition, Wolverton's π^o experiment made use of a simple coarse scintillation counter hodoscope array (with Pb converter), set up and moveable on a track of about 32 inch radius around the target. This was used to detect gamma ray decays from the π^o.

The above apparatus appeared to be immediately useable for measurement of π^- photoproduction which produces two charged particles in the final state. One of the spectrometers

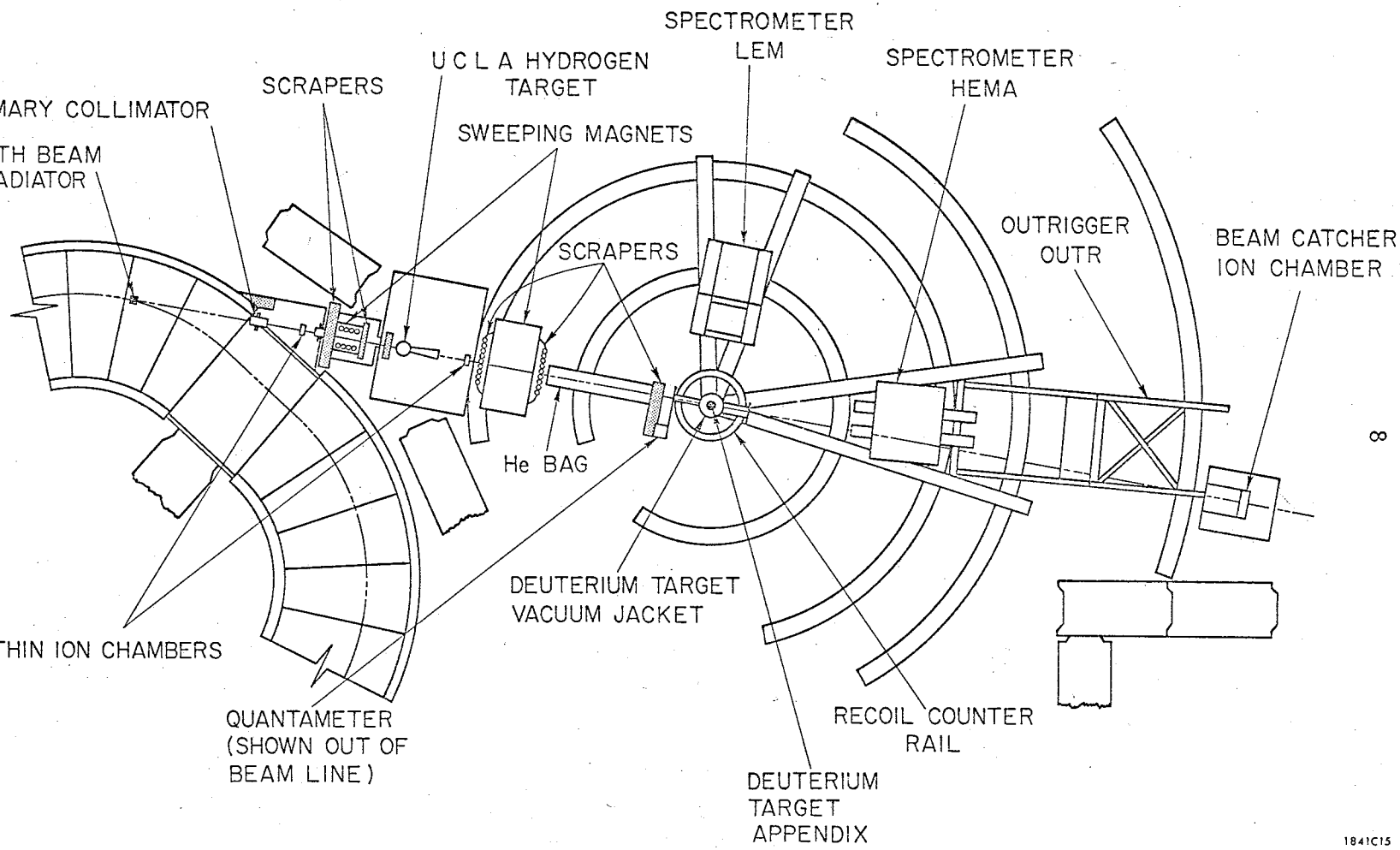
SPECTROMETER
LEM
U C L A HYDROGEN
TARGET
SCRAPERS
SPECTROMETER
HEMA
PRIMARY COLLIMATOR
SWEEPING MAGNETS
SOUTH BEAM
RADIATOR
SCRAPERS
OUTRIGGER
OUTR
BEAM CATCHER
ION CHAMBER
He BAG
DEUTERIUM TARGET
VACUUM JACKET
THIN ION CHAMBERS
QUANTAMETER
(SHOWN OUT OF
BEAM LINE)
RECOIL COUNTER
RAIL
DEUTERIUM
TARGET
APPENDIX
1841C15

FIGURE 2

could be used to detect the pion while a simple hodoscope set up on the track could be used to detect the recoil proton.

The modifications of the existing setup to measure π^- photoproduction were as follows:

1) The "hydrogen" target was, of course, filled with deuterium.

2) The seven channel momentum hodoscope (produced by four overlapping counters) on the low energy magnet was replaced by a four channel hodoscope (produced by four non-overlapping counters).

3) The four channel "gamma counter" hodoscope on the track surrounding the target was replaced by a single channel counter telescope (the "recoil counter").

4) Finally, the electronics of the experiment was completely rewired from scratch, using the newer Tollestrup circuit modules to replace the older Marshall circuit modules.

The magnetic spectrometers had already been calibrated by Thiessen and Wolverton (see Appendix III) and it was deemed unnecessary to recalibrate them except to translate the acceptance parameters for the seven-channel hodoscope on the LEM to acceptance parameters for the new four-channel momentum counter (44). A more detailed description of the

apparatus and electronics is presented in Appendix III.

C. Division of work on the experiment.

This π^- photoproduction experiment was a joint effort of myself (P.S.) and Patrick L. Walden (P.W.). The division of work on the experiment was as follows:

1) Physical modification of apparatus - P.S., P.W., various undergraduates, and the synchrotron crew.

2) Setup of electronics - P.S. and P.W.

3) Initial Monte Carlo study of effects of using "recoil counter" - P.S.

4) Determination of optimum recoil counter size - P.W.

5) Beam energy monitoring analysis - P.S.

6) Reduction of scaler data to true particle rates - P.W.

7) Calculation of acceptances and direct cross sections using spectator model - P.W.

8) Averaging and interpolation of final data, simple resolution correction - P.S.

9) Attempt at partial wave analysis of final cross sections - P.S.

10) Investigation of deuterium effects neglected in the cross section calculation - P.S. and P.W.

PART II

THE DEUTERIUM PROBLEM

As mentioned above, the differential cross section for the reaction $\gamma n \rightarrow \pi^- p$ must be calculated from particle rates of photoproduction off a compound nucleus (deuterium). The actual reaction is then $\gamma d \rightarrow \pi^- pp$. The main considerations with a deuterium target are:

1) The target neutron is bound.

2) The momentum of the bound nucleons in deuterium is not negligible compared with the other particle momenta.

3) In the initial state, the proton in deuterium "shadows" the neutron with consequent effect on the cross section (Glauber effect).

4) In the final state, the outgoing pion and "recoil" proton may interact with the "spectator" proton.

A. The spectator model of photoproduction from deuterium

The spectator model is used to approximate the behavior of the neutron in deuterium to take care of problems 1) and 2). The model is equivalent to the "impulse approximation" for complex nuclei which states that the reaction amplitude is the sum of reaction amplitudes off of each nucleon separately, with no collective effects. The conditions for the validity

of the impulse approximation are discussed by Chew and Lewis [45] and are shown to be satisfied by the deuteron, because of its small binding energy and spread out wave function. Since a single π^- can be photoproduced only from neutrons, the spectator model assumes that in deuterium, only the neutron reacts with the incoming gamma ray to produce a single π^-, while the proton acts as a "spectator" whose momentum in the final state equals its momentum in the initial state. Thus in its simplest form, this model ignores initial and final state interactions with the spectator.

B. Bound nucleon momentum.

A rough derivation of the internal momentum distribution of nucleons in the deuteron can be made assuming a simple nuclear potential and relatively simple form for the deuteron wave function. One such "derivation" [46], using a Yukawa potential, gives the Hulthen wave function $u_i(\vec{\rho})$ and associated Fourier transform momentum space wave function $c(\vec{k})$ (see Appendix IV). The probability density for the magnitude of the nucleon momentum is given by $4\pi k^2 |c(\vec{k})|^2$ and is plotted in Figure 3. The most likely momentum for the target neutron in the deuteron is roughly 50 MeV/c, a quantity which cannot be ignored in comparison with the momenta of the other

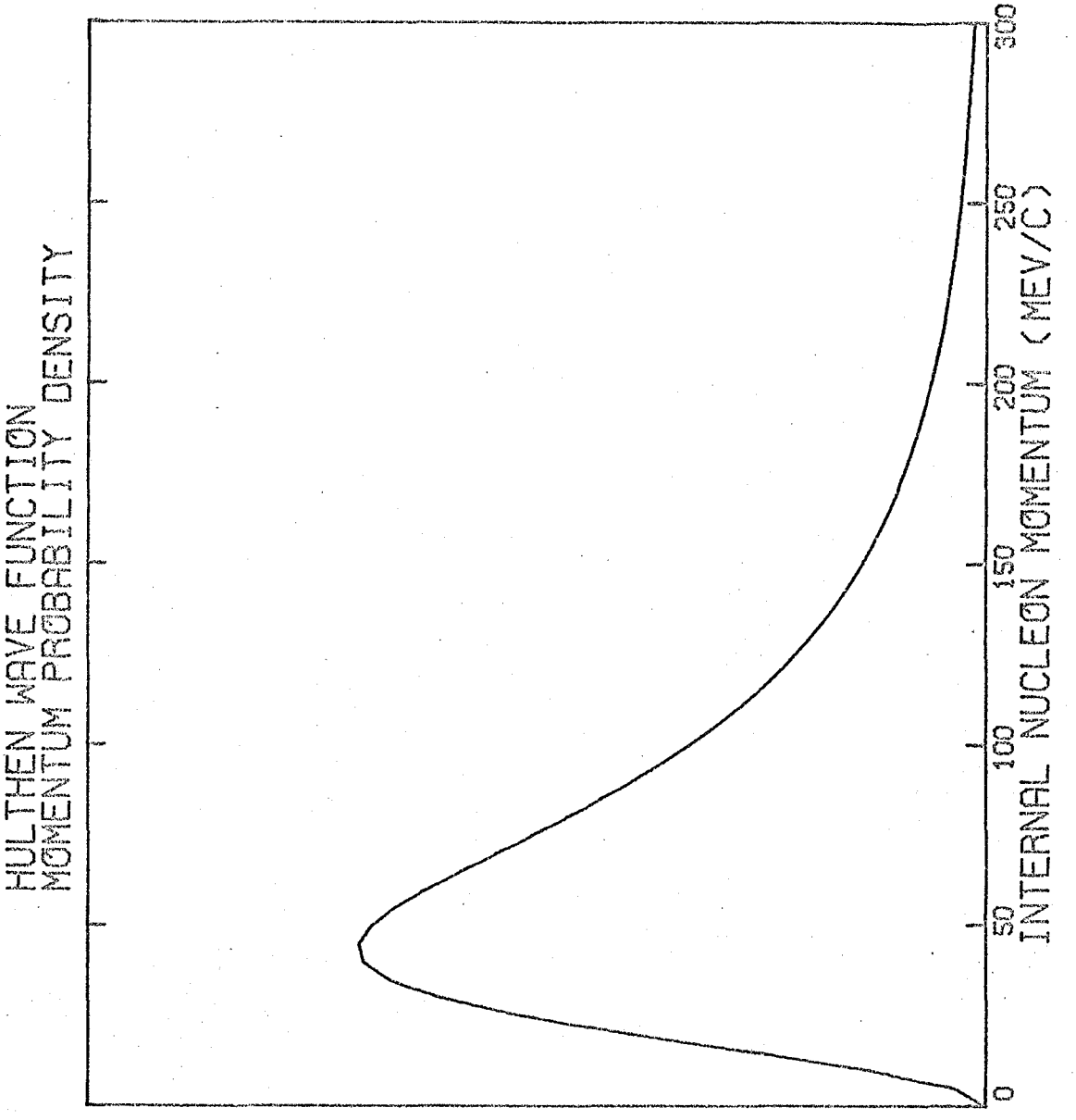
HULTHEN WAVE FUNCTION
MOMENTUM PROBABILITY DENSITY
0
50
100
150
200
250
300
INTERNAL NUCLEON MOMENTUM (MEV/C)

FIGURE 3

particles in the reaction.

On the other hand, because of the simplified assumptions and the approximations used, we know that these functions are somewhat innacurate; and specifically, our lack of any knowledge of the true wave function and potential at small radius ρ is translated into large uncertainty in the momentum distribution at large momenta. In fact, recent measurements of this momentum distribution in πd production experiments (bubble chamber) have shown relatively large numbers of events at spectator momenta greater than 200 MeV/c in disagreement with the Hulthen function prediction.(56)

A comparison of the Hulthen momentum function with the spectator proton momentum distribution obtained in the π^- photoproduction bubble chamber experiment by Hilpert et al. (38) shows that for photon energies below 1.5 GeV, the Hulthen function is in fair agreement with experiment for momenta below 300 MeV/c (Figure 4).

C. Energy resolution of the π^- photoproduction experiment.

The target nucleon momentum has an effect on the calculation of the photon energy at each data point. The gamma ray beam incident on the deuterium target is a bremsstrahlung

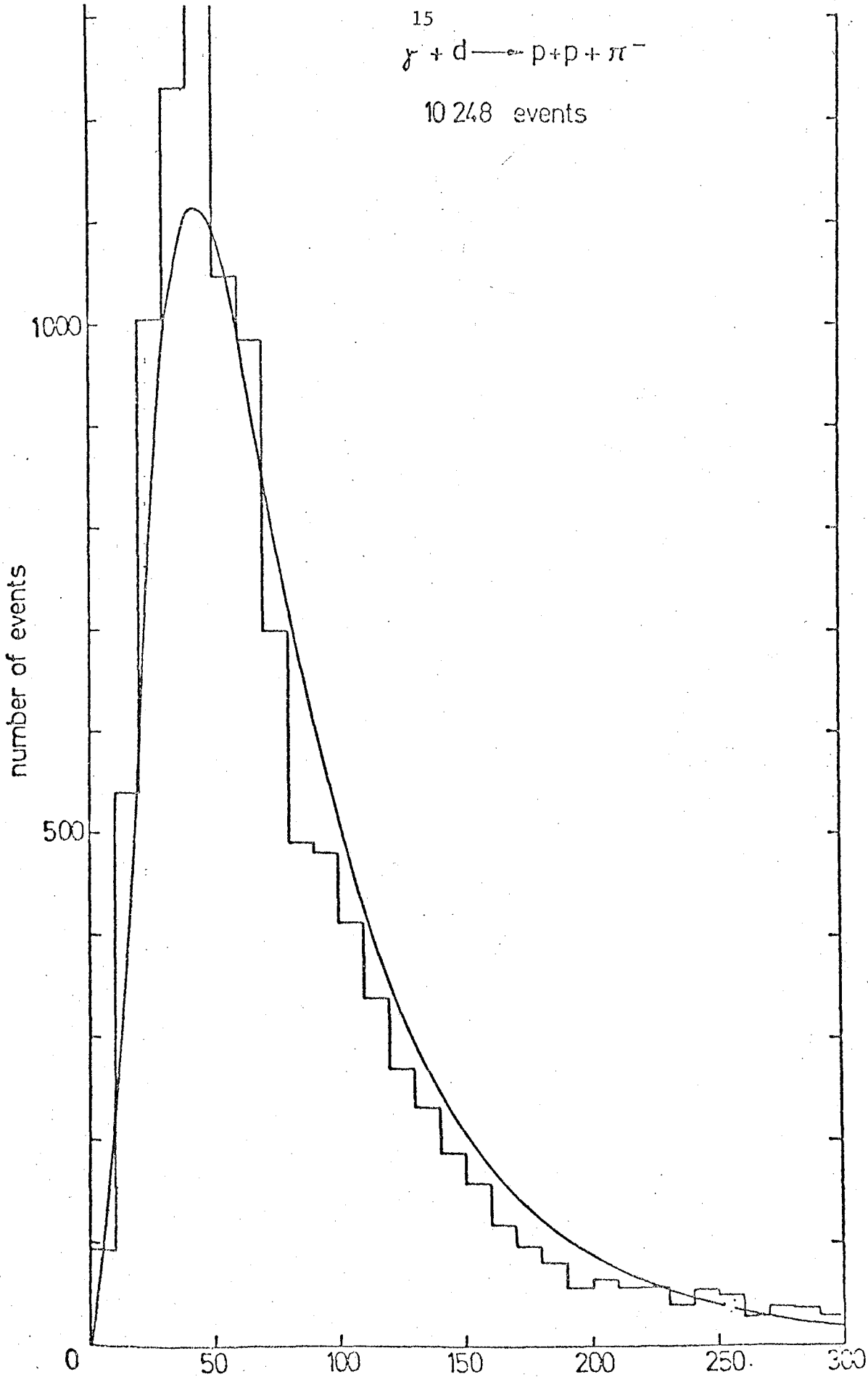
γ + d ⟶ p + p + π⁻
10 248 events
number of events
1000
500
0
50
100
150
200
250
300

FIGURE 4

beam, continuous in energy up to a cutoff equal to the end-point energy of the synchrotron. The specific photon energy for the reaction must be calculated at each data point from kinematics determined by measurement of outgoing particles and our knowledge of the photon beam direction. The finite width of the spectrometer aperture is reflected into a finite resolution width in our knowledge of the photon energy. Other contributions to the resolution width are finite target size and finite beam width.

This resolution width is not too broad in experiments done using a hydrogen target, where the target nucleon (proton) can be considered to be at rest in the lab. The two-body kinematics of the reaction are completely determined by measurement of the vector momentum of one outgoing particle (plus our knowledge of the photon beam direction). The width of the spectrometer aperture, target width, and beam width are reflected into a small resolution width in photon energy, eg. about 25 MeV at forward angles.

However, when a deuterium target is used, the target nucleon is in motion; and, at each data point, events corresponding to many possible target nucleon momenta are counted. If again, only one outgoing particle is detected (in the spectrometer), the two-body kinematics can be calculated

assuming the validity of the spectator model. But now, there is another major contribution to the photon energy resolution width: the uncertainty in the initial momentum of the target nucleon. The effect is to increase the energy resolution width by a factor of two or more.

D. Reduction of energy resolution width by using a "recoil counter" to detect the second charged particle.

It seemed likely that the use of a counter telescope or hodoscope to detect the second charged particle ("recoil proton") in the reaction might help to reduce the resolution width to acceptable levels. I have done a Monte Carlo investigation of the angular distribution of proton recoils as a function of initial target neutron momentum for a given spectrometer setting and aperture. Thus I have been able to determine the effect of using a recoil counter to detect this recoil proton. It was found that events with the largest angular deviation from the central recoil angle had high target neutron momenta , a result which is not very surprising. Thus, a recoil counter of appropriate size could be used to discriminate against these high neutron momenta and improve the resolution of the experiment. Figure 5 shows a typical result of the analysis. The high momentum tail of the Hulthen

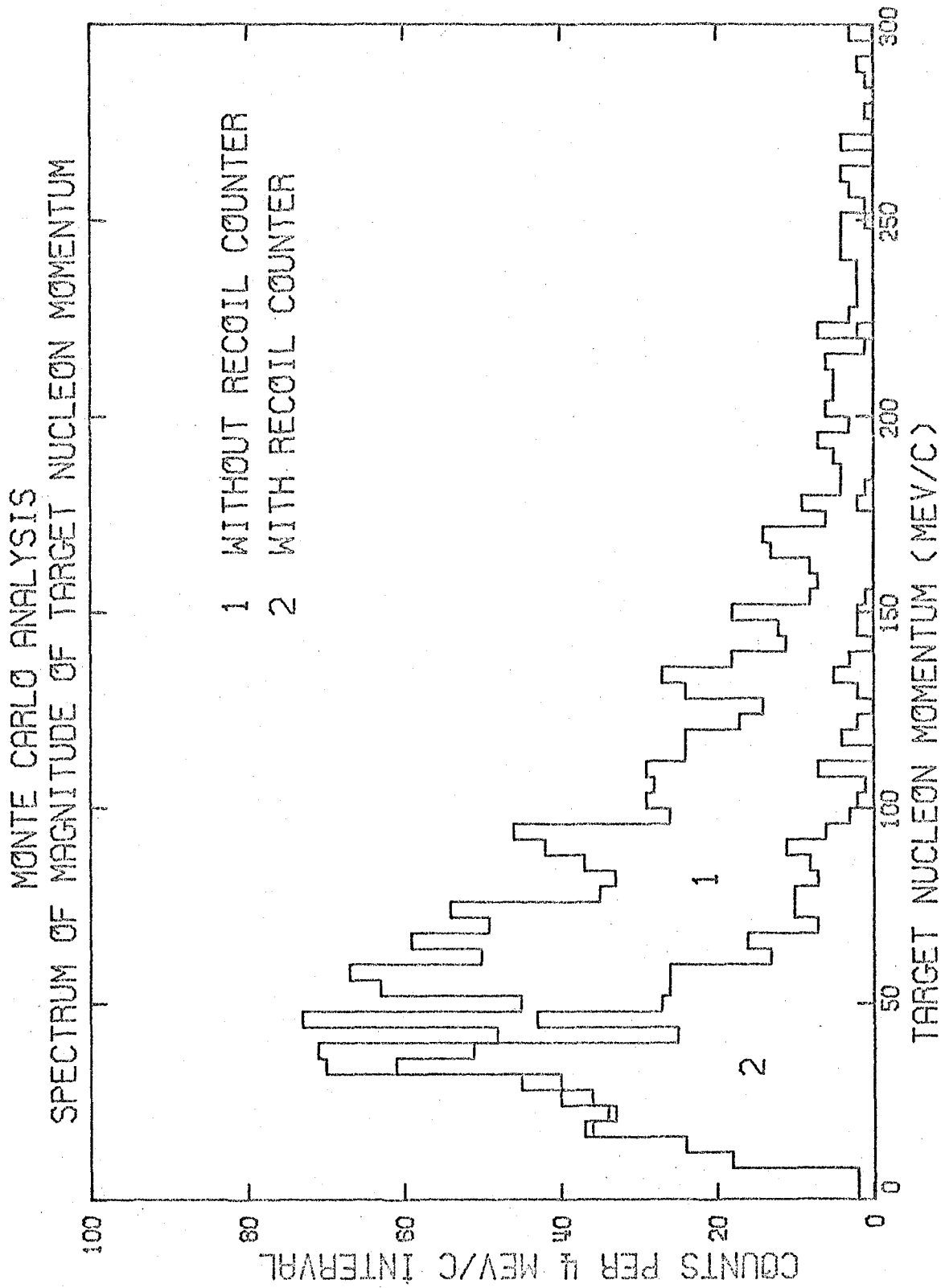
MONTE CARLO ANALYSIS
SPECTRUM OF MAGNITUDE OF TARGET NUCLEON MOMENTUM
1 WITHOUT RECOIL COUNTER
2 WITH RECOIL COUNTER
COUNTS PER 4 MEV/C INTERVAL
TARGET NUCLEON MOMENTUM (MEV/C)
0
20
40
60
80
100
0
50
100
150
200
250
300
1
2

FIGURE 5

momentum distribution has been cut off by the addition of the recoil counter. As may be seen in Figure 6, the CM total energy resolution has been improved, mainly by cutoff of large tails due to high target neutron momenta. Figure 7 shows a similar improvement in the resolution of the CM pion angle.

A study made by Patrick Walden of the tradeoff between percentage of events (corresponding to a pion in the spectrometer) detected by the recoil counter and reduction in resolution width was used to determine the optimum counter size. Roughly, the optimum size was determined to be the angular aperture which accepted 50% of the events corresponding to a pion in the spectrometer. For smaller recoil counter size, the energy resolution width fell off slowly, while for larger counter sizes, the resolution width increased rapidly.

Based on these results, a recoil counter telescope system was designed by Craig Maxwell to be placed on the existing circular track surrounding the target. Details of the recoil counter system are given in Appendix III.

A short summary of the actual resolution widths for this experiment calculated at selected pion CM angles and "free" neutron rest energies (see Appendix I) is given in Table 1.

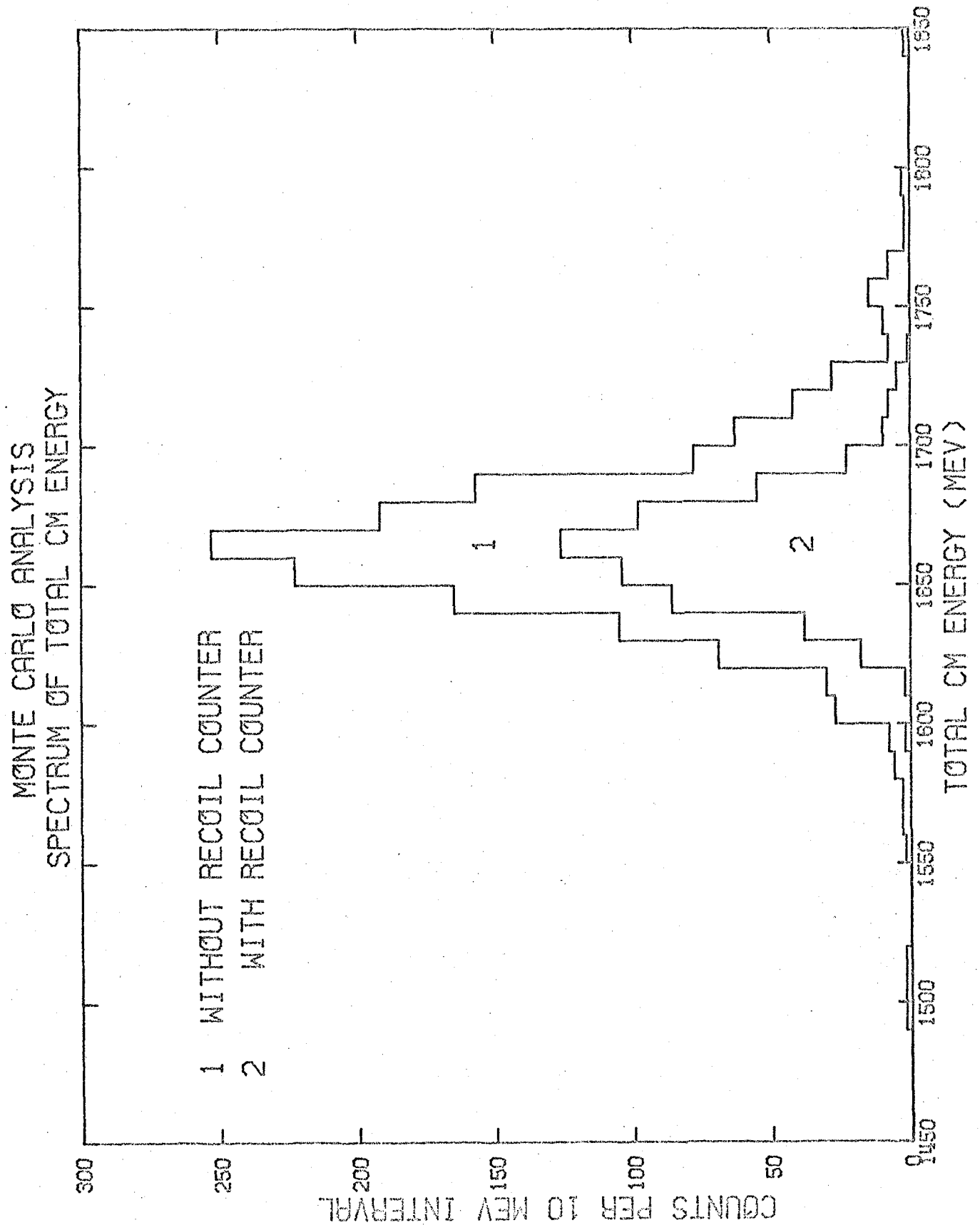
MONTE CARLO ANALYSIS
SPECTRUM OF TOTAL CM ENERGY
1 WITHOUT RECOIL COUNTER
2 WITH RECOIL COUNTER
1
2
COUNTS PER 10 MEV INTERVAL
TOTAL CM ENERGY (MEV)
300
250
200
150
100
50
0
1450
1500
1550
1600
1650
1700
1750
1800
1850

FIGURE 6

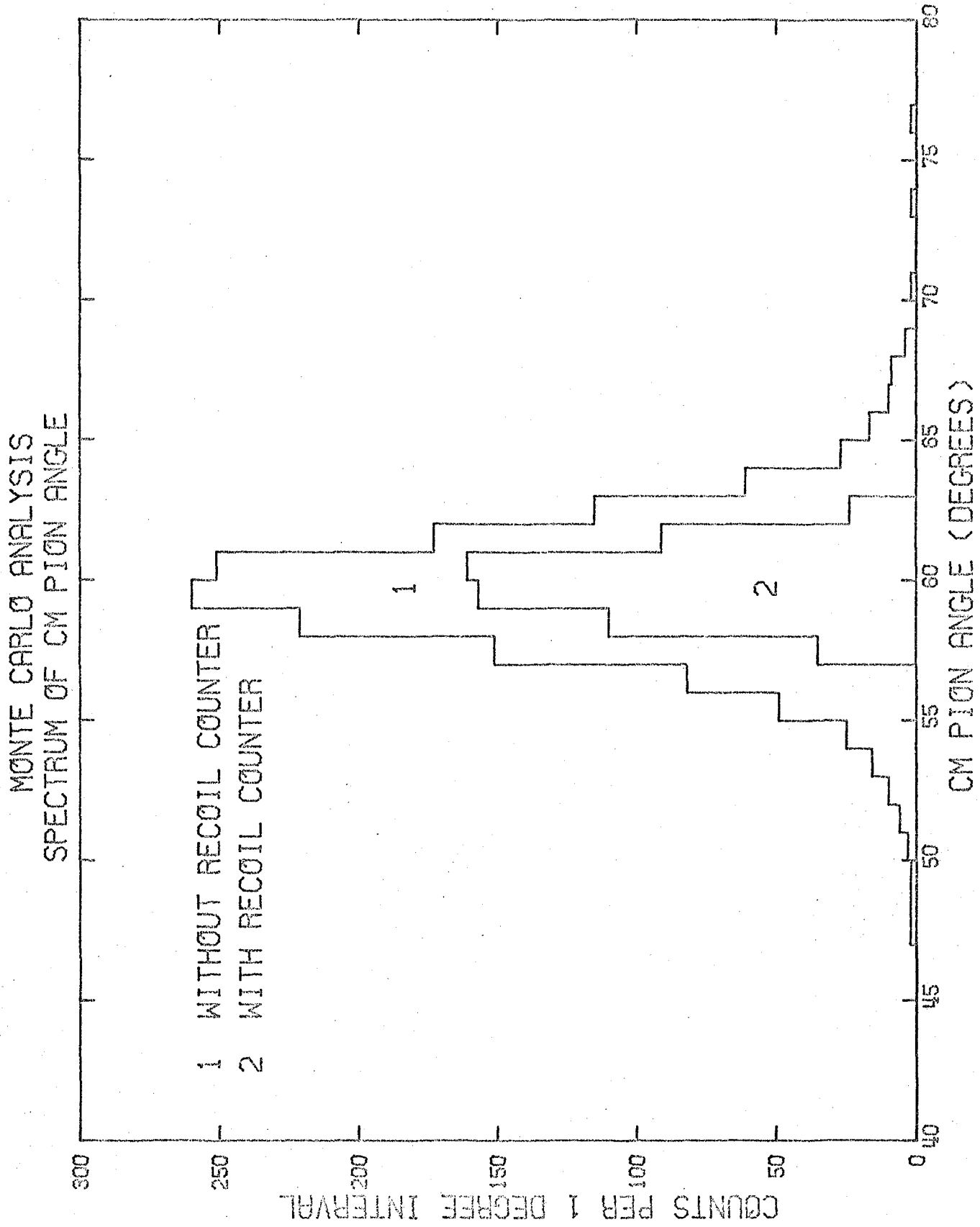
MONTE CARLO ANALYSIS
SPECTRUM OF CM PION ANGLE
1 WITHOUT RECOIL COUNTER
2 WITH RECOIL COUNTER
1
2
COUNTS PER 1 DEGREE INTERVAL
CM PION ANGLE (DEGREES)
0
50
100
150
200
250
300
40
45
50
55
60
65
70
75
80

FIGURE 7

TABLE 1

RESOLUTION WIDTHS FOR

SELECTED PION ANGLES AND PHOTON ENERGIES

CM Pion Angle (deg)	"Lab" Photon Energy (MeV)	2σ (degrees) Angular Resolution Pion Only	2σ (degrees) Angular Resolution With Recoil	2σ (MeV) Energy Resolution Pion Only	2σ (MeV) Energy Resolution With Recoil
6	612	1.1		70	
6	916	1.2		108	
6	1220	1.6		150	
45	612	4.1	1.4	64	29
45	916	3.9	1.4	100	45
45	1220	3.7	1.5	132	68
75	612	6.4	2.5	60	40
75	916	5.8	2.6	90	62
75	1220	5.2	2.8	112	84
120	612	8.0	3.3	72	80
120	916	7.5	3.0	112	106
120	1220	7.6	4.5	146	124
160	672	8.5	1.8	108	90
160	916	8.9	1.7	192	120
160	1220	8.6	1.7	248	148

It is obvious that the energy resolution at backward pion angles is very poor and that the recoil counter is of little help. On the other hand, the angular resolution is greatly improved by the use of the recoil counter.

E. The Glauber effect.

The Glauber effect is the reduction of cross section per nucleon in a compound nucleus from the free nucleon cross section due to the "shadowing" effects on a given nucleon by all the rest. In deuterium, the π^- photoproduction cross section off the target neutron should be slightly reduced compared with the free neutron cross section because for a certain fraction of the time, the proton intersects the line of sight between the incoming photon and target neutron.

The rough effect, as derived by Glauber(47), can be expressed as a relationship between the total cross section from deuterium and the total γN cross section from the free neutron and proton:

$$\sigma_d = \sigma_p + \sigma_n - G.C. \qquad (II.1)$$

where G.C., the Glauber correction, is given by:

$$G.C. = \frac{\sigma_p \sigma_n}{4\pi} \left(\frac{1}{r^2} \right) \qquad \text{(II.2)}$$

where r is the average separation of the nucleons in the deuteron. If we take $r = 1.7$ fermi, and $\sigma_p \simeq \sigma_n = 100$ μb, then this correction is equal to 0.028 μb or 0.028% , which is negligible.

However, it has been shown(48) that the photon can materialize as a ρ^o which interacts strongly in nuclear matter. A rough estimate of the ρN cross section is $\sigma_{\rho N} = 25$ mb. If we replace σ_p and σ_n in equation II.2 with this value, the the correction becomes 6.9%, which is significant. An indication of the fraction of time that the photon spends as a ρ^o while traversing the deuteron may be obtained by application of the uncertainty principle. Consider the materialization of a 1 GeV photon into a ρ^o with the same momentum. The energy of the ρ^o is then given by:

$$E_\rho = \sqrt{(1)^2 + (.765)^2} = 1.26 \text{ GeV}$$

where .765 is the rest mass of the ρ^o. The extra energy needed is $\Delta E = 260$ MeV. Applying the inequality $\Delta E \Delta t > \hbar/2$, we obtain $\Delta t = 1.26 \times 10^{-24}$ sec., which, even at the speed of light, corresponds to only 0.4 fermi. The mean free

path of the ρ^o in nuclear matter is about 3 fermis, and thus the photon has relatively little time to interact as a ρ^o for photon energies $\sim$ 1 GeV.

Thus we conclude that the Glauber effect is negligible ($\sim$ 1% or less) for our experiment.

F. Final state interactions.

There remains the possibility that in the reaction $\gamma d \rightarrow \pi^- p_r p_s$ the outgoing pion or the recoil proton p_r interacts with the spectator proton p_s. The only easily separated component of these final state interactions is the effect of the Pauli exclusion principle on the allowable final states of the two-proton system. A calculation of the effect of the Pauli principle on the deuterium photoproduction cross section has been made by Chew and Lewis [45]. The deuterium cross section is given in terms of the "spin-flip" and "spin-non-flip" cross sections off free nucleons and the deuteron form factor assuming the Hulthen wave function for the deuteron (see Appendix V).

The calculation of other final state effects (eg. πN scattering) is very difficult. Because of this, and because

our experimental results seem to indicate that most of the final state effects seem to be accounted for by the Pauli principle, we have chosen to neglect these other interactions.

PART III

CALCULATION OF THE $\gamma n \to \pi^- p$ DIFFERENTIAL CROSS SECTION

A. Methods.

In order to try to overcome deuterium problems and for comparison purposes, the cross section for $\gamma n \to \pi^- p$ was calculated in three ways. These were:

1) Ratio method.

The spectrometer rates of π^- from the reaction $\gamma d \to \pi^- pp$ and of π^+ from the reaction $\gamma d \to \pi^+ nn$ were measured and used to calculate the cross section for the reaction $\gamma n \to \pi^- p$ according to the formula:

$$\sigma(\gamma n \to \pi^- p) = \frac{\text{Rate}(\gamma d \to \pi^- pp)}{\text{Rate}(\gamma d \to \pi^+ nn)} \times \sigma(\gamma p \to \pi^+ n) \qquad \text{(III.1)}$$

where the proton cross sections were taken from the fit made by Ecklund[6] of the π^+ cross sections from hydrogen measured by Ecklund[6] and Thiessen[7]. This method assumes that the deuterium corrections cancel in the ratio, thus making the ratio equal to that of the free nucleon cross sections. To the extent that deuterium effects, especially final state effects, do <u>not</u> cancel in the ratio, the γn cross sections calculated by this method will be inaccurate.

Final state effects, especially that due to the Pauli exclusion principle, are most prominent at small forward pion angles (corresponding to small recoil nucleon momentum) and thus this ratio calculation probably has a moderate systematic error at our small angle settings 6, 10, 20, and 30 degrees CM. An attempt to calculate this correction by using "spin-flip" and "spin-non-flip" cross sections is made in Part V.

Despite the above problems, the ratio method is the simplest way to determine the π^- cross section off neutrons. Until exact corrections can be worked out in detail, this method provides the best estimate of this cross section, especially at small pion angles.

One disadvantage of the ratio method as we used it is that the energy resolution and angular resolution were poor because the recoil counter rates were not used.

2) Recoil (and reverse recoil) cross sections.

The recoil counter was used to detect the recoil proton when the pion went through the spectrometer; and at backward pion angles the recoil counter was used to detect the pion when the proton went through the spectrometer (reverse recoil runs).

A direct calculation of the γn cross section was made, using the spectator model, Hulthen wave function, and recoil counter rates. Since both outgoing particles were detected, this method gives improved energy and angular resolution, besides reducing background rates.

The calculation of the spectrometer and recoil counter acceptances, and the average CM pion angle and "lab" photon energy at each setting was done by means of a Monte Carlo program written by Patrick Walden. The program randomly chooses the following variables for each experimental setup: the pion (or proton for reverse recoil runs) lab momentum across the acceptance of one momentum channel of the spectrometer, the position of the reaction in the target, the spectator nucleon initial momentum weighted by the Hulthen wave function. The program then calculates the photon energy and weights the total event by the bremsstrahlung spectrum at that photon energy. The program then checks whether or not the recoil proton (or pion for reverse recoil run) went through the recoil counter. By calculating many such events, the program obtains average values of the photon energy, CM pion angle, and spectrometer and recoil counter acceptances for the given experimental setup. Knowledge of the particle rates and system acceptance gives the cross section average

over the acceptance.

The program makes corrections for momentum loss of the spectrometer particle as it travels from the target, through air and various counter materials, to the last counter in the system. Corrections are also made for energy loss of the recoil proton in escaping through the aluminum wall of the target assembly and in traversing the material in the recoil counter system. The effects of pion decay ($\pi^{\pm} \rightarrow \mu^{\pm} + \overline{\nu}$) were investigated by a special Monte Carlo program which was run for a selected number of experimental settings. The results of this program were combined with corrections for nuclear absorption in the spectrometer to produce a final acceptance. This final acceptance was multiplied by the rates to obtain the final recoil cross section. Details on the above corrections and about the geometrical acceptance calculations may be found in the Ph.D. thesis by Patrick Walden.

Unfortunately, the calculation using the recoil counter rates could not be done at forward pion angles, because the recoil proton does not have enough energy to escape through the mylar and aluminum walls of the target assembly. Thus, the "recoil" cross sections were calculated only at angles $\geq 45^{\circ}$ CM.

3) Direct cross sections - pion only.

The third method is a direct calculation of the π^- cross section using only the spectrometer (pion) rates. The calculation proceeds exactly as in 2) except that the recoil counter is ignored. The corrected system acceptance is multiplied by the particle rates to obtain the final "pion only" cross sections.

This method has all the disadvantages of the other two. The energy and angular resolutions are poor. The Hulthen wave function was used at high values for the internal nucleon momentum, an area where it is known to be inaccurate. Finally, background rates were significant, especially at backward pion angles. Also, while this method could be used to calculate cross sections at pion CM angles $< 45^{o}$, the results are very likely not equal to the true γn cross section, because of the predominance of final state effects in this region.

It should be noted that the average lab photon energies and CM pion angles calculated by the Monte Carlo program for each experimental setting by this method are the same angles and energies which have been assigned to the ratio cross sections (Method 1).

B. Elimination of competing reactions.

Since photodisintegration of deuterium ($\gamma d \rightarrow pn$) is eliminated by either requiring a pion in the spectrometer or by requiring two outgoing charged particles, the main competing reactions are multiple pion photoproduction, especially the following:

1) $\gamma d \rightarrow n\pi^+\pi^o n$

2) $\gamma d \rightarrow p\pi^+\pi^- n$

3) $\gamma d \rightarrow p\pi^-\pi^o p$

Reactions 1 and 2 may contaminate π^+ photoproduction (from deuterium) and reactions 2 and 3 may contaminate π^- photoproduction.

These reactions were limited by reducing the synchrotron endpoint below the threshold photon energy required for producing the second pion. This completely eliminated 2π contamination, except perhaps in the lowest of the four momentum channels of the spectrometer. A schematic diagram showing the situation is given in Figure 8.

For single pion photoproduction, the four momentum channels of the spectrometer are reflected into resolution curves in the photon energy. Each curve gives the probability that a photon of given energy will produce a single pion in the given momentum channel. The channel of lowest momentum

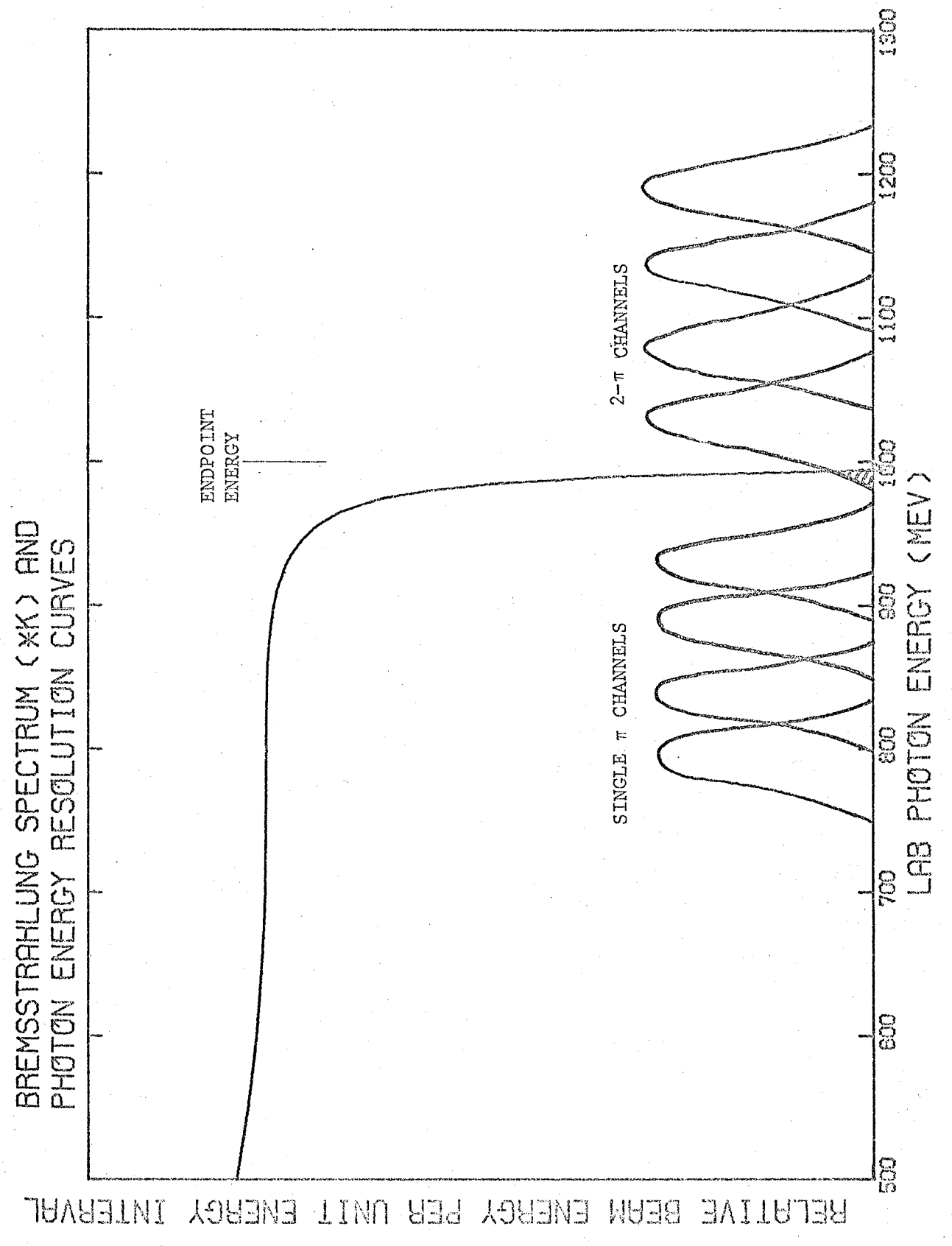
BREMSSTRAHLUNG SPECTRUM (*K) AND
PHOTON ENERGY RESOLUTION CURVES
ENDPOINT
ENERGY
SINGLE π CHANNELS
2-π CHANNELS
RELATIVE BEAM ENERGY PER UNIT ENERGY INTERVAL
LAB PHOTON ENERGY (MEV)
500
600
700
800
900
1000
1100
1200
1300

FIGURE 8

is reflected into the energy resolution curve of lowest energy. A similar set of four energy resolution curves can be generated for double pion photoproduction. These are shown in the figure. For our spectrometer, the highest energy resolution curve for single pion photoproduction is separated from the lowest energy curve for double pion photoproduction by a small gap. Thus if the synchrotron endpoint is set in the gap, only single pions can be produced. However because of the poor resolution due to deuterium smearing, and the fact that the bremsstrahlung endpoint is not sharp, the tail of the bremsstrahlung spectrum and the lower side of the resolution curve for the lowest momentum channel for double pion photoproduction overlap as shown.

Thus our lowest momentum channel may have significant 2π contamination. This problem, however, becomes insignificant in cases where the resolution is improved by addition of the recoil counter. Also we hope that most of the 2π contamination for our bottom channel will cancel out in the ratio method described above. For a detailed calculation of the 2π effects for this experiment, refer to the Ph.D. thesis by Patrick Walden.

PART IV

RESULTS

The π^-/π^+ ratio, π^+ cross sections from deuterium, π^- cross sections from deuterium via the ratio method, via the direct method with pion only detected, and via the direct method with both pion and recoil proton detected are given in Tables 2, 3, and 4 and in Figures 9 and 10.

A. The π^-/π^+ ratio. (Table 2, Figure 9)

The ratio curves show very well the general effect that has been observed in this experiment: the π^- cross section is relatively low compared to the π^+ cross section in the third resonance region at about 1000 MeV photon energy (total CM energy $\simeq$ 1650 MeV). These ratio curves have not been corrected for resolution effects, so that the dip should actually be a little deeper, especially at 45 and 60° CM, where the π^+ cross section shows a pronounced peak at the above energy.

The ratio curves are fairly smooth, indicating a good consistancy from setting to setting in the experiment. There are a few anomalously high points at 135° caused by the π^- results. These are as yet unexplained.

At the angles 20°, 60°, 90°, 120°, 150°, and 160° are plotted the ratio data of Neugebauer(36) (dark points). The agreement is excellent, a result which is not too surprising since the two experiments were performed with almost the same experimental apparatus (nine years apart) at the Caltech synchrotron.

B. The ratio cross sections. (Table 3, Figure 10)

The ratio cross sections have been plotted twice, for comparison with the "recoil" cross sections and the "pion only" cross sections. At small angles, where the ratio cross sections and direct cross sections differ due to final state effects, a few points (half-blacked in) have been artificially generated by interpolation where the π^+ rates were not available to form the ratio. (These points are identified by a * in Table 3.) This was done because we believe the ratio results to be the best indication of the $\gamma n \rightarrow \pi^- p$ cross section at these small angles. The direct cross sections, calculated via the spectator model from the deuterium π^- rates, are expected to be smaller than the γn cross sections due to the above-mentioned final state effects(45). This seems to be born out on our experiment. The difference between our ratio cross sections

and our direct cross sections approaches zero at about 45^{o} CM, a result which is consistant with some preliminary calculations of "spin-flip" and "spin-non-flip" cross sections and the deuterium model used by Chew and Lewis(45). See Part V.

In the ratio cross sections, a simple correction for resolution effects was made at 45^{o} and 60^{o} CM at photon energies around 1000 MeV. (These points are half-blacked in in Figure 10.) Here the (direct) π^- cross section is flat with energy while the π^+ cross section has a pronounced hump. Use of the uncorrected ratio to multiply the Ecklund cross sections would have given a hump to the π^- (ratio) cross section, a result which would be inconsistent with the direct π^- rates. The effect of the correction was, essentially, to set the π^- ratio cross section equal to the direct (pion only) cross section at these few points. A complete unfolding of the cross sections was not done.

C. Direct π^+ cross sections from deuterium. (Table 3, Figure 9)

The π^+ cross sections from deuterium (calculated by method 3 in Section III.A) have been plotted for comparison with the

fits made by Ecklund(6) of the π^+ cross sections from hydrogen measured by Ecklund(6) and Thiessen(7). The deuterium cross sections are lower in the forward direction, a result which is consistent with the expected drop due to final state effects (45).

However, in the backward direction, the deuterium π^+ results appear anomalously high. This apparent jump in the cross section at 90° seems to be correlated with our switching from the high momentum spectrometer (HEMA) to the low momentum spectrometer (LEM). After much thought and calculation (especially by Pat Walden), we think that this might be due to an electron-positron background at large angles, which we previously thought to be negligible. Since the LEM was not equipped to distinguish pions from electrons (as HEMA was), this background will show up in our direct cross section calculations. Thiessen(50) seemed to observe a similar effect in his π^+ experiment (hydrogen target) at wide angles where he used the same spectrometer. He made a small number of measurements of the effect and has made a fit of the results.

Using this fit and normalizing it to the electron rates observed at 75° with the HEMA, Pat Walden has calculated that this effect could completely account for our high results

at backward angles. The ratio cross sections are relatively insensitive to this effect since the direct (pion only) π^- cross sections have a similar high behavior at backward angles. However, since electrons are not expected to completely cancel in the ratio, a small systematic error in the backward ratio cross sections is indicated. The recoil cross sections are believed to be unaffected by the electron problem because a coincidence of two particles is required.

D. Direct π^- cross section (pion only detected) from deuterium. (Table 3, Figure 10)

The direct π^- cross section calculated via the spectator model from the spectrometer pion rates only is plotted with the ratio cross sections for comparison. The direct cross sections are lower than the ratio cross sections at pion angles less than 45° CM, a result which is again consistent with the Chew and Lewis treatment of final state effects. This gives us hope that the ratio cross section might be a good approximation to the real γn cross section.

As in the π^+ case, the direct π^- cross sections (pion only detected) seem to jump at 90°. As I have said above,

we believe that this is due to an unsubtracted electron background.

E. Direct π^- cross section (both pion and recoil proton detected) from deuterium. (Table 4, Figure 10)

These "recoil" cross sections are plotted with the ratio cross sections for comparison. In general, the two cross sections agree well with each other. There are, however, some specific areas of disagreement. At angles less than 75^o at the smallest energies, the recoil results are off. This is due to the problems encountered when trying to correct for protons which do not escape from the target. The details of this correction and the various difficulties involved are discussed by Patrick Walden (44).

At 105^o the recoil results deviate wildly from the ratio cross sections at low energies. We have not been able to explain this behavior and I am inclined to blame the problem on the recoil electronics which may have been acting up that day. At 150 and 160^o, there are some spots at intermediate energies where the recoil and ratio results disagree. This is a region of poor statistics and large accidentals and perhaps one of these is the cause of the discrepancy.

F. Accidentals and dead time at backward pion angles.

Because of a mistake in the setup of the HEMA and LEM electronics, we were not able to distinguish between some accidentals and dead time corrections. This problem was not severe at angles less than 120^{o} as the maximum possible correction was of the order of one percent or less. However, at larger angles and especially at 150 and 160^{o}, the possible corrections grew to as much as 20%. Since we were unsure whether we should add a correction (for dead time) or subtract a correction (for accidentals), we simply increased the error bars in proportion to the possible correction. Thus, at backward angles, the errors listed are not completely statistical but may contain a systematic component due to our uncertainty about this problem. In any case, all runs with an "accidentals" rate of more than about 4% have been thrown out and are not included in the graphs or tables.

G. Backgrounds. (Figures 9 and 10)

Empty target backgrounds were measured for about two thirds of the π^- settings and for a small number of the π^+ settings. For the π^- settings for which no backgrounds were taken, an interpolated background was used to calculate the

the subtracted π^- direct cross sections. (These interpolated points are indicated by vertical bars in Figure 10) The measured and interpolated backgrounds are plotted along with the direct (subtracted) π^- cross sections to show their general level. The few measured π^+ backgrounds are plotted along with the deuterium π^+ cross sections in Figure 9.

An artificial subtraction has been performed on the deuterium π^+ cross sections using the π^- backgrounds divided by the π^-/π^+ ratio. This is equivalent to assuming that the π^+ backgrounds were the same percentage of the foregrounds as the π^- backgrounds were of their foregrounds. Comparison of the measured π^+ backgrounds to the artificially generated ones gives rough agreement.

The π^-/π^+ ratio was calculated from the foregrounds only, which is equivalent to using the above assumption on the backgrounds. The question of whether we should have taken more π^+ backgrounds is still a moot point; time was a factor, and to reserve more time for π^+ backgrounds would have cut time from taking foreground data. The effect on the ratio of using the foregrounds only is very small except perhaps at backward angles, where the background percentages are highest.

Finally, the backgrounds for the recoil runs were very small and we have neglected them in the calculation of the final recoil cross sections.

TABLE 2

π^-/π^+ RATIO

See Appendix I for explanation of

"lab" photon energy.

Lab Photon Energy (MeV)	CM Pion Angle (deg.)	π^-/π^+ Ratio	Stat. Error	Lab Photon Energy (MeV)	CM Pion Angle (deg.)	π^-/π^+ Ratio	Stat. Error
583.9	6.22	1.169	0.068	1170.3	10.24	0.738	0.099
601.1	6.23	1.207	0.070	1198.2	10.30	0.644	0.090
614.1	6.27	1.162	0.069	1216.7	10.46	0.780	0.107
630.8	6.35	1.231	0.068	1243.9	10.56	0.786	0.112
641.0	6.21	1.277	0.077	583.8	20.20	1.099	0.061
659.1	6.22	1.093	0.068	598.7	20.32	1.175	0.065
674.2	6.30	1.164	0.130	617.0	20.38	1.246	0.069
695.5	6.29	1.290	0.083	632.1	20.57	1.186	0.063
713.4	6.20	1.039	0.059	642.5	20.15	1.112	0.062
730.2	6.25	0.987	0.059	659.6	20.29	1.214	0.067
748.0	6.30	0.908	0.056	677.8	20.41	1.113	0.061
764.5	6.38	1.001	0.063	695.3	20.61	1.207	0.068
874.5	6.28	0.575	0.056	711.5	20.09	1.160	0.051
898.8	6.31	0.603	0.060	731.3	20.21	1.104	0.050
922.2	6.35	0.553	0.058	750.8	20.37	1.016	0.048
947.2	6.43	0.693	0.071	768.0	20.53	0.916	0.045
585.4	10.12	1.305	0.108	786.7	20.24	0.769	0.076
601.1	10.18	1.200	0.080	808.8	20.40	0.745	0.047
616.8	10.23	1.236	0.083	829.9	20.53	0.713	0.045
631.6	10.34	1.128	0.073	850.8	20.72	0.646	0.042
642.0	10.09	1.080	0.074	869.5	20.18	0.634	0.033
659.6	10.13	1.277	0.090	896.1	20.23	0.593	0.031
675.8	10.18	1.100	0.076	919.7	20.44	0.586	0.030
694.8	10.29	1.170	0.081	946.4	20.62	0.600	0.032
711.4	10.00	1.255	0.089	967.5	20.28	0.590	0.027
727.6	10.10	1.169	0.105	994.2	20.37	0.582	0.026
747.8	10.18	0.973	0.076	1026.1	20.45	0.586	0.032
770.8	10.22	1.000	0.075	1054.1	20.62	0.625	0.030
790.1	10.18	0.715	0.044	1069.8	20.24	0.658	0.037
808.3	10.24	0.751	0.046	1096.2	20.41	0.740	0.044
831.3	10.28	0.662	0.042	1124.9	20.64	0.708	0.042
850.1	10.42	0.618	0.040	1158.8	20.75	0.797	0.048
875.3	10.19	0.656	0.046	1166.1	20.24	0.838	0.089
896.4	10.22	0.602	0.045	1192.1	20.40	0.901	0.102
923.9	10.29	0.542	0.042	1220.6	20.56	0.901	0.100
947.4	10.35	0.470	0.039	1240.8	20.70	0.894	0.111
1073.3	10.07	0.648	0.042	585.3	30.17	1.122	0.070
1096.3	10.20	0.763	0.118	599.4	30.34	1.081	0.065
1121.7	10.29	0.802	0.058	616.5	30.49	1.108	0.065
1156.4	10.36	0.745	0.075	632.8	30.76	1.098	0.065

Lab Photon Energy (MeV)	CM Pion Angle (deg.)	π^-/π^+ Ratio	Stat. Error
644.6	30.05	1.085	0.051
658.1	30.34	1.030	0.076
676.5	30.52	1.067	0.050
693.1	30.84	1.040	0.048
710.8	30.13	0.965	0.043
728.4	30.37	0.901	0.040
752.0	30.45	0.969	0.045
771.2	30.79	0.844	0.041
785.7	30.16	0.688	0.053
810.9	30.20	0.810	0.063
830.6	30.53	0.662	0.053
856.3	30.72	0.642	0.051
874.1	30.03	0.682	0.026
899.2	30.19	0.646	0.031
923.9	30.44	0.647	0.023
949.9	30.71	0.590	0.022
968.9	30.03	0.608	0.035
998.1	30.18	0.600	0.027
1025.0	30.41	0.577	0.026
1056.7	30.62	0.688	0.032
1164.2	29.99	0.880	0.053
1195.2	30.15	0.916	0.058
1230.5	30.40	0.876	0.058
1264.6	30.68	0.920	0.063
585.0	45.07	0.959	0.078
602.5	45.13	0.964	0.076
617.7	45.57	0.887	0.070
633.3	45.99	0.929	0.069
640.8	45.15	0.832	0.046
659.6	45.34	0.841	0.047
677.5	45.66	0.843	0.046
696.8	45.98	0.797	0.044
712.5	44.96	0.813	0.040
729.4	45.30	0.803	0.040
750.8	45.54	0.756	0.050
773.3	45.87	0.664	0.035
786.2	44.83	0.703	0.031
807.4	45.20	0.712	0.052
833.1	45.44	0.695	0.040
854.8	45.90	0.629	0.030
875.0	44.92	0.623	0.040
898.0	45.19	0.566	0.036
922.0	45.63	0.542	0.035
949.8	45.99	0.527	0.078
971.5	44.78	0.545	0.026
996.8	45.24	0.565	0.029
1027.4	45.57	0.552	0.027
1058.4	45.84	0.568	0.029
1062.3	44.88	0.636	0.030
1098.5	45.02	0.647	0.034
1128.3	45.48	0.768	0.041
1161.6	45.79	0.790	0.045
1161.8	44.77	0.900	0.113
1194.2	45.22	0.933	0.060
1233.7	45.49	0.932	0.064
1270.1	45.83	0.834	0.060
585.5	59.89	0.893	0.058
599.2	60.38	0.920	0.060
619.3	60.54	0.896	0.056
636.2	60.97	0.841	0.052
640.1	59.87	0.832	0.032
659.6	60.14	0.755	0.027
679.2	60.48	0.748	0.033
701.2	60.86	0.714	0.024
707.6	59.89	0.743	0.034
730.6	60.14	0.707	0.057
751.1	60.59	0.691	0.035
776.0	60.99	0.735	0.042
786.1	59.70	0.703	0.044
808.8	60.11	0.618	0.031
835.3	60.52	0.664	0.034
858.6	61.04	0.554	0.031
872.7	59.74	0.587	0.047
898.9	60.22	0.603	0.048
925.2	60.57	0.520	0.041
957.7	60.96	0.427	0.035
967.3	59.60	0.437	0.030
998.7	60.03	0.472	0.027
1028.8	60.49	0.442	0.026
1064.5	60.82	0.509	0.034

Lab Photon Energy (MeV)	CM Pion Angle (deg.)	π^-/π^+ Ratio	Stat. Error
1063.1	59.69	0.481	0.031
1102.7	59.90	0.620	0.043
1131.9	60.47	0.629	0.091
1168.7	60.91	0.820	0.074
1160.3	59.43	0.712	0.058
1196.2	59.89	0.828	0.076
1232.8	60.53	0.837	0.082
1276.9	60.75	0.921	0.104
581.8	74.78	0.852	0.034
599.0	75.32	0.825	0.030
617.4	75.52	0.818	0.050
638.3	75.85	0.790	0.031
639.6	74.67	0.834	0.063
659.1	75.15	0.699	0.071
680.0	75.51	0.818	0.051
699.7	75.97	0.809	0.043
706.1	74.47	0.758	0.043
731.5	74.96	0.802	0.047
752.1	75.59	0.704	0.045
774.4	76.03	0.604	0.044
783.5	74.59	0.660	0.060
809.1	75.03	0.564	0.057
834.9	75.43	0.628	0.070
865.4	75.82	0.577	0.073
866.6	74.56	0.448	0.034
897.8	74.96	0.554	0.044
925.0	75.44	0.391	0.047
959.7	75.84	0.350	0.045
964.9	74.67	0.345	0.028
996.6	74.98	0.399	0.034
1030.7	75.41	0.363	0.035
1064.0	75.95	0.418	0.041
1059.4	74.42	0.379	0.036
1094.1	74.77	0.498	0.049
1132.1	75.44	0.647	0.073
1169.4	75.76	0.647	0.138
1156.3	74.24	0.656	0.104
1198.2	74.83	0.701	0.118
1233.7	75.41	0.815	0.151
1274.8	75.80	0.890	0.181
579.8	89.70	0.916	0.057
598.5	90.06	1.014	0.058
619.2	90.43	0.973	0.060
637.9	90.86	0.919	0.077
636.0	89.54	0.700	0.040
657.6	89.85	0.755	0.043
679.0	90.49	0.773	0.041
700.8	90.78	0.754	0.041
702.6	89.32	0.750	0.025
725.3	89.89	0.757	0.035
750.2	90.33	0.736	0.048
776.1	90.72	0.702	0.029
780.3	89.16	0.719	0.034
803.3	89.92	0.679	0.035
833.1	90.26	0.591	0.036
860.9	90.71	0.557	0.039
577.3	104.4	1.041	0.068
598.7	104.6	1.096	0.120
617.3	105.2	1.058	0.067
637.0	105.6	1.034	0.064
633.4	104.1	1.056	0.073
655.8	104.8	1.024	0.088
676.9	105.1	0.834	0.092
698.3	105.7	0.965	0.065
769.6	104.1	0.725	0.039
799.5	104.7	0.738	0.043
829.2	105.1	0.594	0.046
857.9	105.5	0.604	0.085
854.6	103.8	0.591	0.045
886.6	104.6	0.544	0.045
920.1	105.0	0.553	0.048
949.9	104.9	0.553	0.051
949.5	103.8	0.563	0.069
982.5	104.3	0.590	0.043
1014.8	104.8	0.504	0.040
1051.1	105.3	0.628	0.069
1035.6	108.6	0.672	0.038
1075.1	109.1	0.637	0.041
1115.8	109.6	0.659	0.047
1154.3	109.8	0.577	0.043

Lab Photon Energy (MeV)	CM Pion Angle (deg.)	π^-/π^+ Ratio	Stat. Error	Lab Photon Energy (MeV)	CM Pion Angle (deg.)	π^-/π^+ Ratio	Stat. Error
574.1	119.0	1.421	0.088	681.3	133.7	1.462	0.102
592.5	119.6	1.449	0.085	710.3	134.2	1.285	0.089
617.4	119.9	1.215	0.068	737.7	134.7	1.155	0.085
638.6	120.5	1.470	0.081	767.3	134.6	1.436	0.118
628.0	118.9	1.445	0.091	750.4	133.6	1.526	0.113
652.8	119.5	1.537	0.094	787.3	133.9	1.078	0.086
673.2	119.9	1.231	0.075	814.9	134.7	1.009	0.088
698.1	120.4	1.121	0.069	847.2	134.6	0.906	0.086
692.5	118.9	1.109	0.065	831.2	133.5	1.064	0.089
716.6	119.5	0.966	0.059	865.3	133.9	0.994	0.085
744.0	119.6	1.000	0.063	901.8	134.2	1.045	0.099
769.6	120.0	0.873	0.065	926.0	134.8	0.774	0.084
762.1	119.0	0.897	0.059	926.8	133.6	0.763	0.072
794.0	119.2	0.817	0.057	974.8	134.3	0.777	0.077
824.5	119.7	0.702	0.055	1017.6	134.5	0.695	0.073
850.3	120.2	0.665	0.060	1063.1	135.0	0.659	0.079
846.0	118.9	0.633	0.058	1012.1	133.6	0.599	0.072
878.8	119.0	0.642	0.059	1058.8	133.7	0.581	0.074
909.6	119.7	0.604	0.057	1114.5	134.3	0.568	0.080
944.6	120.0	0.562	0.058	1166.4	134.8	0.772	0.117
943.8	118.8	0.576	0.054	563.6	149.0	2.098	0.169
984.4	119.5	0.522	0.054	584.3	149.1	2.344	0.194
1023.7	120.0	0.520	0.053	611.5	149.2	2.289	0.185
1074.9	120.6	0.572	0.064	629.4	149.5	2.762	0.243
1020.2	118.3	0.550	0.034	617.7	148.8	2.230	0.180
1071.0	118.7	0.533	0.036	640.9	148.9	2.451	0.202
1105.1	119.3	0.711	0.080	666.8	149.3	2.497	0.210
1147.0	119.7	0.558	0.059	690.5	149.3	2.376	0.207
1109.4	118.0	0.643	0.054	679.9	148.6	1.861	0.170
1159.3	118.7	0.720	0.059	706.6	149.2	1.956	0.176
1205.4	119.0	0.696	0.071	733.8	149.1	2.126	0.216
1247.3	119.7	0.716	0.110	755.4	149.3	1.696	0.178
570.7	134.2	2.195	0.164	815.0	148.1	1.663	0.158
587.3	134.1	1.895	0.135	852.4	148.6	1.273	0.128
611.6	134.6	1.849	0.132	898.2	148.8	1.277	0.135
633.7	135.0	2.009	0.154	924.7	149.3	1.266	0.147
622.0	133.8	2.000	0.151	912.3	148.4	1.412	0.152
647.1	134.4	1.843	0.135	953.4	148.6	1.087	0.117
668.4	134.5	1.650	0.118	1006.6	149.2	1.199	0.133
694.1	134.8	1.815	0.141	1057.8	149.7	0.912	0.117

Lab Photon Energy (MeV)	CM Pion Angle (deg.)	π^-/π^+ Ratio	Stat. Error
993.6	148.3	1.107	0.134
1053.9	149.2	0.944	0.115
1104.0	149.5	0.981	0.130
1162.2	149.7	1.171	0.176
1062.9	147.9	0.984	0.123
1114.9	148.4	0.970	0.137
1155.6	148.5	0.948	0.156
1211.9	148.8	0.633	0.122
610.4	158.5	2.495	0.223
636.6	158.6	2.719	0.234
660.4	158.8	3.240	0.300
688.0	158.9	3.095	0.284
673.4	158.6	2.581	0.266
698.4	158.8	2.838	0.307
725.8	158.8	2.163	0.227
755.1	159.0	2.167	0.240
821.3	158.5	2.110	0.211
862.4	158.8	1.794	0.182
906.2	159.0	1.657	0.172
945.7	159.3	1.699	0.190
898.5	158.3	1.923	0.210
949.3	158.7	1.582	0.164
1005.2	159.0	1.740	0.219
1046.4	159.1	1.701	0.228
992.4	158.7	1.482	0.172
1024.7	158.6	1.562	0.149
1081.5	159.1	1.428	0.160
1137.0	159.0	1.752	0.183
1044.2	158.3	1.474	0.211
1104.4	158.4	1.329	0.206
1146.7	158.4	1.342	0.217
1178.1	158.2	1.007	0.188

TABLE 3

1) π^+ (Direct) Cross Section from Deuterium
(pion only detected)

2) π^- (Direct) Cross Section from Deuterium
(pion only detected)

3) π^- (Ratio) Cross Section (neutron cross section calculated from π^-/π^+ ratio and free proton cross section)

See Appendix I for explanation
of "lab" photon energy.

* indicates artificial (interpolated) cross section

Lab Photon Energy (MeV)	CM Pion Angle (deg.)	π^+ Cross Section (μb/sr)	Stat. Error	π^- Cross Section (μb/sr)	Stat. Error	Ratio Cross Section (μb/sr)	Stat. Error
583.9	6.22	14.78	0.75	17.20	0.73	20.72	1.21
601.1	6.23	14.75	0.74	17.65	0.74	21.44	1.24
614.1	6.27	14.96	0.79	17.54	0.71	21.13	1.26
630.8	6.35	14.73	0.72	18.21	0.71	22.00	1.22
641.0	6.21	14.92	0.80	19.23	0.91	23.12	1.39
659.1	6.22	15.01	0.80	16.06	0.85	20.26	1.26
674.2	6.30	14.51	1.66	16.94	0.84	21.29	2.38
695.5	6.29	12.09	0.69	15.73	0.80	22.54	1.45
713.4	6.20	14.29	0.74	14.98	0.68	17.83	1.01
730.2	6.25	13.04	0.69	12.75	0.63	15.30	0.91
748.0	6.30	12.14	0.65	10.84	0.58	13.47	0.84
764.5	6.38	11.13	0.62	11.31	0.57	14.59	0.92
790.9	6.25			10.71	0.55	13.15*	0.48
808.7	6.25			10.25	0.49	12.13*	0.44
828.6	6.33			8.64	0.45	10.54*	0.41
848.8	6.39			7.72	0.41	9.41*	0.38
874.5	6.28	10.23	0.85	5.41	0.54	7.76	0.75
898.8	6.31	9.17	0.78	5.64	0.50	7.59	0.76
922.2	6.35	8.61	0.74	4.74	0.46	6.78	0.70
947.2	6.43	7.58	0.68	5.63	0.47	7.40	0.76
1070.8	6.14			3.80	0.36	5.03*	0.33
1097.4	6.18			4.16	0.35	5.48*	0.30
1123.7	6.26			3.41	0.52	4.41*	0.51
1155.6	6.34			3.09	0.30	4.34*	0.26
1170.0	6.41			4.13	0.45	4.92*	0.35
1191.5	6.58			4.03	0.43	4.68*	0.35
1213.7	6.69			3.30	0.44	4.30*	0.33
1250.2	6.70			3.06	0.40	3.86*	0.30
585.4	10.12	12.68	0.72	16.57	1.11	20.32	1.68
601.1	10.18	13.72	0.75	16.45	0.78	18.63	1.24
616.8	10.23	12.55	0.70	15.54	0.73	19.42	1.31
631.6	10.34	13.84	0.73	15.57	0.73	17.38	1.12
642.0	10.09	13.46	0.72	14.66	0.77	17.00	1.16
659.6	10.13	11.73	0.67	14.94	0.79	20.27	1.43
675.8	10.18	12.55	0.69	13.58	0.75	17.17	1.19
694.8	10.29	11.76	0.65	13.88	0.72	17.55	1.21
711.4	10.00	10.86	0.65	13.41	0.66	18.57	1.32
727.6	10.10	10.26	0.63	12.06	0.88	15.90	1.43
747.8	10.18	11.36	0.66	11.16	0.67	12.30	0.96
770.8	10.22	10.21	0.62	10.26	0.55	12.07	0.90

Lab Photon Energy (MeV)	CM Pion Angle (deg.)	π^+ Cross Section (μb/sr)	Stat. Error	π^- Cross Section (μb/sr)	Stat. Error	Ratio Cross Section (μb/sr)	Stat. Error
790.1	10.18	10.28	0.47	7.20	0.39	8.55	0.52
808.3	10.24	9.78	0.46	7.39	0.38	9.01	0.55
831.3	10.28	9.46	0.44	6.22	0.35	7.62	0.49
850.1	10.42	9.16	0.43	5.81	0.32	6.89	0.45
875.3	10.19	8.85	0.44	5.81	0.38	7.29	0.52
896.4	10.22	8.06	0.41	4.83	0.34	6.31	0.47
923.9	10.29	8.05	0.40	4.29	0.32	5.42	0.42
947.4	10.35	7.60	0.39	3.66	0.28	4.17	0.35
970.5	10.17			3.40	0.27	4.27*	0.25
994.8	10.25			3.56	0.28	4.43*	0.26
1025.2	10.31			2.86	0.25	3.78*	0.23
1050.8	10.38			3.42	0.28	4.14*	0.28
1073.3	10.07	5.04	0.28	3.35	0.18	3.83	0.25
1096.3	10.20	4.14	0.25	3.18	0.50	4.11	0.63
1121.7	10.29	3.91	0.24	3.09	0.20	3.86	0.28
1156.4	10.36	3.90	0.24	3.04	0.28	3.17	0.32
1170.3	10.24	3.73	0.34	2.84	0.31	3.22	0.43
1198.2	10.30	3.91	0.36	2.48	0.31	2.62	0.37
1216.7	10.46	3.54	0.34	2.65	0.32	2.99	0.41
1243.9	10.56	3.11	0.31	2.50	0.29	2.77	0.39
583.8	20.20	11.02	0.49	12.17	0.50	13.02	0.73
598.7	20.32	10.64	0.48	12.46	0.51	13.81	0.76
617.0	20.38	9.87	0.45	12.29	0.50	14.32	0.79
632.1	20.57	10.42	0.45	12.36	0.49	13.71	0.74
642.5	20.15	10.77	0.48	12.05	0.50	13.15	0.73
659.6	20.29	10.14	0.46	12.22	0.51	14.17	0.78
677.8	20.41	10.23	0.46	11.30	0.48	13.03	0.72
695.3	20.61	9.30	0.43	11.33	0.46	13.98	0.78
711.5	20.09	9.38	0.33	10.96	0.39	13.24	0.58
731.3	20.21	8.82	0.32	9.72	0.36	11.62	0.53
750.8	20.37	8.03	0.30	8.10	0.33	9.86	0.47
768.0	20.53	7.95	0.30	7.27	0.31	8.30	0.41
786.7	20.24	7.58	0.69	5.80	0.33	6.87	0.68
808.8	20.40	7.29	0.28	5.47	0.31	6.62	0.41
829.9	20.53	7.25	0.28	5.21	0.30	5.90	0.37
850.8	20.72	6.99	0.27	4.47	0.28	5.31	0.35
869.5	20.18	7.53	0.27	4.66	0.22	5.34	0.28
896.1	20.23	7.29	0.26	4.40	0.20	4.96	0.26
919.7	20.44	7.35	0.26	4.28	0.20	4.75	0.24
946.4	20.62	6.91	0.25	4.21	0.19	4.76	0.25

Lab Photon Energy (MeV)	CM Pion Angle (deg.)	π^+ Cross Section (μb/sr)	Stat. Error	π^- Cross Section (μb/sr)	Stat. Error	Ratio Cross Section (μb/sr)	Stat. Error
967.5	20.28	6.76	0.25	3.90	0.12	4.73	0.21
994.2	20.37	6.88	0.26	3.98	0.12	4.57	0.21
1026.1	20.45	6.43	0.24	3.77	0.11	4.40	0.24
1054.1	20.62	5.60	0.22	3.55	0.11	4.25	0.20
1069.8	20.24	5.80	0.22	3.86	0.19	4.32	0.24
1096.2	20.41	4.79	0.20	3.56	0.18	4.42	0.26
1124.9	20.64	4.95	0.20	3.50	0.18	3.72	0.22
1158.8	20.75	4.31	0.19	3.38	0.18	3.69	0.22
1166.1	20.24	3.75	0.23	3.14	0.29	3.80	0.40
1192.1	20.40	3.06	0.20	2.74	0.27	4.00	0.45
1220.6	20.56	3.27	0.21	2.94	0.28	3.81	0.42
1249.8	20.70	2.62	0.19	2.36	0.25	3.62	0.45
585.3	30.17	9.25	0.44	10.49	0.46	12.26	0.76
599.4	30.34	9.87	0.45	10.59	0.47	11.71	0.70
616.5	30.49	9.71	0.44	10.70	0.46	11.86	0.70
632.8	30.76	9.56	0.43	10.52	0.45	11.82	0.70
644.6	30.05	9.67	0.35	10.52	0.38	11.95	0.56
658.1	30.34	9.87	0.68	10.01	0.38	11.40	0.85
676.5	30.52	9.24	0.34	9.91	0.36	12.12	0.57
693.1	30.84	9.37	0.34	9.82	0.35	11.78	0.55
710.8	30.13	10.05	0.34	9.71	0.33	10.80	0.48
728.4	30.37	10.23	0.35	9.17	0.32	9.30	0.41
752.0	30.45	8.52	0.31	8.29	0.30	9.09	0.42
771.2	30.79	8.25	0.30	6.96	0.27	7.32	0.35
785.7	30.16	7.73	0.46	5.28	0.29	5.76	0.44
810.9	30.20	6.98	0.44	5.70	0.30	6.55	0.51
830.6	30.53	6.98	0.43	4.64	0.26	5.02	0.40
856.3	30.72	7.26	0.44	4.63	0.27	4.87	0.38
874.1	30.03	6.72	0.18	4.61	0.15	5.38	0.20
899.2	30.19	6.91	0.19	4.49	0.16	5.32	0.26
923.9	30.44	7.09	0.20	4.54	0.15	5.25	0.19
949.9	30.71	7.06	0.18	4.18	0.15	5.00	0.18
968.9	30.03	7.90	0.29	4.72	0.18	5.41	0.31
998.1	30.18	7.64	0.28	4.44	0.16	5.43	0.24
1025.0	30.41	7.62	0.28	4.33	0.12	5.19	0.23
1056.7	30.62	6.57	0.26	4.50	0.13	5.62	0.26
1064.9	30.02	6.49	0.25				
1095.8	30.24	6.06	0.24				
1126.8	30.44	5.24	0.22				
1160.2	30.70	4.67	0.21				

Lab Photon Energy (MeV)	CM Pion Angle (deg.)	π^+ Cross Section (μb/sr)	Stat. Error	π^- Cross Section (μb/sr)	Stat. Error	Ratio Cross Section (μb/sr)	Stat. Error
1065.2	30.04			4.57	0.21	5.08*	0.21
1094.0	30.26			4.28	0.21	4.85*	0.20
1128.3	30.42			4.36	0.20	4.81*	0.20
1160.3	30.68			4.47	0.21	4.90*	0.21
1164.2	29.99	4.91	0.22	4.31	0.22	4.44	0.27
1195.2	30.15	4.29	0.20	3.76	0.22	4.32	0.27
1230.5	30.40	3.94	0.19	3.54	0.19	3.85	0.26
1264.6	30.68	3.75	0.19	3.54	0.19	3.94	0.27
585.0	45.07	9.65	0.46	9.28	0.65	10.08	0.82
602.5	45.13	9.99	0.46	9.48	0.65	10.21	0.80
617.7	45.57	10.25	0.46	9.15	0.63	9.53	0.75
633.3	45.99	11.08	0.48	10.36	0.66	9.97	0.74
640.8	45.15	10.56	0.42	8.82	0.37	9.07	0.50
659.6	45.34	9.59	0.39	8.00	0.35	9.57	0.54
677.5	45.66	10.10	0.40	8.47	0.36	9.95	0.54
696.8	45.98	9.80	0.39	7.88	0.34	9.29	0.52
712.5	44.96	10.23	0.49	8.40	0.21	9.39	0.47
729.4	45.30	10.05	0.48	8.12	0.20	8.34	0.41
750.8	45.54	9.04	0.44	6.76	0.35	7.16	0.48
773.3	45.87	8.84	0.44	5.80	0.17	5.65	0.30
786.2	44.83	7.65	0.26	5.30	0.18	5.50	0.24
807.4	45.20	6.65	0.46	4.67	0.17	5.04	0.37
833.1	45.44	6.50	0.33	4.43	0.16	4.57	0.26
854.8	45.90	6.58	0.24	3.96	0.30	4.00	0.19
875.0	44.92	6.49	0.30	4.27	0.20	4.17	0.27
898.0	45.19	7.21	0.32	3.87	0.15	4.08	0.26
922.0	45.63	6.88	0.31	3.82	0.15	4.00	0.26
949.8	45.99	7.77	0.34	4.02	0.31	4.12	0.61
971.5	44.75	7.78	0.21	4.32	0.15	4.33	0.23
997.5	45.21	8.03	0.21	4.42	0.18	4.67	0.26
1027.1	45.55	7.52	0.20	4.10	0.15	4.29	0.24
1059.1	45.81	6.58	0.19	3.77	0.14	3.73	0.24
1063.3	44.84	6.80	0.42				
1097.9	45.02	6.04	0.23				
1128.5	45.46	4.72	0.20				
1162.1	45.78	4.39	0.24				
1062.3	44.88			4.22	0.13	4.38	0.24
1098.5	45.02			3.89	0.15	4.20	0.22
1128.3	45.48			3.62	0.12	4.02	0.21
1161.6	45.79			3.37	0.12	3.36	0.20

Lab Photon Energy (MeV)	CM Pion Angle (deg.)	π^+ Cross Section (μb/sr)	Stat. Error	π^- Cross Section (μb/sr)	Stat. Error	Ratio Cross Section (μb/sr)	Stat. Error
1161.8	44.77	4.02	0.21	3.56	0.44	3.91	0.49
1194.2	45.22	3.62	0.20	3.44	0.15	3.50	0.23
1233.7	45.49	3.17	0.18	2.89	0.15	3.05	0.21
1270.1	45.83	3.19	0.19	2.72	0.14	2.63	0.19
585.5	59.89	9.41	0.53	8.48	0.32	8.50	0.55
599.2	60.38	8.83	0.51	8.03	0.32	8.96	0.59
619.3	60.54	9.32	0.51	8.35	0.32	8.92	0.56
636.2	60.97	9.79	0.52	8.25	0.32	8.63	0.53
640.1	59.87	9.84	0.46	8.14	0.30	8.69	0.33
659.6	60.14	11.06	0.32	8.42	0.41	8.18	0.30
679.2	60.48	10.24	0.46	7.84	0.30	8.42	0.37
701.2	60.86	10.45	0.35	7.61	0.29	8.03	0.27
707.6	59.89	10.05	0.59	7.41	0.23	8.35	0.38
730.6	60.14	9.13	0.55	7.02	0.22	7.26	0.58
751.1	60.59	8.44	0.53	6.11	0.24	6.28	0.32
776.0	60.99	6.69	0.47	5.07	0.25	5.57	0.31
786.1	59.70	6.73	0.22	4.65	0.21	4.83	0.30
808.8	60.11	6.30	0.24	3.86	0.15	3.50	0.18
835.3	60.52	5.42	0.20	3.35	0.14	3.12	0.17
858.6	61.04	5.36	0.20	2.96	0.13	2.56	0.14
872.7	59.74	5.06	0.28	2.92	0.14	2.81	0.23
898.9	60.22	5.01	0.27	3.01	0.13	3.01	0.24
925.2	60.57	5.50	0.29	2.84	0.13	2.75	0.22
957.7	60.96	5.74	0.30	2.44	0.12	2.45	0.20
967.3	59.60	5.82	0.26			2.63	0.19
998.7	60.03	5.88	0.26			2.82	0.19
1028.8	60.49	5.80	0.26			2.59	0.17
1064.5	60.82	4.83	0.25			2.88	0.19
967.5	59.60			2.70	0.09		
999.1	60.02			2.73	0.08		
1028.2	60.52			2.76	0.10		
1063.0	60.88			2.66	0.12		
1063.1	59.69	5.36	0.25	2.55	0.14	2.84	0.18
1102.7	59.90	3.97	0.21	2.47	0.13	2.74	0.19
1131.9	60.47	3.54	0.20	2.23	0.31	2.17	0.32
1168.7	60.91	2.30	0.16	1.90	0.12	2.04	0.18
1160.3	59.43	2.90	0.19	2.07	0.11	2.03	0.17
1196.2	59.89	2.22	0.17	1.84	0.10	1.84	0.17
1232.8	60.53	1.89	0.15	1.58	0.10	1.47	0.14
1276.9	60.75	1.57	0.15	1.44	0.10	1.46	0.16

Lab Photon Energy (MeV)	CM Pion Angle (deg.)	π^+ Cross Section (μb/sr)	Stat. Error	π^- Cross Section (μb/sr)	Stat. Error	Ratio Cross Section (μb/sr)	Stat. Error
581.8	74.79	8.54	0.26	7.19	0.24	6.71	0.27
598.8	75.32	8.99	0.26	7.41	0.25	6.62	0.24
617.3	75.51	8.99	0.26	7.24	0.61	6.77	0.42
638.3	75.85	9.17	0.59	7.12	0.73	6.95	0.27
639.5	74.64	8.58	0.26	7.20	0.53	7.47	0.56
659.1	75.23	9.73	0.91	7.14	0.19	6.42	0.65
680.0	75.52	9.01	0.22	7.45	0.37	7.98	0.50
699.7	75.97	8.44	0.22	6.95	0.30	7.97	0.42
706.1	74.47	8.66	0.36			7.62	0.44
731.5	74.96	8.24	0.36			7.69	0.45
752.1	75.59	7.26	0.33			5.67	0.36
774.4	76.03	6.26	0.31			4.03	0.29
706.9	74.55			6.59	0.24		
730.9	74.98			6.26	0.39		
753.3	75.51			5.05	0.20		
776.4	75.90			3.85	0.18		
783.5	74.59	5.72	0.38	3.71	0.18	3.98	0.36
809.1	75.03	5.22	0.37	3.14	0.16	2.54	0.26
834.9	75.43	3.96	0.32	2.52	0.15	2.28	0.25
865.4	75.82	3.37	0.30	1.81	0.13	1.77	0.22
866.6	74.56	3.93	0.22	1.75	0.10	1.42	0.11
897.8	74.96	3.32	0.20	1.85	0.11	1.63	0.13
925.0	75.44	3.64	0.21	1.42	0.16	1.21	0.14
959.7	75.84	3.37	0.37	1.18	0.09	1.12	0.14
964.9	74.67	3.84	0.25	1.34	0.06	1.19	0.10
996.6	74.98	3.31	0.23	1.29	0.06	1.46	0.12
1030.7	75.41	3.31	0.23	1.20	0.05	1.28	0.12
1064.0	75.95	2.89	0.24	1.18	0.06	1.26	0.12
1059.4	74.42	3.05	0.20	1.13	0.09	1.27	0.12
1094.1	74.77	2.48	0.18	1.24	0.09	1.30	0.13
1132.1	75.44	1.68	0.15	1.08	0.09	1.25	0.14
1169.4	75.76	1.35	0.14	0.89	0.17	0.83	0.18
1156.3	74.24	1.65	0.15	1.01	0.08	1.09	0.17
1198.2	74.83	1.28	0.13	0.85	0.07	0.85	0.14
1233.7	75.41	1.01	0.12	0.81	0.07	0.74	0.14
1274.8	75.80	0.90	0.12	0.74	0.08	0.68	0.14
579.8	89.70	7.18	0.32	6.51	0.33	5.74	0.36
598.5	90.06	7.22	0.33	7.34	0.32	6.19	0.36
619.2	90.43	7.30	0.33	7.10	0.35	6.34	0.39
637.9	90.86	7.62	0.34	7.06	0.54	6.26	0.52

Lab Photon Energy (MeV)	CM Pion Angle (deg.)	π^+ Cross Section (μb/sr)	Stat. Error	π^- Cross Section (μb/sr)	Stat. Error	Ratio Cross Section (μb/sr)	Stat. Error
636.0	89.54	7.56	0.32	5.29	0.26	4.87	0.28
657.6	89.85	7.58	0.33	5.74	0.27	5.48	0.31
679.0	90.49	8.48	0.35	6.60	0.29	6.09	0.32
700.8	90.78	8.60	0.37	6.44	0.31	6.07	0.33
702.6	89.32	8.37	0.21	6.30	0.18	6.20	0.21
725.4	89.88	8.10	0.21	6.09	0.31	6.31	0.29
750.3	90.32	6.79	0.36	5.01	0.16	5.16	0.34
776.0	90.72	5.92	0.24	4.20	0.16	3.99	0.17
780.3	89.16	6.43	0.24	4.62	0.19	3.96	0.19
803.3	89.92	5.55	0.22	3.80	0.17	2.90	0.15
833.1	90.26	4.39	0.19	2.61	0.14	1.95	0.12
860.9	90.71	3.72	0.18	2.01	0.14	1.40	0.10
577.3	104.3	5.28	0.29	5.55	0.26	5.08	0.33
598.7	104.6	5.49	0.59	6.02	0.28	5.17	0.57
617.3	105.2	5.66	0.31	5.89	0.28	5.30	0.33
637.0	105.6	6.38	0.35	6.63	0.31	5.36	0.33
633.4	104.1	6.02	0.32	6.38	0.34	5.58	0.38
655.8	104.8	6.41	0.49	6.60	0.35	5.77	0.50
676.9	105.1	6.87	0.71	5.74	0.33	5.12	0.56
698.3	105.7	6.93	0.36	6.64	0.37	6.14	0.41
698.0	104.4	6.52	0.26				
723.7	104.8	7.03	0.27				
749.1	105.2	6.18	0.26				
775.5	105.4	5.10	0.25				
696.6	104.0			5.75	0.23		
720.5	104.6			5.56	0.23		
750.7	105.0			4.09	0.20		
775.2	105.5			3.99	0.20		
769.6	104.1	5.80	0.24	4.30	0.18	3.84	0.21
799.5	104.7	4.93	0.22	3.59	0.15	3.18	0.18
829.2	105.1	4.27	0.21	2.72	0.22	2.05	0.16
857.9	105.5	3.54	0.20	2.15	0.19	1.64	0.23
854.6	103.8	3.52	0.19	2.06	0.10	1.63	0.12
886.6	104.6	3.21	0.18	1.82	0.10	1.35	0.11
920.1	105.0	3.02	0.18	1.69	0.10	1.36	0.12
949.9	104.9	3.03	0.20	1.48	0.14	1.38	0.13
949.5	103.8	2.99	0.16	1.75	0.20	1.38	0.17
982.5	104.3	3.16	0.17	1.93	0.11	1.43	0.10
1014.8	104.8	3.10	0.18	1.53	0.11	1.15	0.10
1051.1	105.3	2.43	0.17	1.42	0.16	1.15	0.13

Lab Photon Energy (MeV)	CM Pion Angle (deg.)	π^+ Cross Section (μb/sr)	Stat. Error	π^- Cross Section (μb/sr)	Stat. Error	Ratio Cross Section (μb/sr)	Stat. Error
1035.6	108.6	2.26	0.14	1.62	0.10	1.50	0.08
1075.1	109.1	2.04	0.14	1.27	0.11	1.01	0.06
1115.8	109.6	1.71	0.11	1.14	0.10	0.62	0.04
1154.3	109.8	1.60	0.12	0.84	0.12	0.35	0.03
574.1	119.0	4.32	0.22	6.14	0.29	5.09	0.32
592.5	119.6	4.37	0.21	6.34	0.29	5.49	0.32
617.4	119.9	4.75	0.21	5.75	0.29	4.75	0.27
638.6	120.5	4.69	0.22	6.92	0.33	6.03	0.33
628.0	118.9	4.43	0.23	6.40	0.30	5.86	0.37
652.8	119.5	4.65	0.24	7.17	0.32	6.86	0.42
673.2	119.9	5.23	0.26	6.43	0.31	5.84	0.36
698.1	120.3	5.88	0.31	6.59	0.34	5.84	0.36
692.5	118.9	5.48	0.26	6.11	0.28	5.76	0.34
716.6	119.5	5.43	0.26	5.25	0.26	5.41	0.33
744.0	119.6	5.25	0.27	5.25	0.28	5.08	0.32
769.6	120.0	4.31	0.25	3.72	0.24	3.91	0.29
762.1	119.0	4.58	0.24	4.15	0.23	4.22	0.28
794.0	119.2	4.63	0.25	3.81	0.23	3.30	0.23
824.5	119.7	4.08	0.24	2.85	0.20	2.31	0.18
850.3	120.2	3.61	0.24	2.36	0.20	1.98	0.18
846.0	118.9	3.73	0.23	2.36	0.19	1.92	0.18
878.8	119.0	4.00	0.25	2.57	0.21	1.83	0.17
909.6	119.7	3.97	0.26	2.40	0.20	1.77	0.17
944.6	120.0	4.05	0.29	2.27	0.22	1.68	0.17
943.8	118.8	3.12	0.23	1.86	0.17	1.71	0.16
984.4	119.5	2.73	0.21	1.51	0.14	1.67	0.17
1023.7	120.0	2.84	0.22	1.44	0.16	1.53	0.16
1074.9	120.6	2.32	0.20	1.21	0.17	1.12	0.13
1020.2	118.3	2.58	0.16	1.50	0.09	1.60	0.10
1071.0	118.7	2.43	0.16	1.26	0.12	1.06	0.07
1105.1	119.3	1.82	0.21	1.32	0.12	0.93	0.10
1147.0	119.7	1.89	0.16	0.98	0.15	0.42	0.04
1109.4	118.0	1.61	0.15	1.15	0.07	0.77	0.06
1159.3	118.7	1.33	0.12	0.79	0.13	0.46	0.04
1205.4	119.0	1.20	0.12	0.91	0.09	0.26	0.03
1247.3	119.7	1.11	0.13	0.78	0.16	0.25	0.04
570.7	134.2	3.29	0.23	7.22	0.37	5.61	0.42
587.3	134.1	3.72	0.24	7.05	0.37	5.70	0.41
611.6	134.6	3.80	0.25	7.02	0.37	6.03	0.43
633.7	135.0	3.52	0.25	7.08	0.40	6.50	0.50

Lab Photon Energy (MeV)	CM Pion Angle (deg.)	π^+ Cross Section (μb/sr)	Stat. Error	π^- Cross Section (μb/sr)	Stat. Error	Ratio Cross Section (μb/sr)	Stat. Error
622.0	133.8	3.64	0.25	7.28	0.39	6.41	0.49
647.1	134.4	4.00	0.26	7.36	0.39	6.35	0.46
668.4	134.5	4.63	0.30	7.65	0.41	6.19	0.44
694.1	134.8	4.14	0.29	7.51	0.44	7.64	0.59
681.3	133.7	4.35	0.27	6.39	0.35	5.81	0.41
710.3	134.2	4.67	0.28	6.01	0.34	5.69	0.39
737.7	134.7	4.53	0.29	5.20	0.33	4.80	0.35
767.3	134.6	3.67	0.27	5.24	0.36	5.28	0.44
750.4	133.6	3.73	0.25	5.79	0.32	6.07	0.45
787.3	133.9	3.74	0.25	4.03	0.28	3.52	0.28
814.9	134.7	3.55	0.26	3.55	0.28	2.78	0.24
847.2	134.6	3.53	0.28	3.14	0.28	2.40	0.23
831.2	133.5	3.39	0.24	3.70	0.25	2.80	0.23
865.3	133.9	3.54	0.26	3.67	0.25	2.75	0.23
901.8	134.2	3.00	0.24	3.07	0.25	2.95	0.28
926.0	134.8	3.37	0.30	2.44	0.27	2.21	0.24
926.8	133.6	3.32	0.25	2.56	0.22	2.20	0.21
974.8	134.3	2.98	0.24	2.42	0.20	2.34	0.23
1017.6	134.5	2.95	0.24	2.03	0.20	2.11	0.22
1063.1	135.0	2.51	0.23	1.54	0.20	1.62	0.20
1012.1	133.6	2.74	0.25	1.60	0.20	1.84	0.22
1058.8	133.7	2.48	0.24	1.49	0.18	1.47	0.19
1114.5	134.3	2.13	0.22	1.23	0.17	0.86	0.12
1166.4	134.8	1.71	0.21	1.29	0.20	0.75	0.11
563.6	149.0	3.33	0.24	6.96	0.38	4.99	0.40
584.3	149.1	3.20	0.24	7.49	0.41	6.35	0.53
611.5	149.2	3.44	0.26	7.89	0.42	6.69	0.54
629.4	149.5	2.97	0.25	8.23	0.46	7.88	0.69
617.7	148.8	3.42	0.25	7.63	0.40	6.40	0.52
640.9	148.9	3.25	0.24	7.97	0.41	7.00	0.58
666.8	149.3	3.30	0.25	8.24	0.44	7.74	0.65
690.5	149.3	3.26	0.26	7.75	0.44	8.03	0.70
679.9	148.6	3.98	0.33	7.43	0.40	5.97	0.54
706.6	149.2	4.18	0.34	8.21	0.42	6.84	0.62
733.8	149.1	3.12	0.29	6.63	0.39	6.92	0.70
755.4	149.3	3.52	0.34	5.94	0.41	5.24	0.36
815.0	148.1	3.03	0.25	5.07	0.34	3.81	0.36
852.4	148.6	3.19	0.26	4.05	0.32	2.94	0.30
898.2	148.8	3.11	0.27	3.96	0.33	3.14	0.33
924.7	149.3	3.20	0.32	4.05	0.37	3.14	0.36

Lab Photon Energy (MeV)	CM Pion Angle (deg.)	π^+ Cross Section (μb/sr)	Stat. Error	π^- Cross Section (μb/sr)	Stat. Error	Ratio Cross Section (μb/sr)	Stat. Error
912.3	148.4	2.68	0.25	3.81	0.28	3.50	0.38
953.4	148.6	3.08	0.28	3.36	0.27	2.67	0.29
1006.6	149.2	2.74	0.26	3.29	0.27	2.99	0.33
1057.8	149.7	2.69	0.28	2.41	0.25	2.00	0.26
993.6	148.3	2.48	0.24			2.76	0.34
1053.9	149.2	2.70	0.25			2.13	0.26
1104.0	149.5	2.43	0.25			1.62	0.22
1162.2	149.7	2.13	0.26			1.38	0.21
994.8	148.4			2.93	0.23		
1054.0	149.1			2.69	0.20		
1103.6	149.4			2.44	0.20		
1157.1	149.7			2.42	0.21		
1062.9	147.9	2.68	0.27	2.55	0.28	2.17	0.27
1114.9	148.4	2.34	0.27	2.37	0.25	1.50	0.21
1155.6	148.5	2.06	0.27	2.02	0.26	1.15	0.19
1211.9	148.8	2.69	0.38	1.62	0.31	0.70	0.14
610.4	158.5	3.01	0.25	7.58	0.41	7.18	0.64
636.6	158.6	3.18	0.25	8.45	0.46	7.63	0.66
660.4	158.8	2.89	0.26	9.51	0.50	9.32	0.86
688.0	158.9	3.35	0.30	10.34	0.59	9.08	0.84
673.4	158.6	3.24	0.31	8.37	0.51	7.32	0.75
698.4	158.8	2.93	0.30	8.33	0.53	8.88	0.96
725.8	158.8	3.58	0.34	7.74	0.52	6.04	0.63
755.1	159.0	3.70	0.38	8.01	0.58	5.46	0.60
821.3	158.5	2.64	0.25	5.48	0.38	4.76	0.48
862.4	158.8	2.93	0.27	5.36	0.37	3.94	0.40
906.2	159.0	2.89	0.27	4.81	0.37	3.83	0.40
945.7	159.3	2.70	0.28	4.56	0.39	4.00	0.45
898.5	158.3	2.51	0.25	4.85	0.35	4.41	0.48
949.3	158.8	3.02	0.28	4.80	0.36	3.72	0.39
1005.2	159.0	2.10	0.23	3.60	0.33	3.86	0.49
1046.4	159.1	2.13	0.25	3.64	0.35	3.22	0.43
992.4	158.7	2.50	0.32	3.55	0.46	3.31	0.38
1024.7	158.6	2.13	0.23	3.35	0.37	3.31	0.32
1081.5	159.1	2.00	0.23	2.64	0.42	2.24	0.25
1137.0	159.0	1.68	0.22	3.28	0.27	2.02	0.21
1044.2	158.3	1.81	0.25	2.97	0.29	2.87	0.41
1104.4	158.4	1.81	0.26	2.53	0.31	1.87	0.29
1146.7	158.4	1.87	0.28	2.46	0.36	1.51	0.24
1178.1	158.2	2.28	0.38	1.92	0.47	1.02	0.19

TABLE 4

"Recoil" Cross Sections

direct calculation from rates where
both pion and nucleon are detected.

1) Forward recoil runs - pion through spectrometer
and recoil proton through recoil counter -
6° - 110° (also 120° points marked *)

2) Reverse recoil runs - recoil proton through spectrometer
and pion through recoil counter -
120° - 160°

See Appendix I for explanation of
"lab" photon energy.

Lab Photon Energy (MeV)	CM Pion Angle (deg.)	Recoil Cross Section (μb/sr)	Stat. Error	Lab Photon Energy (MeV)	CM Pion Angle (deg.)	Recoil Cross Section (μb/sr)	Stat. Error
608.5	44.85	14.21	4.11	714.0	59.47	7.20	0.45
615.6	45.32	17.22	4.09	735.1	59.83	5.86	0.44
632.6	45.42	8.92	2.14	757.9	60.18	5.45	0.39
648.7	45.77	17.45	3.31	782.7	60.58	4.66	0.31
657.4	44.93	10.80	1.65	791.1	59.49	4.16	0.45
673.1	45.18	11.50	1.52	811.2	59.93	3.37	0.41
691.9	45.33	9.18	1.16	839.1	60.35	2.84	0.36
708.0	45.74	10.20	1.15	866.0	60.75	2.21	0.31
725.7	44.77	9.44	0.76	876.4	59.53	1.77	0.49
738.9	45.07	8.89	0.71	906.1	59.86	2.40	0.30
761.6	45.33	5.54	0.41	932.1	60.29	2.27	0.18
783.4	45.62	5.26	0.50	963.3	60.80	2.00	0.16
797.0	44.59	4.94	0.46	971.6	59.35	2.25	0.11
818.7	44.92	4.18	0.36	1004.7	59.79	2.46	0.12
842.3	45.17	4.23	0.36	1036.0	60.20	2.46	0.12
867.6	45.48	3.54	0.32	1069.1	60.67	2.50	0.14
882.7	44.67	5.18	0.47	1067.2	59.58	2.42	0.19
904.7	44.92	3.62	0.35	1101.8	59.89	2.30	0.21
930.7	45.34	4.20	0.38	1135.8	60.29	1.94	0.16
960.8	45.61	3.77	0.35	1174.8	60.70	1.70	0.15
976.9	44.60	3.96	0.28	1163.1	59.41	1.73	0.16
1007.5	44.97	4.05	0.45	1199.2	59.73	1.63	0.14
1038.8	45.26	4.32	0.31	1240.0	60.30	1.30	0.12
1066.3	45.59	3.80	0.27	1281.6	60.70	1.22	0.12
1072.7	44.57	4.14	0.26	586.2	74.41	4.84	0.93
1102.7	44.94	3.78	0.24	604.1	74.84	5.92	0.62
1138.2	45.17	3.27	0.25	622.6	75.21	5.79	0.39
1168.7	45.61	3.47	0.24	641.5	75.66	5.65	0.64
1166.5	44.61	3.03	0.29	642.7	74.55	5.95	0.27
1204.6	44.92	3.23	0.32	662.9	74.96	5.26	0.41
1239.2	45.33	2.81	0.23	684.3	75.33	6.10	0.27
1276.7	45.64	2.67	0.22	706.3	75.76	5.97	0.27
591.0	59.59	7.72	0.62	711.0	74.37	5.98	0.44
605.7	59.91	7.06	0.56	733.5	74.86	6.53	0.48
624.6	60.22	7.58	0.59	757.6	75.23	4.36	0.35
643.1	60.61	8.02	0.59	782.3	75.68	3.54	0.32
645.5	59.57	6.65	0.52	787.4	74.43	3.15	0.22
665.1	59.82	7.06	0.71	812.5	74.93	2.60	0.20
684.5	60.21	7.42	0.52	839.2	75.24	1.95	0.19
706.3	60.68	6.66	0.48	869.1	75.75	1.32	0.13

Lab Photon Energy (MeV)	CM Pion Angle (deg.)	Recoil Cross Section (μb/sr)	Stat. Error	Lab Photon Energy (MeV)	CM Pion Angle (deg.)	Recoil Cross Section (μb/sr)	Stat. Error
871.3	74.41	1.46	0.13	858.2	104.3	1.38	0.10
903.2	74.88	1.30	0.12	892.7	104.8	1.29	0.10
933.1	75.30	1.06	0.11	926.2	105.1	1.21	0.09
964.9	75.82	0.93	0.10	958.0	105.5	1.12	0.11
968.8	74.33	1.05	0.07	953.7	104.2	0.94	0.13
1001.3	74.88	1.00	0.07	991.2	104.6	1.14	0.11
1037.2	75.30	0.89	0.08	1022.5	105.2	0.95	0.10
1072.1	75.70	0.95	0.10	1058.9	105.6	0.77	0.20
1064.3	74.32	0.75	0.09	1043.2	109.3	0.77	0.09
1098.5	74.77	0.90	0.09	1082.1	109.7	0.62	0.09
1138.6	75.32	0.93	0.10	1124.9	110.1	0.46	0.12
1173.5	75.87	0.75	0.09	1165.8	110.5	0.30	0.06
1159.7	74.31	0.78	0.09	594.1	119.8	4.71	0.50
1199.3	74.88	0.72	0.10	605.5	119.7	5.47	0.38
1239.7	75.38	0.70	0.08	626.3	120.0	4.98	0.33
1281.4	75.82	0.67	0.09	648.2	120.1	5.52	0.44
583.0	89.50	5.42	0.58	647.0	119.6	5.58	0.56
601.8	89.87	5.28	0.38	666.7	119.7	6.07	0.49
623.2	90.38	5.40	0.38	688.2	120.0	5.43	0.42
641.5	90.74	5.94	0.46	709.9	120.1	5.96	0.46
639.8	89.53	4.35	0.32	713.6	119.6	5.11	0.35
660.4	89.85	4.79	0.34	735.4	119.8	4.95	0.33
681.5	90.35	5.49	0.36	758.7	119.9	4.10	0.34
703.9	90.71	5.03	0.34	782.9	120.1	3.42	0.31
705.5	89.31	5.21	0.24	789.9	120.1	2.91	0.28
730.2	89.73	4.78	0.22	816.7	120.3	2.34	0.24
754.6	90.23	3.91	0.18	842.0	120.2	2.13	0.23
780.4	90.60	3.08	0.42	864.0	120.2	1.56	0.18
783.1	89.35	3.76	0.23	876.2	119.8	1.64	0.18
810.6	89.79	2.95	0.19	903.9	119.8	1.56	0.17
837.1	90.36	1.85	0.14	929.8	119.8	1.46	0.16
866.2	90.80	1.26	0.12	964.6	119.9	1.22	0.15
636.9	104.4	5.32	0.40	972.5	119.6	1.38	0.16
658.7	104.9	5.81	0.42	1000.0	119.7	1.40	0.16
682.3	105.1	4.87	0.38	1040.7	119.8	0.92	0.13
706.4	105.6	6.42	0.45	1068.4	119.6	0.88	0.12
775.5	104.4	3.56	0.23	1119.5	118.9	0.53*	0.05
806.4	104.9	2.21	0.22	1169.6	119.5	0.29*	0.04
834.9	105.3	1.67	0.42	1217.5	119.8	0.21*	0.07
866.7	105.7	1.30	0.22	1262.2	120.0	0.23*	0.05

Lab Photon Energy (MeV)	CM Pion Angle (deg.)	Recoil Cross Section (μb/sr)	Stat. Error	Lab Photon Energy (MeV)	CM Pion Angle (deg.)	Recoil Cross Section (μb/sr)	Stat. Error
587.6	134.8	5.76	0.48	976.8	149.7	2.29	0.28
613.4	134.8	5.55	0.45	1000.0	149.8	2.35	0.30
628.6	135.0	5.22	0.42	1023.8	149.7	2.53	0.33
646.8	135.1	6.46	0.50	1046.9	149.7	2.08	0.29
645.0	134.7	6.40	0.58	1061.5	149.7	1.26	0.19
665.7	135.0	6.74	0.55	1096.1	149.8	1.79	0.23
694.8	135.0	5.95	0.43	1128.0	149.8	1.66	0.22
703.6	134.8	5.73	0.44	1153.8	149.8	1.20	0.20
716.7	134.8	5.64	0.47	1172.8	149.9	1.12	0.20
726.9	134.6	5.17	0.44	1203.8	149.8	0.68	0.15
756.4	134.7	3.95	0.32	1231.0	149.8	1.06	0.19
786.3	135.1	3.86	0.36	1259.3	149.7	1.05	0.20
790.6	134.7	3.67	0.29	592.4	159.8	7.27	0.68
812.9	134.8	3.24	0.26	609.5	159.8	8.50	0.76
841.3	134.8	2.55	0.21	623.9	159.7	7.44	0.58
870.1	135.0	1.97	0.19	642.1	159.9	7.60	0.73
874.9	134.7	1.94	0.17	640.5	159.7	9.35	0.76
898.3	134.8	2.12	0.18	657.9	159.7	8.56	0.62
933.0	134.9	2.02	0.18	673.9	159.6	8.67	0.66
970.3	135.0	1.68	0.16	702.5	159.7	9.17	0.78
590.0	149.7	7.20	0.57	705.6	159.6	8.72	0.73
604.4	149.7	6.95	0.53	733.2	159.7	9.32	0.80
629.8	149.9	8.36	0.67	756.5	159.6	7.32	0.59
646.3	149.9	8.28	0.81	782.9	159.8	6.78	0.58
644.0	149.8	7.81	0.61	779.6	159.5	6.01	0.53
659.1	149.8	8.83	0.69	817.4	159.6	6.24	0.58
683.0	149.9	9.48	0.74	834.8	159.7	5.39	0.49
707.1	150.0	7.48	0.75	853.4	159.6	5.09	0.46
713.0	149.7	7.84	0.68	875.0	159.8	3.80	0.40
732.1	149.7	6.27	0.52	893.9	159.8	4.94	0.57
756.1	149.7	5.85	0.50	925.0	159.8	4.53	0.47
781.1	149.8	5.20	0.47	938.1	159.7	4.02	0.47
786.9	149.8	5.49	0.50	981.3	159.8	3.63	0.41
816.1	149.7	4.48	0.41	1002.5	159.7	3.92	0.46
837.6	149.8	4.42	0.40	1028.8	159.8	3.61	0.45
866.7	149.8	3.48	0.32	1056.8	159.8	2.72	0.34
870.8	149.8	3.26	0.31	1071.0	159.7	2.66	0.33
906.4	149.8	3.59	0.35	1098.8	159.7	3.12	0.38
923.2	149.6	3.30	0.31	1124.4	159.7	1.91	0.27
957.6	149.8	2.78	0.27	1145.2	159.7	1.86	0.28

Lab Photon Energy (MeV)	CM Pion Angle (deg.)	Recoil Cross Section (μb/sr)	Stat. Error
1171.7	159.9	1.36	0.24
1205.2	159.8	1.68	0.28
1219.3	159.8	1.82	0.30
1253.0	159.6	1.06	0.24

FIGURE 9

1) TOP - π^-/π^+ Ratio

Dark points at 20, 60, 90, 120, 150, and 160° are from Neugebauer et al. (36).

Dark points in Fig. 9.9 are for 110°.

2) BOTTOM - π^+ Cross Section from Deuterium (background subtracted) and π^+ backgrounds.

Ecklund's fit to π^+ photoproduction from hydrogen has been plotted for comparison ("X").

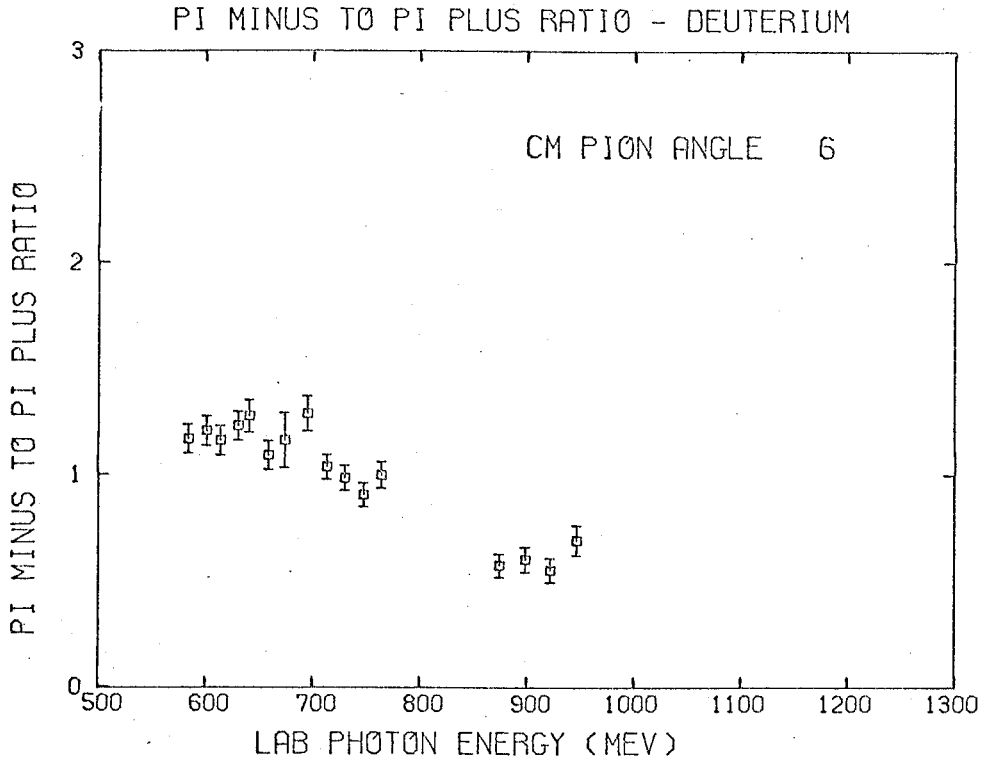
PI MINUS TO PI PLUS RATIO - DEUTERIUM
CM PION ANGLE 6
PI MINUS TO PI PLUS RATIO
LAB PHOTON ENERGY (MEV)
0
1
2
3
500
600
700
800
900
1000
1100
1200
1300

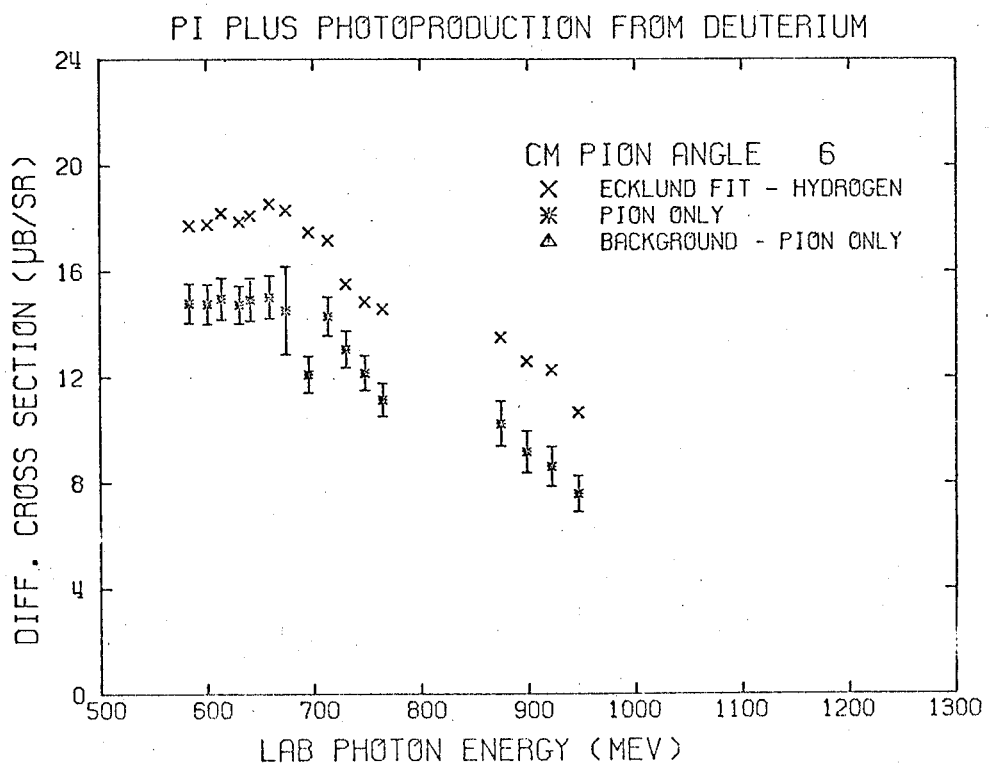
PI PLUS PHOTOPRODUCTION FROM DEUTERIUM
CM PION ANGLE 6
ECKLUND FIT - HYDROGEN
PION ONLY
BACKGROUND - PION ONLY
DIFF. CROSS SECTION (μB/SR)
LAB PHOTON ENERGY (MEV)
0
4
8
12
16
20
24
500
600
700
800
900
1000
1100
1200
1300

FIGURE 9.1

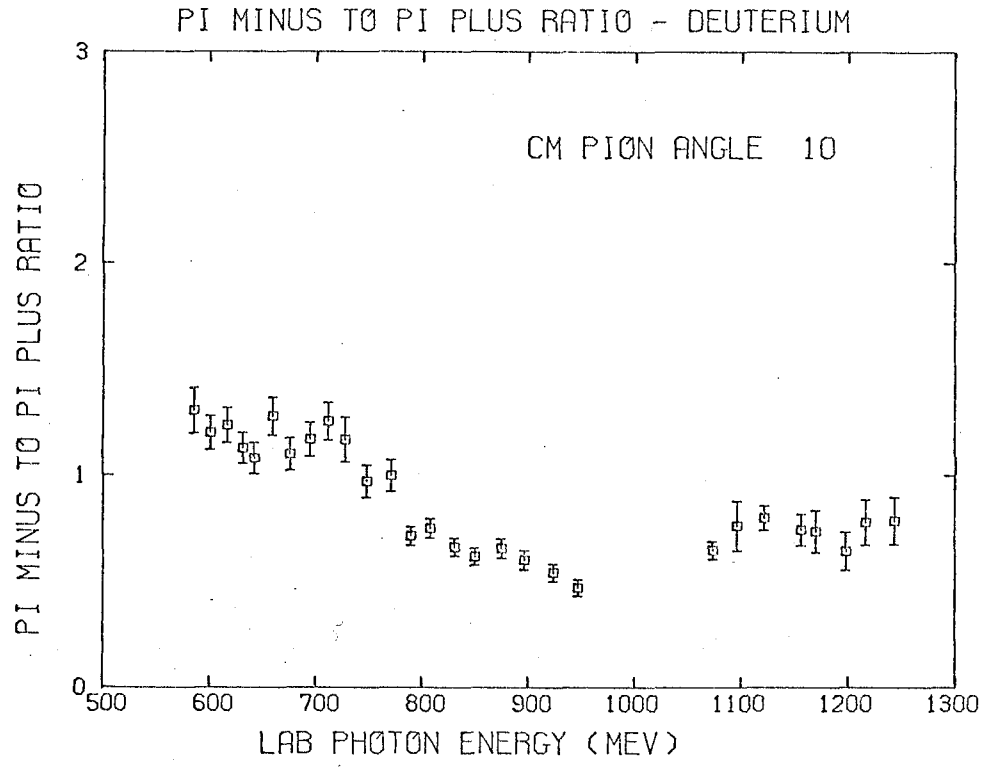
PI MINUS TØ PI PLUS RATIØ - DEUTERIUM
CM PIØN ANGLE 10
PI MINUS TØ PI PLUS RATIØ
LAB PHØTØN ENERGY (MEV)
0
1
2
3
500
600
700
800
900
1000
1100
1200
1300

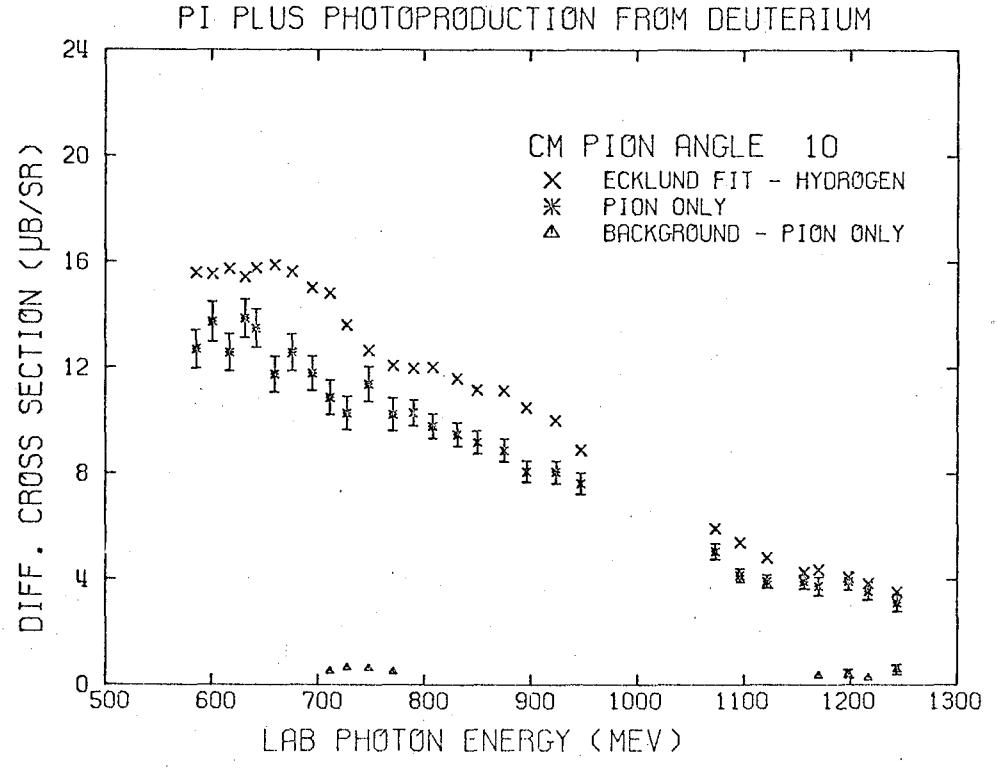
PI PLUS PHOTOPRODUCTION FROM DEUTERIUM
CM PION ANGLE 10
ECKLUND FIT - HYDROGEN
PION ONLY
BACKGROUND - PION ONLY
DIFF. CROSS SECTION (μB/SR)
LAB PHOTON ENERGY (MEV)
0
4
8
12
16
20
24
500
600
700
800
900
1000
1100
1200
1300

FIGURE 9.2

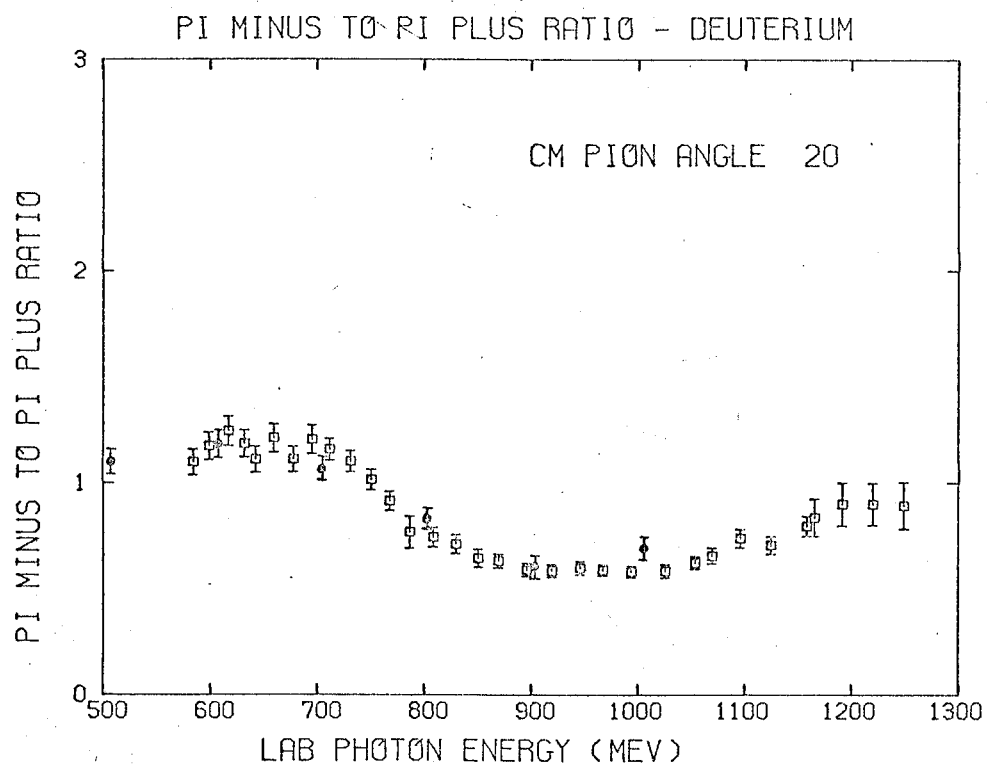
PI MINUS TO PI PLUS RATIO - DEUTERIUM
CM PION ANGLE 20
PI MINUS TO PI PLUS RATIO
LAB PHOTON ENERGY (MEV)
0
1
2
3
500
600
700
800
900
1000
1100
1200
1300

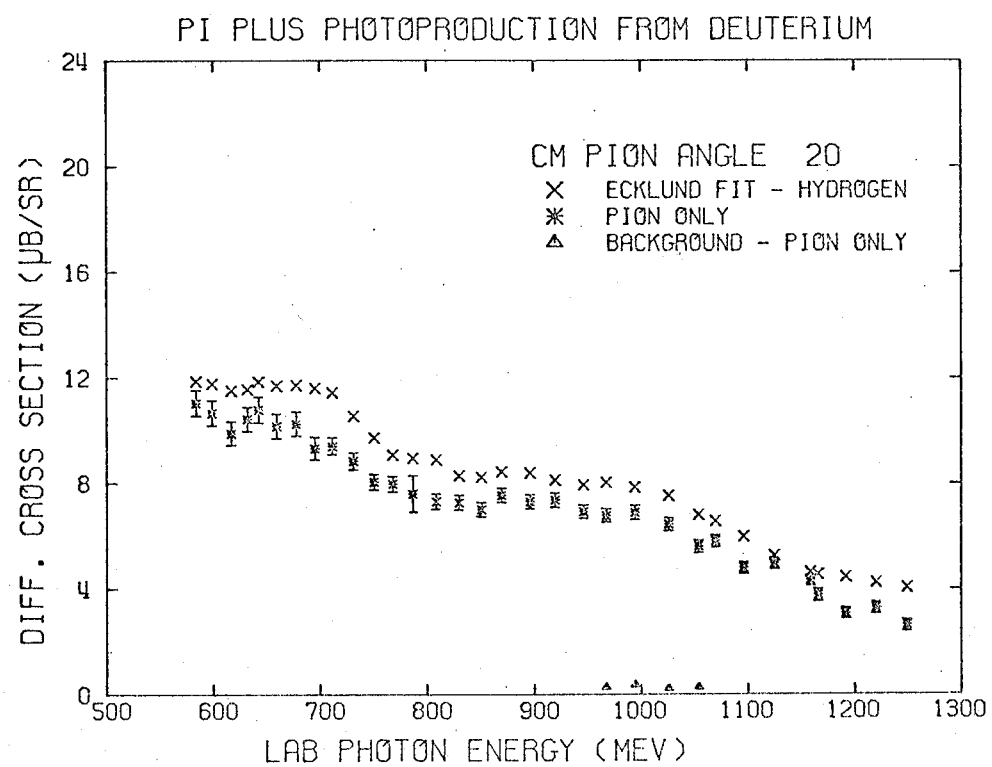
PI PLUS PHOTOPRODUCTION FROM DEUTERIUM
CM PION ANGLE 20
ECKLUND FIT - HYDROGEN
PION ONLY
BACKGROUND - PION ONLY
DIFF. CROSS SECTION (μB/SR)
LAB PHOTON ENERGY (MEV)
0
4
8
12
16
20
24
500
600
700
800
900
1000
1100
1200
1300

FIGURE 9.3

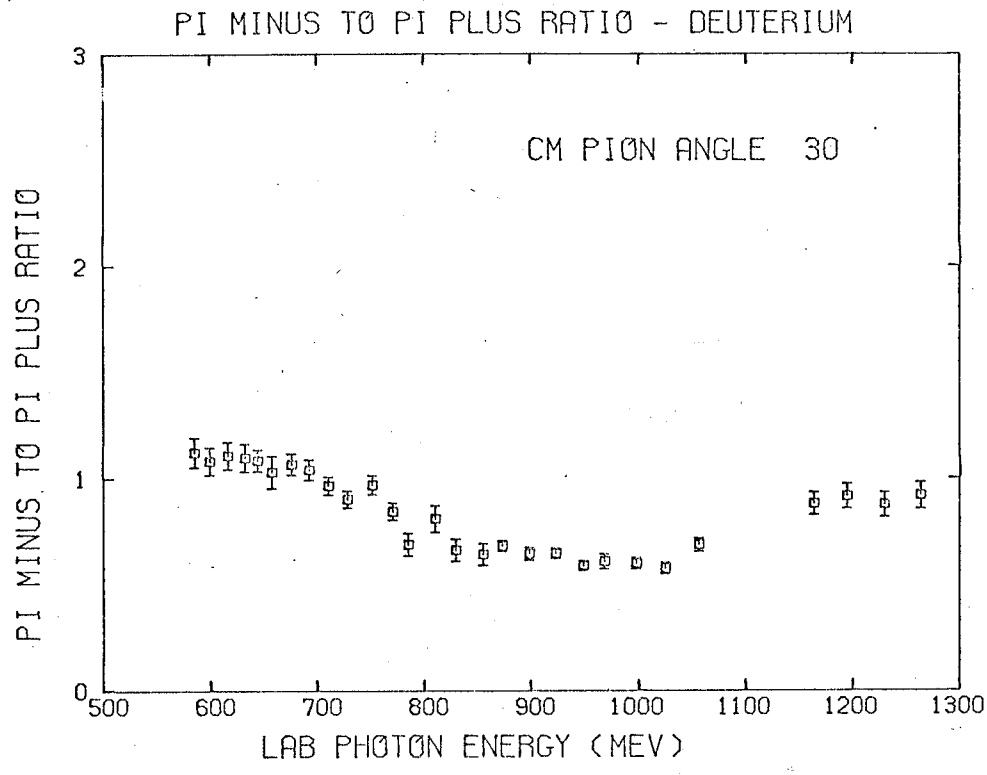
PI MINUS TØ PI PLUS RATIØ - DEUTERIUM
CM PIØN ANGLE 30
PI MINUS TØ PI PLUS RATIØ
LAB PHØTØN ENERGY (MEV)
0
1
2
3
500
600
700
800
900
1000
1100
1200
1300

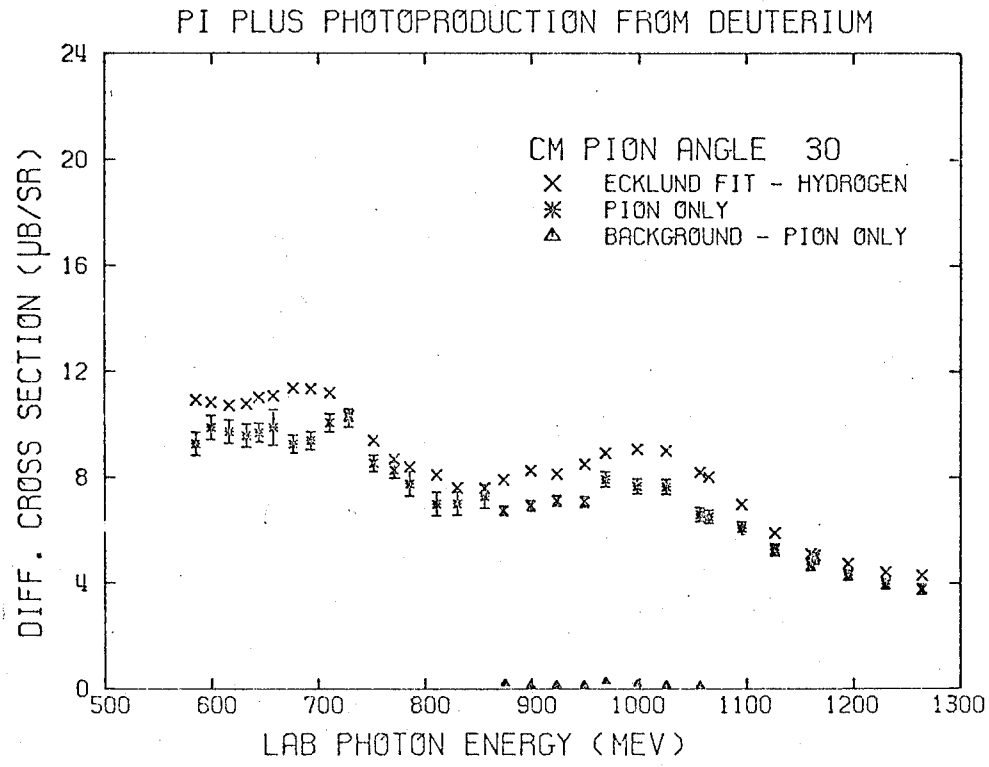
PI PLUS PHØTØPRØDUCTIØN FRØM DEUTERIUM
CM PIØN ANGLE 30
ECKLUND FIT - HYDRØGEN
PIØN ØNLY
BACKGRØUND - PIØN ØNLY
DIFF. CRØSS SECTIØN (μB/SR)
LAB PHØTØN ENERGY (MEV)
0
4
8
12
16
20
24
500
600
700
800
900
1000
1100
1200
1300

FIGURE 9.4

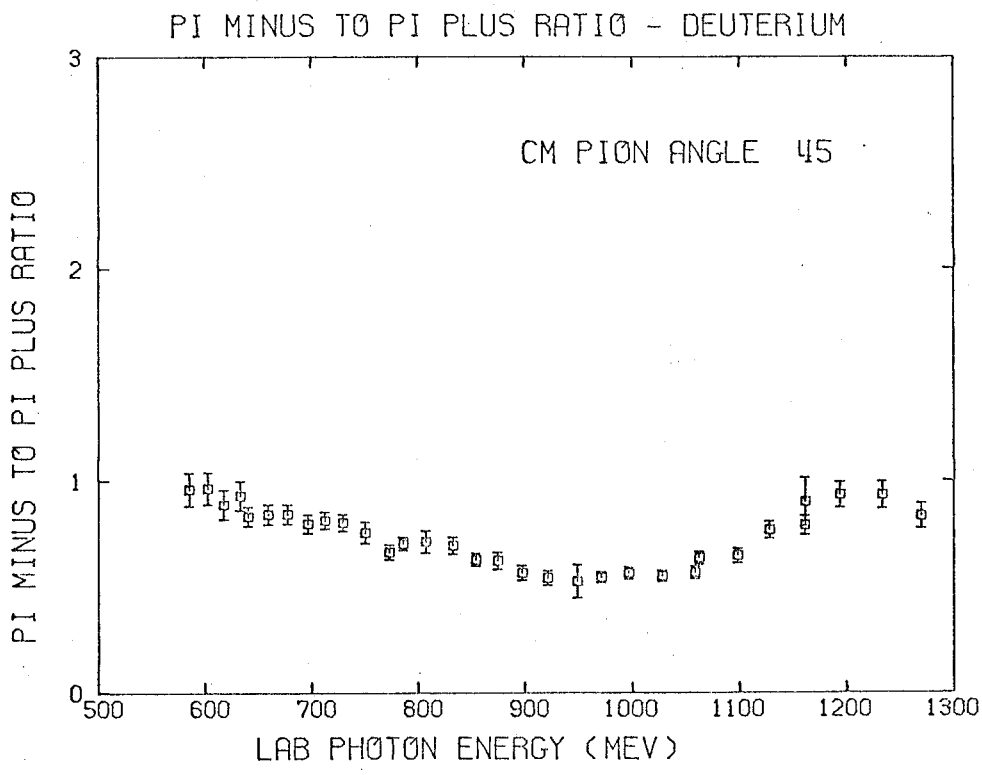
PI MINUS TØ PI PLUS RATIØ - DEUTERIUM
CM PIØN ANGLE 45
PI MINUS TØ PI PLUS RATIØ
LAB PHØTØN ENERGY (MEV)
0
1
2
3
500
600
700
800
900
1000
1100
1200
1300

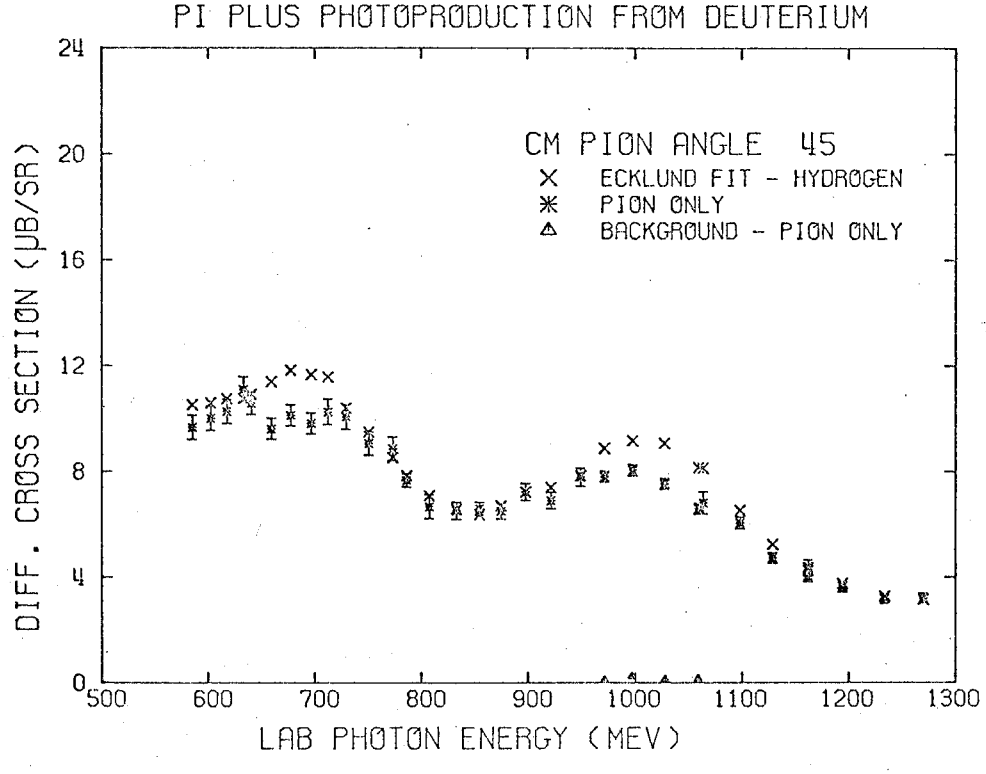
PI PLUS PHØTØPRØDUCTIØN FRØM DEUTERIUM
CM PIØN ANGLE 45
ECKLUND FIT - HYDRØGEN
PIØN ØNLY
BACKGRØUND - PIØN ØNLY
DIFF. CRØSS SECTIØN (μB/SR)
LAB PHØTØN ENERGY (MEV)
0
4
8
12
16
20
24
500
600
700
800
900
1000
1100
1200
1300

FIGURE 9.5

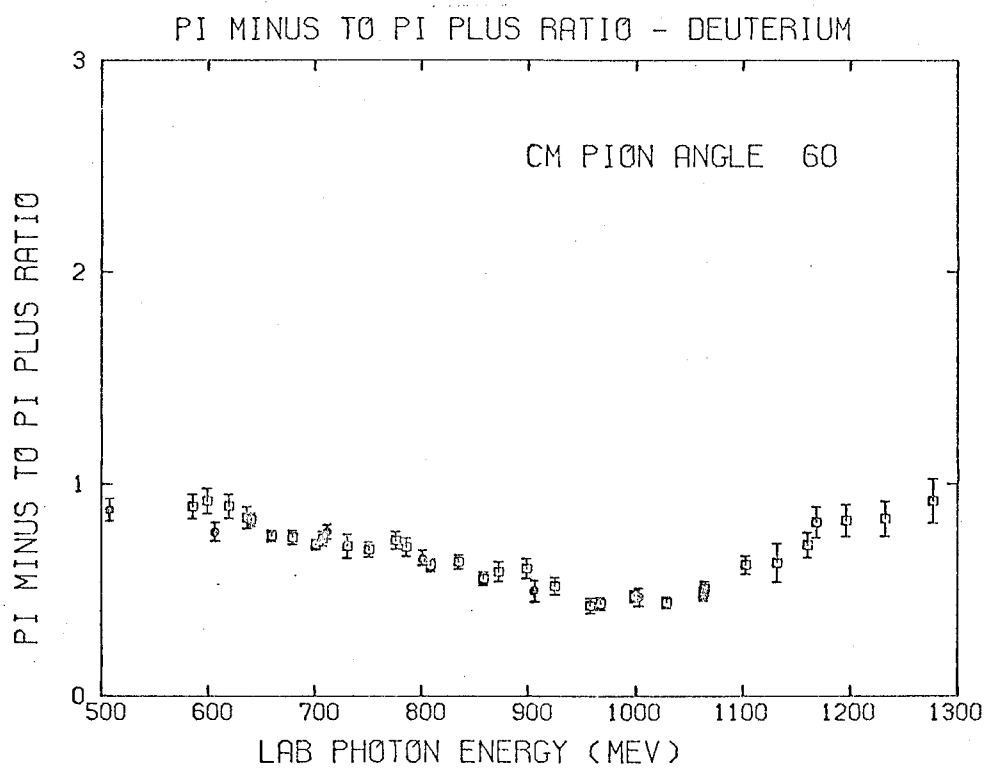
PI MINUS TO PI PLUS RATIO - DEUTERIUM
CM PION ANGLE 60
PI MINUS TO PI PLUS RATIO
LAB PHOTON ENERGY (MEV)
0
1
2
3
500
600
700
800
900
1000
1100
1200
1300

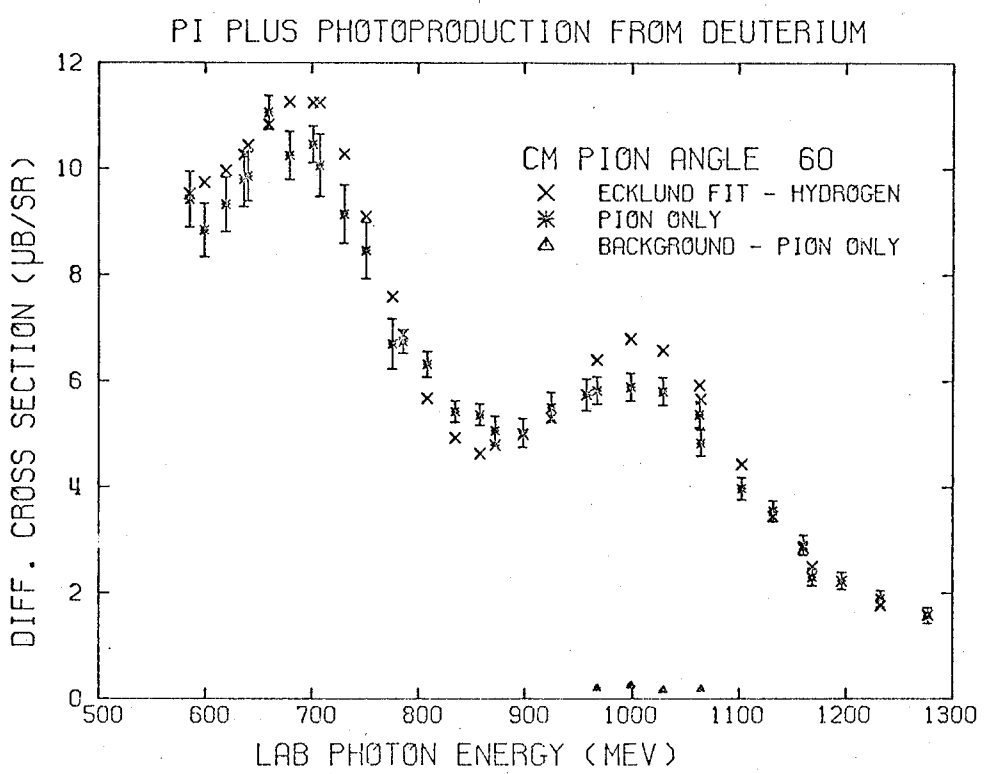
PI PLUS PHOTOPRODUCTION FROM DEUTERIUM
CM PION ANGLE 60
ECKLUND FIT - HYDROGEN
PION ONLY
BACKGROUND - PION ONLY
DIFF. CROSS SECTION (UB/SR)
LAB PHOTON ENERGY (MEV)
0
2
4
6
8
10
12
500
600
700
800
900
1000
1100
1200
1300

FIGURE 9.6

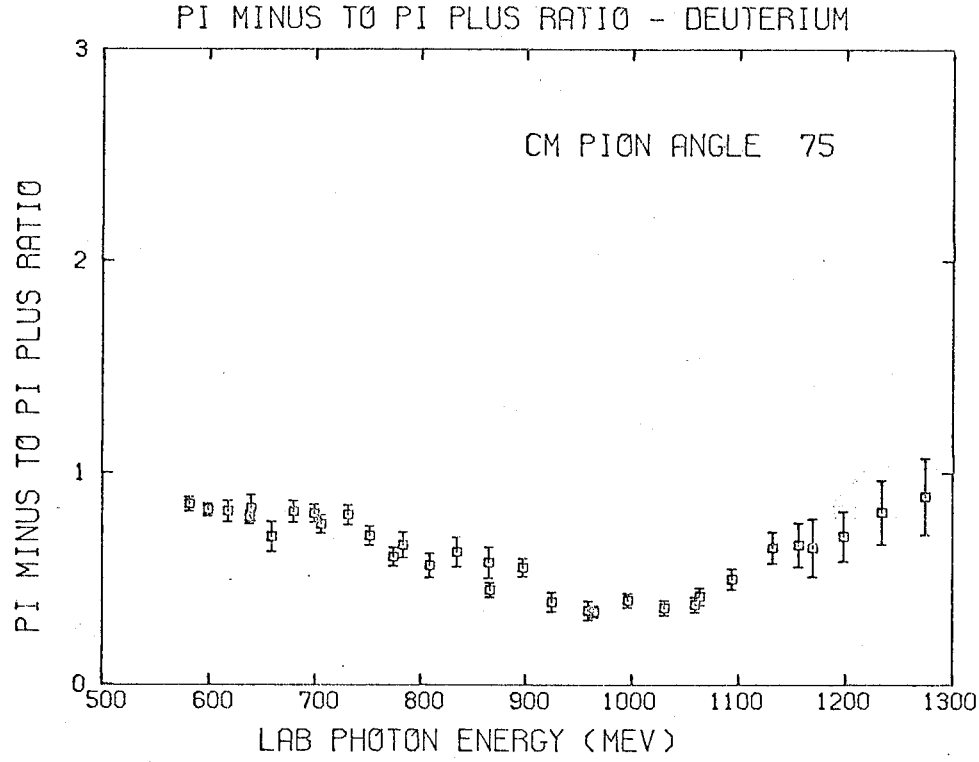
PI MINUS TØ PI PLUS RATIØ - DEUTERIUM
CM PIØN ANGLE 75
PI MINUS TØ PI PLUS RATIØ
LAB PHØTØN ENERGY (MEV)
0
1
2
3
500
600
700
800
900
1000
1100
1200
1300

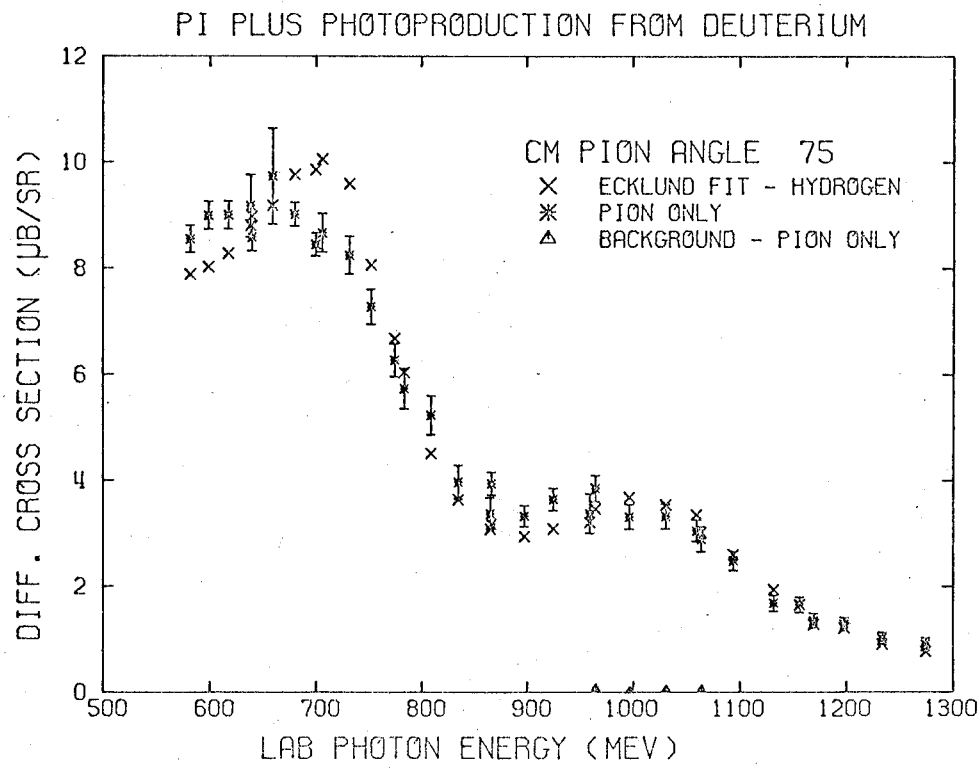
PI PLUS PHØTØPRØDUCTIØN FRØM DEUTERIUM
CM PIØN ANGLE 75
ECKLUND FIT - HYDROGEN
PIØN ØNLY
BACKGROUND - PIØN ØNLY
DIFF. CROSS SECTIØN (μB/SR)
LAB PHØTØN ENERGY (MEV)
0
2
4
6
8
10
12
500
600
700
800
900
1000
1100
1200
1300

FIGURE 9.7

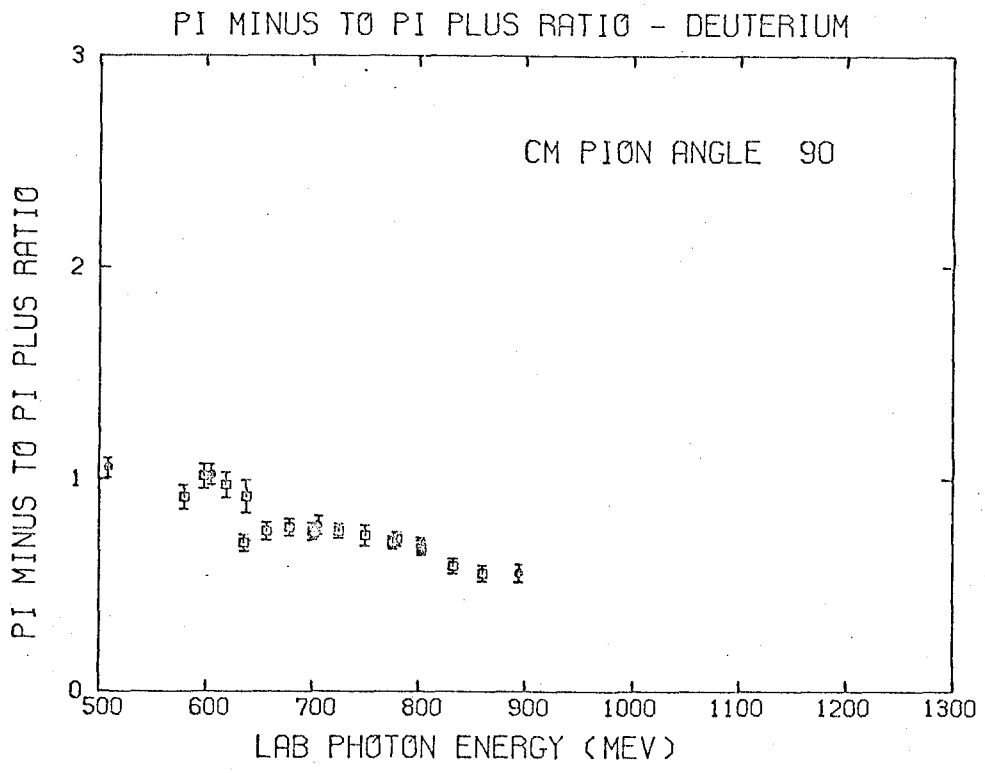
PI MINUS TØ PI PLUS RATIØ - DEUTERIUM
CM PIØN ANGLE 90
PI MINUS TØ PI PLUS RATIØ
LAB PHØTØN ENERGY (MEV)
0
1
2
3
500
600
700
800
900
1000
1100
1200
1300

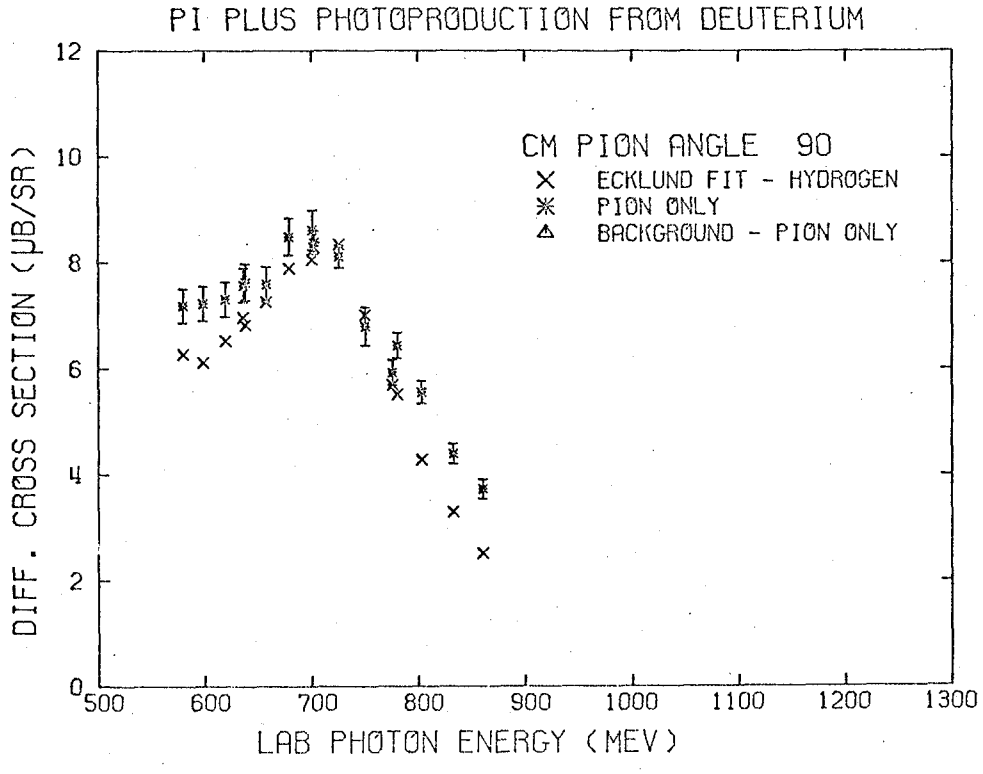
PI PLUS PHØTØPRØDUCTIØN FRØM DEUTERIUM
CM PIØN ANGLE 90
ECKLUND FIT - HYDROGEN
PIØN ØNLY
BACKGROUND - PIØN ØNLY
DIFF. CROSS SECTIØN (μB/SR)
LAB PHØTØN ENERGY (MEV)
0
2
4
6
8
10
12
500
600
700
800
900
1000
1100
1200
1300

FIGURE 9.8

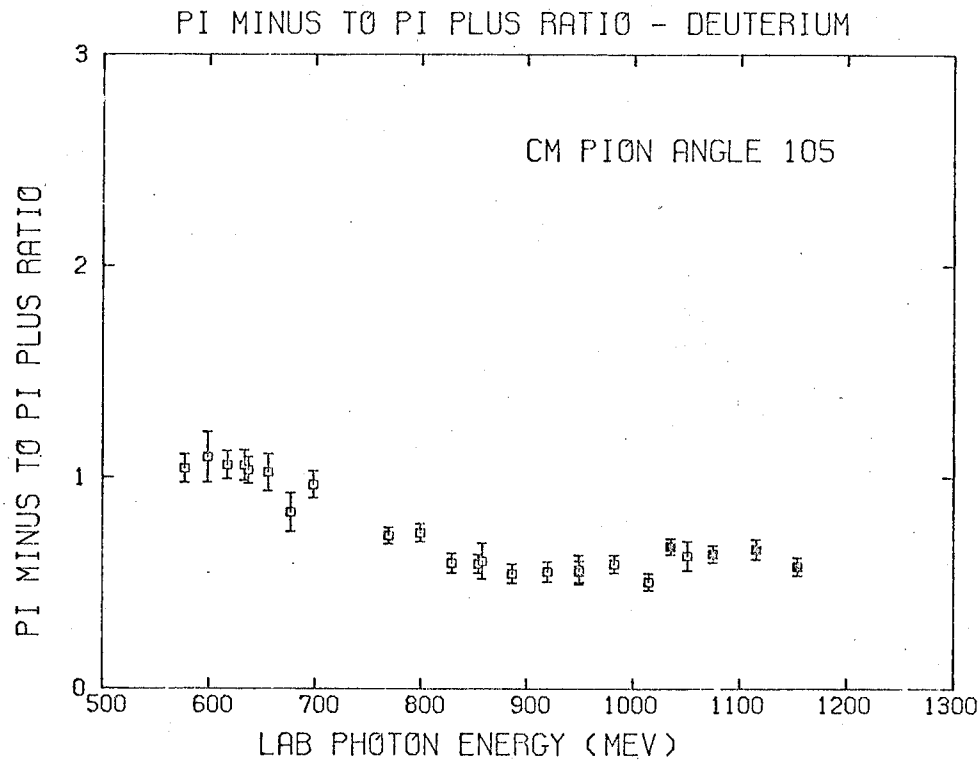
PI MINUS TØ PI PLUS RATIØ - DEUTERIUM
CM PIØN ANGLE 105
PI MINUS TØ PI PLUS RATIØ
LAB PHØTØN ENERGY (MEV)
0
1
2
3
500
600
700
800
900
1000
1100
1200
1300

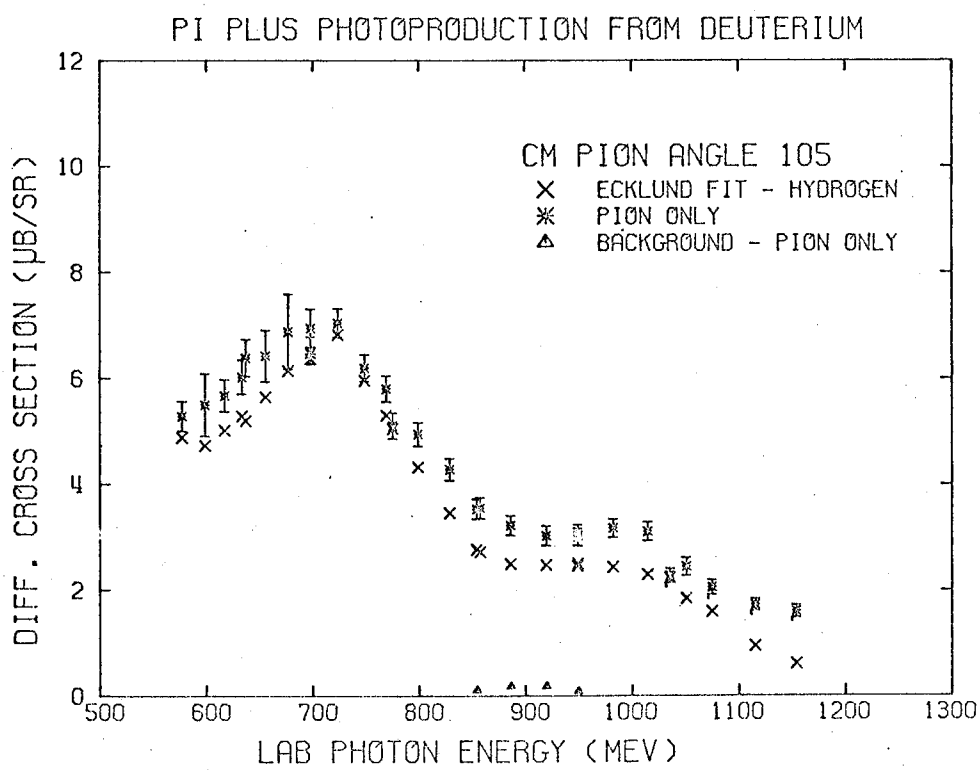
PI PLUS PHØTØPRØDUCTIØN FRØM DEUTERIUM
CM PIØN ANGLE 105
ECKLUND FIT - HYDROGEN
PIØN ONLY
BACKGROUND - PIØN ONLY
DIFF. CRØSS SECTIØN (μB/SR)
LAB PHØTØN ENERGY (MEV)
0
2
4
6
8
10
12
500
600
700
800
900
1000
1100
1200
1300

FIGURE 9.9

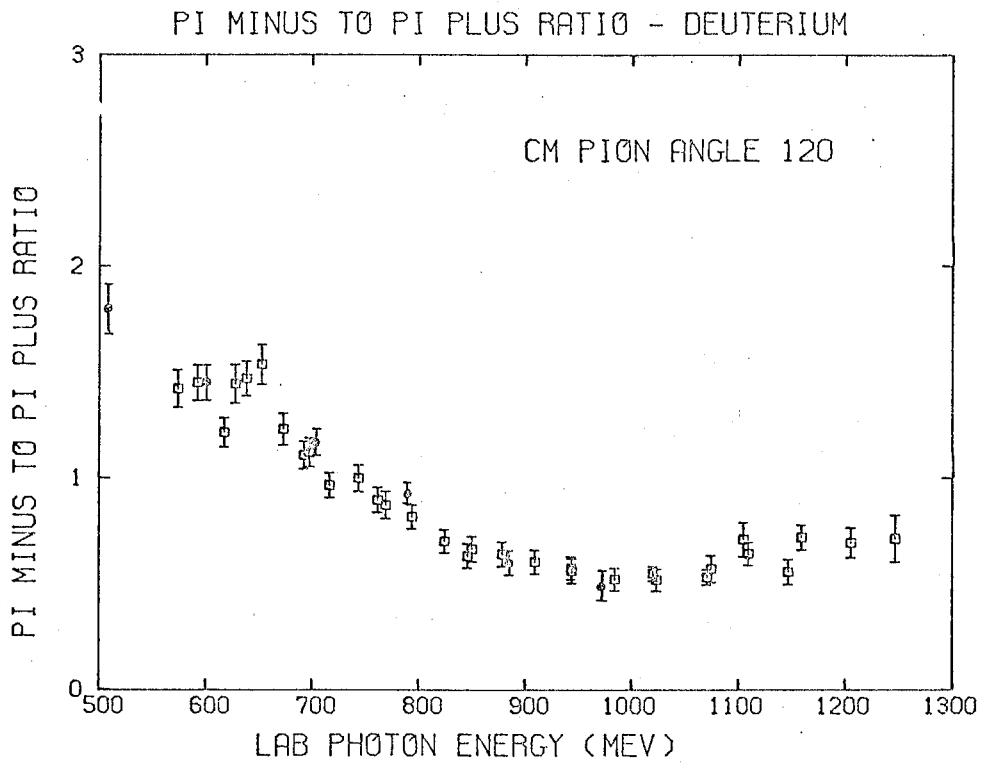
PI MINUS TO PI PLUS RATIO - DEUTERIUM
CM PION ANGLE 120
PI MINUS TO PI PLUS RATIO
LAB PHOTON ENERGY (MEV)
0
1
2
3
500
600
700
800
900
1000
1100
1200
1300

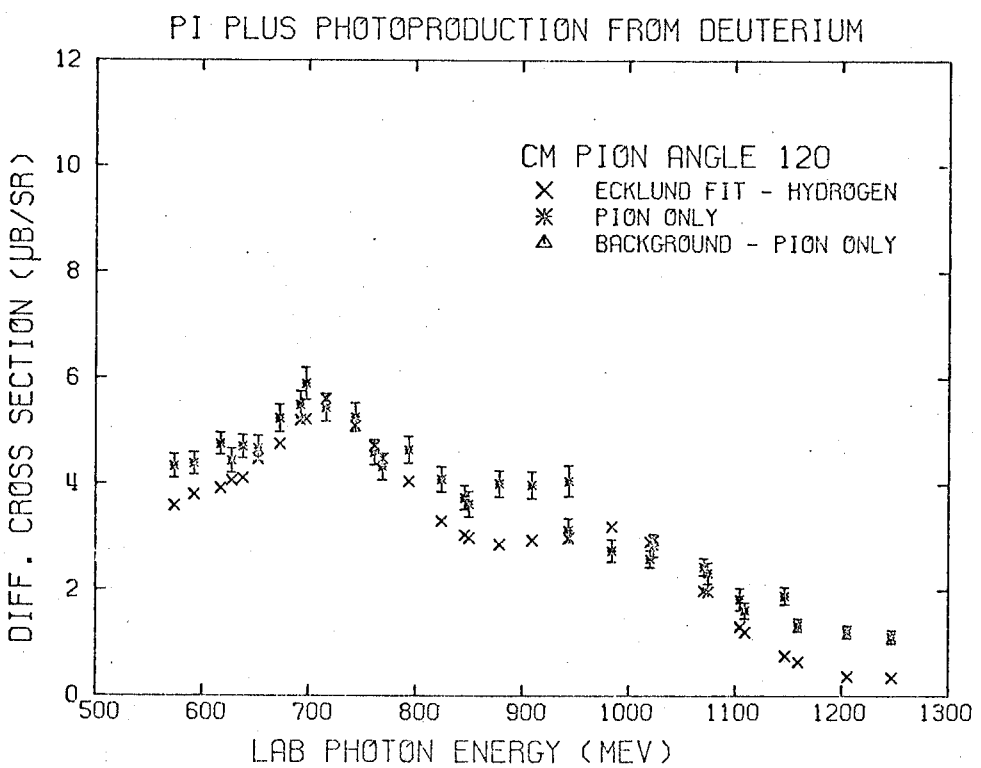
PI PLUS PHOTOPRODUCTION FROM DEUTERIUM
CM PION ANGLE 120
ECKLUND FIT - HYDROGEN
PION ONLY
BACKGROUND - PION ONLY
DIFF. CROSS SECTION (μB/SR)
LAB PHOTON ENERGY (MEV)
0
2
4
6
8
10
12
500
600
700
800
900
1000
1100
1200
1300

FIGURE 9.10

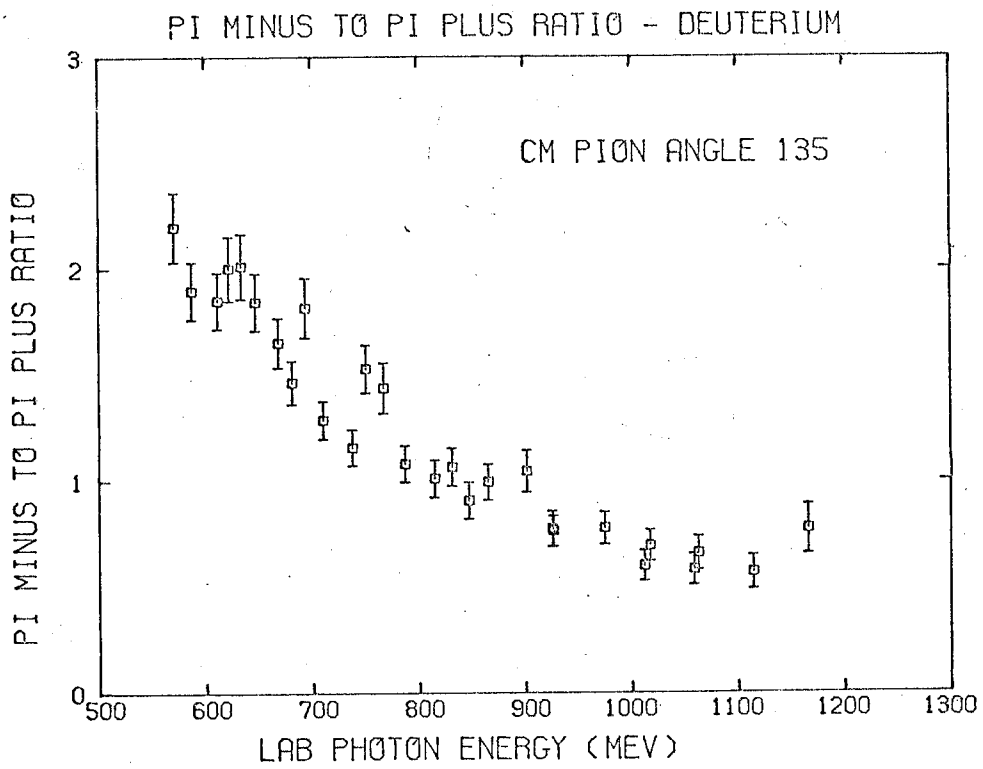
PI MINUS TØ PI PLUS RATIØ - DEUTERIUM
CM PIØN ANGLE 135
PI MINUS TØ PI PLUS RATIØ
LAB PHØTØN ENERGY (MEV)
0
1
2
3
500
600
700
800
900
1000
1100
1200
1300

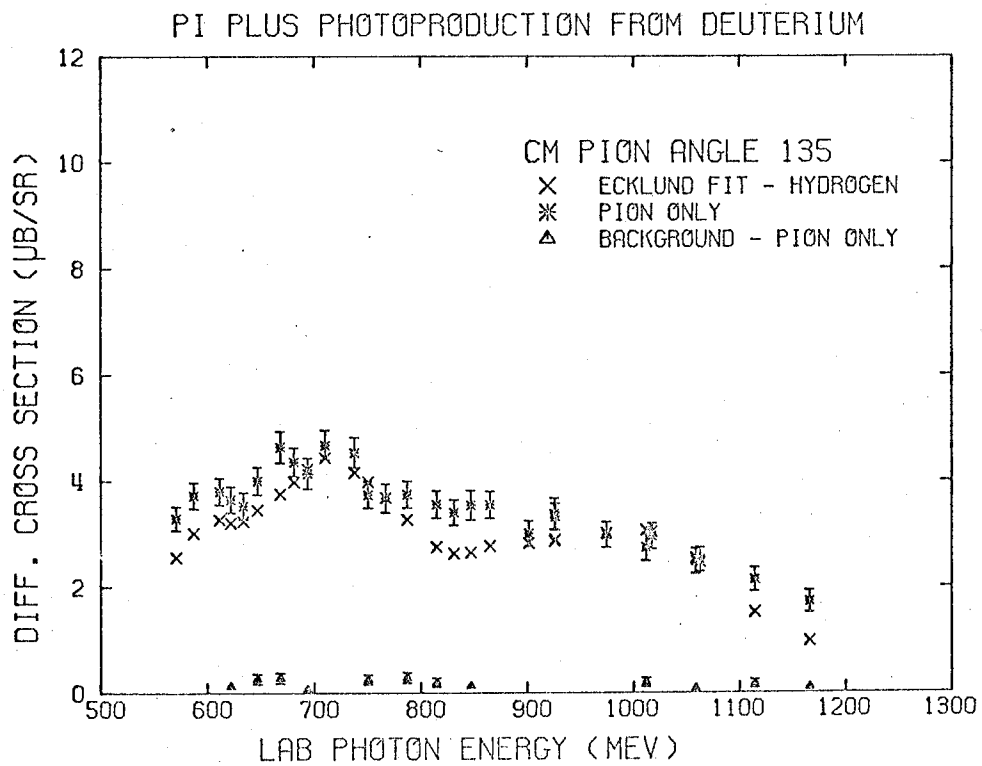
PI PLUS PHØTØPRØDUCTIØN FRØM DEUTERIUM
CM PIØN ANGLE 135
ECKLUND FIT - HYDROGEN
PIØN ØNLY
BACKGROUND - PIØN ØNLY
DIFF. CRØSS SECTIØN (μB/SR)
LAB PHØTØN ENERGY (MEV)
0
2
4
6
8
10
12
500
600
700
800
900
1000
1100
1200
1300

FIGURE 9.11

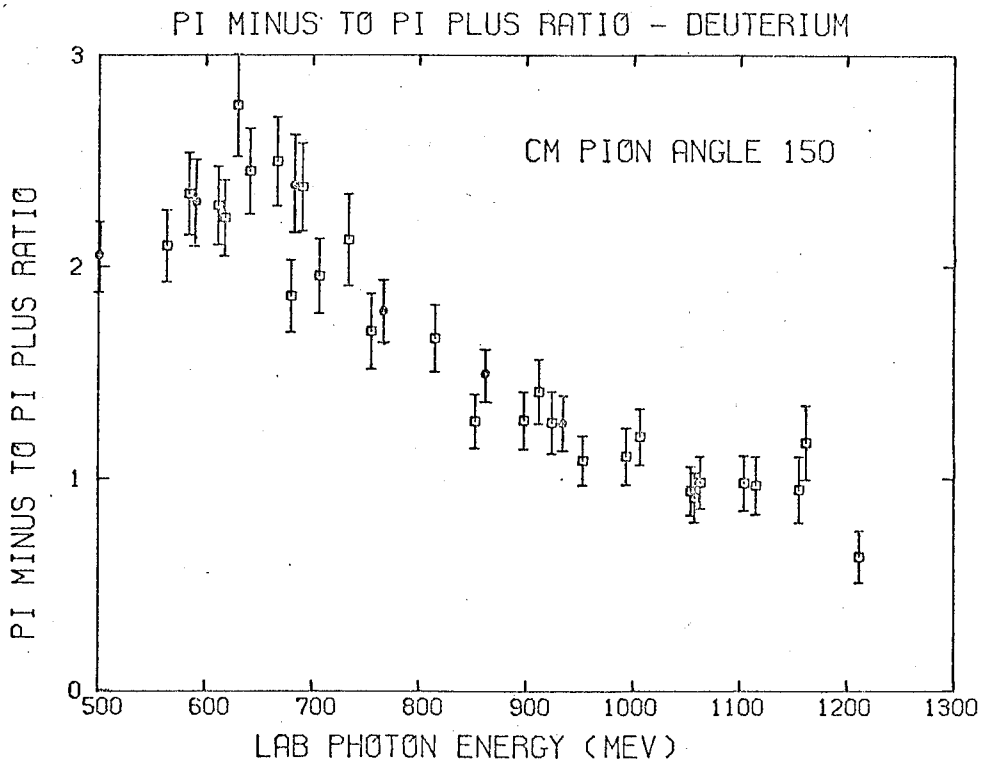
PI MINUS TØ PI PLUS RATIØ - DEUTERIUM
CM PIØN ANGLE 150
PI MINUS TØ PI PLUS RATIØ
LAB PHØTØN ENERGY (MEV)
0
1
2
3
500
600
700
800
900
1000
1100
1200
1300

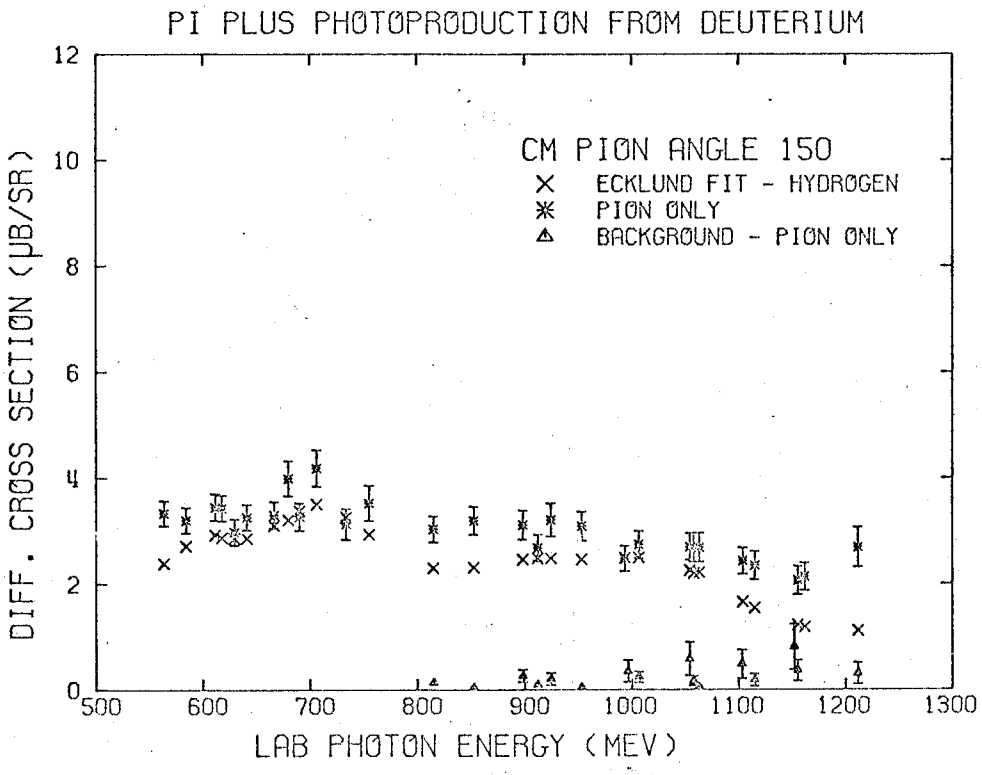
PI PLUS PHØTØPRØDUCTIØN FRØM DEUTERIUM
CM PIØN ANGLE 150
ECKLUND FIT - HYDROGEN
PIØN ØNLY
BACKGROUND - PIØN ØNLY
DIFF. CROSS SECTIØN (μB/SR)
LAB PHØTØN ENERGY (MEV)
0
2
4
6
8
10
12
500
600
700
800
900
1000
1100
1200
1300

FIGURE 9.12

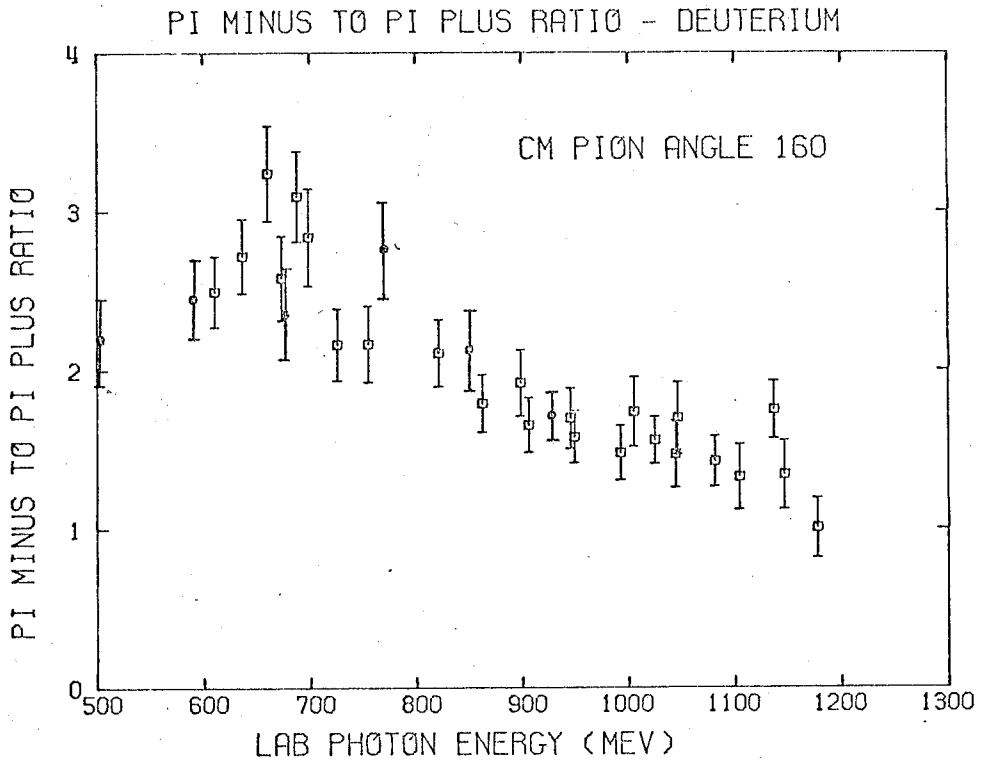
PI MINUS TØ PI PLUS RATIØ - DEUTERIUM
CM PIØN ANGLE 160
PI MINUS TØ PI PLUS RATIØ
LAB PHØTØN ENERGY (MEV)
0
1
2
3
4
500
600
700
800
900
1000
1100
1200
1300

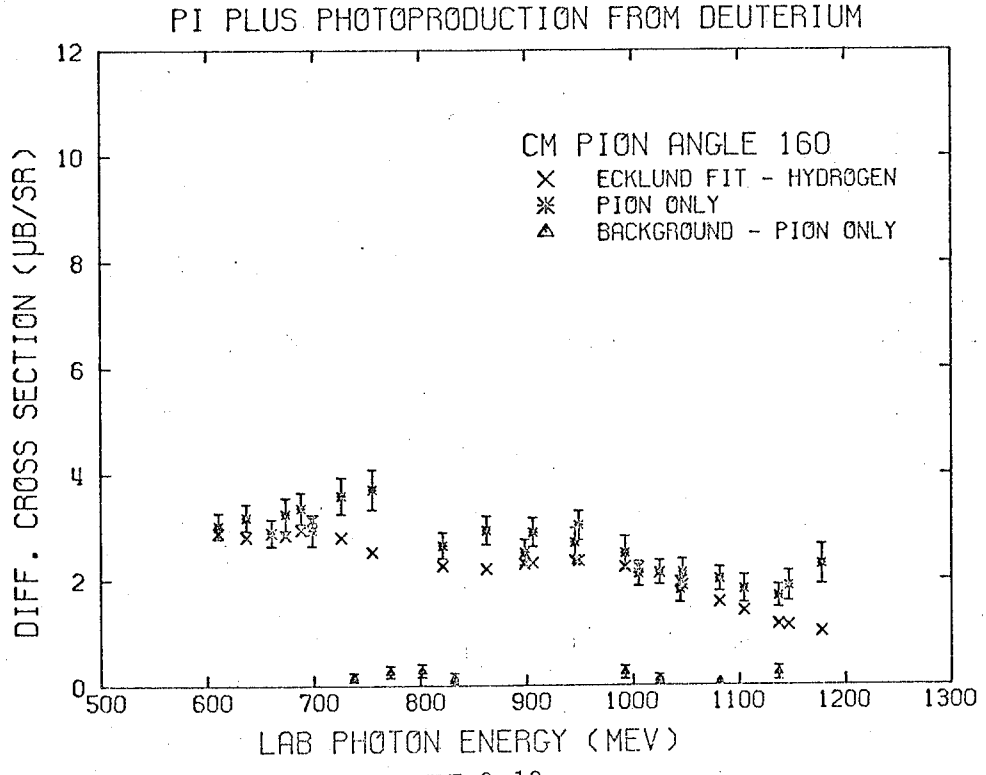
PI PLUS PHØTØPRØDUCTIØN FRØM DEUTERIUM
CM PIØN ANGLE 160
ECKLUND FIT - HYDROGEN
PIØN ØNLY
BACKGROUND - PIØN ØNLY
DIFF. CRØSS SECTIØN (μB/SR)
LAB PHØTØN ENERGY (MEV)
0
2
4
6
8
10
12
500
600
700
800
900
1000
1100
1200
1300

FIGURE 9.13

FIGURE 10

1) TOP - Ratio Cross sections and Recoil Cross Sections

Half-dark points are artificial (interpolated) cross sections.

Dark points in Fig. 10.9 are for 110^{o}

2) BOTTOM - Ratio Cross Sections and π^{-} (pion only detected) Cross Sections from Deuterium (background subtracted) and π^{-} Backgrounds.

Half-dark points are artificial (interpolated) cross sections.

Dark points in Fig. 10.9 are for 110^{o}.

Artificial (interpolated) background points are identified by a vertical bar.

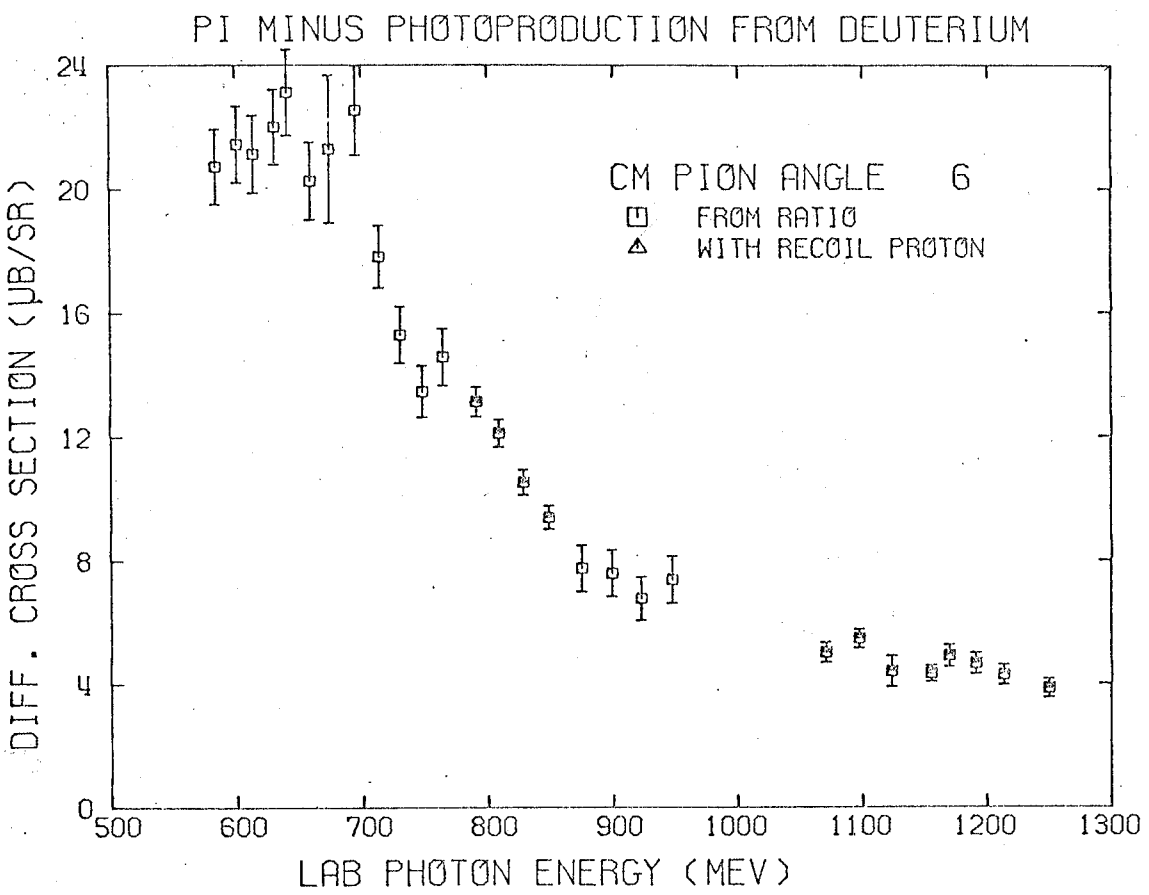
PI MINUS PHOTOPRODUCTION FROM DEUTERIUM
CM PION ANGLE 6
FROM RATIO
WITH RECOIL PROTON
DIFF. CROSS SECTION (μB/SR)
LAB PHOTON ENERGY (MEV)
0
4
8
12
16
20
24
500
600
700
800
900
1000
1100
1200
1300

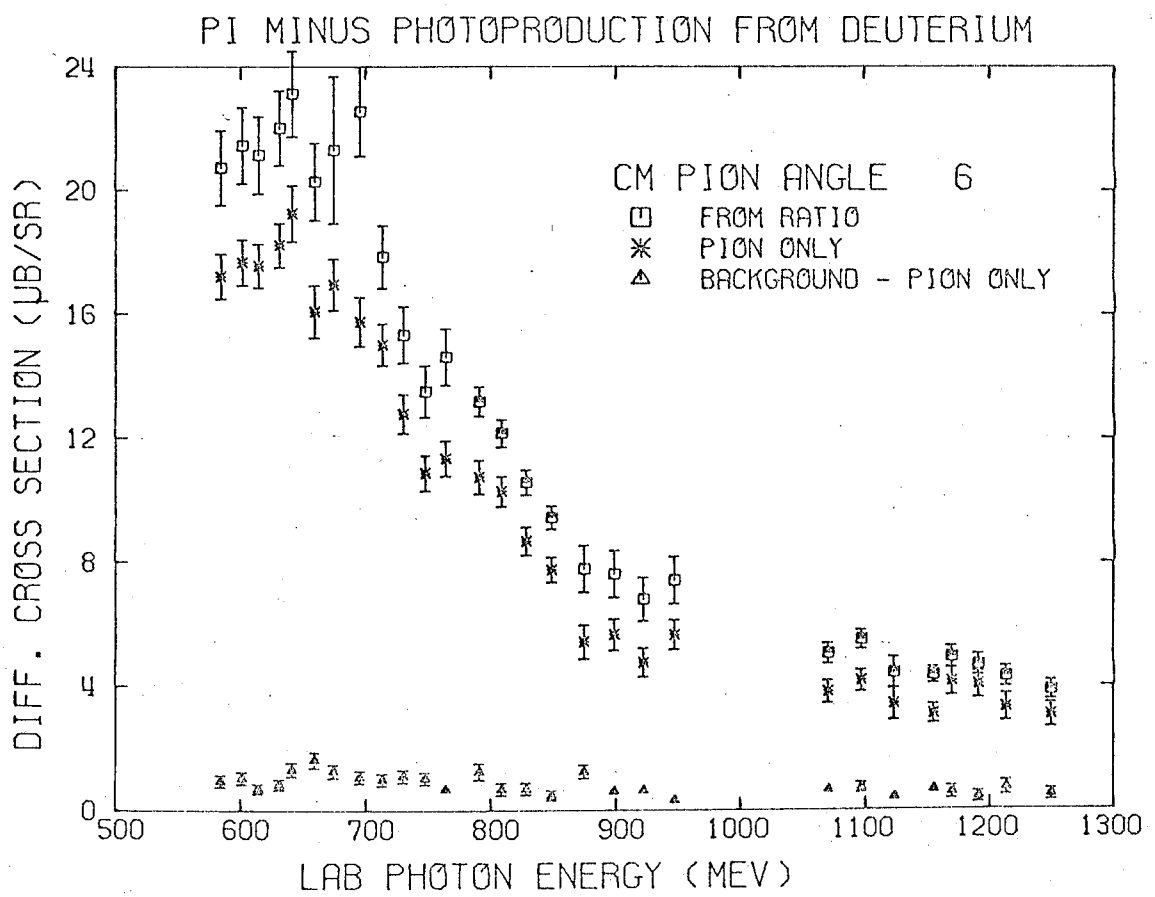
PI MINUS PHOTOPRODUCTION FROM DEUTERIUM
CM PION ANGLE 6
FROM RATIO
PION ONLY
BACKGROUND - PION ONLY
DIFF. CROSS SECTION (μB/SR)
LAB PHOTON ENERGY (MEV)
0
4
8
12
16
20
24
500
600
700
800
900
1000
1100
1200
1300

FIGURE 10.1

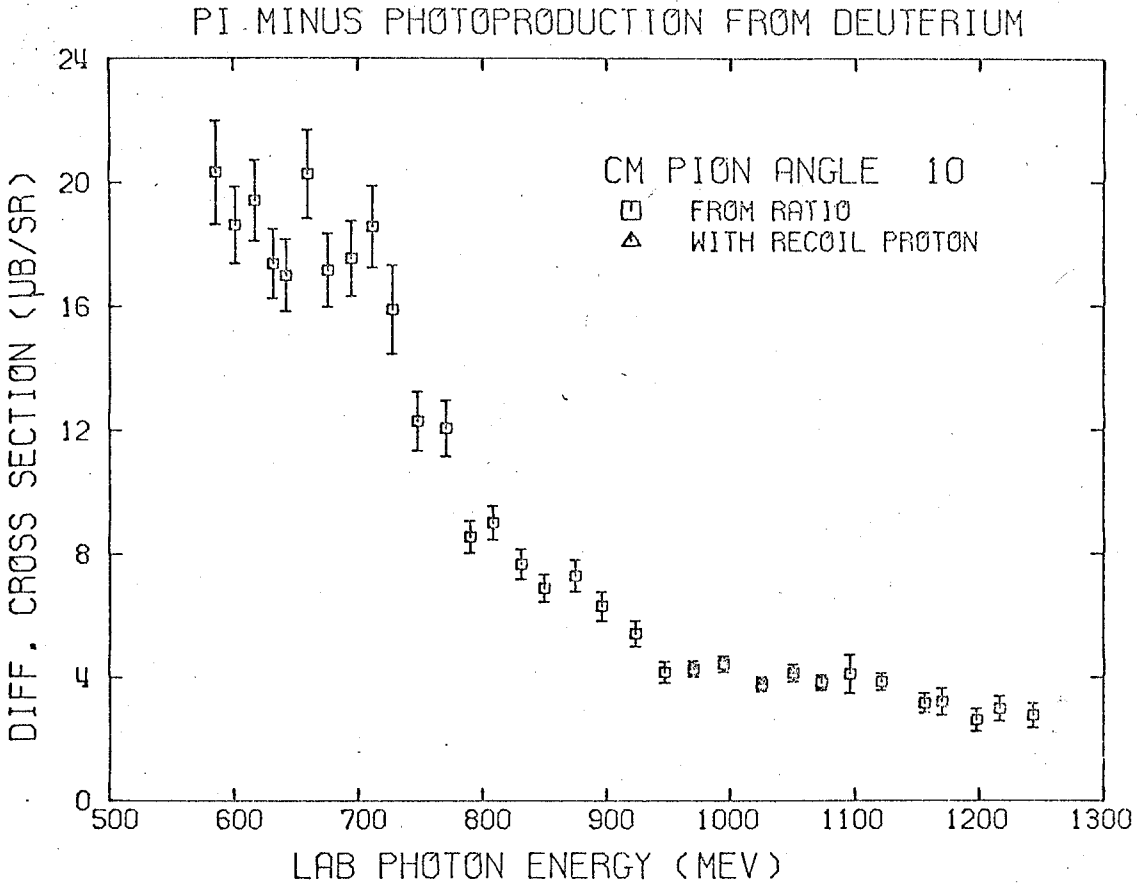
PI MINUS PHOTOPRODUCTION FROM DEUTERIUM
CM PION ANGLE 10
FROM RATIO
WITH RECOIL PROTON
DIFF. CROSS SECTION (μB/SR)
LAB PHOTON ENERGY (MEV)
0
4
8
12
16
20
24
500
600
700
800
900
1000
1100
1200
1300

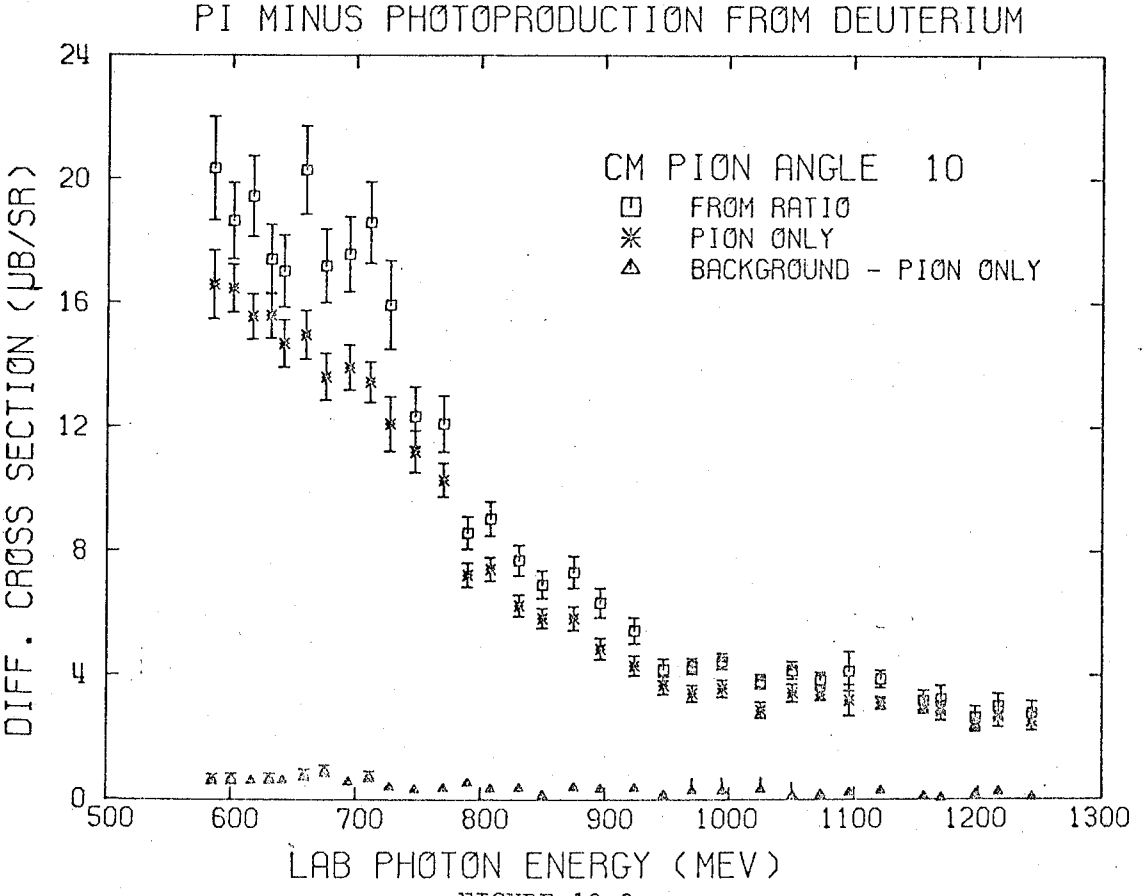
PI MINUS PHOTOPRODUCTION FROM DEUTERIUM
CM PION ANGLE 10
FROM RATIO
PION ONLY
BACKGROUND - PION ONLY
DIFF. CROSS SECTION (μB/SR)
LAB PHOTON ENERGY (MEV)
0
4
8
12
16
20
24
500
600
700
800
900
1000
1100
1200
1300

FIGURE 10.2

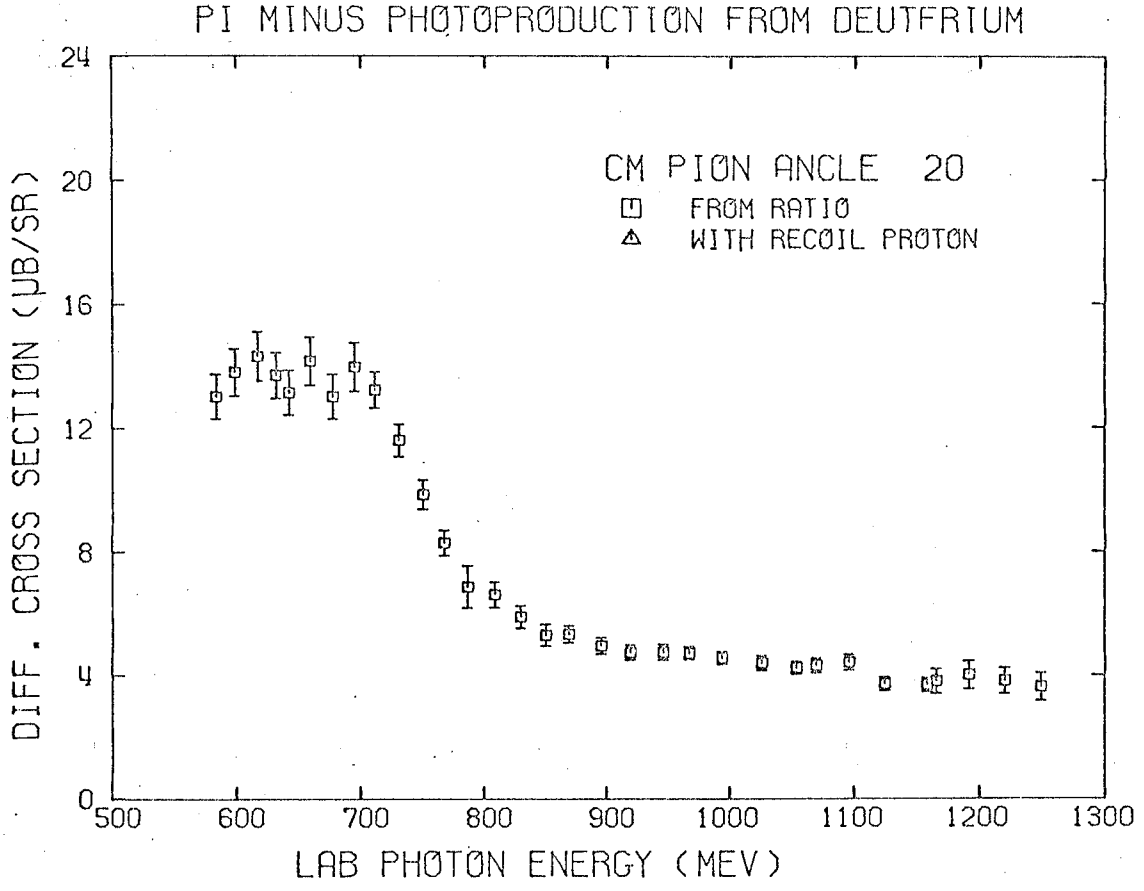
PI MINUS PHOTOPRODUCTION FROM DEUTERIUM
CM PION ANGLE 20
FROM RATIO
WITH RECOIL PROTON
DIFF. CROSS SECTION (μB/SR)
LAB PHOTON ENERGY (MEV)
0
4
8
12
16
20
24
500
600
700
800
900
1000
1100
1200
1300

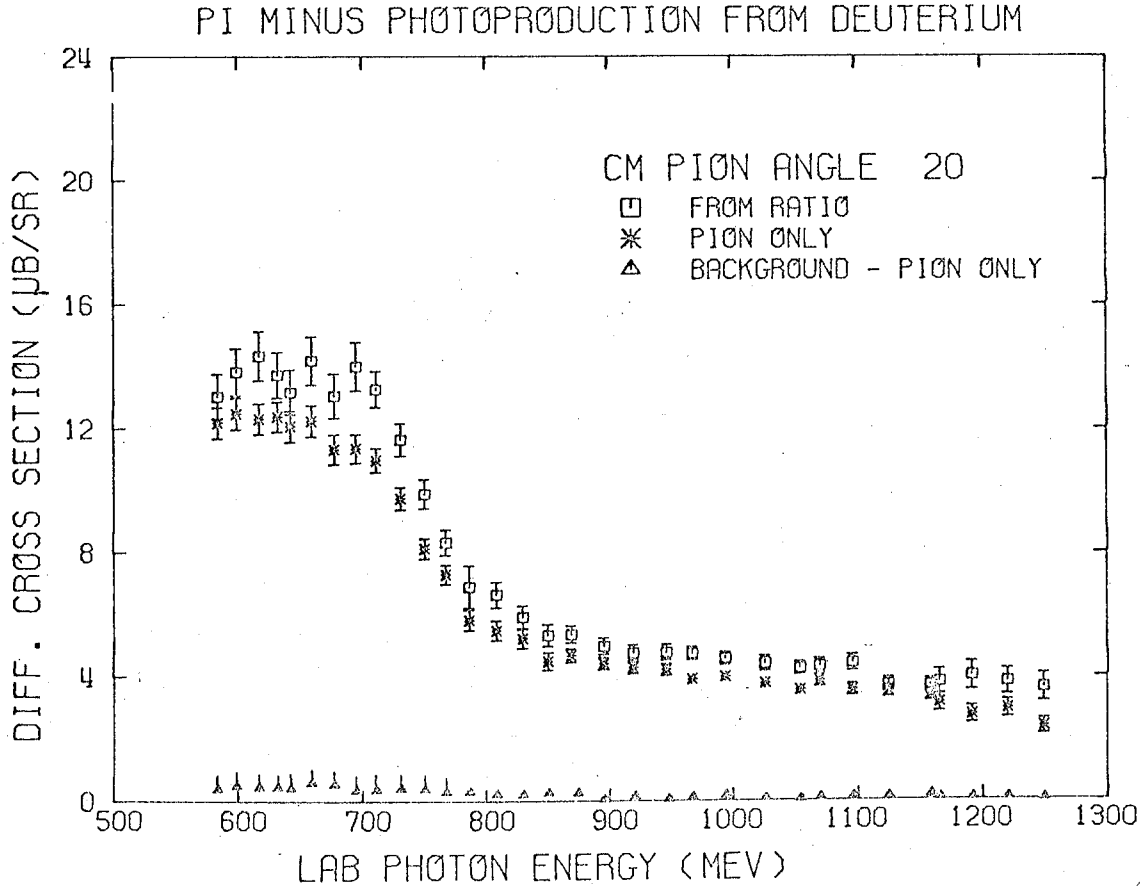
PI MINUS PHOTOPRODUCTION FROM DEUTERIUM
CM PION ANGLE 20
FROM RATIO
PION ONLY
BACKGROUND - PION ONLY
DIFF. CROSS SECTION (μB/SR)
LAB PHOTON ENERGY (MEV)
0
4
8
12
16
20
24
500
600
700
800
900
1000
1100
1200
1300

FIGURE 10.3

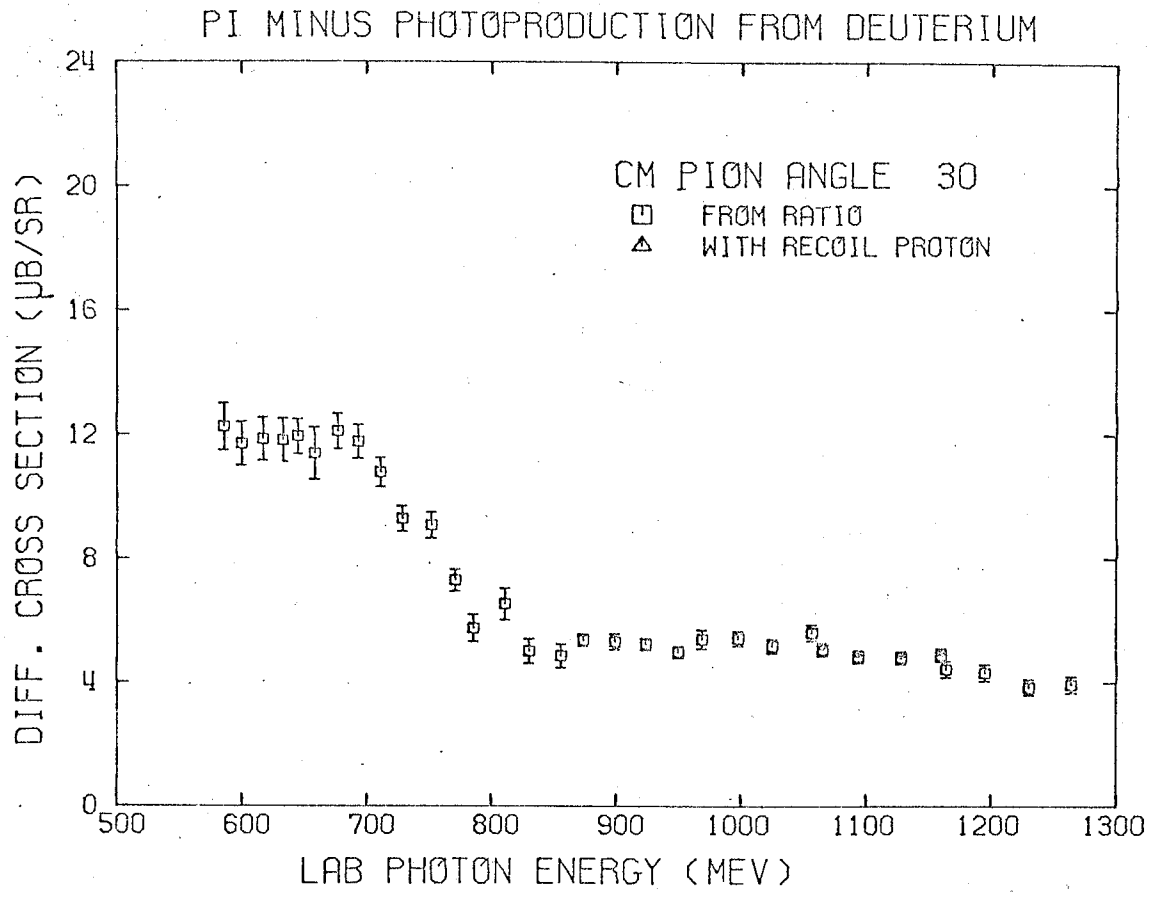
PI MINUS PHOTOPRODUCTION FROM DEUTERIUM
CM PION ANGLE 30
FROM RATIO
WITH RECOIL PROTON
DIFF. CROSS SECTION (μB/SR)
LAB PHOTON ENERGY (MEV)
0
4
8
12
16
20
24
500
600
700
800
900
1000
1100
1200
1300

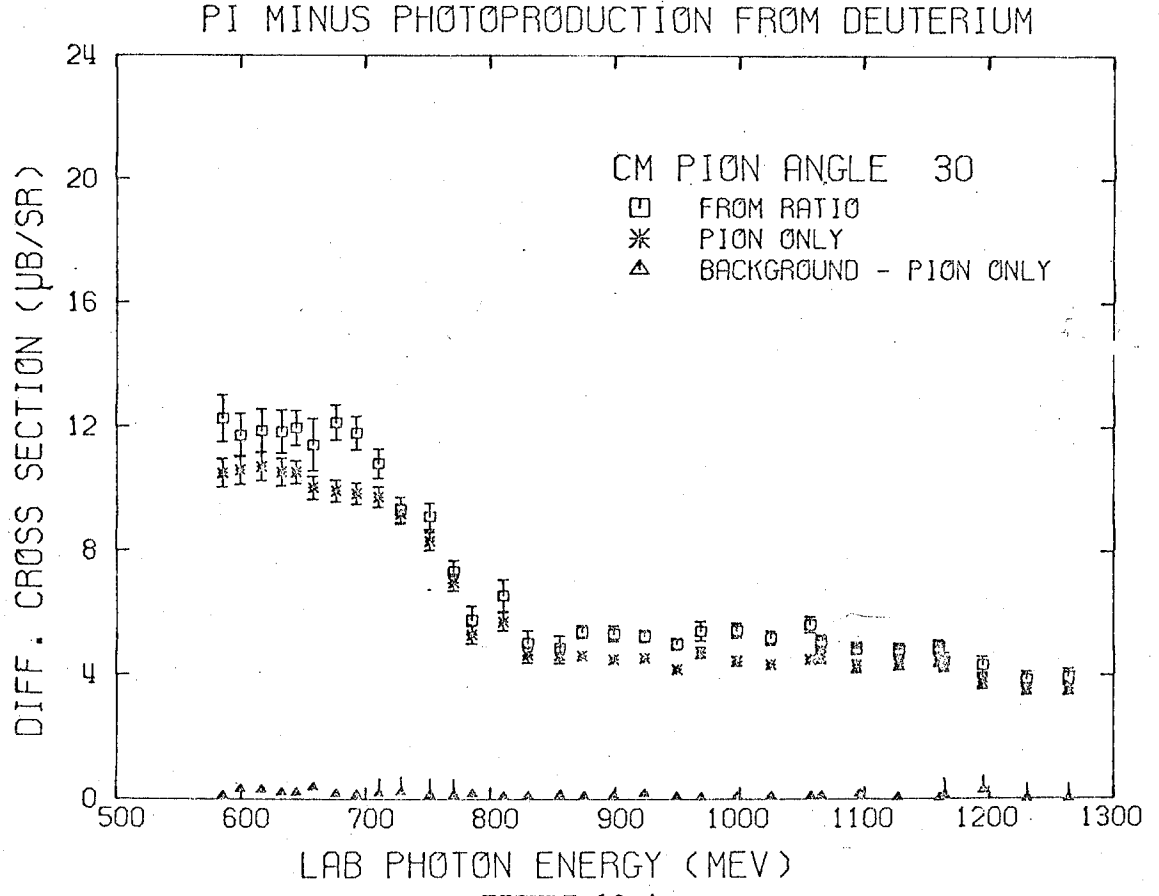
PI MINUS PHOTOPRODUCTION FROM DEUTERIUM
CM PION ANGLE 30
FROM RATIO
PION ONLY
BACKGROUND - PION ONLY
DIFF. CROSS SECTION (μB/SR)
LAB PHOTON ENERGY (MEV)
0
4
8
12
16
20
24
500
600
700
800
900
1000
1100
1200
1300

FIGURE 10.4

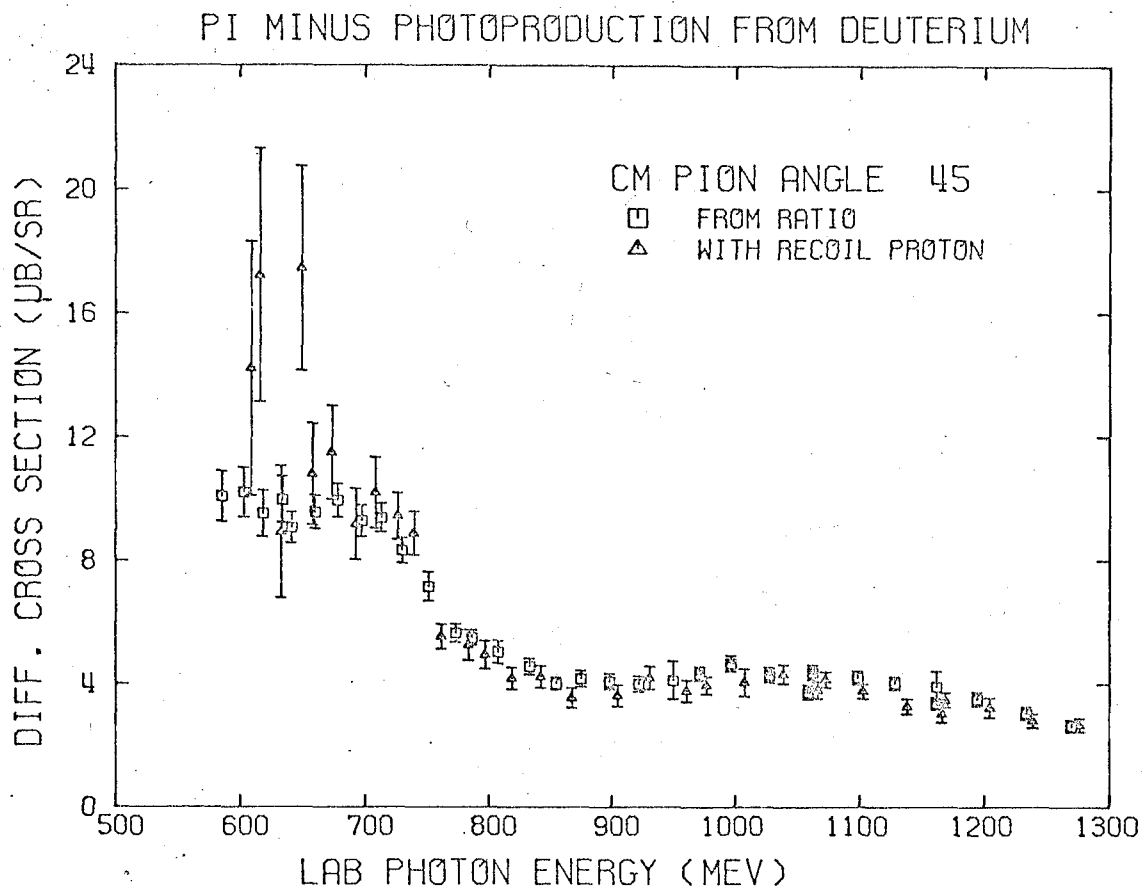
PI MINUS PHOTOPRODUCTION FROM DEUTERIUM
CM PION ANGLE 45
FROM RATIO
WITH RECOIL PROTON
DIFF. CROSS SECTION (μB/SR)
LAB PHOTON ENERGY (MEV)
0
4
8
12
16
20
24
500
600
700
800
900
1000
1100
1200
1300

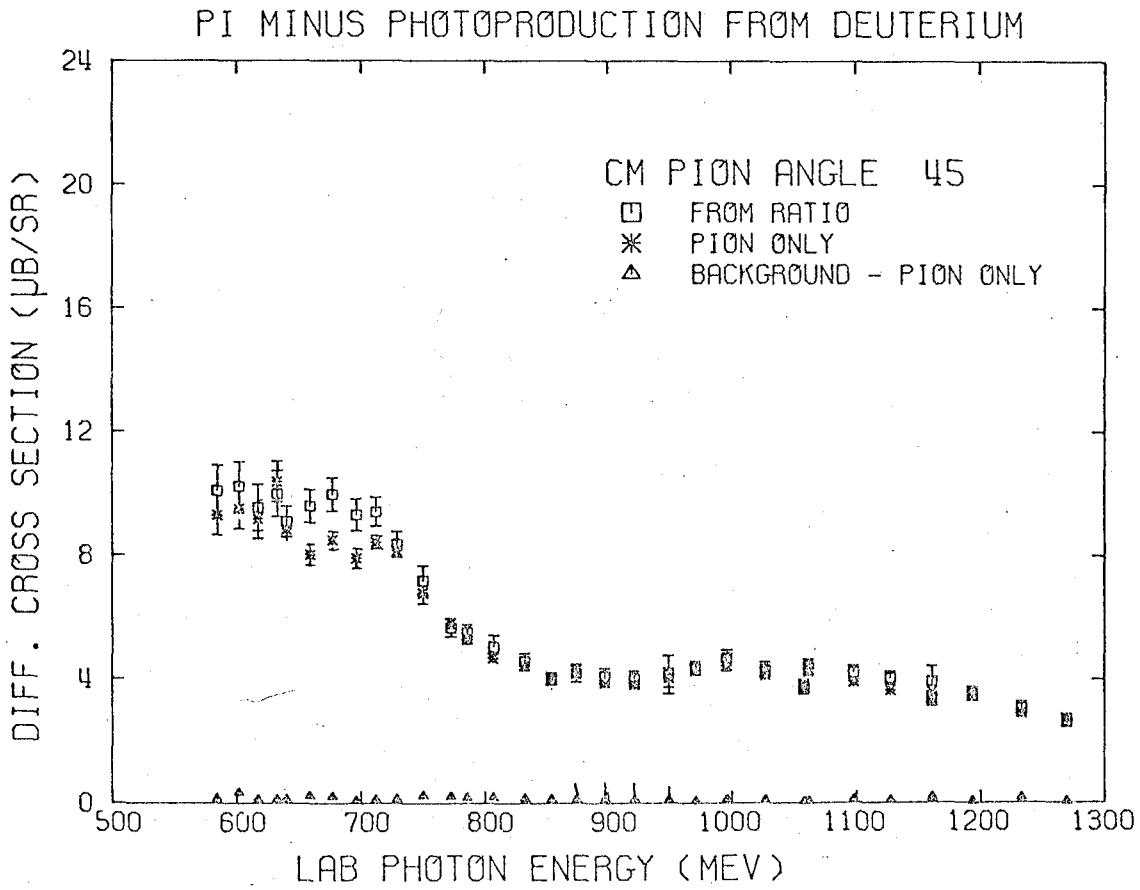
PI MINUS PHOTOPRODUCTION FROM DEUTERIUM
CM PION ANGLE 45
FROM RATIO
PION ONLY
BACKGROUND - PION ONLY
DIFF. CROSS SECTION (μB/SR)
LAB PHOTON ENERGY (MEV)
0
4
8
12
16
20
24
500
600
700
800
900
1000
1100
1200
1300

FIGURE 10.5

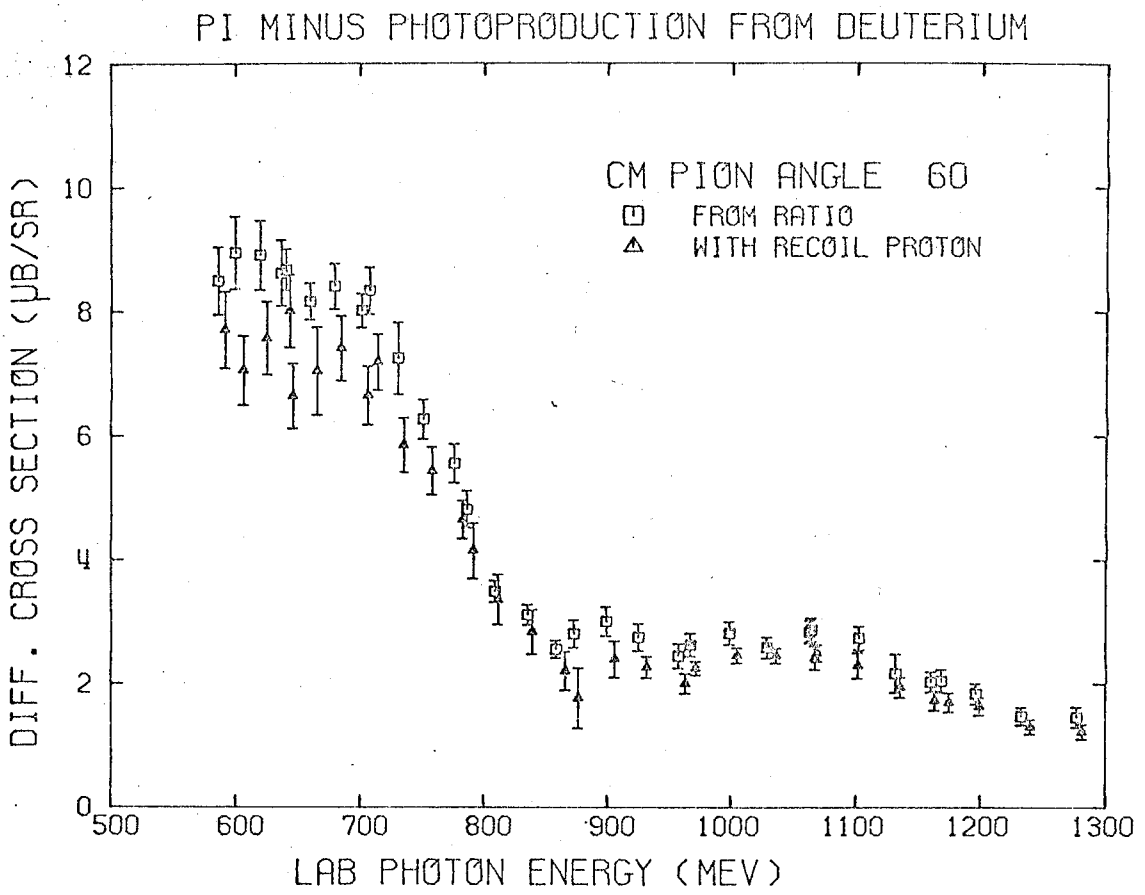
PI MINUS PHOTOPRODUCTION FROM DEUTERIUM
CM PION ANGLE 60
FROM RATIO
WITH RECOIL PROTON
DIFF. CROSS SECTION (μB/SR)
LAB PHOTON ENERGY (MEV)
0
2
4
6
8
10
12
500
600
700
800
900
1000
1100
1200
1300

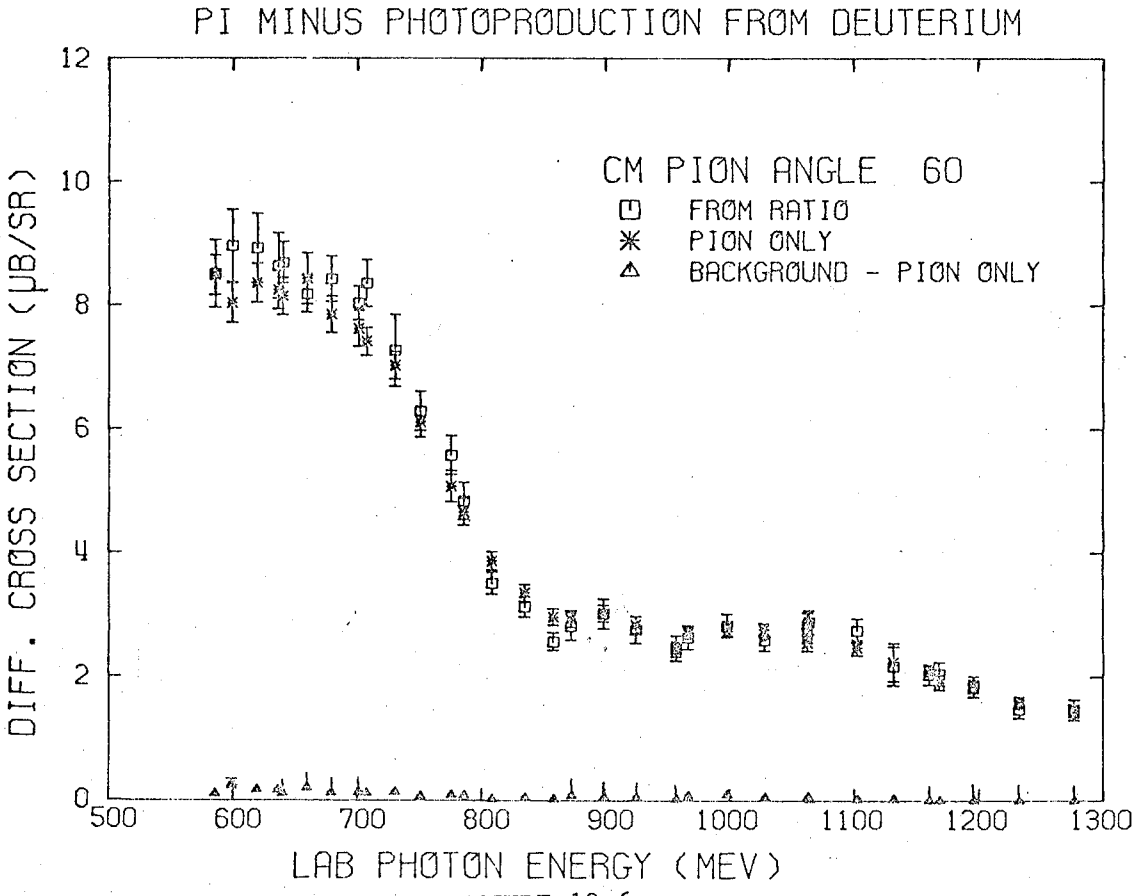
PI MINUS PHOTOPRODUCTION FROM DEUTERIUM
CM PION ANGLE 60
FROM RATIO
PION ONLY
BACKGROUND - PION ONLY
DIFF. CROSS SECTION (μB/SR)
LAB PHOTON ENERGY (MEV)
0
2
4
6
8
10
12
500
600
700
800
900
1000
1100
1200
1300

FIGURE 10.6

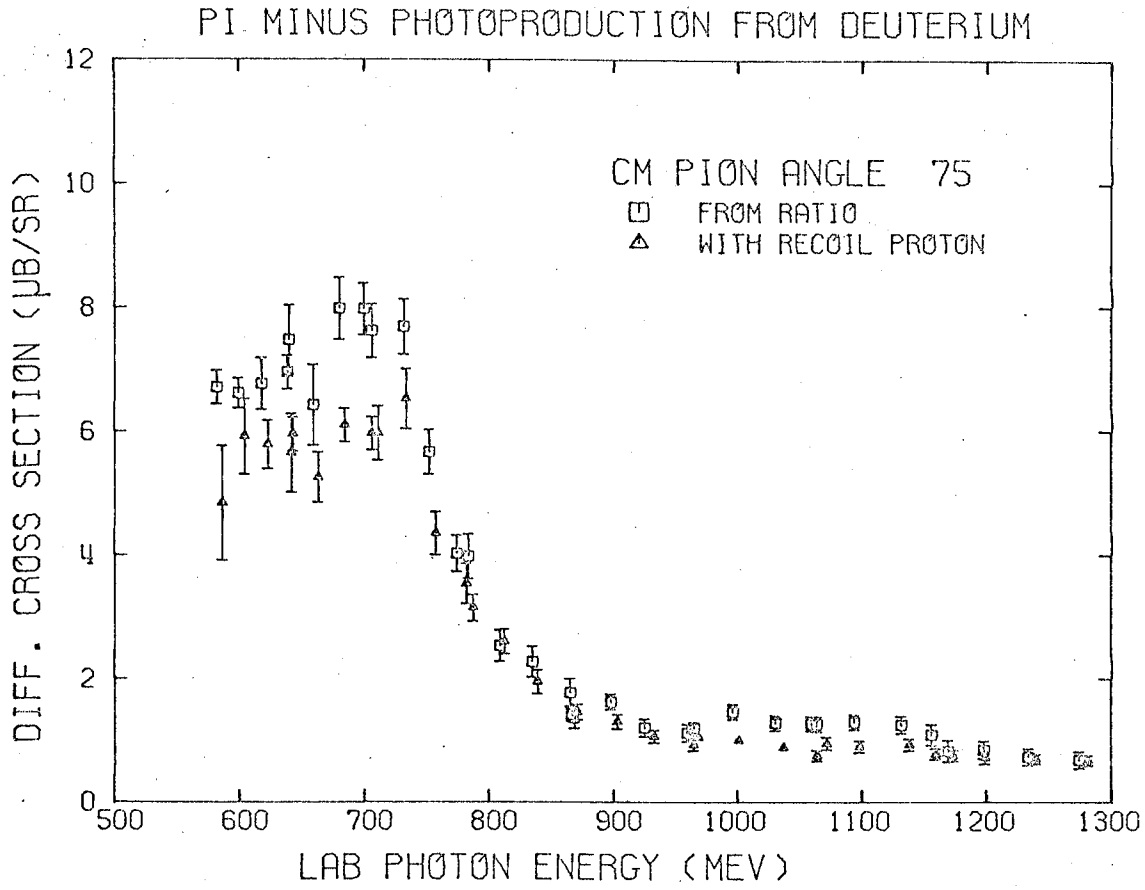
PI MINUS PHOTOPRODUCTION FROM DEUTERIUM
CM PION ANGLE 75
FROM RATIO
WITH RECOIL PROTON
DIFF. CROSS SECTION (μB/SR)
LAB PHOTON ENERGY (MEV)
0
2
4
6
8
10
12
500
600
700
800
900
1000
1100
1200
1300

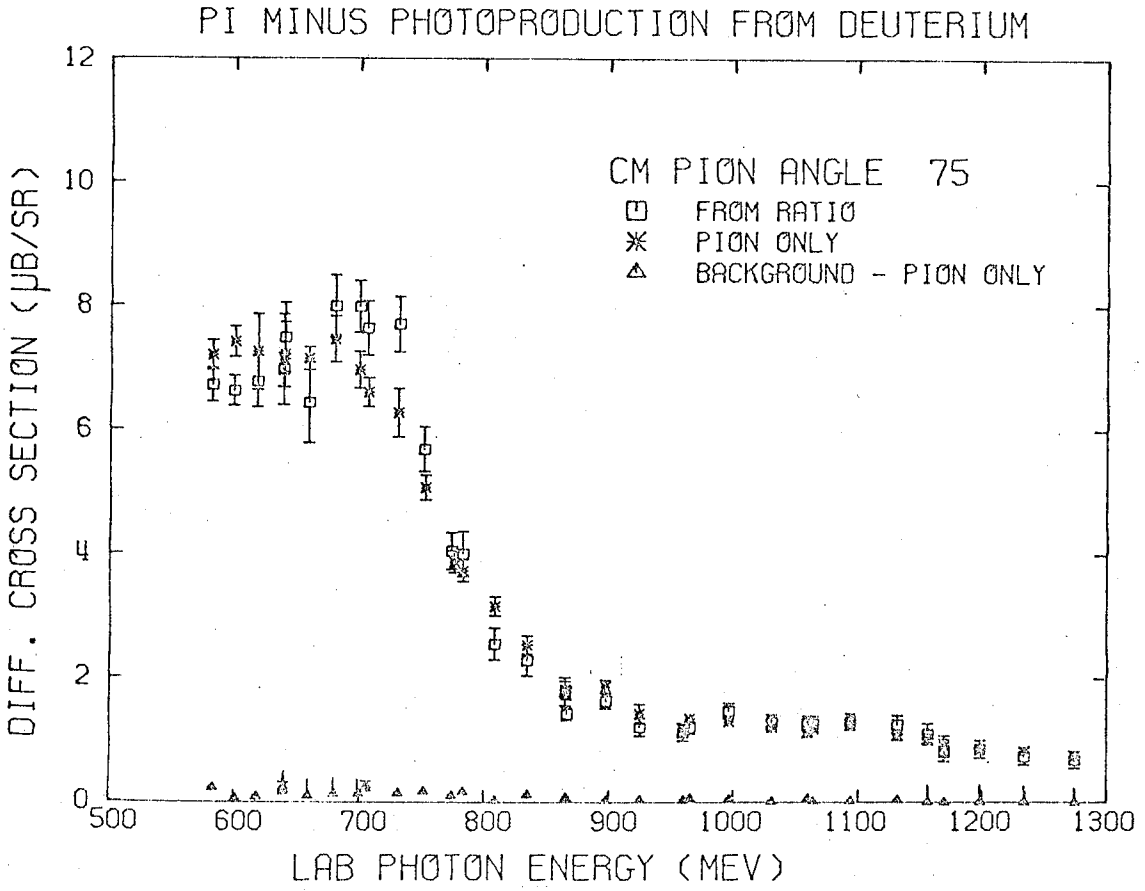
PI MINUS PHOTOPRODUCTION FROM DEUTERIUM
CM PION ANGLE 75
FROM RATIO
PION ONLY
BACKGROUND - PION ONLY
DIFF. CROSS SECTION (μB/SR)
LAB PHOTON ENERGY (MEV)
0
2
4
6
8
10
12
500
600
700
800
900
1000
1100
1200
1300

FIGURE 10.7

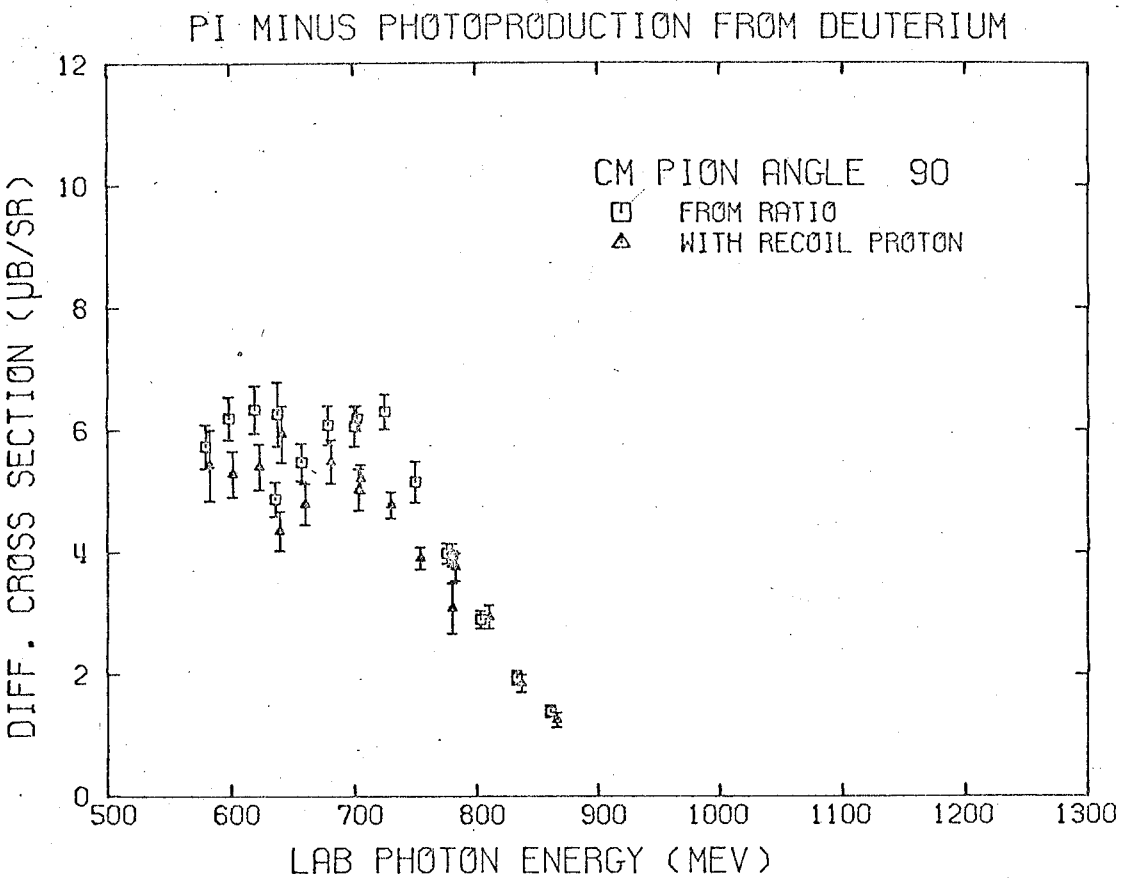
PI MINUS PHOTOPRODUCTION FROM DEUTERIUM
CM PION ANGLE 90
FROM RATIO
WITH RECOIL PROTON
DIFF. CROSS SECTION (μB/SR)
LAB PHOTON ENERGY (MEV)
0
2
4
6
8
10
12
500
600
700
800
900
1000
1100
1200
1300

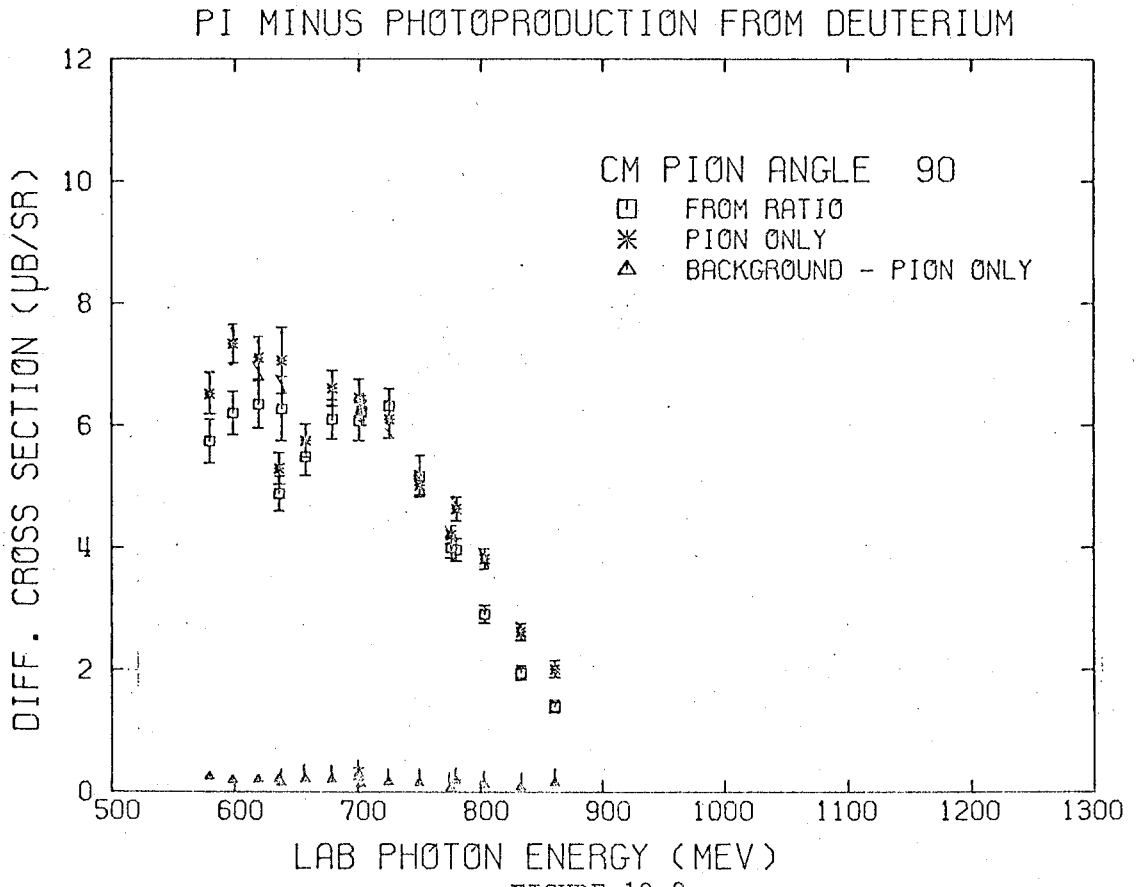
PI MINUS PHOTOPRODUCTION FROM DEUTERIUM
CM PION ANGLE 90
FROM RATIO
PION ONLY
BACKGROUND - PION ONLY
DIFF. CROSS SECTION (μB/SR)
LAB PHOTON ENERGY (MEV)
0
2
4
6
8
10
12
500
600
700
800
900
1000
1100
1200
1300

FIGURE 10.8

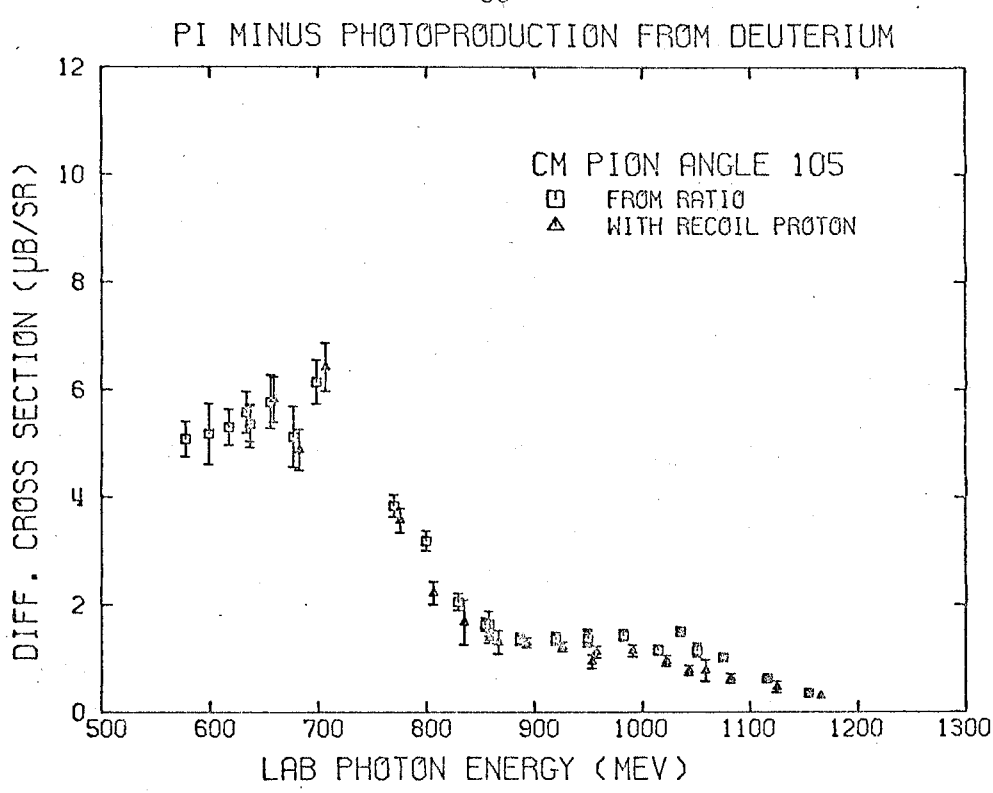
PI MINUS PHOTOPRODUCTION FROM DEUTERIUM
CM PION ANGLE 105
FROM RATIO
WITH RECOIL PROTON
DIFF. CROSS SECTION (μB/SR)
LAB PHOTON ENERGY (MEV)
0
2
4
6
8
10
12
500
600
700
800
900
1000
1100
1200
1300

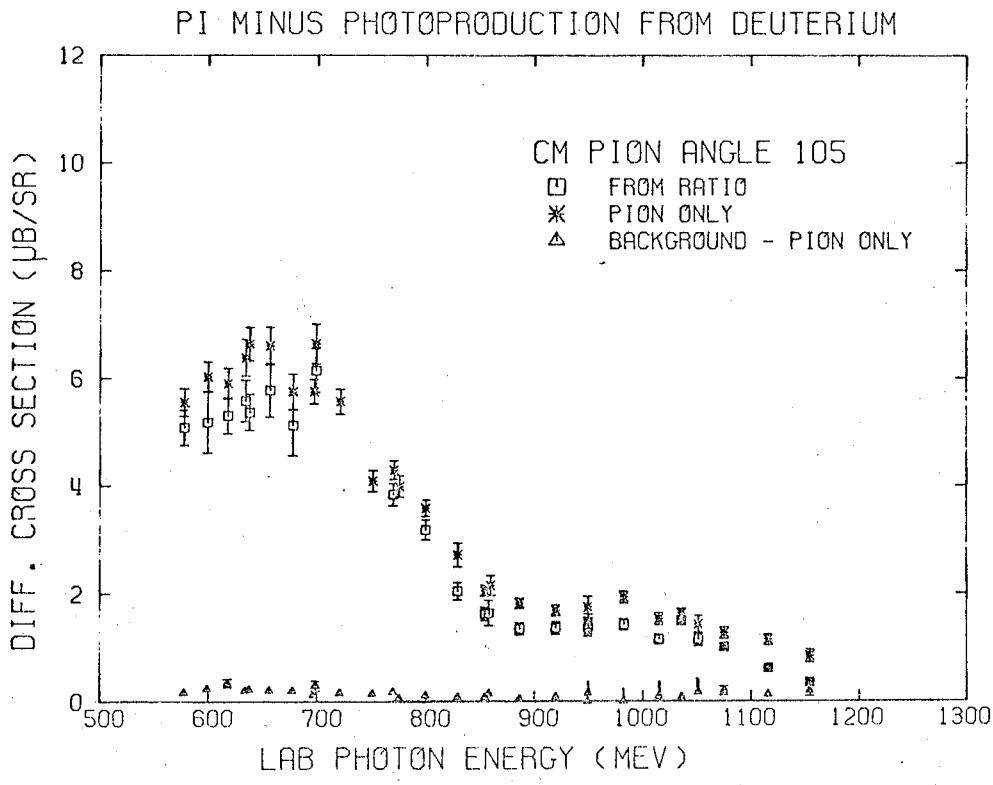
PI MINUS PHOTOPRODUCTION FROM DEUTERIUM
CM PION ANGLE 105
FROM RATIO
PION ONLY
BACKGROUND - PION ONLY
DIFF. CROSS SECTION (μB/SR)
LAB PHOTON ENERGY (MEV)
0
2
4
6
8
10
12
500
600
700
800
900
1000
1100
1200
1300

FIGURE 10.9

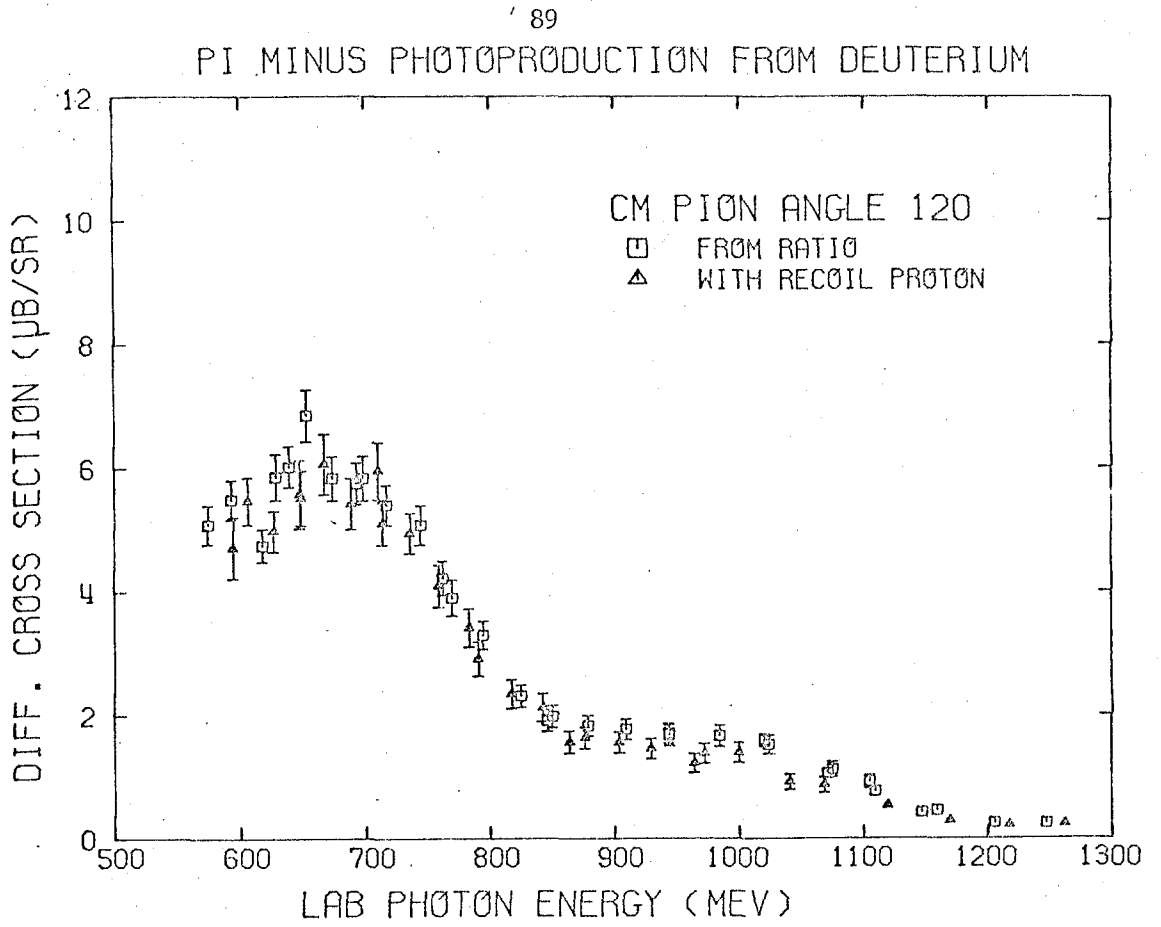
PI MINUS PHOTOPRODUCTION FROM DEUTERIUM
CM PION ANGLE 120
FROM RATIO
WITH RECOIL PROTON
DIFF. CROSS SECTION (μB/SR)
LAB PHOTON ENERGY (MEV)
0
2
4
6
8
10
12
500
600
700
800
900
1000
1100
1200
1300

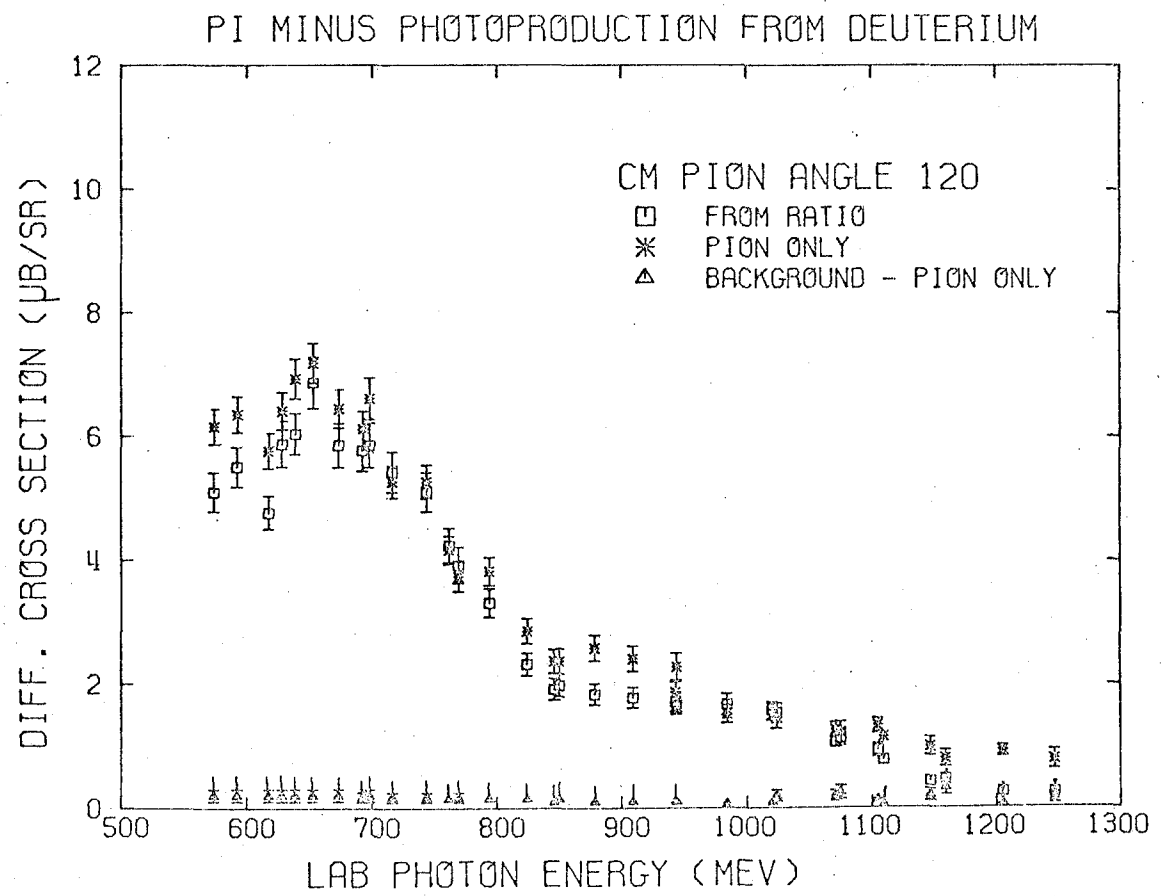
PI MINUS PHOTOPRODUCTION FROM DEUTERIUM
CM PION ANGLE 120
FROM RATIO
PION ONLY
BACKGROUND - PION ONLY
DIFF. CROSS SECTION (μB/SR)
LAB PHOTON ENERGY (MEV)
0
2
4
6
8
10
12
500
600
700
800
900
1000
1100
1200
1300

FIGURE 10.10

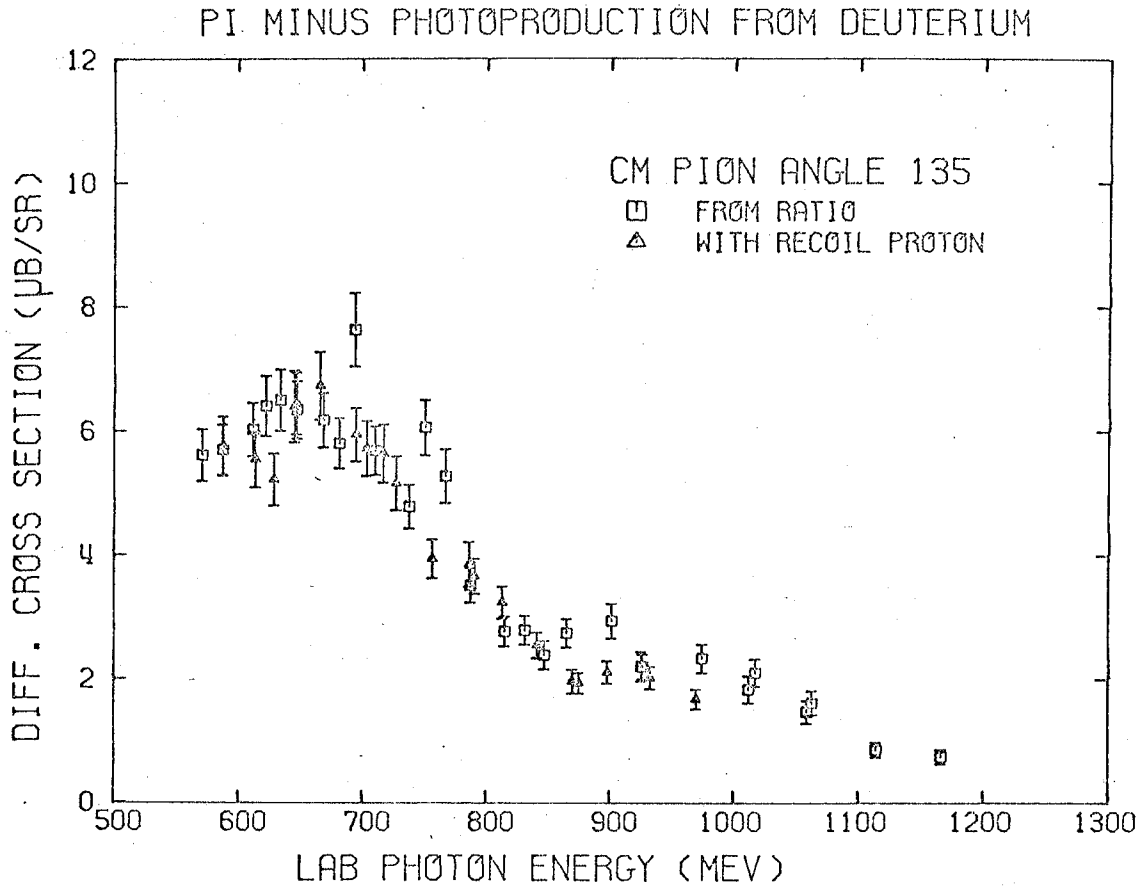
PI MINUS PHOTOPRODUCTION FROM DEUTERIUM
CM PION ANGLE 135
FROM RATIO
WITH RECOIL PROTON
DIFF. CROSS SECTION (μB/SR)
LAB PHOTON ENERGY (MEV)

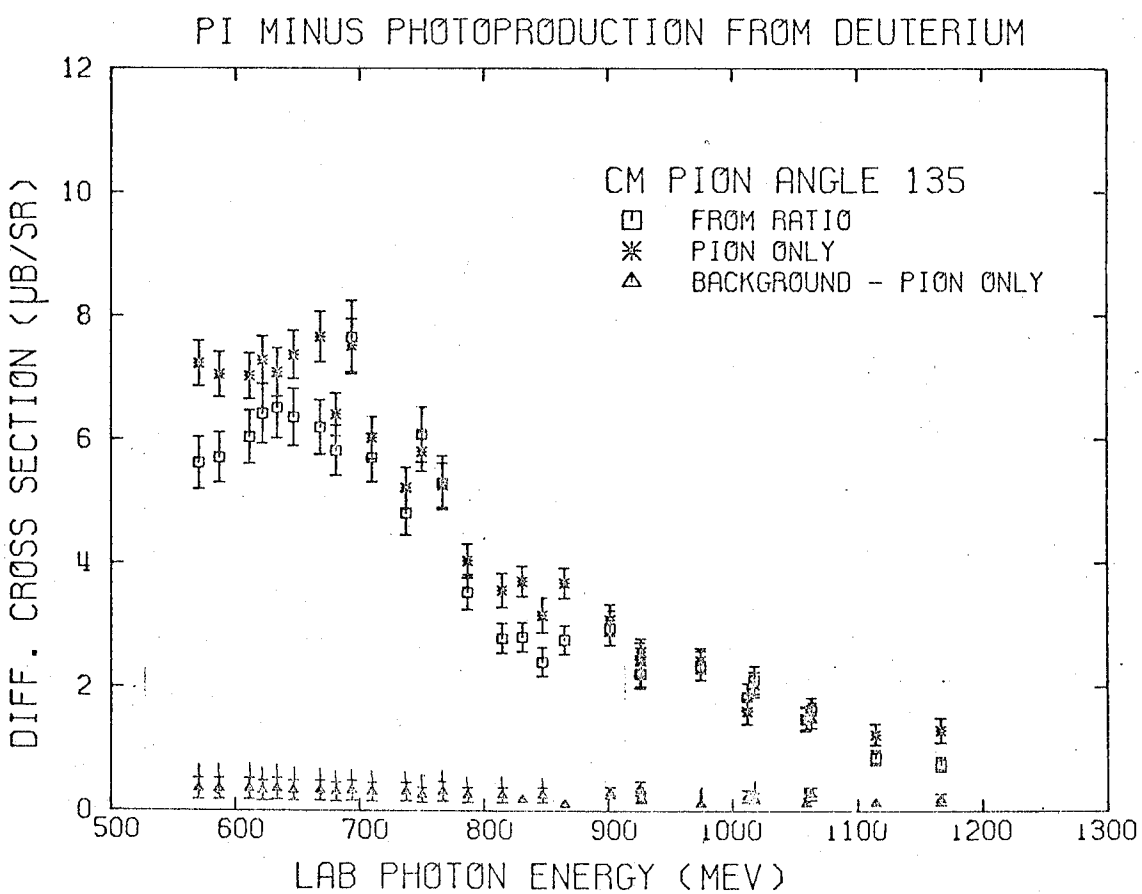
PI MINUS PHOTOPRODUCTION FROM DEUTERIUM
CM PION ANGLE 135
FROM RATIO
PION ONLY
BACKGROUND - PION ONLY
DIFF. CROSS SECTION (μB/SR)
LAB PHOTON ENERGY (MEV)

FIGURE 10.11

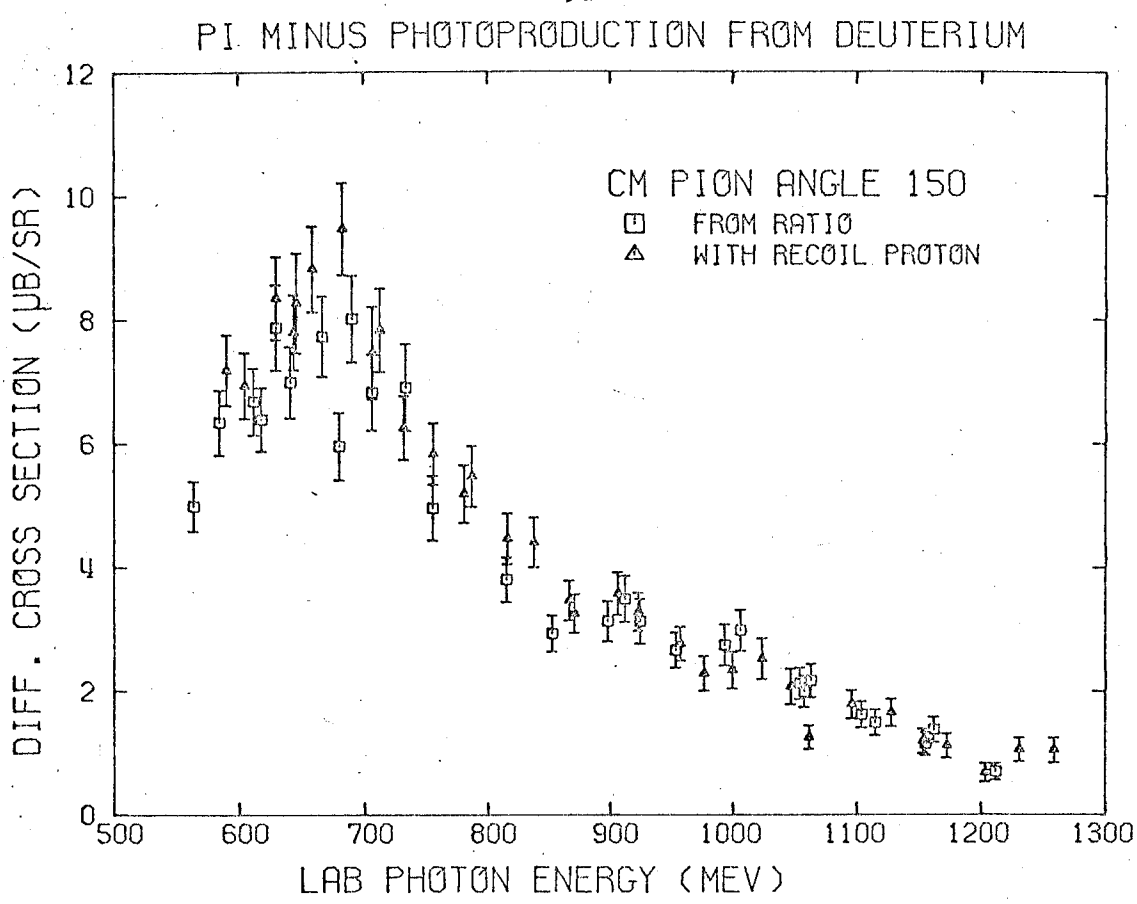
PI MINUS PHOTOPRODUCTION FROM DEUTERIUM
CM PION ANGLE 150
FROM RATIO
WITH RECOIL PROTON
DIFF. CROSS SECTION (μB/SR)
LAB PHOTON ENERGY (MEV)
0
2
4
6
8
10
12
500
600
700
800
900
1000
1100
1200
1300

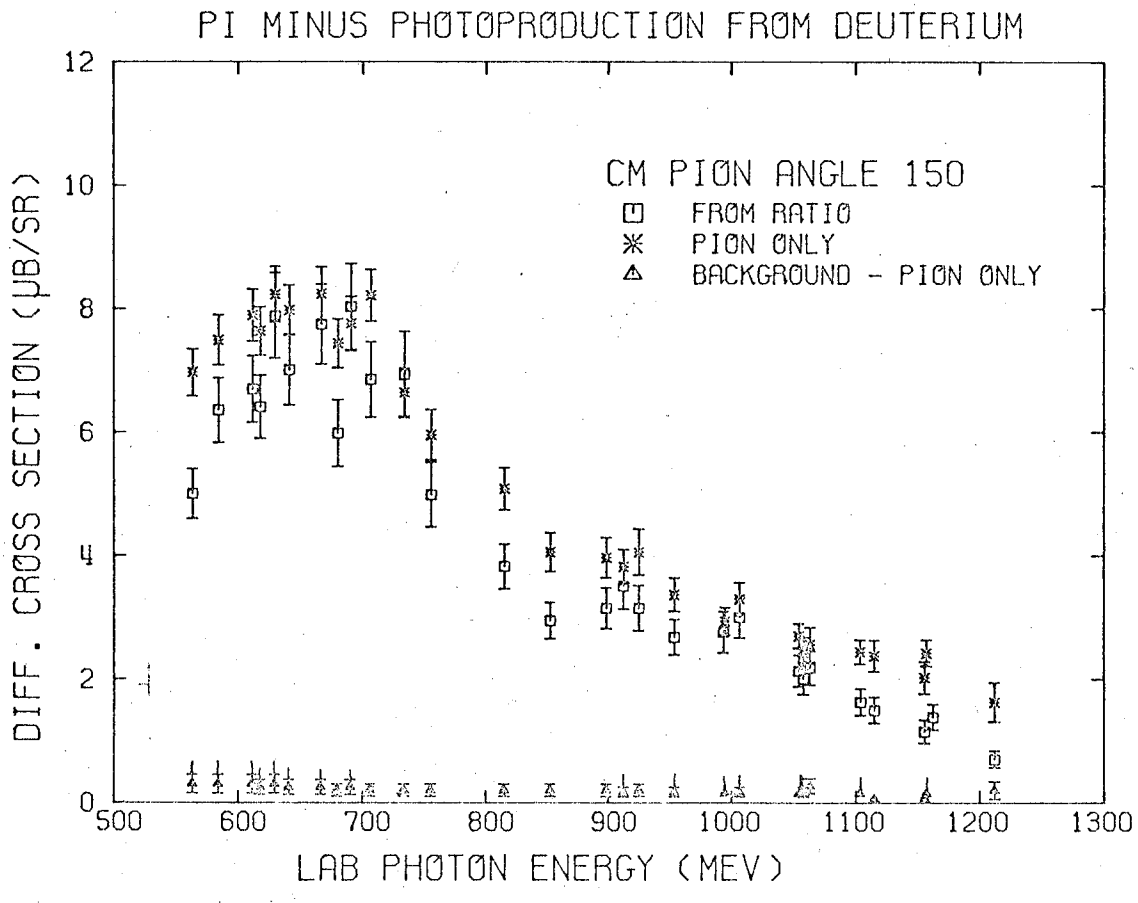
PI MINUS PHOTOPRODUCTION FROM DEUTERIUM
CM PION ANGLE 150
FROM RATIO
PION ONLY
BACKGROUND - PION ONLY
DIFF. CROSS SECTION (μB/SR)
LAB PHOTON ENERGY (MEV)
0
2
4
6
8
10
12
500
600
700
800
900
1000
1100
1200
1300

FIGURE 10.12

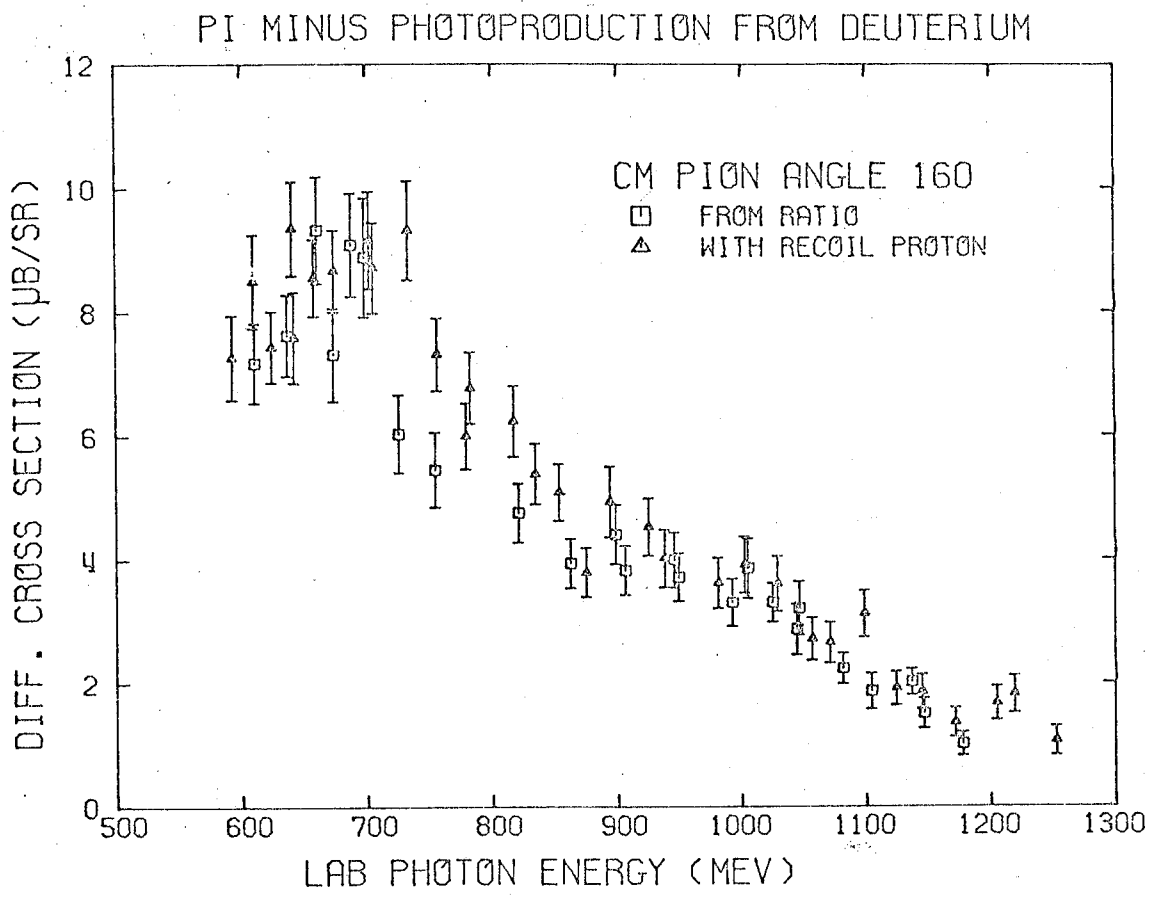
PI MINUS PHOTOPRODUCTION FROM DEUTERIUM
CM PION ANGLE 160
FROM RATIO
WITH RECOIL PROTON
DIFF. CROSS SECTION (μB/SR)
LAB PHOTON ENERGY (MEV)
0
2
4
6
8
10
12
500
600
700
800
900
1000
1100
1200
1300

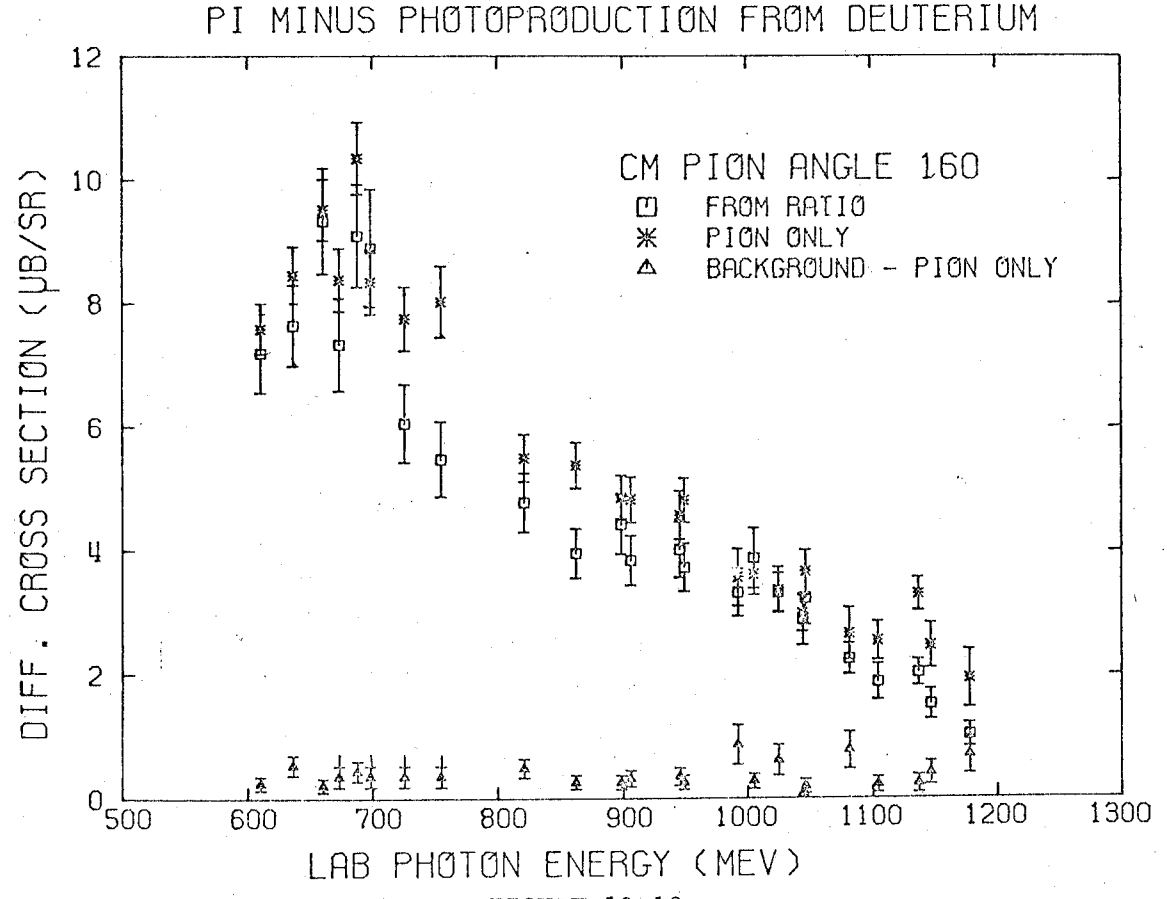
PI MINUS PHOTOPRODUCTION FROM DEUTERIUM
CM PION ANGLE 160
FROM RATIO
PION ONLY
BACKGROUND - PION ONLY
DIFF. CROSS SECTION (μB/SR)
LAB PHOTON ENERGY (MEV)
0
2
4
6
8
10
12
500
600
700
800
900
1000
1100
1200
1300

FIGURE 10.13

H. Final π^- cross sections ($\gamma n \rightarrow \pi^- p$)

To obtain a final set of data points for publication and fitting purposes, the following procedure was used. The ratio cross sections and recoil cross sections were separately interpolated to standard energies at each rough angular setting. The interpolated ratio cross sections and interpolated recoil cross sections were then averaged to obtain the final cross section for the reaction $\gamma n \rightarrow \pi^- p$. These final cross sections are listed in Table 5 and plotted in Figures 11 and 12.

Details of the interpolation and averaging were as follows. A straight line interpolation between data points was used. While this type of interpolation tended to smooth out large deviations, the later averaging of the two types of cross section would do the same thing. Therefore, I considered a linear interpolation to be adequate.

The final cross section was a weighted average according to the formula:

$$C = \frac{C_1/E_1^2 + C_2/E_2^2}{1/E_1^2 + 1/E_2^2} \qquad \text{(IV.1)}$$

where C_1 and C_2 are respectively the ratio and recoil cross

sections and E_1 and E_2 are their statistical errors. The final errors of the averaged cross sections were set equal to the larger of the following:

1) The standard deviation of the data points from their average:

$$S.D. = \frac{\sqrt{((C_1-C)/E_1)^2 + ((C_2-C)/E_2)^2}}{\sqrt{1/E_1^2 + 1/E_2^2}} \qquad (IV.2)$$

2) The standard error in the average of the two data points:

$$\sigma = \frac{1}{\sqrt{1/E_1^2 + 1/E_2^2}} \qquad (IV.3)$$

I. Total cross section, 0° cross section, 180° cross section.

By means of Moravcsik fits, Pat Walden(44) has obtained values for the 0° cross section, 180° cross section, and total integrated cross section at each energy. These are given in Table 6 and plotted in Figures 13, 14, and 15. The errors given are due to the possible error of the fit. A notable characteristic of all three curves is the sharp dropoff occuring between 700 and 800 MeV lab photon energy. A discussion of this behavior is given in Part V.

TABLE 5

FINAL CROSS SECTIONS FOR THE REACTION $\gamma n \rightarrow \pi^- p$

Average of Ratio and Recoil Cross Sections (only Ratio cross sections at angles less than 45° CM)

k_γ^{lab}	θ_π^{CM}	$\sigma(\theta)$	$\Delta\sigma(\theta)$	k_γ^{lab}	θ_π^{CM}	$\sigma(\theta)$	$\Delta\sigma(\theta)$
600	6.2	21.39	1.24	660	6.2	20.33	1.32
600	10.2	18.75	1.27	660	10.1	20.19	1.42
600	20.3	13.85	0.76	660	20.3	14.15	0.78
600	30.3	11.72	0.70	660	30.4	11.48	0.82
600	45.1	10.19	0.81	660	45.3	9.58	0.54
600	60.4	8.95	0.58	660	60.1	8.18	0.30
600	75.3	6.63	0.25	660	75.2	6.49	0.65
600	90.1	6.21	0.36	660	89.9	5.55	0.31
600	104.6	5.18	0.55	660	104.9	5.64	0.51
600	119.7	5.22	0.25	660	119.7	6.27	0.31
600	134.6	5.78	0.31	660	134.6	6.41	0.35
600	149.4	6.78	0.38	660	149.5	8.14	0.65
600	159.8	7.82	0.71	660	159.4	8.82	0.51
620	6.3	21.44	1.24	680	6.3	21.63	2.13
620	10.3	18.98	1.27	680	10.2	17.25	1.20
620	20.4	14.20	0.78	680	20.4	13.15	0.72
620	30.5	11.86	0.70	680	30.6	12.05	0.57
620	45.6	9.59	0.75	680	45.7	9.86	0.54
620	60.6	8.91	0.56	680	60.5	8.41	0.37
620	75.6	6.79	0.40	680	75.5	7.98	0.50
620	90.4	6.34	0.39	680	90.5	6.09	0.32
620	105.2	5.31	0.33	680	105.2	5.27	0.54
620	119.9	4.99	0.22	680	120.0	5.77	0.28
620	134.8	5.79	0.40	680	134.8	6.59	0.35
620	149.3	7.09	0.40	680	149.1	7.40	1.00
620	159.2	7.54	0.45	680	159.1	8.56	0.44
640	6.2	23.01	1.38	700	6.3	21.35	1.34
640	10.1	17.07	1.15	700	10.2	17.87	1.25
640	20.3	13.29	0.73	700	20.5	13.77	0.72
640	30.3	11.90	0.62	700	30.6	11.40	0.52
640	45.2	9.17	0.52	700	45.8	9.31	0.51
640	59.9	8.68	0.34	700	60.8	8.05	0.29
640	74.7	7.45	0.56	700	75.9	7.96	0.42
640	89.6	4.99	0.29	700	90.8	6.07	0.33
640	104.3	5.63	0.42	700	119.4	5.67	0.27
640	119.6	5.84	0.51	700	134.4	5.77	0.29
640	134.6	6.18	0.33	700	149.4	7.19	0.70
640	149.3	7.46	0.64	700	159.3	8.96	0.60
640	159.2	7.73	0.50				

k_γ^{lab}	θ_π^{CM}	$\sigma(\theta)$	$\Delta\sigma(\theta)$
720	6.2	16.83	0.97
720	10.0	17.15	1.38
720	20.1	12.55	0.56
720	30.3	10.01	0.44
720	45.1	8.92	0.44
720	60.0	7.76	0.44
720	74.7	7.66	0.44
720	89.8	6.28	0.27
720	119.6	5.22	0.24
720	134.5	5.42	0.29
720	149.4	7.09	0.45
720	159.2	7.73	1.19
740	6.3	14.30	0.87
740	10.1	13.69	1.14
740	20.3	10.83	0.50
740	30.4	9.20	0.42
740	45.4	7.76	0.44
740	60.3	6.81	0.46
740	75.2	6.86	0.41
740	90.1	5.63	0.32
740	119.7	4.96	0.23
740	134.6	4.74	0.26
740	149.7	6.13	0.51
740	159.2	6.99	1.46
760	6.4	14.28	0.90
760	10.2	12.18	0.93
760	20.5	9.03	0.44
760	30.6	8.35	0.39
760	45.5	6.18	0.38
760	60.5	5.76	0.32
760	75.5	4.69	0.41
760	90.4	4.14	0.48
760	119.9	4.22	0.23
760	134.4	4.68	0.48
760	149.7	5.75	0.49
760	159.6	7.25	0.59
780	6.3	13.74	0.66
780	10.2	10.39	0.72
780	20.3	7.38	0.59
780	30.4	6.38	0.41
780	45.4	5.51	0.23
780	60.5	5.02	0.26
780	75.4	3.80	0.23
780	89.5	3.81	0.32
780	104.4	3.50	0.15
780	119.5	3.63	0.20
780	134.4	3.96	0.23
780	149.8	5.23	0.47
780	159.6	6.30	0.41
800	6.3	12.63	0.46
800	10.2	8.80	0.54
800	20.3	6.72	0.52
800	30.2	6.21	0.48
800	44.9	5.07	0.26
800	59.9	3.97	0.20
800	74.7	2.93	0.17
800	89.7	3.13	0.12
800	104.7	2.88	0.33
800	119.7	2.94	0.20
800	134.5	3.33	0.19
800	149.7	5.03	0.46
800	159.6	6.13	0.56
825	6.3	10.83	0.41
825	10.3	8.04	0.50
825	20.5	6.06	0.38
825	30.4	5.46	0.43
825	45.2	4.50	0.25
825	60.3	3.24	0.16
825	75.1	2.33	0.16
825	90.1	2.26	0.10
825	105.1	2.15	0.15
825	119.9	2.29	0.14
825	134.7	2.80	0.17
825	148.9	3.94	0.43
825	159.0	5.20	0.59

k_γ^{lab}	θ_π^{CM}	$\sigma(\theta)$	$\Delta\sigma(\theta)$
850	6.4	9.33	0.39
850	10.4	6.90	0.45
850	20.7	5.33	0.35
850	30.7	4.91	0.39
850	45.7	4.10	0.18
850	60.8	2.74	0.14
850	75.5	1.83	0.14
850	90.5	1.60	0.08
850	105.4	1.68	0.18
850	119.7	1.94	0.11
850	134.4	2.54	0.19
850	149.1	3.40	0.50
850	159.1	4.62	0.48
875	6.3	7.76	0.75
875	10.2	7.29	0.51
875	20.2	5.27	0.27
875	30.0	5.38	0.20
875	45.0	4.23	0.22
875	59.8	2.64	0.39
875	74.6	1.46	0.08
875	104.4	1.38	0.07
875	119.4	1.74	0.12
875	134.5	2.21	0.40
875	149.3	3.17	0.22
875	159.3	3.85	0.28
900	6.3	7.55	0.75
900	10.2	6.19	0.47
900	20.3	4.93	0.26
900	30.2	5.32	0.25
900	45.1	4.04	0.21
900	60.1	2.76	0.34
900	74.9	1.45	0.14
900	104.8	1.31	0.07
900	119.6	1.68	0.12
900	134.6	2.36	0.38
900	149.3	3.33	0.24
900	159.0	4.25	0.29
925	6.4	6.85	0.71
925	10.3	5.36	0.41
925	20.5	4.75	0.25
925	30.4	5.24	0.19
925	45.5	4.03	0.23
925	60.4	2.52	0.23
925	75.3	1.16	0.09
925	105.1	1.27	0.07
925	119.8	1.60	0.13
925	134.8	2.11	0.14
925	149.1	3.26	0.23
925	159.1	4.14	0.25
950	10.3	4.18	0.34
950	20.6	4.75	0.24
950	30.7	5.00	0.19
950	45.6	3.97	0.31
950	60.7	2.28	0.20
950	75.6	1.04	0.08
950	104.9	1.21	0.10
950	119.4	1.51	0.19
950	134.5	2.02	0.19
950	149.2	2.82	0.20
950	159.2	3.80	0.29
975	10.2	4.30	0.25
975	20.3	4.68	0.21
975	30.1	5.42	0.30
975	44.8	4.21	0.22
975	59.5	2.38	0.18
975	74.5	1.11	0.11
975	104.3	1.23	0.18
975	119.5	1.53	0.15
975	134.3	2.34	0.23
975	149.3	2.55	0.23
975	159.4	3.73	0.30

k_γ^{lab}	θ_π^{CM}	$\sigma(\theta)$	$\Delta\sigma(\theta)$
1000	10.3	4.32	0.25
1000	20.4	4.54	0.21
1000	30.2	5.41	0.24
1000	45.2	4.46	0.27
1000	59.8	2.54	0.17
1000	74.9	1.10	0.18
1000	104.7	1.19	0.10
1000	119.7	1.50	0.12
1000	134.4	2.20	0.23
1000	149.1	2.64	0.18
1000	159.0	3.62	0.24
1025	10.3	3.78	0.23
1025	20.4	4.41	0.24
1025	30.4	5.19	0.23
1025	45.4	4.29	0.20
1025	60.2	2.51	0.10
1025	75.2	1.03	0.17
1025	105.1	1.05	0.11
1025	119.1	1.43	0.13
1025	134.1	1.88	0.15
1025	149.3	2.52	0.18
1025	159.0	3.45	0.22
1050	10.4	4.13	0.28
1050	20.6	4.27	0.21
1050	30.6	5.53	0.25
1050	45.6	3.97	0.19
1050	60.5	2.57	0.13
1050	75.5	1.03	0.17
1050	105.3	1.04	0.16
1050	109.0	1.08	0.28
1050	119.2	1.20	0.12
1050	134.3	1.65	0.14
1050	149.5	2.08	0.15
1050	159.0	2.85	0.20
1075	6.1	5.10	0.33
1075	10.1	3.85	0.28
1075	20.3	4.34	0.25
1075	30.1	5.00	0.21
1075	44.8	4.22	0.17
1075	59.7	2.61	0.21
1075	74.5	0.96	0.23
1075	109.3	0.88	0.17
1075	118.8	1.04	0.08
1075	133.9	1.29	0.17
1075	149.1	1.75	0.18
1075	159.0	2.46	0.18
1100	6.2	5.37	0.32
1100	10.2	4.07	0.58
1100	20.4	4.33	0.25
1100	30.3	4.84	0.20
1100	45.0	4.02	0.19
1100	59.9	2.54	0.22
1100	74.8	1.04	0.18
1100	109.5	0.72	0.09
1100	119.2	0.95	0.10
1100	134.1	1.02	0.14
1100	149.2	1.71	0.13
1100	159.0	2.27	0.29
1125	6.3	4.41	0.50
1125	10.3	3.79	0.28
1125	20.6	3.72	0.22
1125	30.4	4.82	0.20
1125	45.3	3.79	0.28
1125	60.2	2.13	0.15
1125	75.2	1.03	0.16
1125	109.7	0.54	0.04
1125	118.8	0.60	0.06
1125	134.4	0.84	0.12
1125	149.2	1.53	0.12
1125	159.0	1.91	0.14

k_γ^{lab}	θ_π^{CM}	$\sigma(\theta)$	$\Delta\sigma(\theta)$
1150	6.3	4.35	0.31
1150	10.3	3.30	0.31
1150	20.7	3.69	0.22
1150	30.6	4.87	0.21
1150	45.5	3.50	0.15
1150	60.5	1.93	0.13
1150	75.5	0.92	0.08
1150	109.9	0.38	0.03
1150	118.9	0.45	0.07
1150	134.7	0.78	0.12
1150	149.3	1.29	0.12
1150	159.0	1.59	0.18
1175	6.4	4.86	0.35
1175	10.3	3.11	0.42
1175	20.3	3.87	0.42
1175	30.0	4.40	0.27
1175	44.8	3.32	0.32
1175	59.6	1.81	0.13
1175	74.5	0.81	0.10
1175	119.1	0.35	0.05
1175	149.2	1.04	0.13
1175	158.9	1.19	0.16
1200	6.6	4.53	0.34
1200	10.3	2.66	0.37
1200	20.4	3.94	0.44
1200	30.2	4.25	0.27
1200	45.1	3.36	0.18
1200	59.8	1.70	0.11
1200	74.9	0.76	0.08
1200	119.1	0.27	0.02
1200	149.3	0.77	0.11
1200	159.8	1.63	0.27
1225	6.7	4.17	0.32
1225	10.5	2.92	0.40
1225	20.6	3.78	0.42
1225	30.4	3.92	0.26
1225	45.3	3.09	0.17
1225	60.2	1.48	0.10
1225	75.2	0.72	0.07
1225	119.4	0.24	0.03
1225	149.8	0.97	0.18
1225	159.7	1.69	0.29
1250	6.7	3.86	0.30
1250	30.6	3.90	0.26
1250	45.5	2.82	0.15
1250	60.5	1.35	0.09
1250	75.5	0.70	0.07
1250	120.0	0.23	0.05
1250	149.7	1.05	0.20
1250	159.6	1.13	0.24

FIGURE 11

ANGULAR DISTRIBUTIONS OF FINAL π^- CROSS SECTIONS

Points at 180° are from the experiment by Fujii et al.(11)

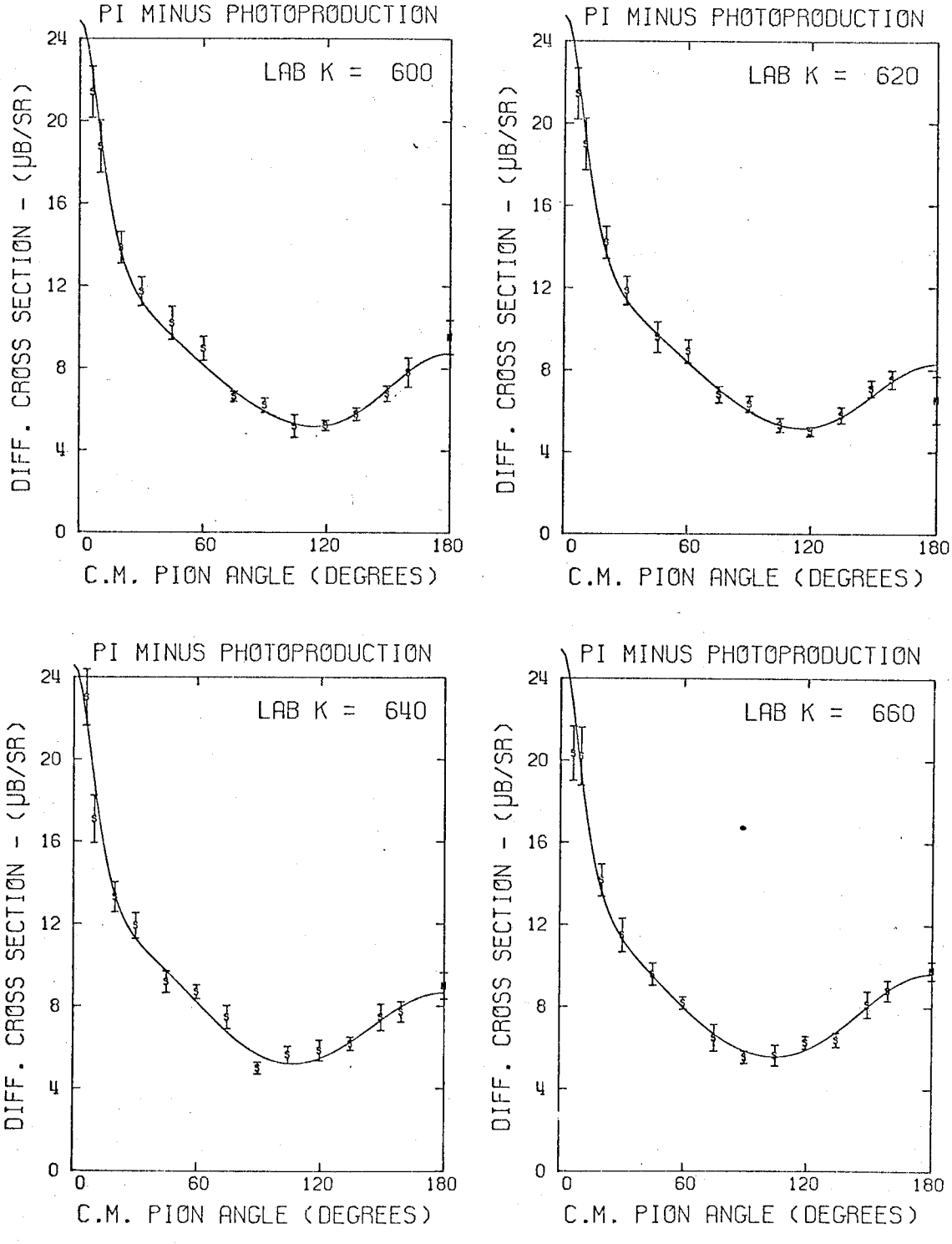
PI MINUS PHOTOPRODUCTION
LAB K = 600
DIFF. CROSS SECTION - (μB/SR)
C.M. PION ANGLE (DEGREES)
PI MINUS PHOTOPRODUCTION
LAB K = 620
DIFF. CROSS SECTION - (μB/SR)
C.M. PION ANGLE (DEGREES)
PI MINUS PHOTOPRODUCTION
LAB K = 640
DIFF. CROSS SECTION - (μB/SR)
C.M. PION ANGLE (DEGREES)
PI MINUS PHOTOPRODUCTION
LAB K = 660
DIFF. CROSS SECTION - (μB/SR)
C.M. PION ANGLE (DEGREES)

FIGURE 11.1

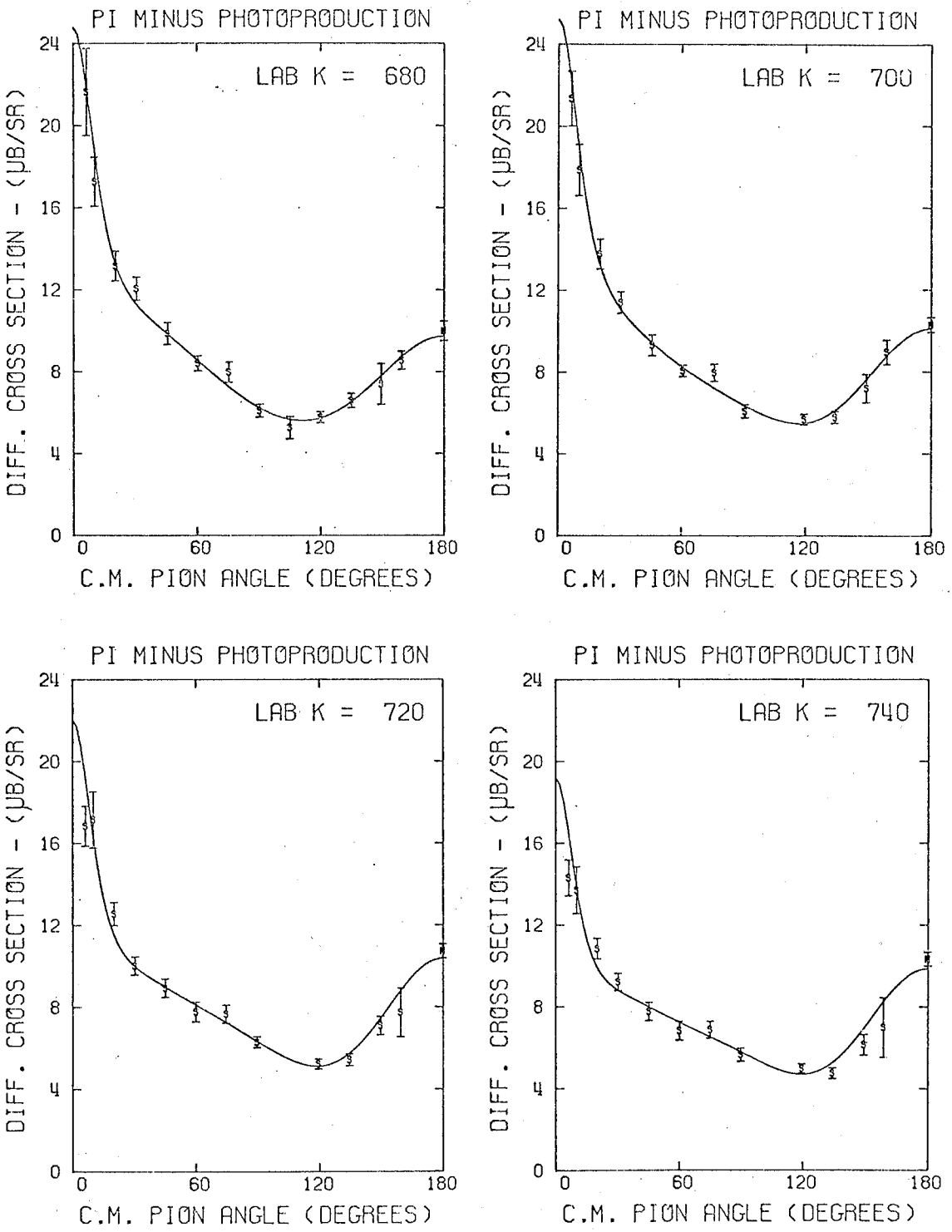
PI MINUS PHOTOPRODUCTION
LAB K = 680
DIFF. CROSS SECTION - (μB/SR)
C.M. PION ANGLE (DEGREES)
PI MINUS PHOTOPRODUCTION
LAB K = 700
DIFF. CROSS SECTION - (μB/SR)
C.M. PION ANGLE (DEGREES)
PI MINUS PHOTOPRODUCTION
LAB K = 720
DIFF. CROSS SECTION - (μB/SR)
C.M. PION ANGLE (DEGREES)
PI MINUS PHOTOPRODUCTION
LAB K = 740
DIFF. CROSS SECTION - (μB/SR)
C.M. PION ANGLE (DEGREES)

FIGURE 11.2

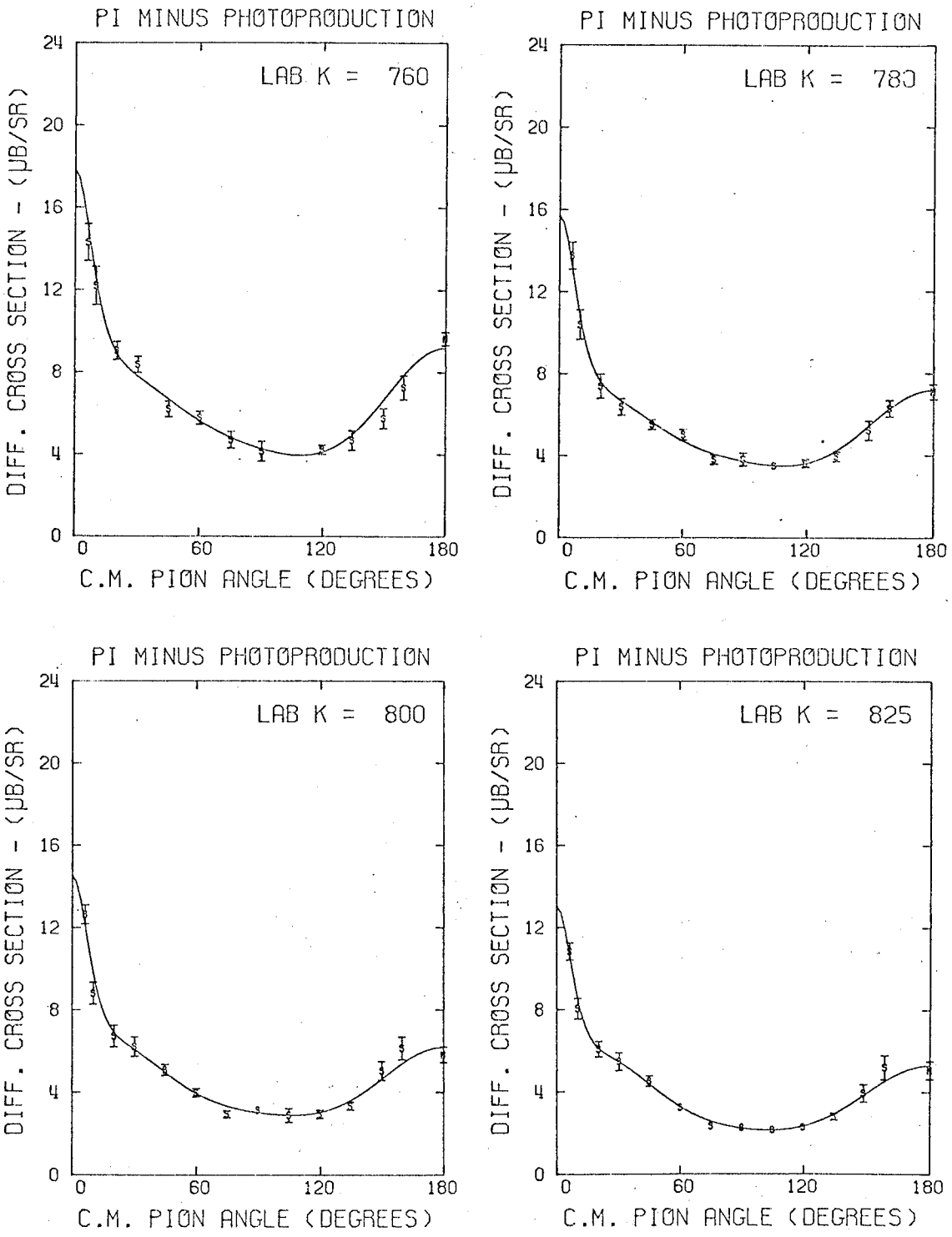
PI MINUS PHOTOPRODUCTION
LAB K = 760
DIFF. CROSS SECTION - (μB/SR)
C.M. PION ANGLE (DEGREES)
PI MINUS PHOTOPRODUCTION
LAB K = 780
DIFF. CROSS SECTION - (μB/SR)
C.M. PION ANGLE (DEGREES)
PI MINUS PHOTOPRODUCTION
LAB K = 800
DIFF. CROSS SECTION - (μB/SR)
C.M. PION ANGLE (DEGREES)
PI MINUS PHOTOPRODUCTION
LAB K = 825
DIFF. CROSS SECTION - (μB/SR)
C.M. PION ANGLE (DEGREES)

FIGURE 11.3

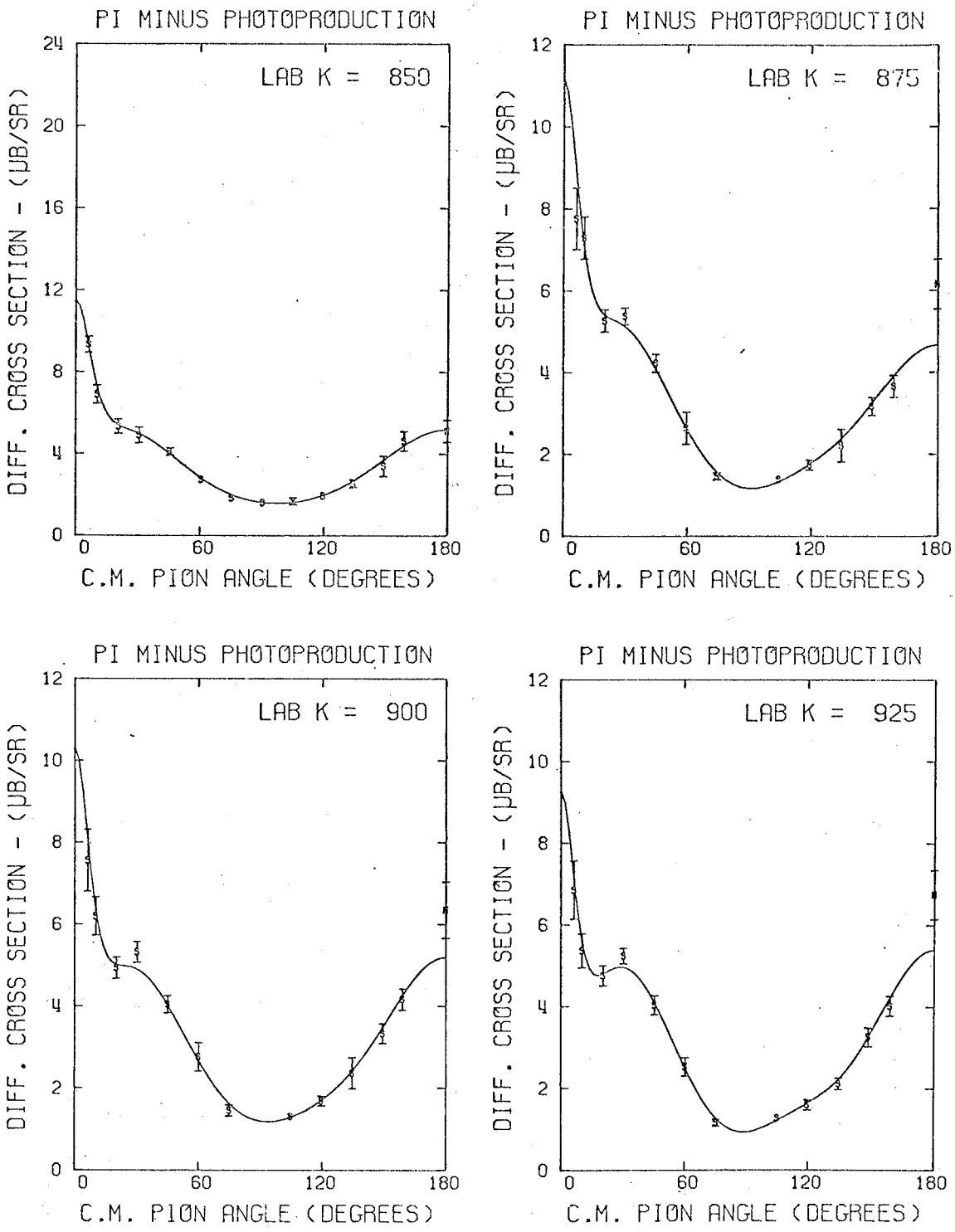
PI MINUS PHOTOPRODUCTION
LAB K = 850
DIFF. CROSS SECTION - (μB/SR)
C.M. PION ANGLE (DEGREES)
PI MINUS PHOTOPRODUCTION
LAB K = 875
DIFF. CROSS SECTION - (μB/SR)
C.M. PION ANGLE (DEGREES)
PI MINUS PHOTOPRODUCTION
LAB K = 900
DIFF. CROSS SECTION - (μB/SR)
C.M. PION ANGLE (DEGREES)
PI MINUS PHOTOPRODUCTION
LAB K = 925
DIFF. CROSS SECTION - (μB/SR)
C.M. PION ANGLE (DEGREES)

FIGURE 11.4

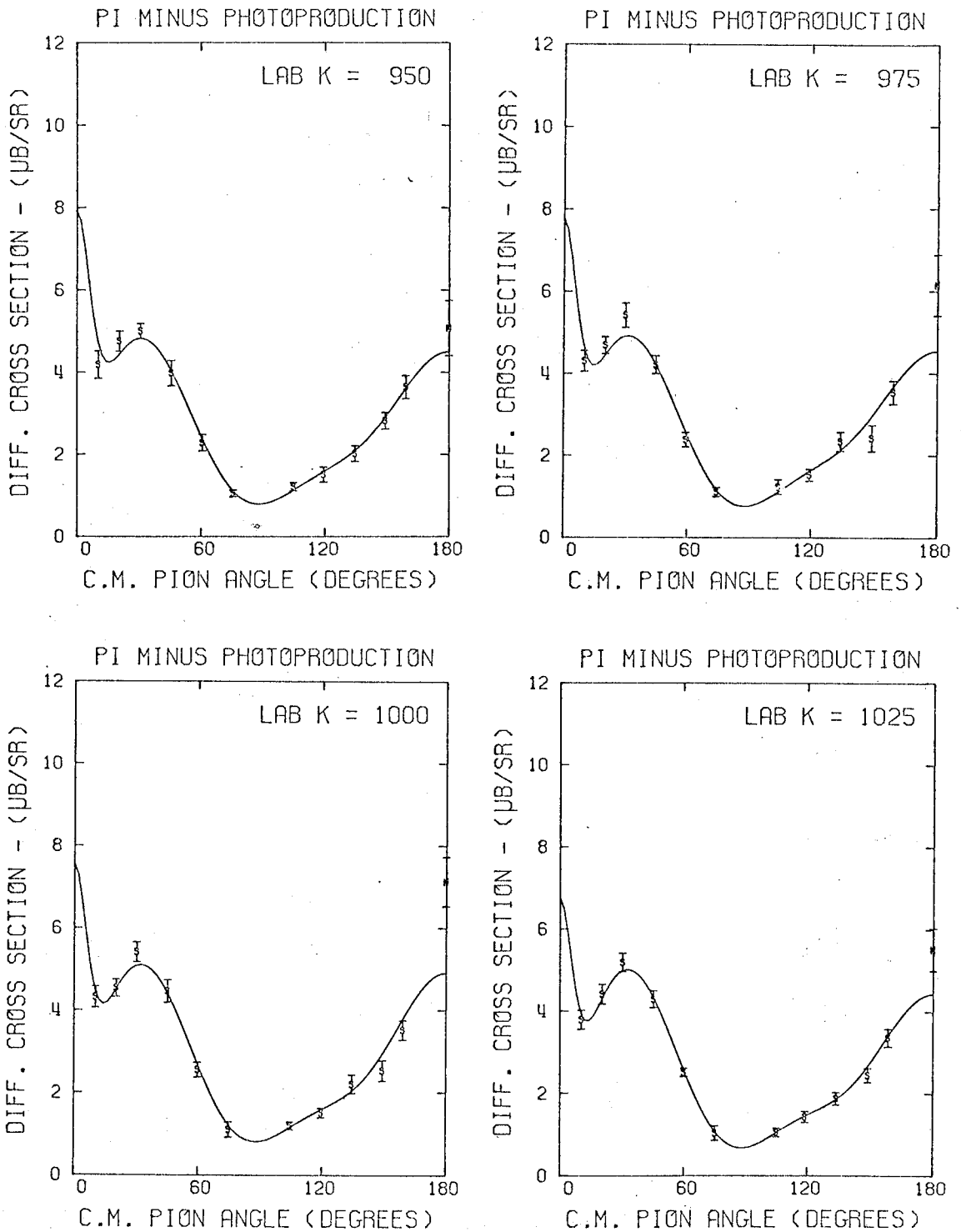
PI MINUS PHOTOPRODUCTION
LAB K = 950
DIFF. CROSS SECTION - (μB/SR)
C.M. PION ANGLE (DEGREES)
PI MINUS PHOTOPRODUCTION
LAB K = 975
DIFF. CROSS SECTION - (μB/SR)
C.M. PION ANGLE (DEGREES)
PI MINUS PHOTOPRODUCTION
LAB K = 1000
DIFF. CROSS SECTION - (μB/SR)
C.M. PION ANGLE (DEGREES)
PI MINUS PHOTOPRODUCTION
LAB K = 1025
DIFF. CROSS SECTION - (μB/SR)
C.M. PION ANGLE (DEGREES)

FIGURE 11.5

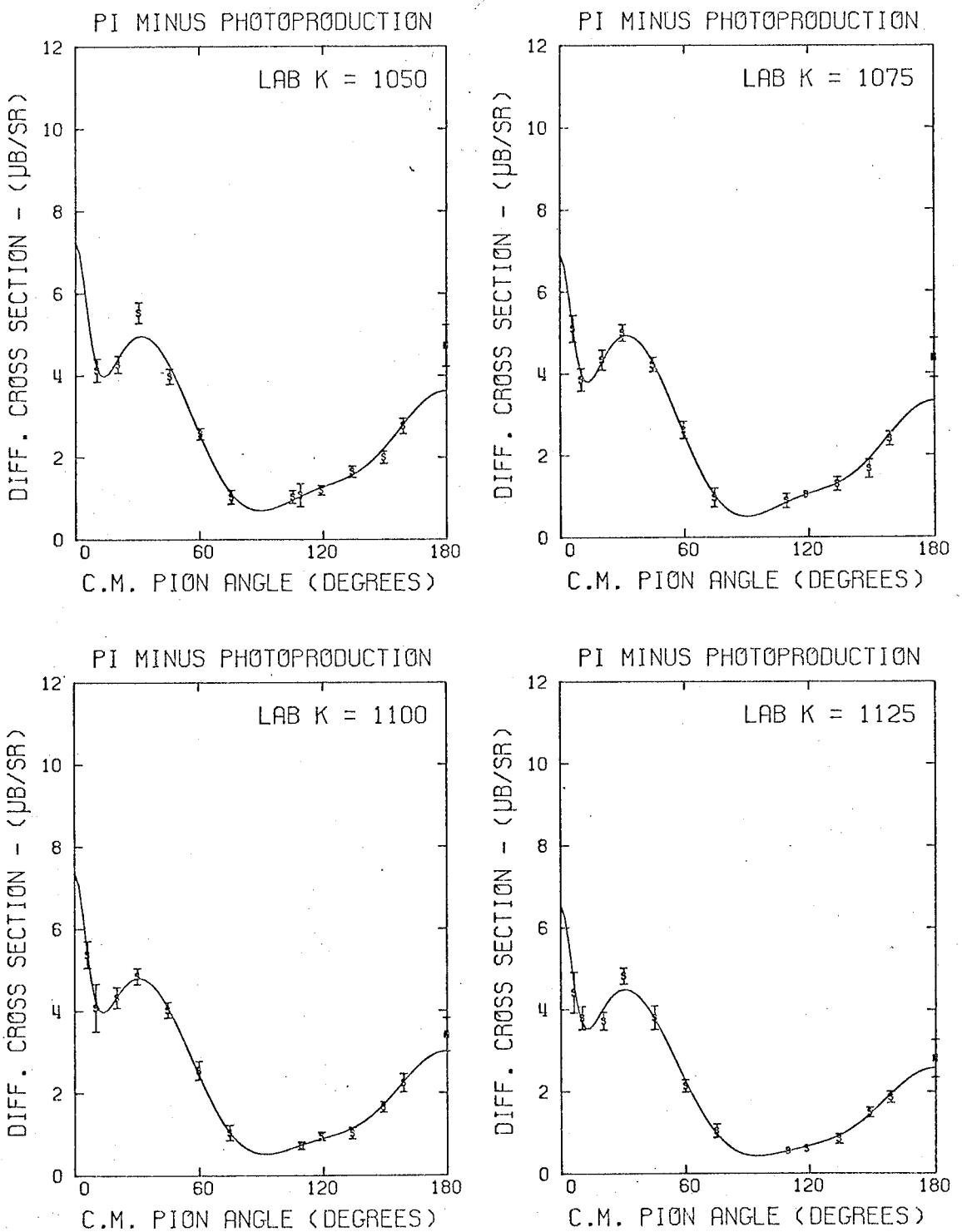
PI MINUS PHOTOPRODUCTION
LAB K = 1050
DIFF. CROSS SECTION - (μB/SR)
C.M. PION ANGLE (DEGREES)
PI MINUS PHOTOPRODUCTION
LAB K = 1075
DIFF. CROSS SECTION - (μB/SR)
C.M. PION ANGLE (DEGREES)
PI MINUS PHOTOPRODUCTION
LAB K = 1100
DIFF. CROSS SECTION - (μB/SR)
C.M. PION ANGLE (DEGREES)
PI MINUS PHOTOPRODUCTION
LAB K = 1125
DIFF. CROSS SECTION - (μB/SR)
C.M. PION ANGLE (DEGREES)

FIGURE 11.6

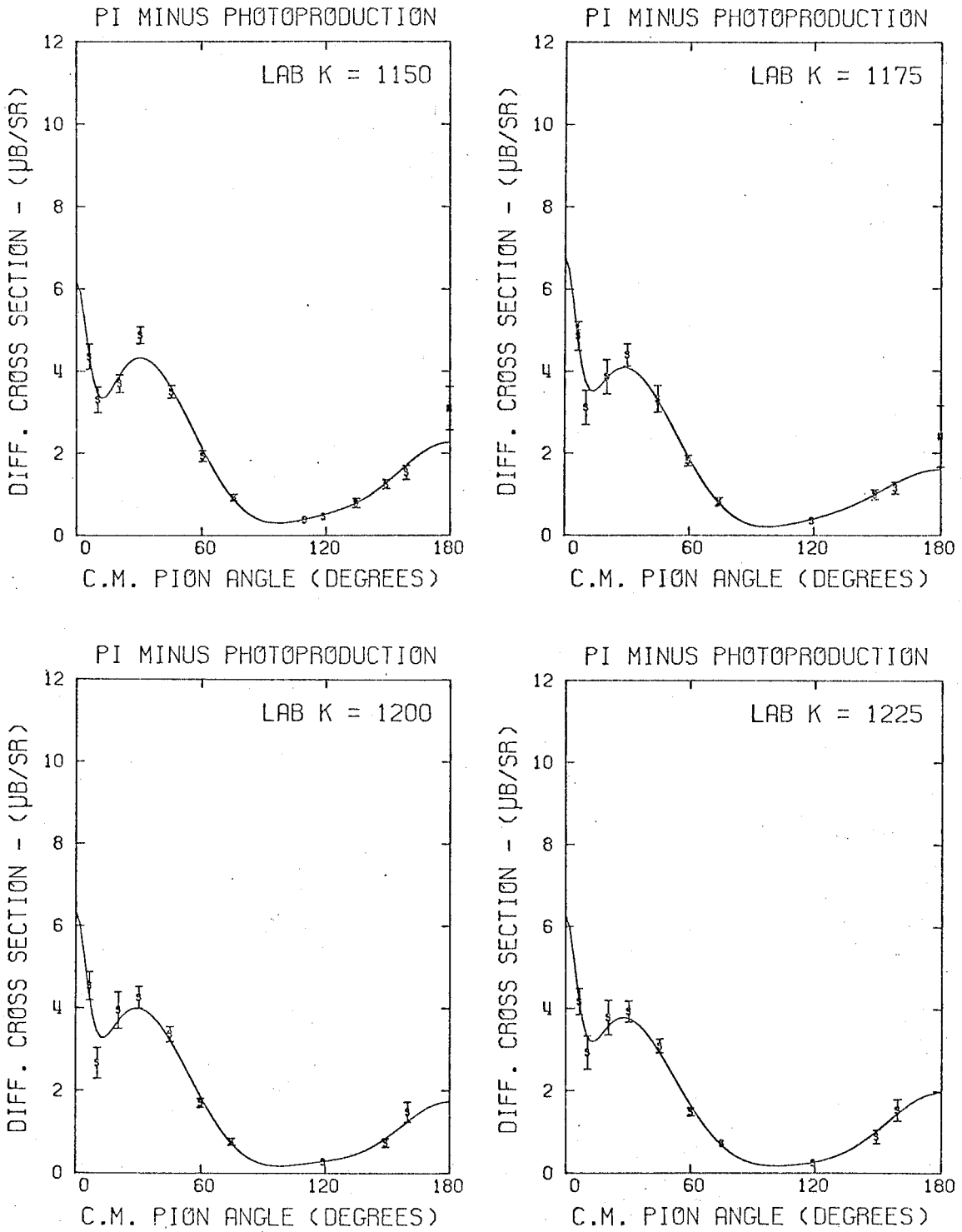
PI MINUS PHOTOPRODUCTION
LAB K = 1150
DIFF. CROSS SECTION - (μB/SR)
C.M. PION ANGLE (DEGREES)
PI MINUS PHOTOPRODUCTION
LAB K = 1175
DIFF. CROSS SECTION - (μB/SR)
C.M. PION ANGLE (DEGREES)
PI MINUS PHOTOPRODUCTION
LAB K = 1200
DIFF. CROSS SECTION - (μB/SR)
C.M. PION ANGLE (DEGREES)
PI MINUS PHOTOPRODUCTION
LAB K = 1225
DIFF. CROSS SECTION - (μB/SR)
C.M. PION ANGLE (DEGREES)

FIGURE 11.7

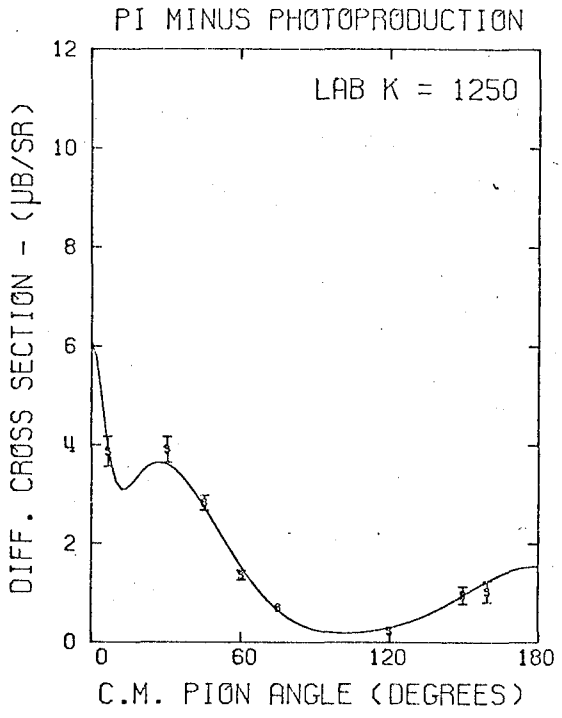
PI MINUS PHOTOPRODUCTION
LAB K = 1250
DIFF. CROSS SECTION - (μB/SR)
0
2
4
6
8
10
12
0
60
120
180
C.M. PION ANGLE (DEGREES)

FIGURE 11.8

FIGURE 12

ENERGY DISTRIBUTIONS OF FINAL π^- CROSS SECTIONS

(at rough angular settings)

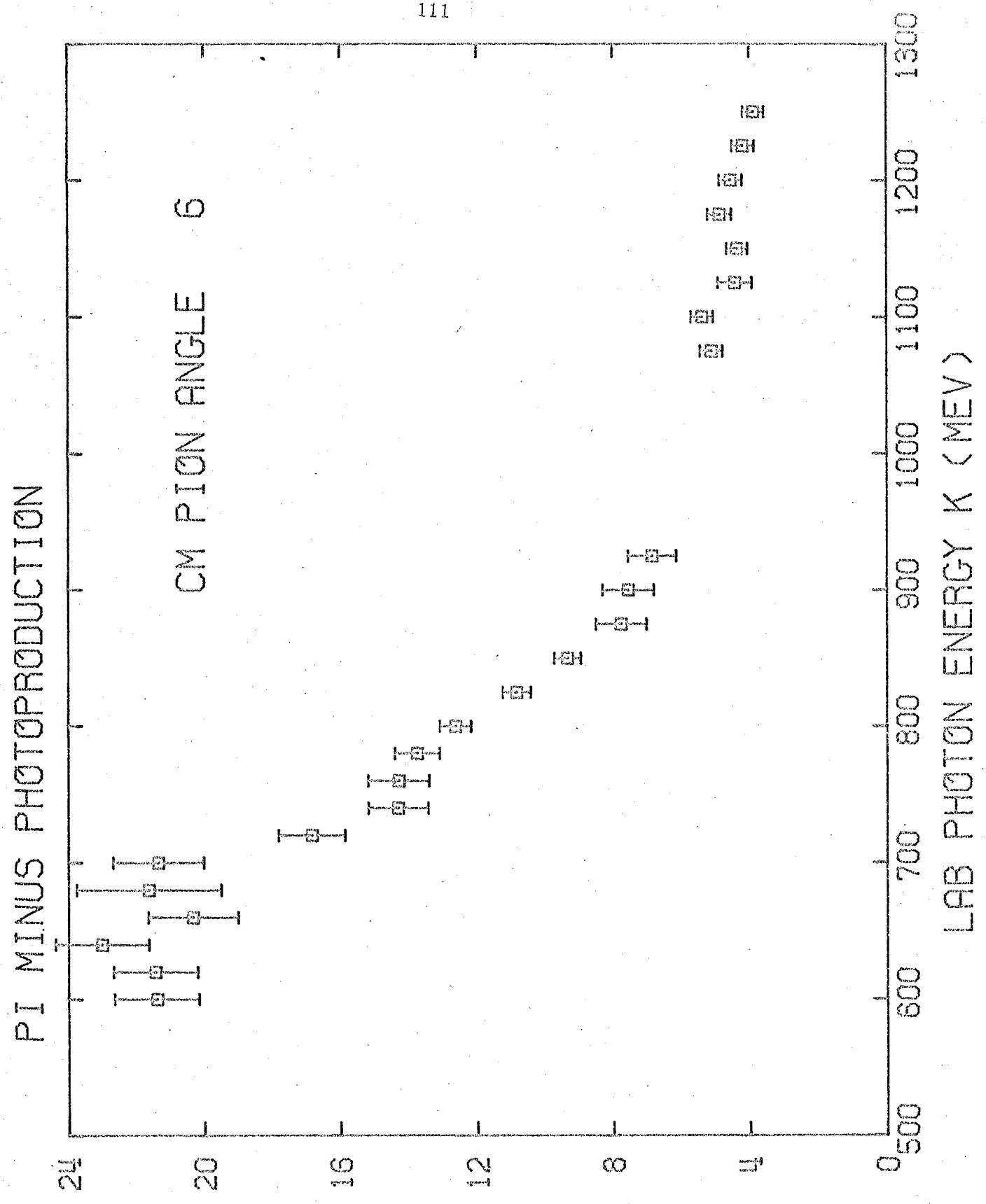
PI MINUS PHOTOPRODUCTION
CM PION ANGLE 6
DIFF. CROSS SECTION (UB/SR)
LAB PHOTON ENERGY K (MEV)
24
20
16
12
8
4
0
500
600
700
800
900
1000
1100
1200
1300

FIGURE 12.1

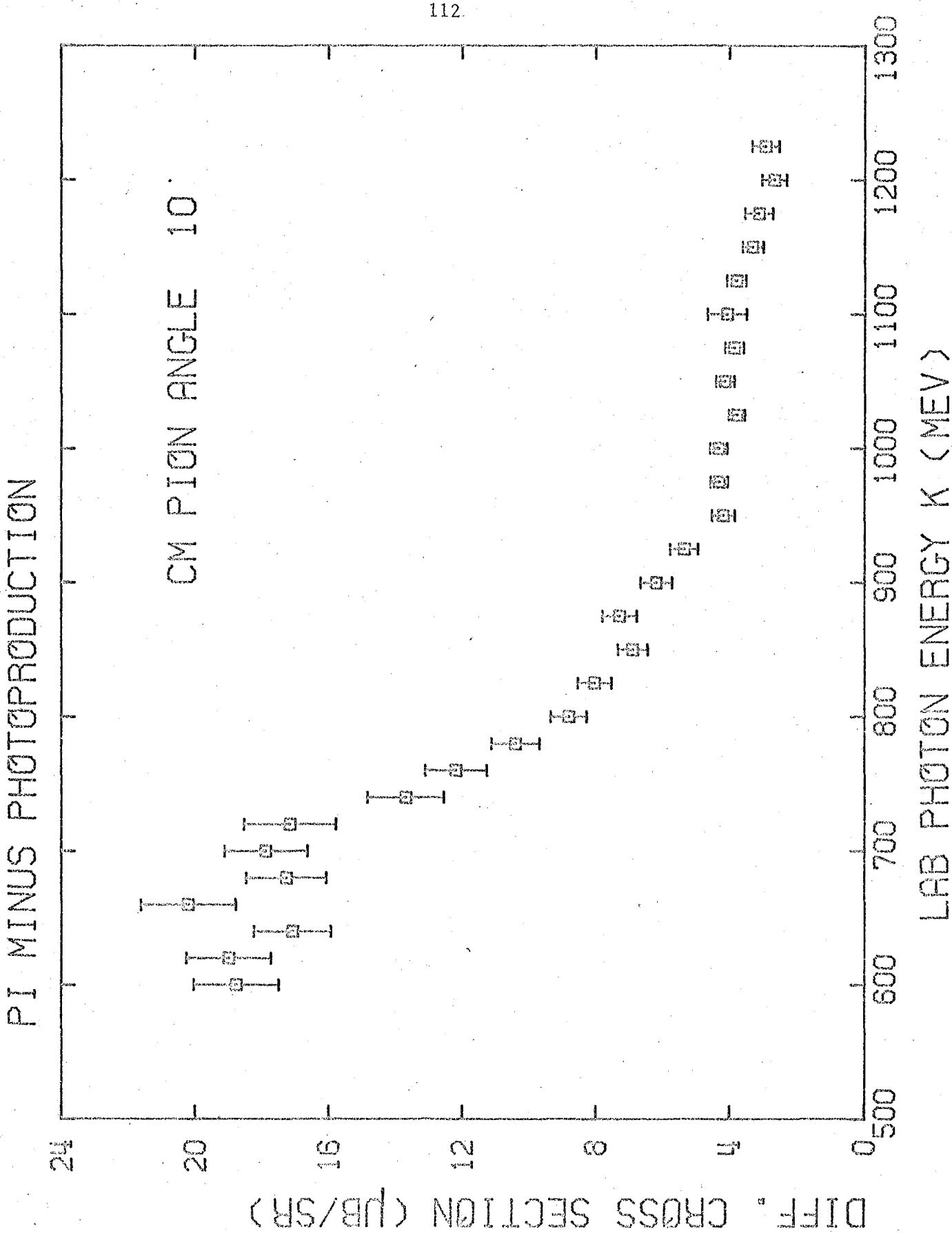
PI MINUS PHOTOPRODUCTION
CM PION ANGLE 10°
DIFF. CROSS SECTION (μB/SR)
LAB PHOTON ENERGY K (MEV)
24
20
16
12
8
4
0
500
600
700
800
900
1000
1100
1200
1300

FIGURE 12.2

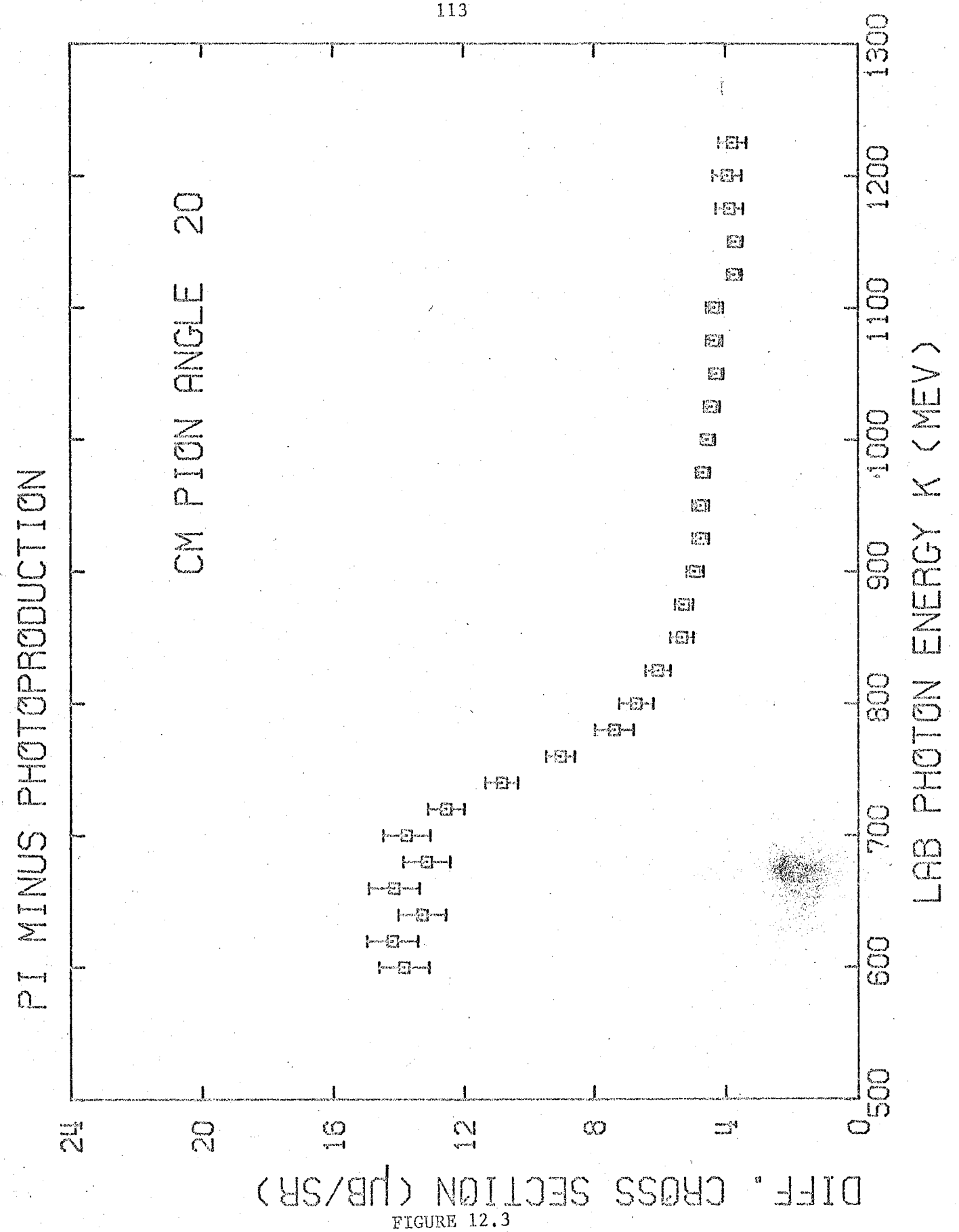
PI MINUS PHOTOPRODUCTION
CM PION ANGLE 20
DIFF. CROSS SECTION (UB/SR)
LAB PHOTON ENERGY K (MEV)
24
20
16
12
8
4
0
500
600
700
800
900
1000
1100
1200
1300

FIGURE 12.3

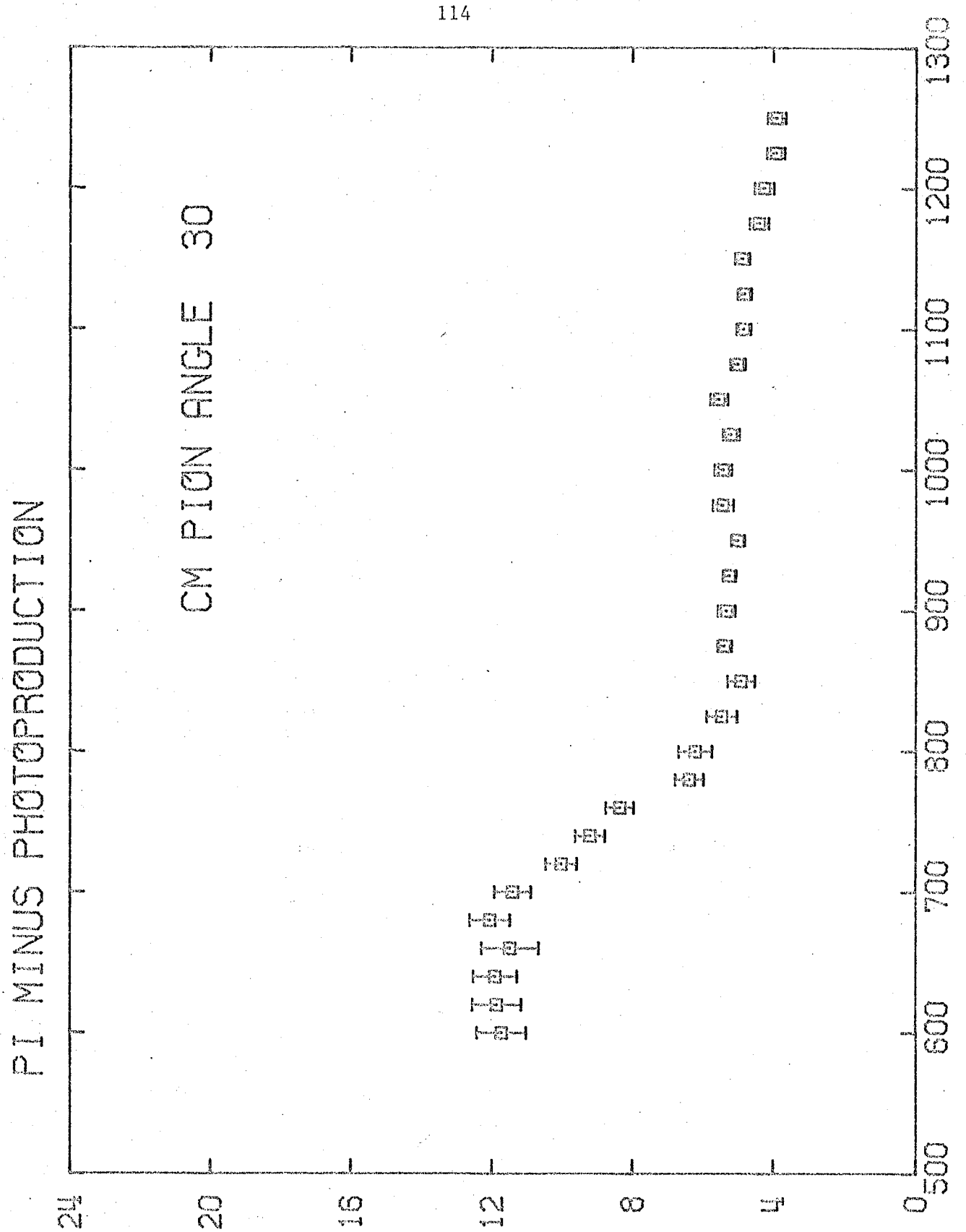
PI MINUS PHOTOPRODUCTION
CM PION ANGLE 30
DIFF. CROSS SECTION (UB/SR)
LAB PHOTON ENERGY K (MEV)
24
20
16
12
8
4
0
500
600
700
800
900
1000
1100
1200
1300

FIGURE 12.4

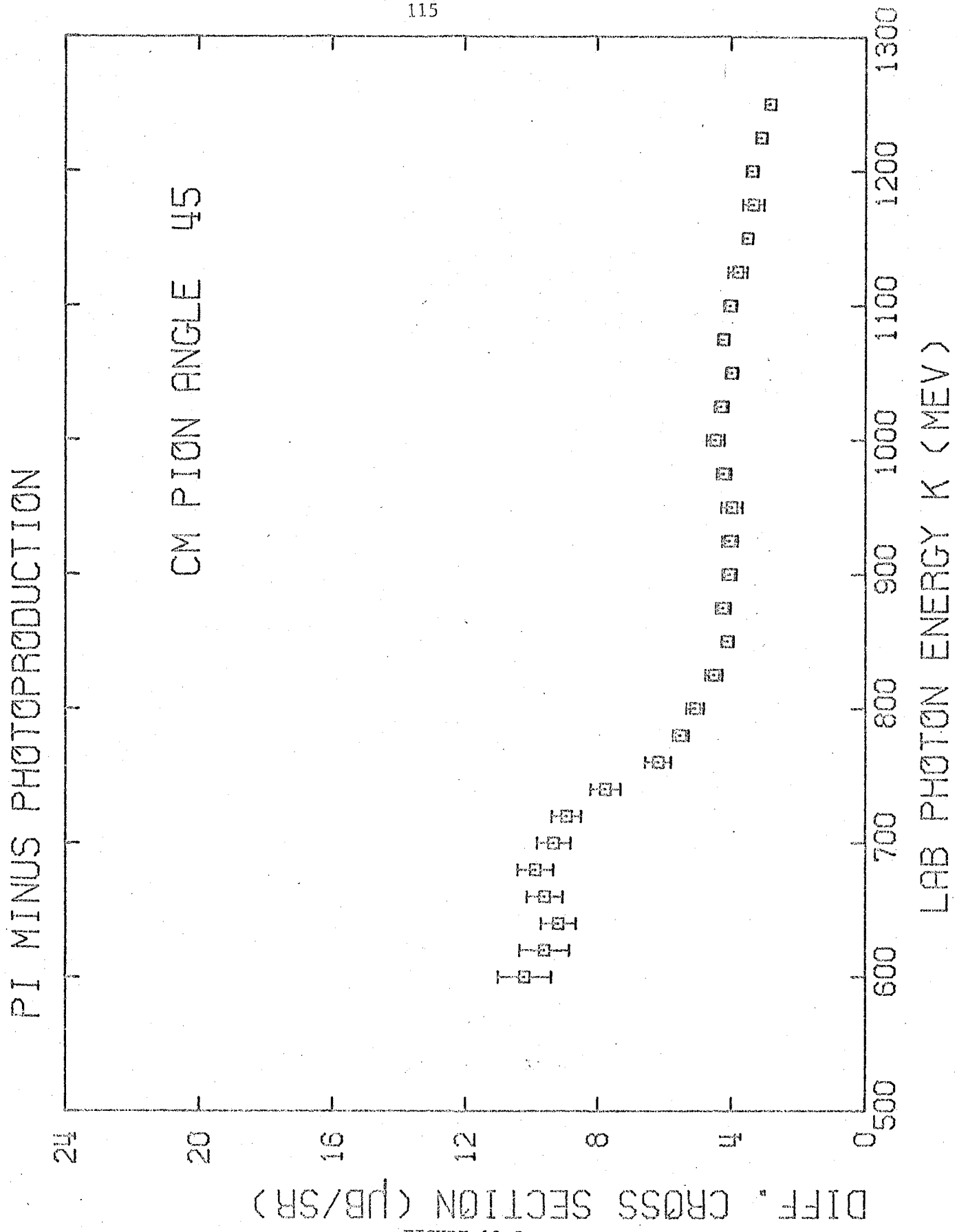
PI MINUS PHOTOPRODUCTION
CM PION ANGLE 45
DIFF. CROSS SECTION (UB/SR)
LAB PHOTON ENERGY K (MEV)
0
4
8
12
16
20
24
500
600
700
800
900
1000
1100
1200
1300

FIGURE 12.5

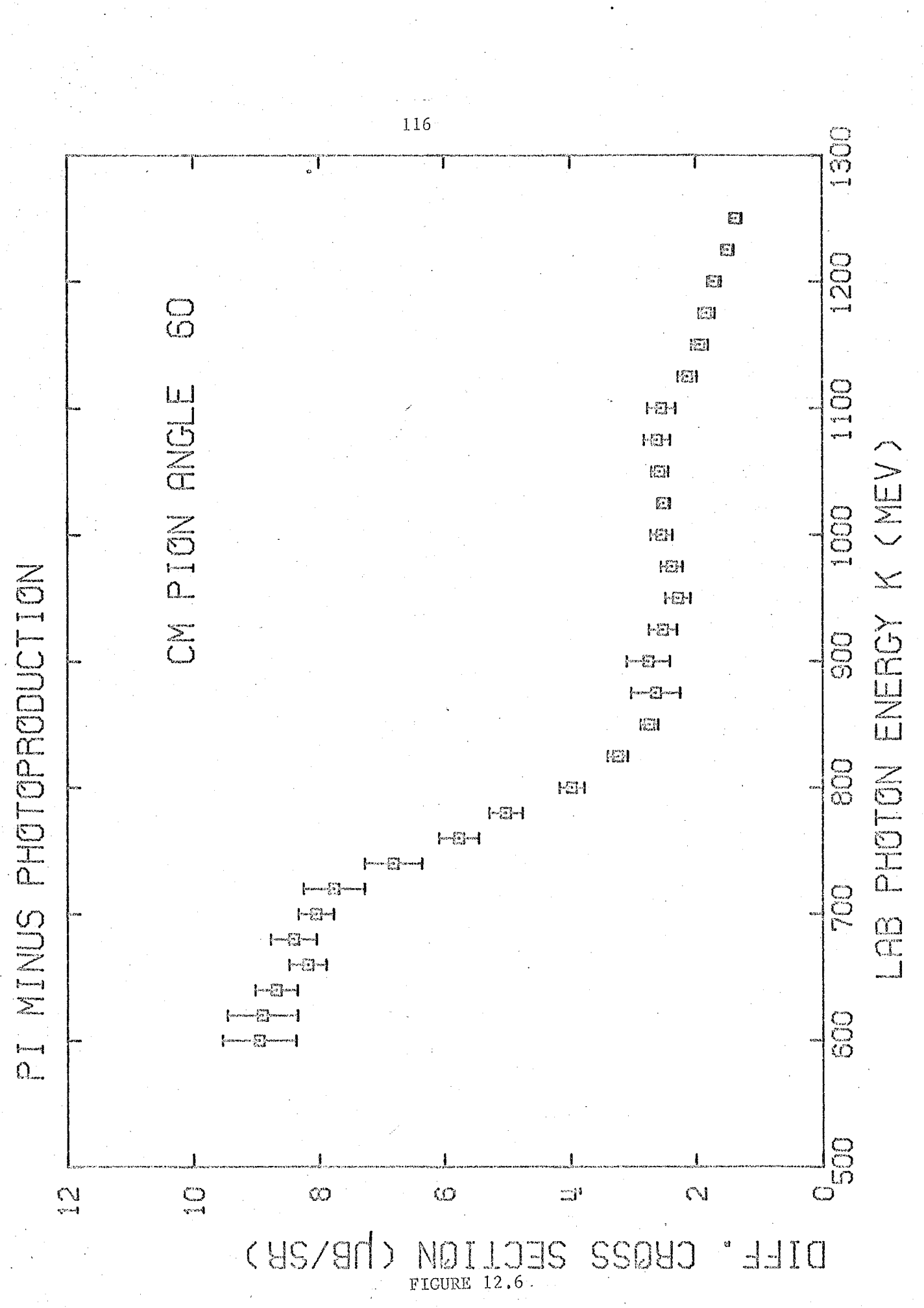
PI MINUS PHOTOPRODUCTION
CM PION ANGLE 60
DIFF. CROSS SECTION (UB/SR)
LAB PHOTON ENERGY K (MEV)
0
2
4
6
8
10
12
500
600
700
800
900
1000
1100
1200
1300

FIGURE 12.6

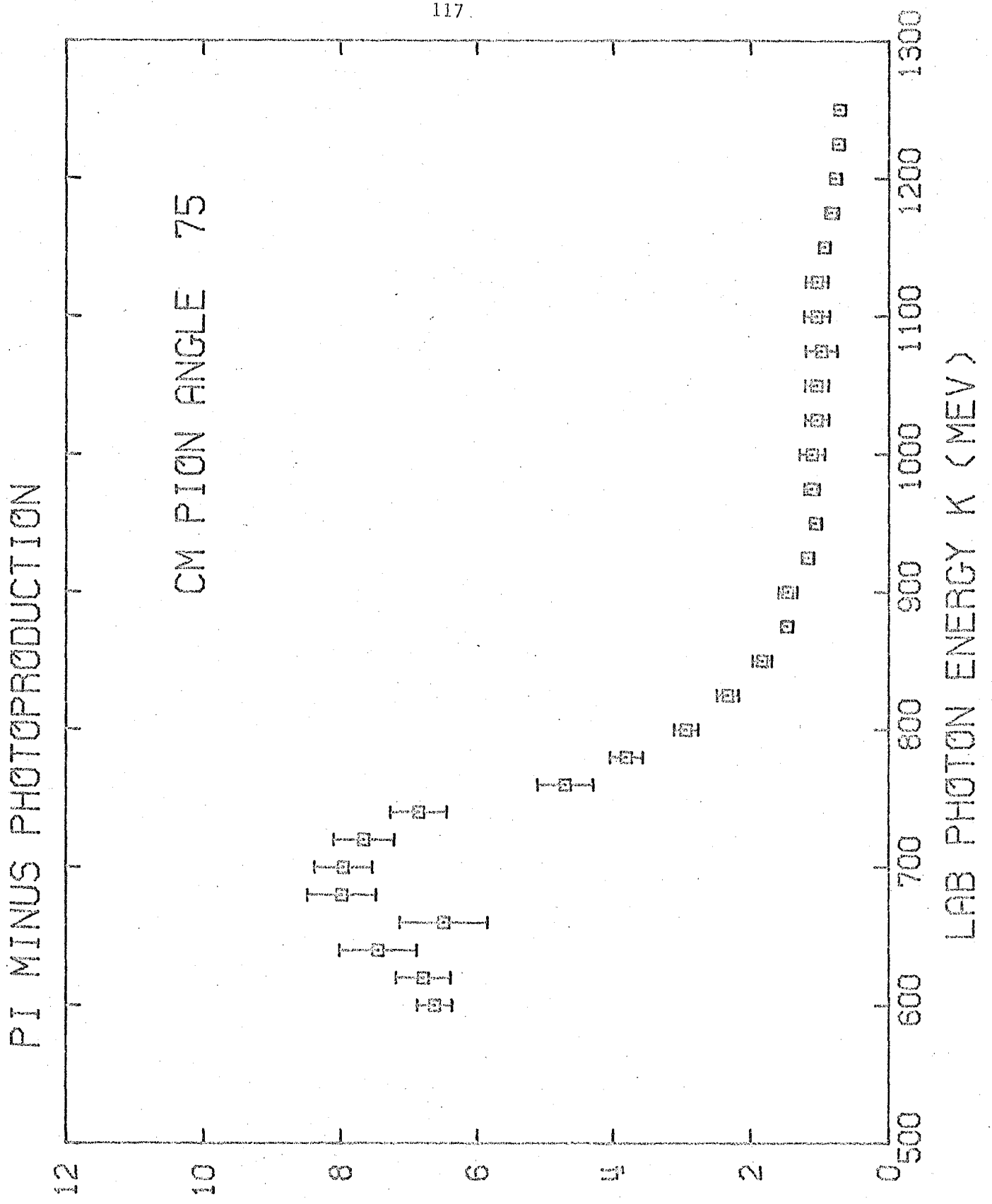
PI MINUS PHOTOPRODUCTION
CM PION ANGLE 75
DIFF. CROSS SECTION (UB/SR)
LAB PHOTON ENERGY K (MEV)
0
2
4
6
8
10
12
500
600
700
800
900
1000
1100
1200
1300

FIGURE 12.7

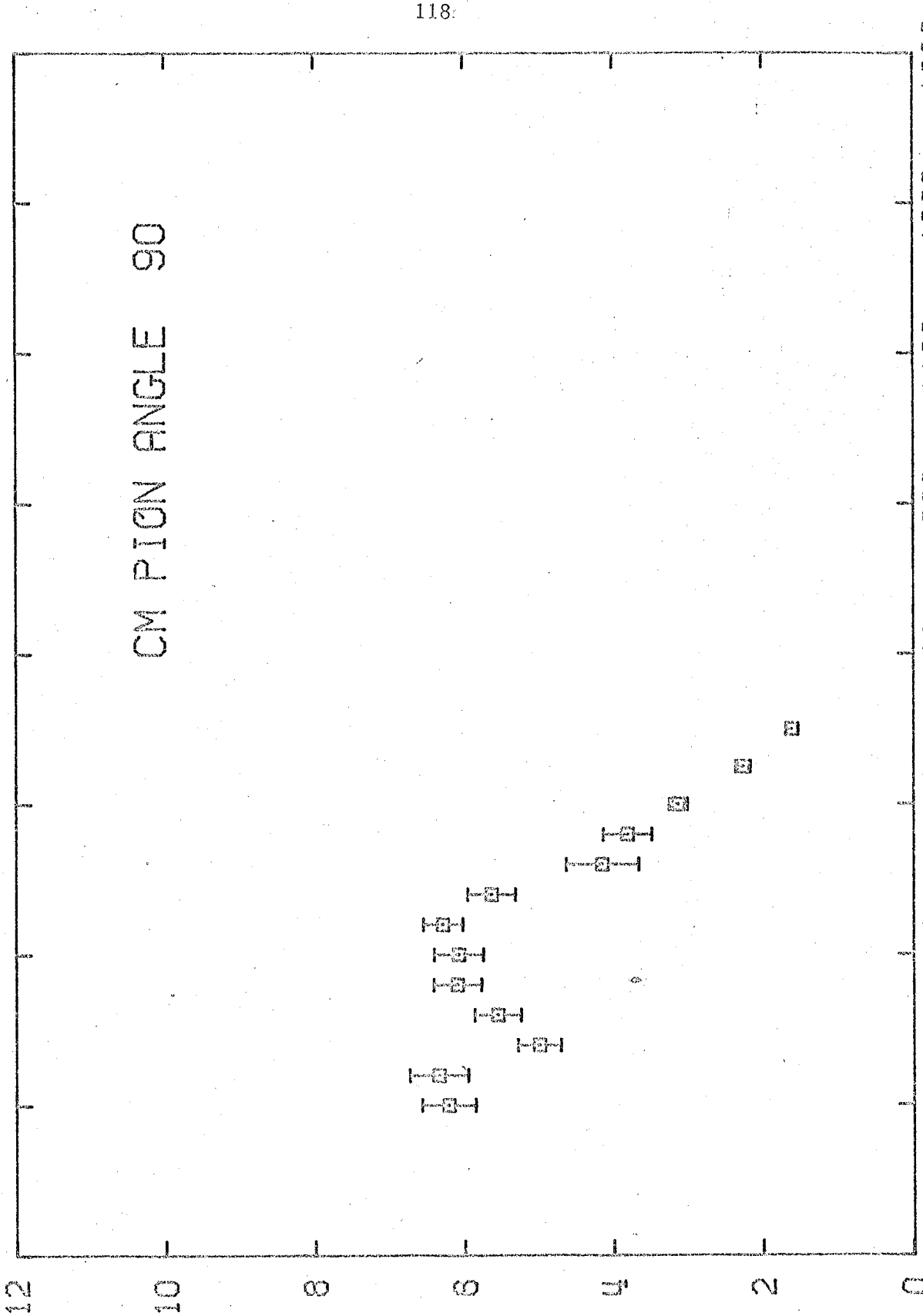
PI MINUS PHOTOPRODUCTION
CM PION ANGLE 90
DIFF. CROSS SECTION (UB/SR)
LAB PHOTON ENERGY K (MEV)
0
2
4
6
8
10
12
500
600
700
800
900
1000
1100
1200
1300

FIGURE 12.8

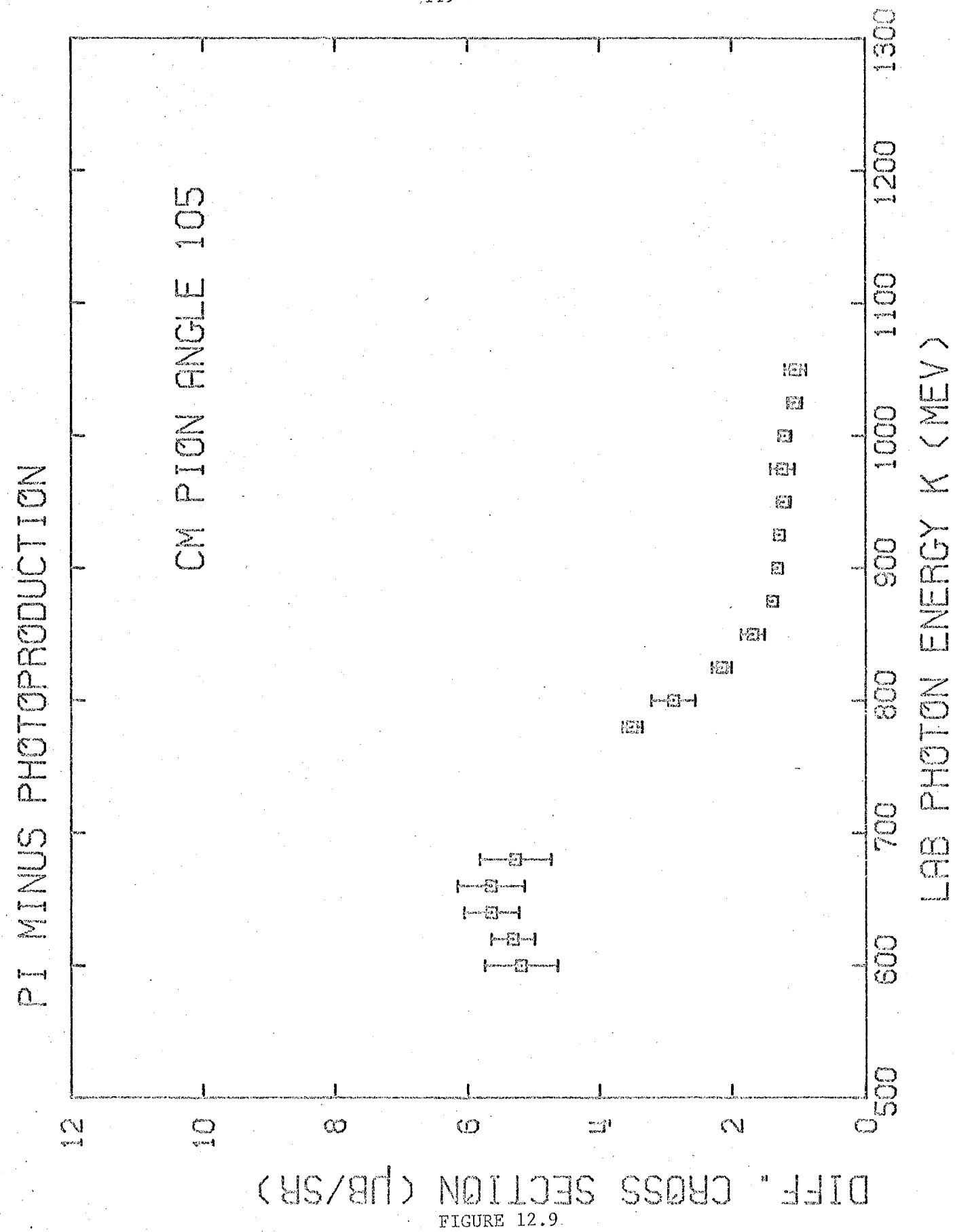
PI MINUS PHOTOPRODUCTION
CM PION ANGLE 105
DIFF. CROSS SECTION (UB/SR)
LAB PHOTON ENERGY K (MEV)
0
2
4
6
8
10
12
500
600
700
800
900
1000
1100
1200
1300

FIGURE 12.9

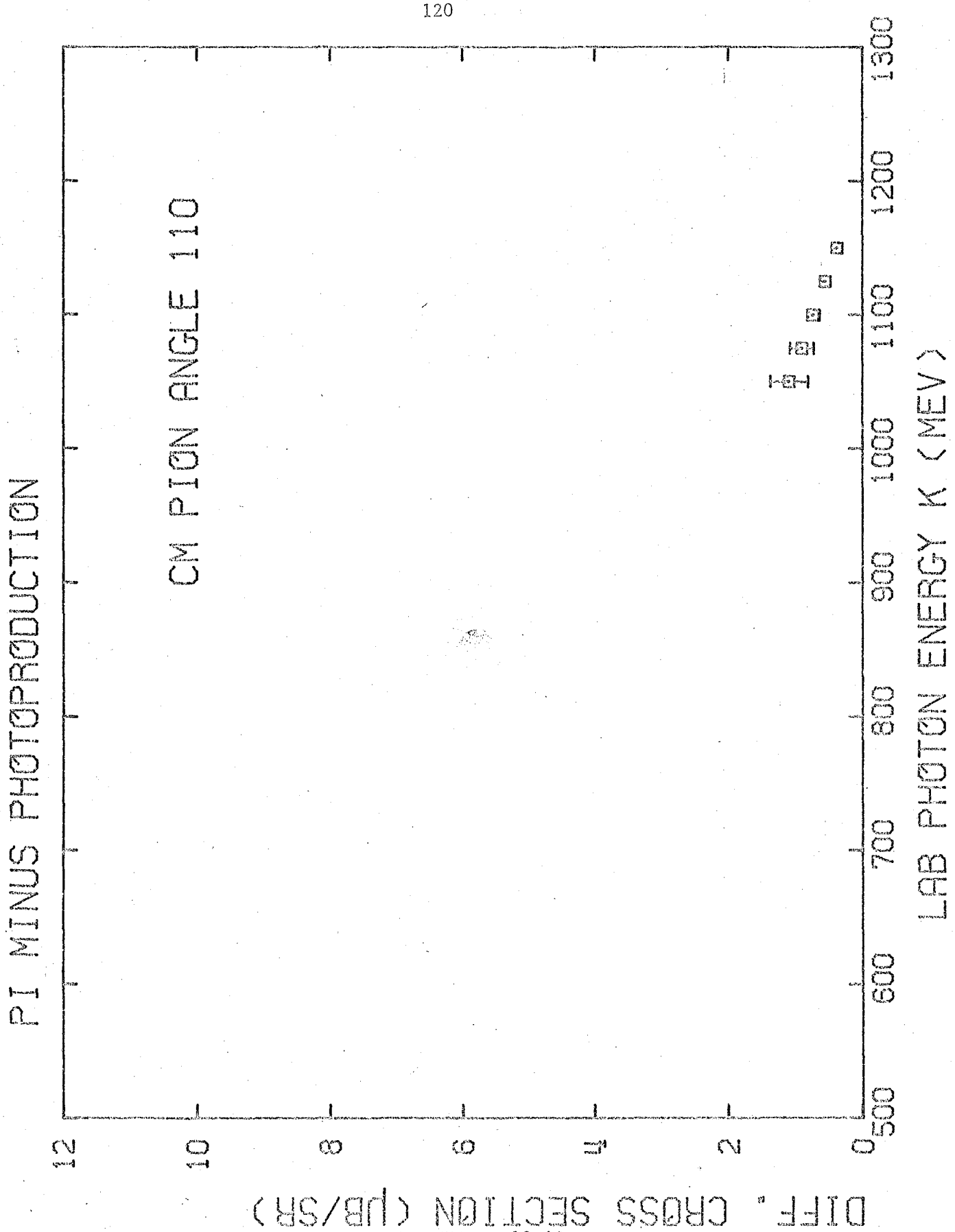
PI MINUS PHOTOPRODUCTION
CM PION ANGLE 110
DIFF. CROSS SECTION (UB/SR)
LAB PHOTON ENERGY K (MEV)
0
2
4
6
8
10
12
500
600
700
800
900
1000
1100
1200
1300

FIGURE 12.10

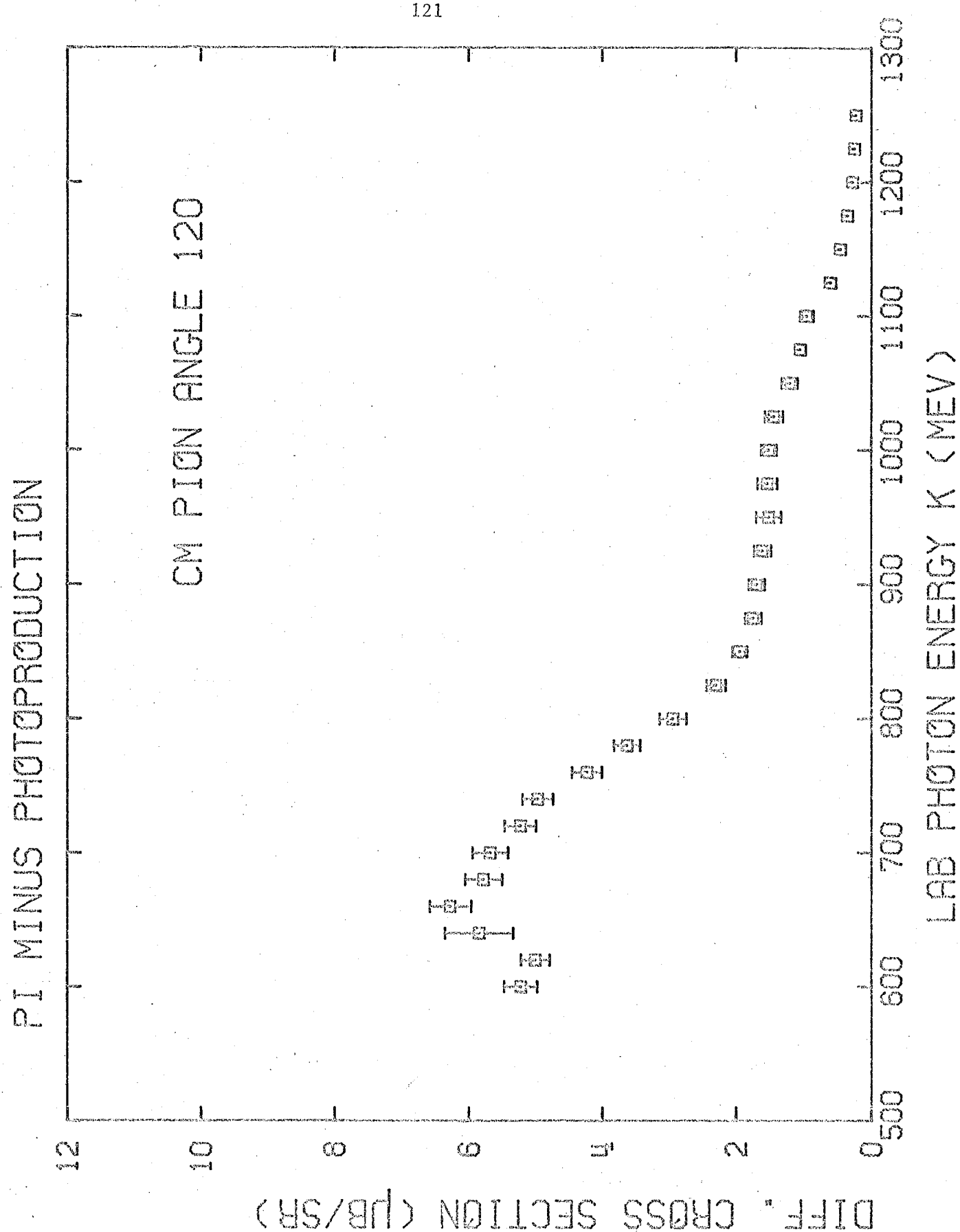
PI MINUS PHOTOPRODUCTION
CM PION ANGLE 120
DIFF. CROSS SECTION (UB/SR)
LAB PHOTON ENERGY K (MEV)
0
2
4
6
8
10
12
500
600
700
800
900
1000
1100
1200
1300

FIGURE 12.11

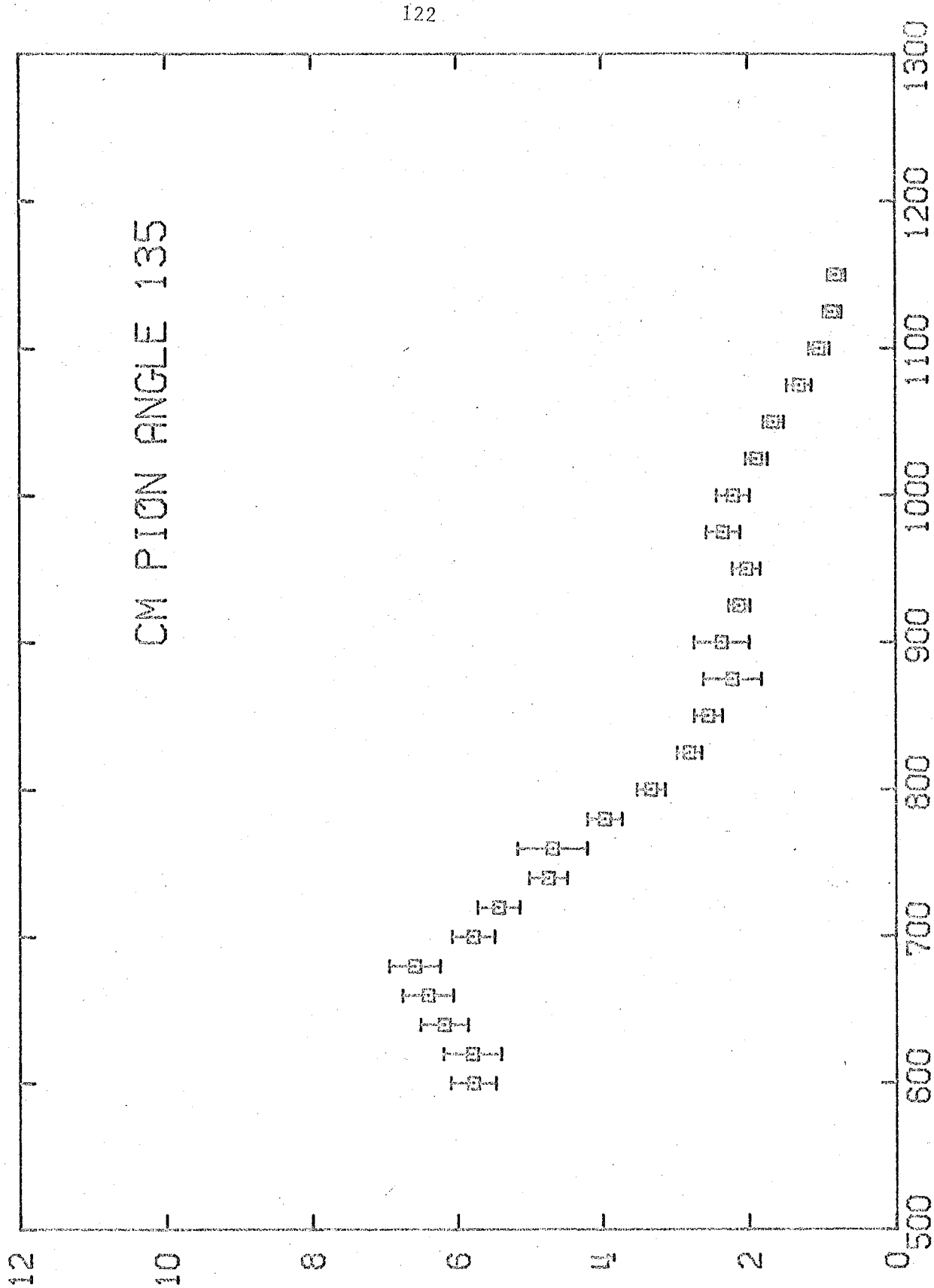
PI MINUS PHOTOPRODUCTION
CM PION ANGLE 135
DIFF. CROSS SECTION (UB/SR)
LAB PHOTON ENERGY K (MEV)
0
2
4
6
8
10
12
500
600
700
800
900
1000
1100
1200
1300

FIGURE 12.12

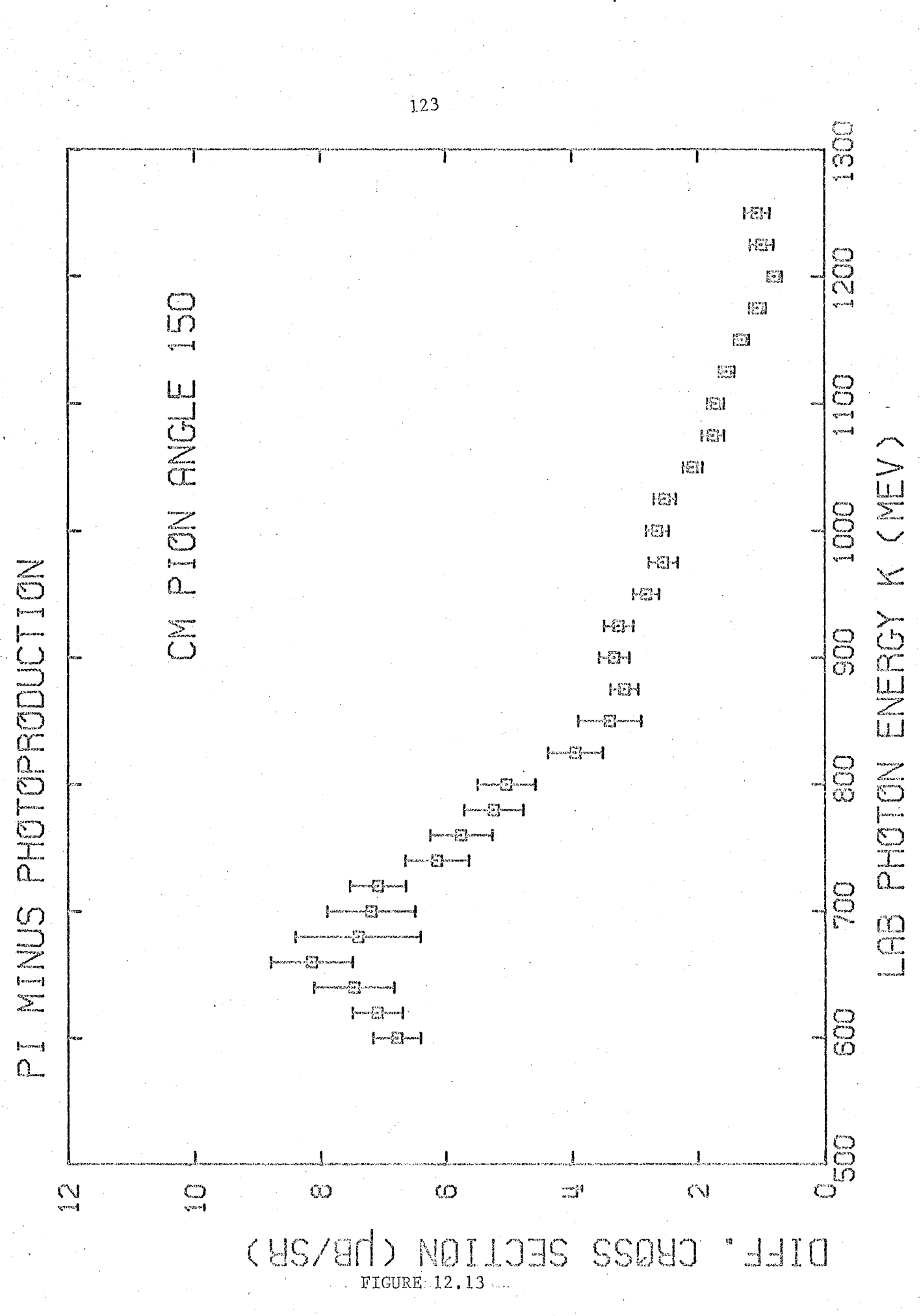
PI MINUS PHOTOPRODUCTION
CM PION ANGLE 150
DIFF. CROSS SECTION (UB/SR)
LAB PHOTON ENERGY K (MEV)
0
2
4
6
8
10
12
500
600
700
800
900
1000
1100
1200
1300

FIGURE 12.13

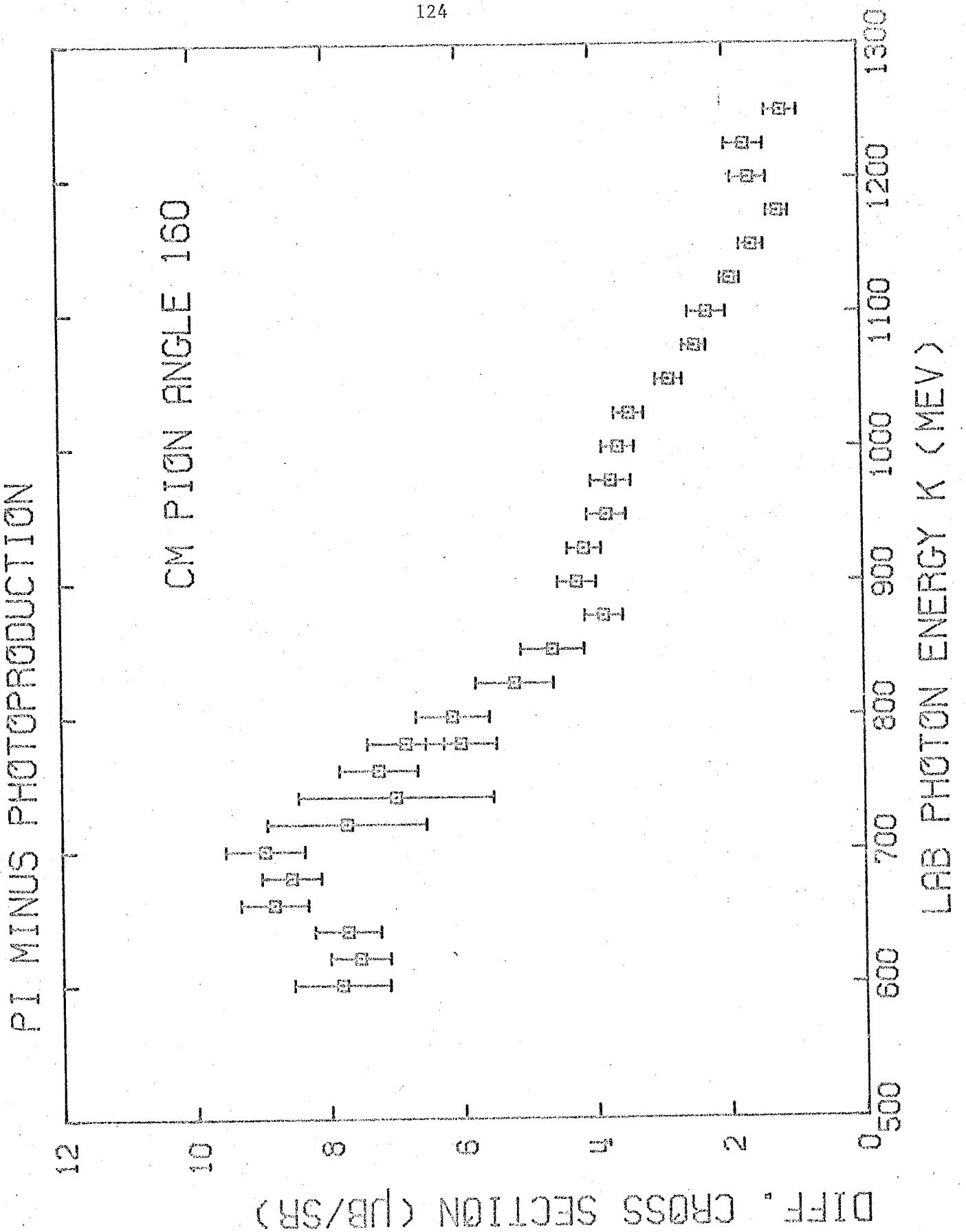
PI MINUS PHOTOPRODUCTION
CM PION ANGLE 160
DIFF. CROSS SECTION (UB/SR)
LAB PHOTON ENERGY K (MEV)
0
2
4
6
8
10
12
500
600
700
800
900
1000
1100
1200
1300

FIGURE 12.14

TABLE 6

1) Total π^- Cross Section

2) 0° π^- Cross Section

3) 180° π^- Cross Section

from Moravcsik fits of final π^- angular distributions.

See Ph.D. Thesis by Patrick Walden.

k_γ^{lab} (MeV)	σ_{tot}	$\Delta\sigma_{tot}$	$\sigma(0^o)$	$\Delta\sigma(0^o)$	$\sigma(180^o)$	$\Delta\sigma(180^o)$
600.0	93.63	1.63	23.49	1.00	7.62	0.37
620.0	94.48	1.77	23.74	1.02	7.72	0.34
640.0	93.28	1.65	23.49	1.02	8.30	0.38
660.0	96.15	1.64	24.33	1.09	9.15	0.40
680.0	97.98	1.64	22.67	1.23	8.67	0.39
700.0	96.64	1.60	23.91	1.25	9.98	0.75
720.0	91.15	1.58	20.22	1.04	9.43	0.86
740.0	81.65	1.63	16.87	0.94	7.98	0.95
760.0	68.72	1.68	16.63	0.92	7.91	0.67
780.0	58.43	1.01	16.04	0.69	6.96	0.51
800.0	49.96	0.93	14.30	0.52	6.84	0.59
825.0	41.46	0.83	13.12	0.51	6.55	0.78
850.0	35.31	0.74	11.61	0.48	5.65	0.67
875.0	32.05	0.65	10.50	0.72	4.72	0.44
900.0	31.73	0.74	9.66	0.72	5.21	0.46
925.0	30.15	0.60	8.71	0.66	5.39	0.39
950.0	28.18	0.68	6.60	0.76	4.71	0.46
975.0	28.56	0.76	6.56	0.63	4.35	0.48
1000.0	28.84	0.72	7.03	0.65	4.56	0.41
1025.0	27.49	0.64	6.26	0.61	4.29	0.37
1050.0	26.16	0.70	6.85	0.71	3.53	0.34
1075.0	24.06	0.91	6.82	0.41	3.20	0.34
1100.0	23.03	0.76	7.32	0.45	3.01	0.40
1125.0	20.88	0.57	6.21	0.46	1.89	0.13
1150.0	18.71	0.42	5.82	0.37	1.53	0.13
1175.0	16.11	0.56	6.50	0.44	1.30	0.15
1200.0	15.17	0.44	6.00	0.43	1.11	0.16
1225.0	14.41	0.44	6.13	0.42	1.49	0.23
1250.0	13.54	0.49	6.01	0.44	1.26	0.22

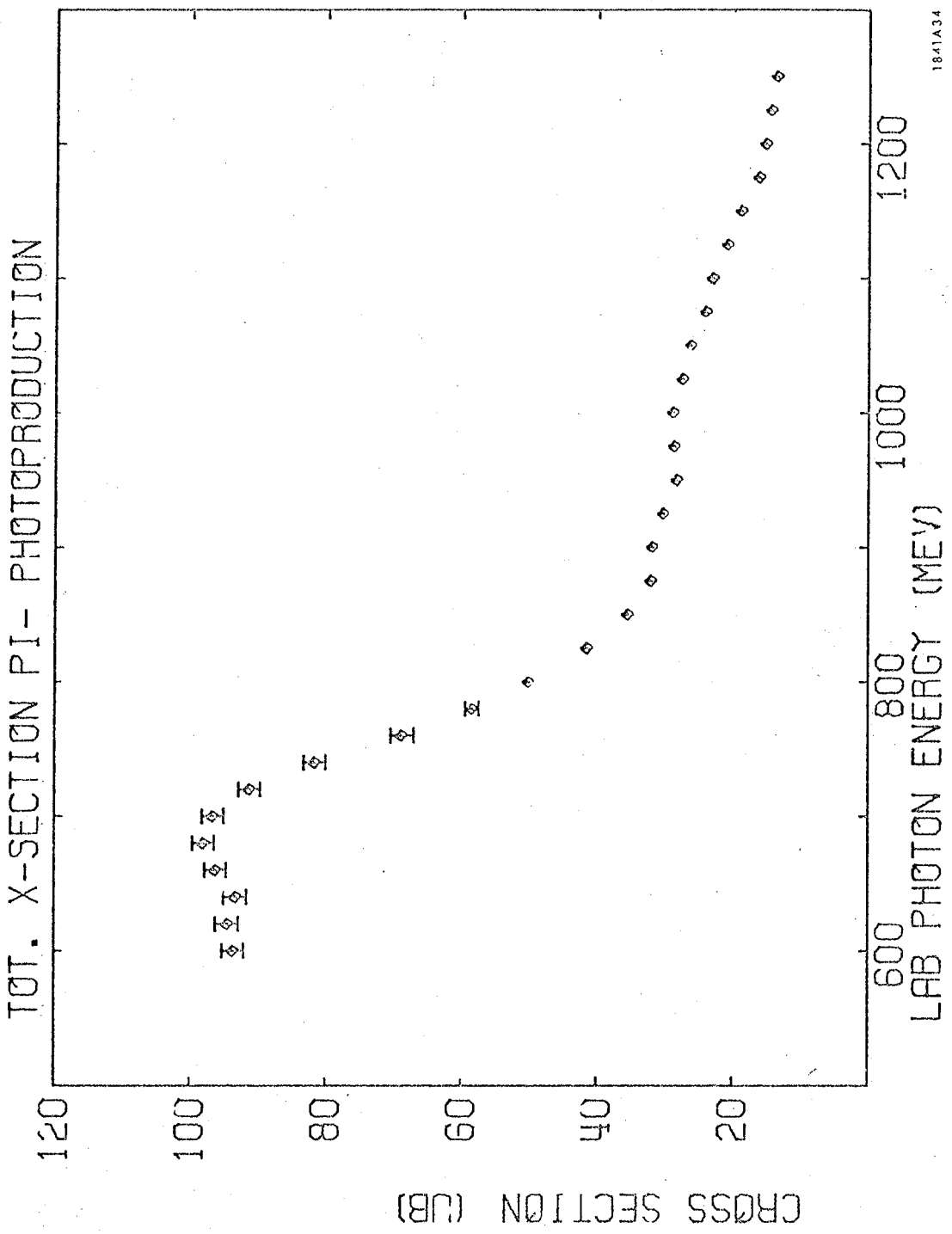
TOT. X-SECTION PI- PHOTOPRODUCTION
CROSS SECTION (UB)
120
100
80
60
40
20
600
800
1000
1200
LAB PHOTON ENERGY (MEV)
1841A34

FIGURE 13

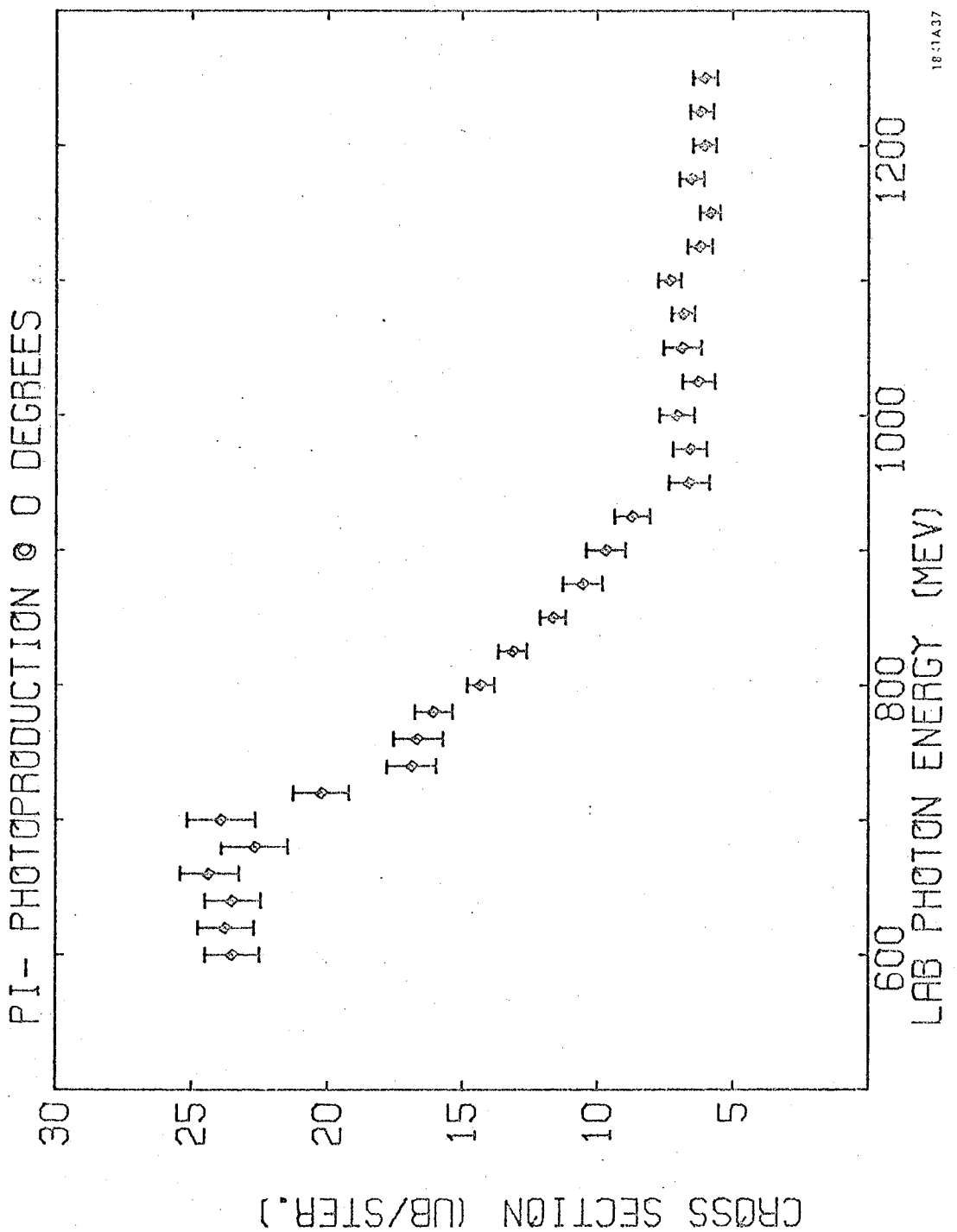
PI- PHOTOPRODUCTION @ 0 DEGREES
CROSS SECTION (UB/STER.)
LAB PHOTON ENERGY (MEV)
30
25
20
15
10
5
600
800
1000
1200

FIGURE 14

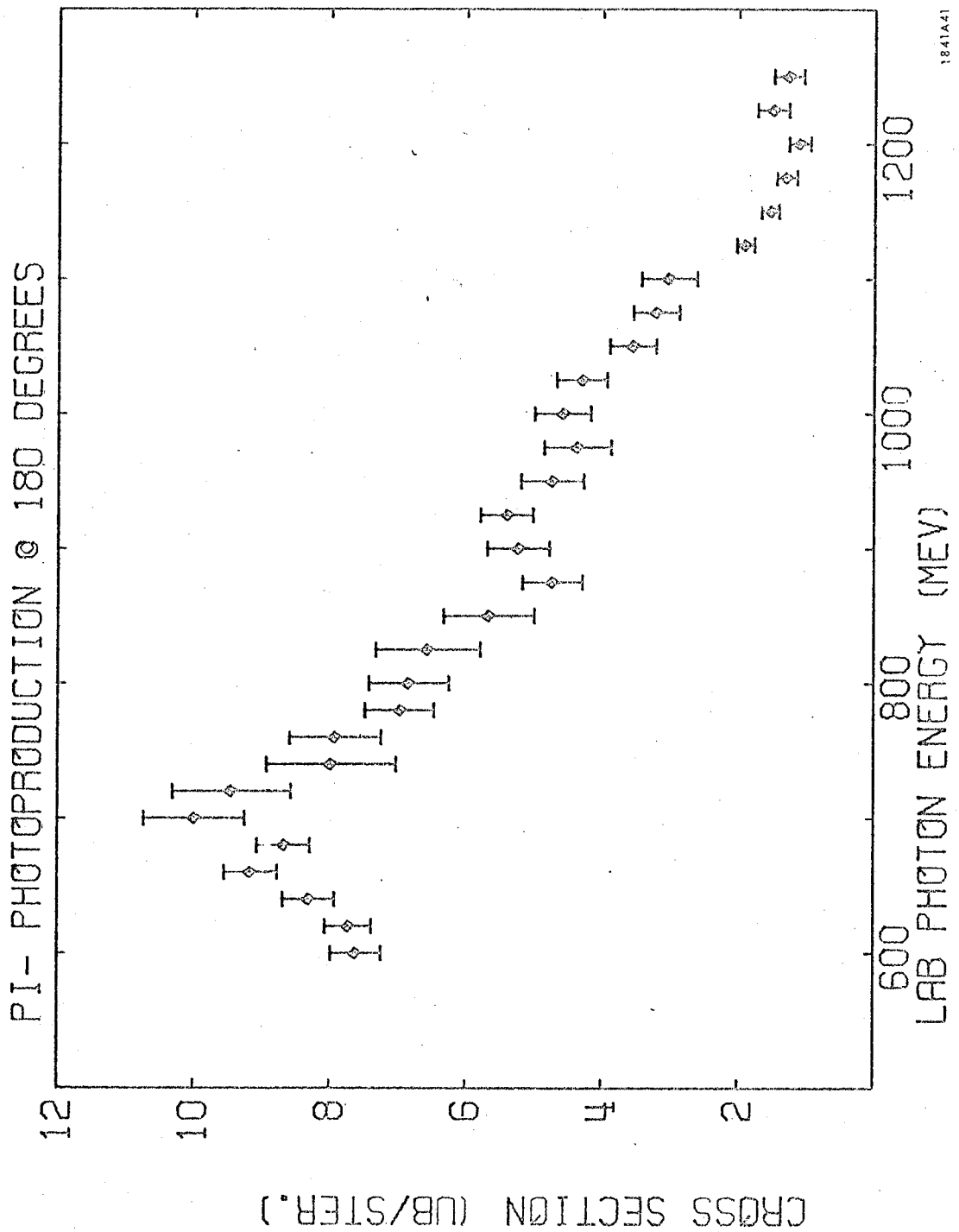
PI- PHOTOPRODUCTION @ 180 DEGREES
CROSS SECTION (UB/STER.)
LAB PHOTON ENERGY (MEV)
12
10
8
6
4
2
600
800
1000
1200
1841A41

FIGURE 15

J. Comparison with other experiments.

Since the present experiment was started, the results of several other π^- photoproduction experiments have been published. Comparison of the results of our experiment with these new data are given in Figures 16, 17, 18, 19, and 20. The total cross section for the bubble chamber experiment of Hilpert et al. (38) (Figure 16) is in good agreement with the total cross section obtained from the Moravcsik fit of our data. However, some of the differential cross sections from the bubble chamber experiment disagree with ours; these occur mostly where very few events were observed in a given energy-angle bin for Hilpert et al. and thus where their statistics were very poor.

The bubble chamber experiment done by Lodi-Rizzini et al. (37) is in poor agreement with ours in the region just above the second resonance. The total cross sections are compared in Figure 17. The drop in the cross section above the second resonance has been displaced downward about 50 MeV in the bubble chamber experiment. This disagreement, as yet unexplained, may cast some doubt on the partial wave analysis of π^- photoproduction in this energy region, especially on the values of the S11, P11, and D13 resonances (see Part V).

Comparison of the results of Ito et al. (40) at zero degrees with the results of the Moravcsik fit of our experiment at this angle is given in Figure 18. The agreement is very good except perhaps at 1100 MeV where the discrepancy is about three standard deviations.

The counter experiment of Beneventano et al. (39) at 90° is compared with our fit in Figure 19. There is a slight disagreement at about 620 MeV. Since we had a couple of anomalously low points near this energy, I am inclined to believe the data of Beneventano here.

Finally, the results of Fujii et al. (11) at 180° are compared with our fit in Figure 20. In general Fujii's results are higher than ours while also showing more structure. The resolution of our experiment was very poor at 180° and this explains our lack of structure. However there is still probably a slight normalization disagreement between the two experiments. The results of Fujii et al. have been used in the partial wave analysis of π^- photoproduction described in Part V.

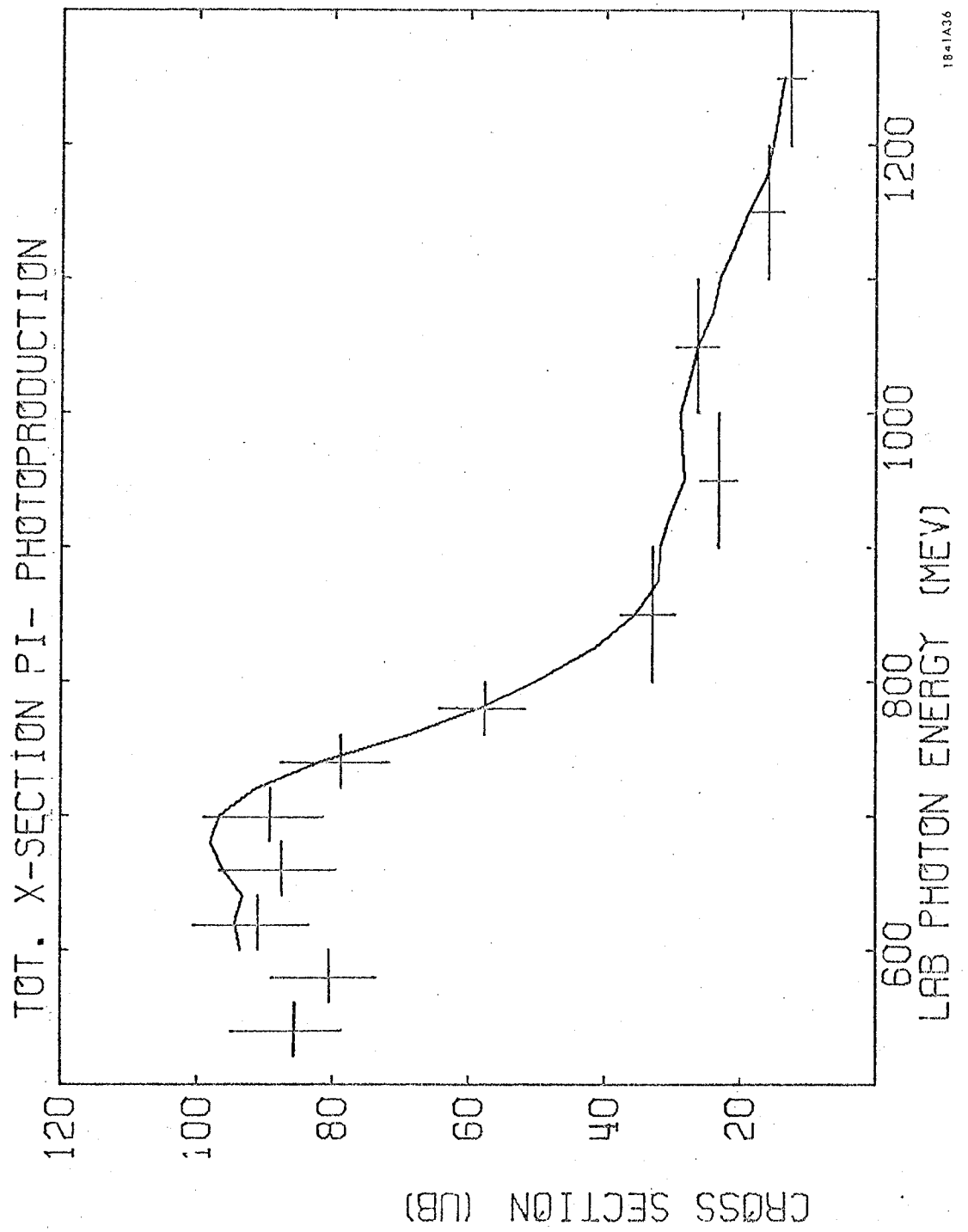
TOT. X-SECTION PI- PHOTOPRODUCTION
CROSS SECTION (UB)
120
100
80
60
40
20
600
800
1000
1200
LAB PHOTON ENERGY (MEV)
18A1A36

FIGURE 16

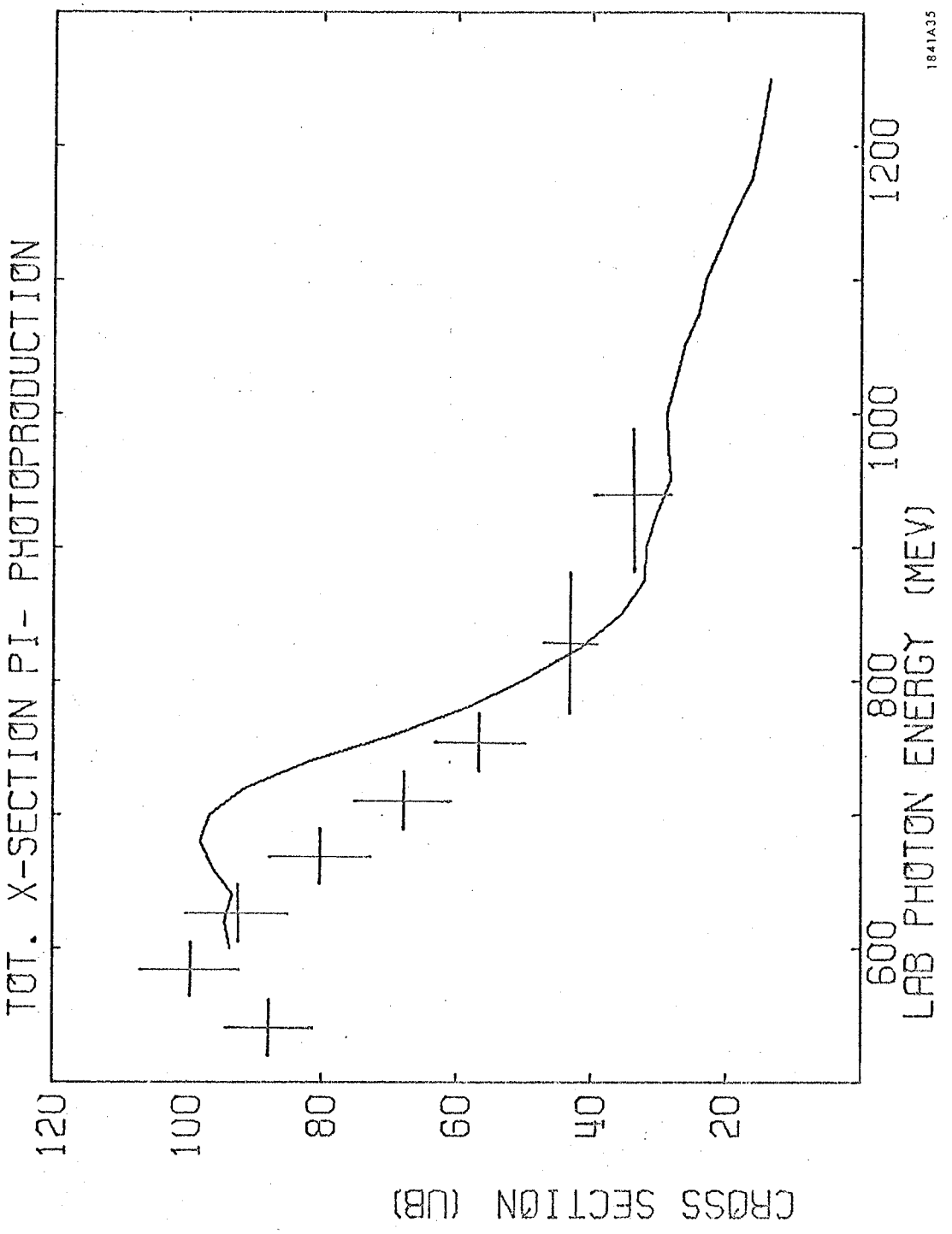
TOT. X-SECTION PI- PHOTOPRODUCTION
CROSS SECTION (UB)
120
100
80
60
40
20
600
800
1000
1200
LAB PHOTON ENERGY (MEV)
1841A35

FIGURE 17

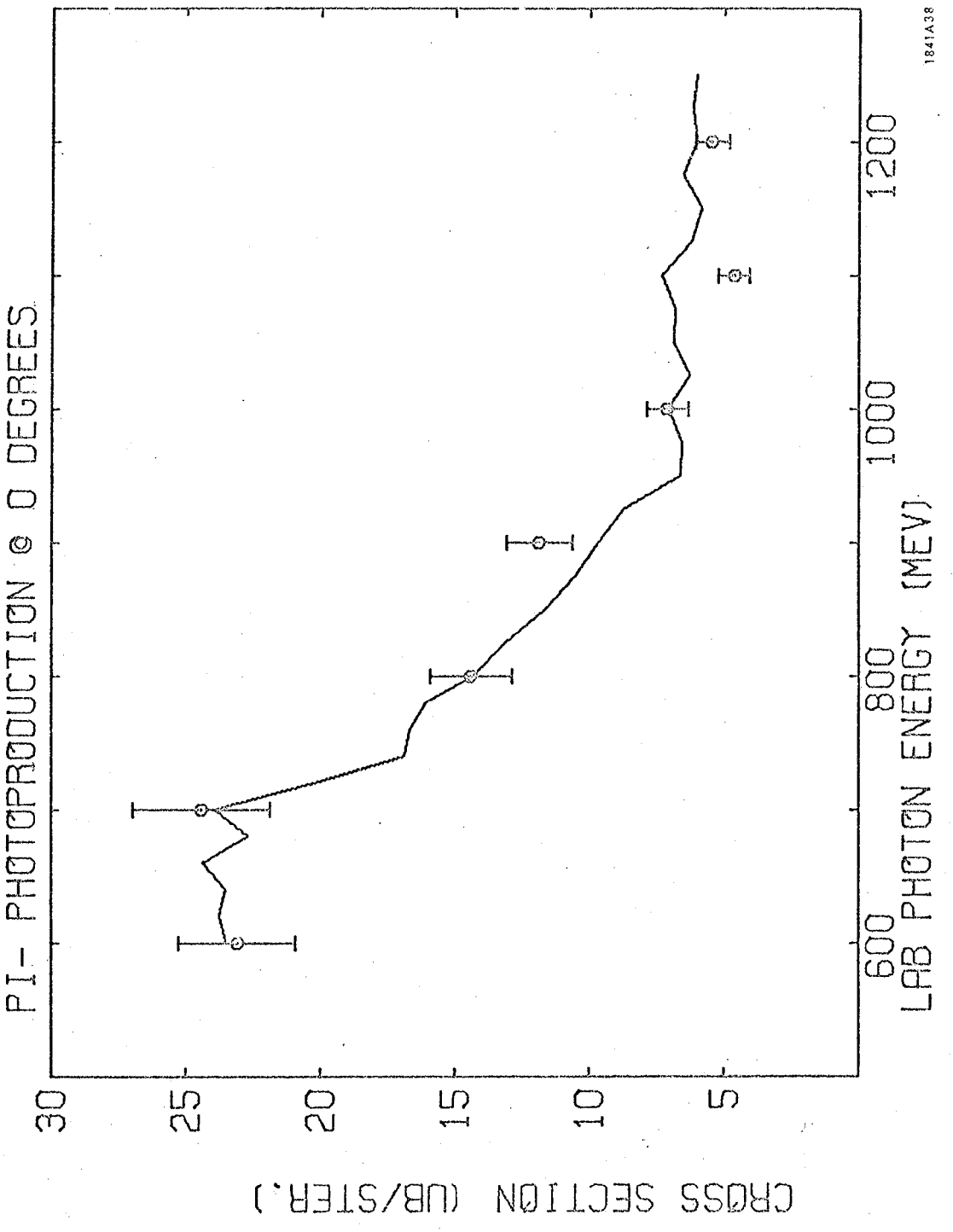
PI- PHOTOPRODUCTION @ 0 DEGREES
CROSS SECTION (UB/STER.)
LAB PHOTON ENERGY (MEV)
30
25
20
15
10
5
600
800
1000
1200
1841A38

FIGURE 18

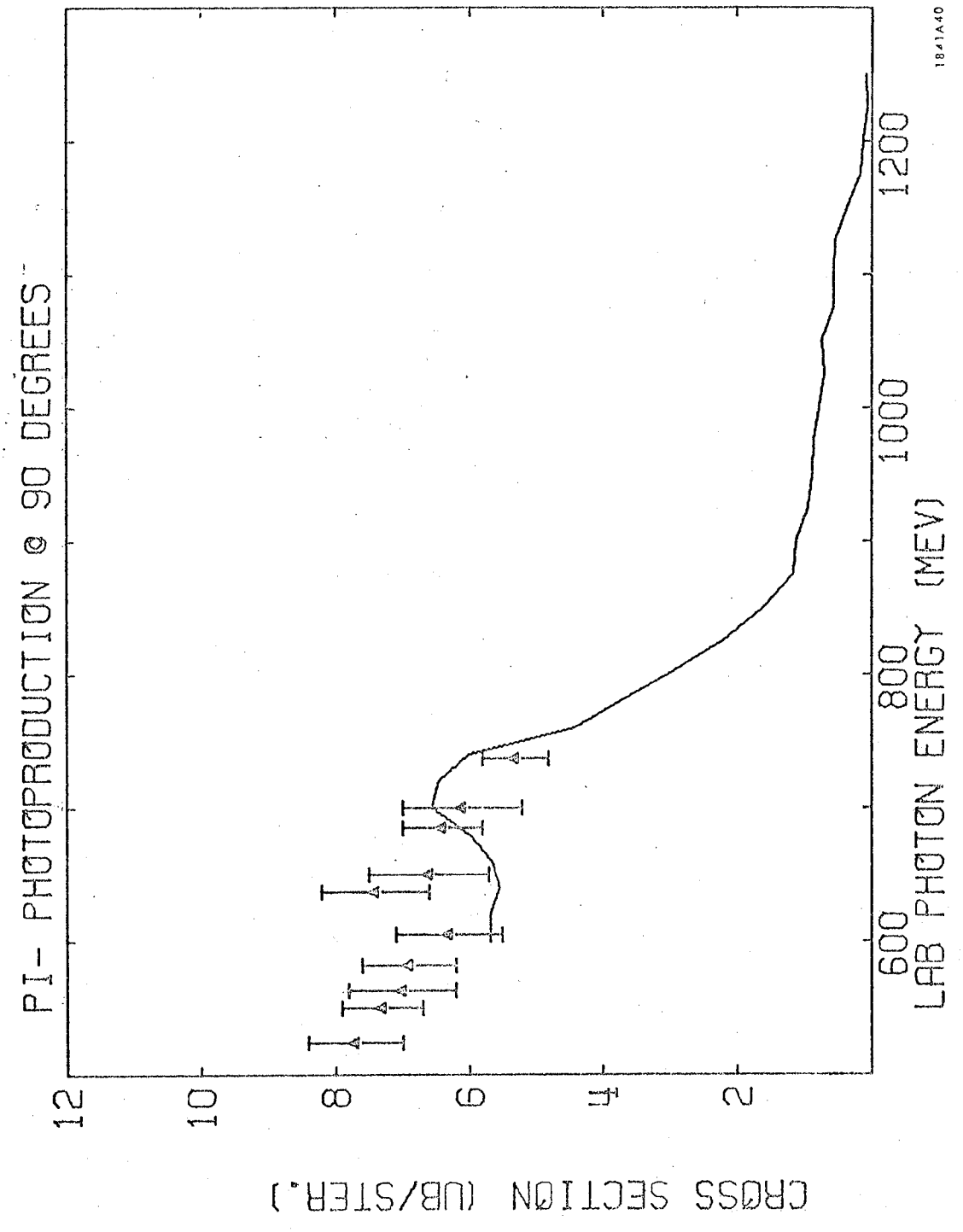
PI- PHOTOPRODUCTION @ 90 DEGREES
CROSS SECTION (UB/STER.)
LAB PHOTON ENERGY (MEV)
12
10
8
6
4
2
600
800
1000
1200
1841A40

FIGURE 19

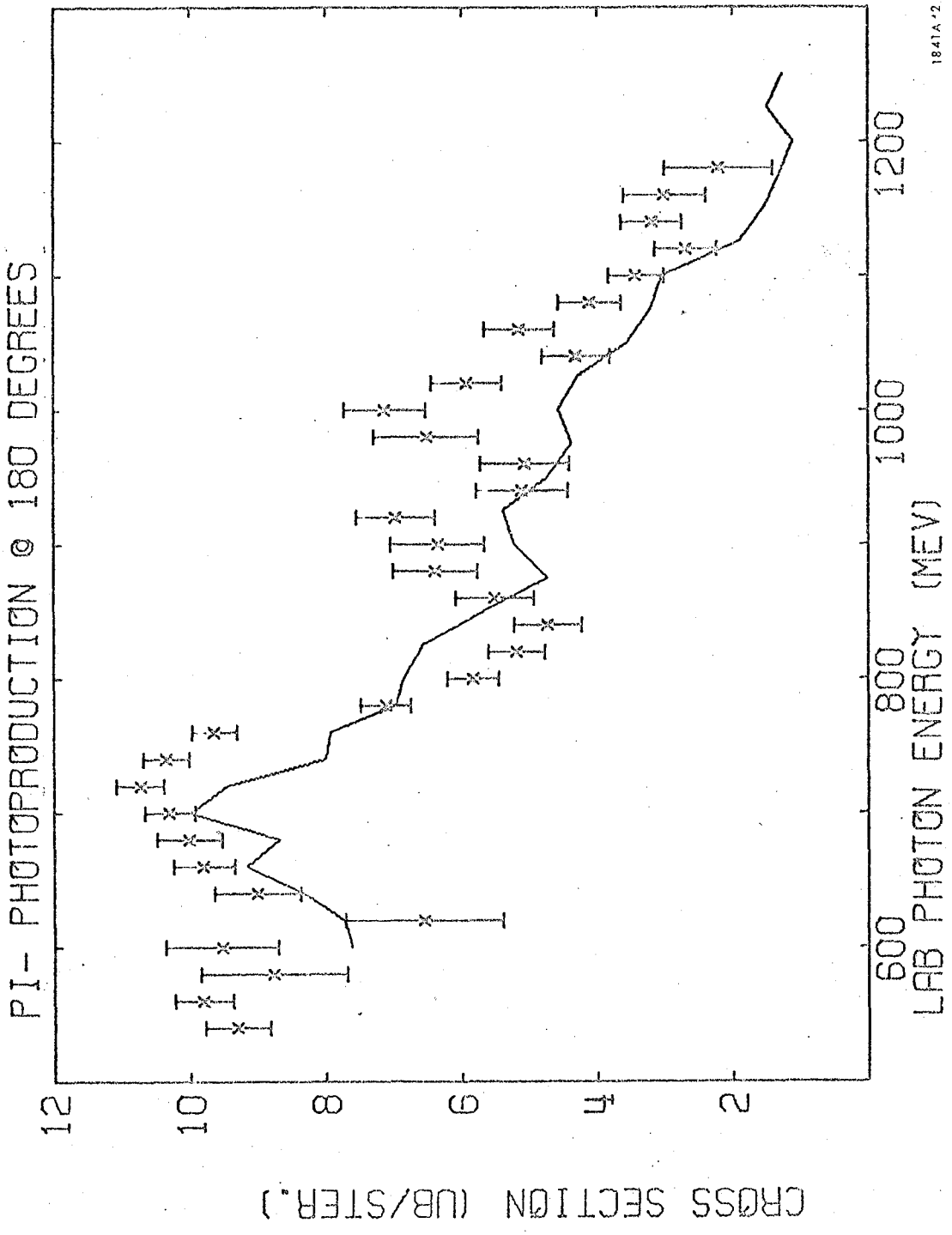
PI- PHOTOPRODUCTION @ 180 DEGREES
CROSS SECTION (UB/STER.)
LAB PHOTON ENERGY (MEV)
12
10
8
6
4
2
600
800
1000
1200
1841A-2

FIGURE 20

PART V

PARTIAL WAVE ANALYSIS

The large amount of new data for single pion photoproduction from this experiment and others will help in the determination of partial wave amplitudes. An analysis of the three reactions $\gamma p \to \pi^+ n$, $\gamma p \to \pi^o p$, and $\gamma n \to \pi^- p$ has been made by Walker(3) based on data taken before 1967. I will present here a refinement of Walker's analysis for the first and third reactions which uses some selected data taken up to 1971. A list of the experiments included in the analysis is given in Table 7. An attempt has also been made to analyse the second reaction ($\gamma p \to \pi^o p$) but the results have not been clear cut due to disagreements of different π^o experiments. Work on the analysis of these single pion photoproduction reactions is being continued by William J. Metcalf and Robert L. Walker.

In my analysis, the new polarization and asymmetry data have a large effect on the partial wave amplitudes, especially bringing into question the amplitudes for the $S_{11}(1535)$ and $P_{11}(1470)$ resonances.

In the π^- reaction, new amplitudes will be given for the $S_{11}(1535)$, $D_{13}(1520)$ (helicity 1/2 part), and the $F_{15}(1688)$ resonances. In the π^+ reaction, new amplitudes will be given

TABLE 7

EXPERIMENTS USED IN PARTIAL WAVE ANALYSES

1) π^- photoproduction

a) Scheffler and Walden (52) - cross sections 600 - 1250 MeV.

b) Fujii et al. (11) - 180° cross sections.

c) Neugebauer (36) with Thiessen (7) - cross sections at 510 MeV.

d) Beneventano et al. (42) - 90° recoil proton polarizations. Interpolated.

e) Metcalf (43) - 90° recoil proton polarizations. Interpolated.

f) Kondo et al. (53) - 90° polarized beam asymmetries. Interpolated.

g) Alspector et al. (20) - 90° polarized beam asymmetries. Interpolated.

2) π^+ photoproduction

a) Betourne et al. (5) - cross sections 400 - 750 MeV.

b) Ecklund and Walker (6) - cross sections 600 - 1270 MeV.

c) Thiessen (7) - cross sections 500 - 1250 MeV.

d) Fujii et al. (11) - 180° cross sections.

e) Hahn et al. (19) - 60° and 90° recoil neutron polarization. Interpolated.

f) Grilli et al. (18) - 90° polarized beam asymmetry near 400 MeV. Interpolated.

TABLE 7 (continued)

g) Liu et al.(54) - 90° polarized beam asymmetry.
Interpolated.

h) Alspector et al.(20) - 90° polarized beam asymmetry.
Interpolated.

i) Althoff et al.(28) - 40° polarized target asymmetry.
Interpolated.

for the $P_{11}(1470)$, $F_{15}(1688)$ (helicity 3/2 part) and perhaps the $S_{11}(1535)$ resonances.

A. Model for the partial wave analysis.

The model used is the same as that given by Walker(3). The relatively poor precision of photoproduction data, combined with the small excitation of higher partial waves in the energy region of interest (k_γ^{lab} = 500 to 1300 MeV), precludes any reasonably precise determination of partial waves for $j_{tot} > 5/2$. Instead of setting these equal to zero, Walker sets them equal to the partial wave decomposition of the electric Born approximation (see Appendix VII) which is (perhaps) closer to reality. In any case, these amplitudes are small for $j_{tot} > 5/2$. Also, the electric Born approximation is known to have roughly the same qualitative behavior as the photoproduction cross section (eg. the forward peak for π^+ photoproduction and the forward and backward peaks for π^- photoproduction) so that the Born terms are also added to the lower partial waves to try to reduce the background. The parameters of the fit are then the extra lowest partial waves (j_{tot} = 1/2, 3/2, 5/2) which are added to the Born terms to give the best fit to the experimental

data.

Walker divides these extra lowest partial waves into two parts, resonant and non-resonant. Using the N and Δ resonance widths and energies obtained from πN scattering analyses, and Breit-Wigner forms for the resonances (Appendix VII), he then determines the resonance amplitudes which make the non-resonant (background) part of the fit as small and as smooth as possible with energy.

Explicitly, the parameters of the fit are the resonance amplitudes (helicity 1/2 and helicity 3/2 parts) and the extra add-on helicity elements $A_{\ell\pm}$ and $B_{\ell\pm}$ which are added to the electric Born terms and the resonances. The total helicity elements $A_{\ell\pm}$ and $B_{\ell\pm}$ are then obtained by summing the Born contribution, the resonance contribution, and the add-on helicity element contribution.

The definition of the helicity amplitudes and helicity elements are given in Appendices V and VI. The helicity element $A_{\ell\pm}$ is the amplitude for an initial state of total CM helicity 1/2 (in the photon direction), total angular momentum $j_{tot} = \ell \pm 1/2$, to go into a final state of orbital angular momentum ℓ (parity $-(-1)^{\ell}$), and total angular momentum $j_{tot} = \ell \pm 1/2$. The element $B_{\ell\pm}$ is similarly the amplitude for an initial state of total helicity 3/2, total angular momentum

$j_{tot} = \ell \pm 1/2$, to go into a final state as above. Note that the amplitude is not given for a final state of definite helicity, but rather of definite parity (or equivalently of definite orbital angular momentum). These amplitudes can then be used to describe resonant behavior, since the resonances have definite parity.

The (initial) helicity 3/2 ($B_{\ell\pm}$) and helicity 1/2 ($A_{\ell\pm}$) components of the (resonance) amplitudes are linear combinations of the (perhaps more familiar) electric ($E_{\ell\pm}$) and magnetic ($M_{\ell\pm}$) multipole components which were introduced by CGLN(51). Expressing the $E_{\ell\pm}$, $M_{\ell\pm}$ in terms of the $A_{\ell\pm}$, $B_{\ell\pm}$, we have:

$$
\begin{aligned}
E_{\ell+} &= (\ell+1)^{-1}\,(A_{\ell+} + \tfrac{1}{2}\ell\, B_{\ell+}) \\
M_{\ell+} &= (\ell+1)^{-1}\,(A_{\ell+} - \tfrac{1}{2}(\ell+2)\, B_{\ell+}) \\
E_{(\ell+1)-} &= -(\ell+1)^{-1}\,(A_{(\ell+1)-} - \tfrac{1}{2}(\ell+2)\, B_{(\ell+1)-} \\
M_{(\ell+1)-} &= (\ell+1)^{-1}\,(A_{(\ell+1)-} + \tfrac{1}{2}\ell\, B_{(\ell+1)-})
\end{aligned}
\qquad (V.1)
$$

For further orientation, Table 8 gives the properties of the lowest order helicity elements and their relationship to electric and magnetic multipoles.

TABLE 8

Relationship of Helicity Elements

to Electric and Magnetic Multipoles

Helicity Element	Final Orbital Angular Momentum ℓ	Total Angular Momentum j_{tot}	Parity $P = -(-1)^{\ell}$	Angular Momentum of (Photon) Multipole $j_\gamma = j_{tot} \pm \frac{1}{2}$	j_γ^P	CGLN Coeff.	Multipole	Multipole Name
A_{0+}	0	1/2	-1	1	1^-	E_{0+}	E1	Elec. Dipole
A_{1-}	1	1/2	+1	1	1^+	M_{1-}	M1	Mag. Dipole
A_{1+}, B_{1+}	1	3/2	+1	1	1^+	M_{1+}	M1	Mag. Dipole
				2	2^+	E_{1+}	E2	Elec. Quadrupole
A_{2-}, B_{2-}	2	3/2	-1	1	1^-	E_{2-}	E1	Elec. Dipole
				2	2^-	M_{2-}	M2	Mag. Quadrupole
A_{2+}, B_{2+}	2	5/2	-1	2	2^-	M_{2+}	M2	Mag. Quadrupole
				3	3^-	E_{2+}	E3	Elec. Octupole
A_{3-}, B_{3-}	3	5/2	+1	2	2^+	E_{3-}	E2	Elec. Quadrupole
				3	3^+	M_{3-}	M3	Mag. Octupole

B. Fitting procedure.

Walker's fit was done essentially "by hand". That is, a set of parameters was chosen and the calculated cross sections, polarizations, and asymmetries were plotted for visual comparison with the data. A table of first derivatives was printed to determine the first order effects on the cross sections, etc. of small changes in the parameters. Then the parameters were adjusted according to the effects of their derivatives to improve the agreement between the fit and experiment. This procedure was done at many energies (roughly 50 to 100 MeV apart) and an attempt was made to smooth the energy dependence of the add-on helicity elements and still keep a fairly good fit at each energy. The smoothing is part of the model and is justified by the belief that the true amplitudes are smooth. The smoothing was necessary because there are not enough data to determine all the parameters very well at each energy. A free energy by energy fit would in some cases cause large variations in the parameters because of statistical fluctuations of the data.

The above procedure was very tedious and time-consuming, but nevertheless has given a set of helicity elements and resonance parameters which fit the available data very well.

I have written a computer program which will adjust all

the parameters automatically by minimizing χ^2 at each energy. The procedure for minimizing χ^2 is described in Appendix VIII. The main problem in fitting the photoproduction data was to find a way to automatically smooth the data with energy. I have tried two methods:

1) In a grand design to fit all energies at once, the add-on helicity element parameters were approximated as polynimials with respect to photon energy. For example, $A_{1+}(k)$ was given by:

$$A_{1+}(k) = c_o + C_1 k + C_2 k^2 \qquad (V.2)$$

a second order polinomial in k described by the three parameters C_o, C_1, and C_2. While this method may yet work for small energy regions or larger order polynomials, I had much more success with a second method which I now describe.

2) The initial set of add-on helicity elements (the initial parameters of an energy by energy fit) were treated as experimental data points and were assigned "errors". These artificial data points were included in the calculation of χ^2; and thus the fitted add-on helicity elements were prevented from departing too far from their initial values. As an initial set of parameters (add-on heleicity elements), I used the final results of Walker's analysis. Assuming that the initial set of (smooth) parameters is close to the true parameters, this method seems to be a good way to constrain the fitted parameters to be relatively

smooth with energy and is also a good method to observe any resonant behavior which we have not yet removed from the add-on elements. Any large deviation of the fitted parameters from the initial set probably represents a real behavior of the helicity elements, since they are straining to increase the artificial part of χ^2 while the total χ^2 was reduced. Any observed resonant behavior in the fitted add-on elements should be removed and added to the resonance amplitudes.

C. Results of partial wave analysis.

1) π^- Photoproduction.

Some striking behavior was observed in the initial fit of π^- photoproduction using the second method described above. The initial values for the add-on elements were set equal to the final values of Walker's analysis. The resonance parameters were set equal to Walker's with some small changes in the energies and widths. The data used in the fit were taken from the experiments listed in Table 7.

The results of the initial fit are shown in the ten graphs of Figure 21. The plotted points are the initial set of add-on helicity elements (Walker's final values). The jagged lines are the program's fitted set of add-on elements.

Also plotted for comparison are the resonance amplitudes and (in some cases) the decomposition of the electric Born approximation for the particular helicity element (see page 148 for key).

A striking resonant behavior is observed for the A_{0+} add-on element (Figure 21.1), which seems to want to cancel the given resonance amplitude due to the $S_{11}(1535)$. (For a list of the resonances and the helicity elements they affect, refer to Table 9.) The resonant behavior of the add-on element is shifted down by about 40 MeV, which indicates that perhaps the central energy used for the S_{11}, 1535 MeV, is slightly off. This new behavior disagrees with the quark model prediction(2), which supports a large negative amplitude, in agreement with Walker's value.

Another fitted add-on element with a possible resonant behavior is the A_{2-} (Figure 21.5). The resonance corresponding to this element is the helicity 1/2 component of the $D_{13}(1520)$ which is located at a photon energy of about 760 MeV. The real part of the fitted add-on amplitude has a strange behavior between 600 and 700 MeV, but it does decrease rapidly at the resonance energy, a behavior which is characteristic of a positive resonance (see Appendix VII). Walker's analysis was unable to determine any definite finite value for the helicity 1/2 component of the $D_{13}(1520)$ and so it was set to zero. The present fit, perhaps, wants to give the A_{2-} resonant element a definite positive value.

FIGURE 21

INITIAL FIT OF ADD-ON HELICITY

ELEMENTS FOR π^- PHOTOPRODUCTION

The Figure, consisting of ten graphs, is a little confusing on first glance; so a short explanation is given here.

There are ten graphs for the ten lowest order heleicity elements: A_{0+} and A_{1-} ($j_{tot} = 1/2$); A_{1+}, B_{1+}, A_{2-}, B_{2-} ($j_{tot} = 3/2$); A_{2+}, B_{2+}, A_{3-}, B_{3-} ($j_{tot} = 5/2$). Refer to Table 8 (page 143) for the characteristics of these helicity elements.

As described in Section V.A on Walker's model, the total helicity element is composed of three parts: the Born part, the resonance part, and the add-on or background part. In my fit, the Born part and the resonance part are initially set and are not varied during the fit. The add-on part is initially set to Walker's values and is varied during the fit to minimize χ^2.

Figure 21 is a plot of four distinct quantities:

1) A continuous plot of the Born part of the particular helicity element (line identified by △). The Born amplitude is completely real.
2) A continuous plot of the resonance part of the particular helicity element (curves are identified by ○ for real part and ✕ for imaginary part). Typical behavior of a resonant amplitude is given on page 239.
3) A set of points showing the initial add-on elements of the fit. These are taken from Walker's analysis. The real part is given by ⋈ and the imaginary part by + .
4) A jagged plot of the final fitted add-on elements. The fit was done at energies 510, 600, 620, 640, 660, 680, 700, 720, 740, 760, 780, 800, 825, 850, 875, 900, 925, 950, 975, 1000, 1025, 1050, 1075, 1100, 1125, 1150, 1175, 1200, 1225, and 1250 MeV. A continuous (jagged) curve was drawn through the points at these energies. The curve for the real part is identified by ◇ and the imaginary curve is identified by Y .

The interesting point is to compare the curves 4) with Walker's points 3), to see how much the fit wanted to change the add-on elements from their initial values. Remember that the fitted add-on elements were constrained not to depart too far from their initial (Walker) values by the artificial errors assigned to the Walker values (see page 145). The artificial errors used in this fit were ±.2 for the $j_{tot} = 1/2$ elements, ±.1 for the $j_{tot} = 3/2$ elements, and ±.05 for the $j_{tot} = 5/2$ elements. For convenience, the artificial error is shown on the left of each graph.

Note: for a list of the resonances and the helicity elements which they affect, see Table 9, page 161.

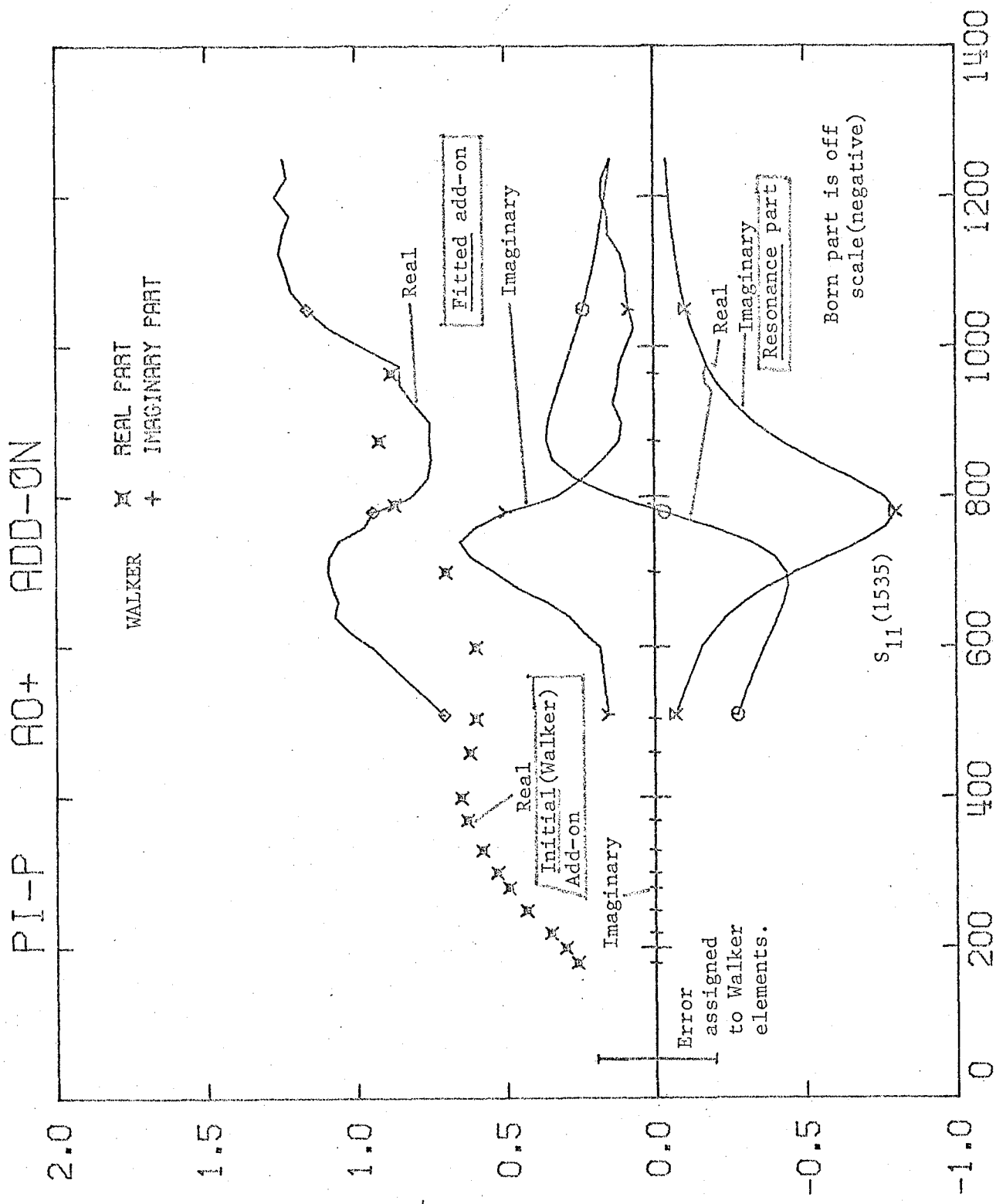
PI-P A0+ ADD-ON
WALKER
REAL PART
IMAGINARY PART
Real
Imaginary
Fitted add-on
Real
Imaginary
Initial(Walker)
Add-on
Real
Imaginary
Resonance part
Born part is off
scale(negative)
Error
assigned
to Walker
elements.
$S_{11}(1535)$
HELICITY ELEMENT (UB/SR)1/2
LAB PHOTON ENERGY (MEV)
2.0
1.5
1.0
0.5
0.0
-0.5
-1.0
0
200
400
600
800
1000
1200
1400

FIGURE 21.1

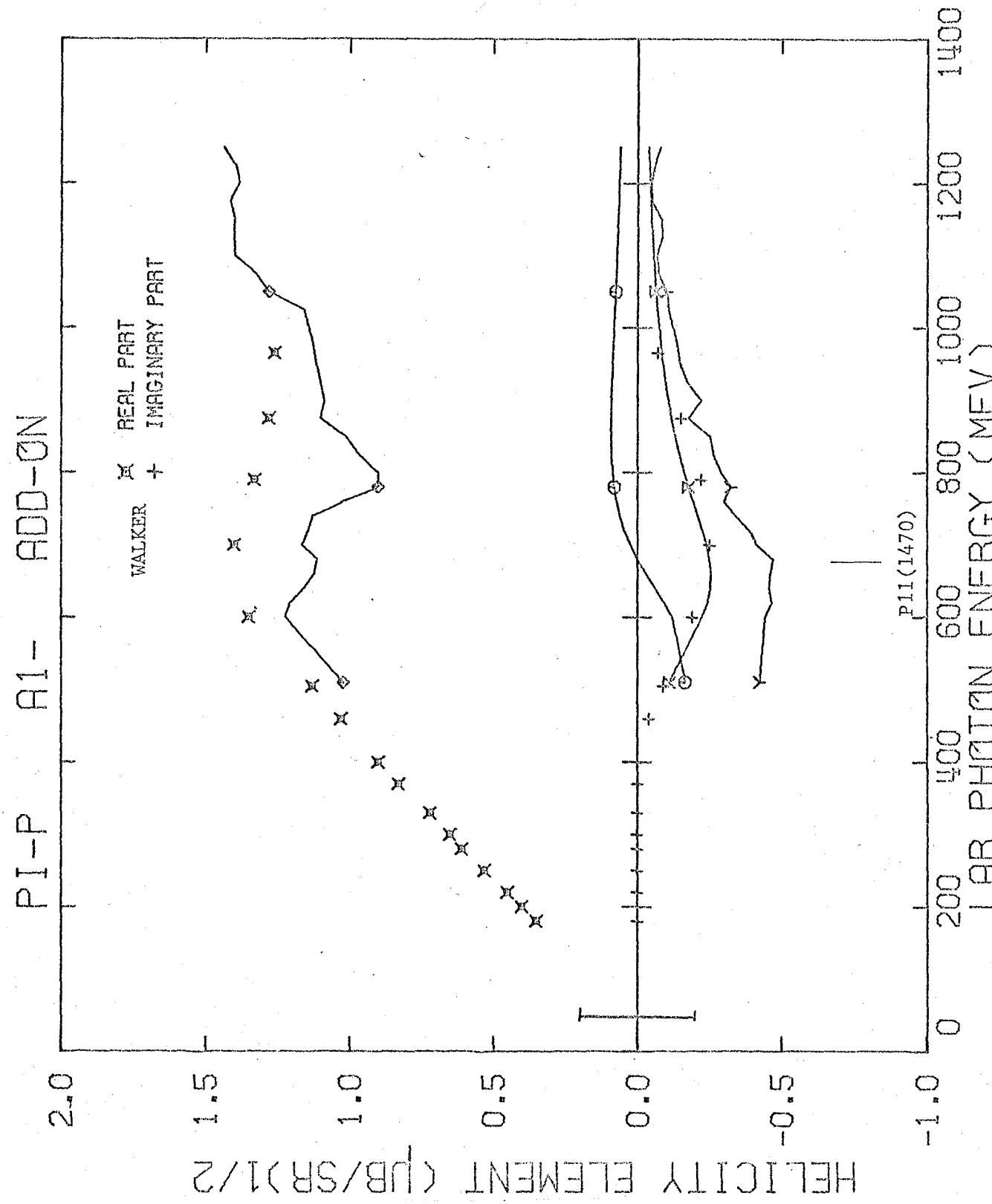
PI-P A1- ADD-ON
WALKER
REAL PART
IMAGINARY PART
P11(1470)
HELICITY ELEMENT (UB/SR)1/2
LAB PHOTON ENERGY (MEV)
2.0
1.5
1.0
0.5
0.0
-0.5
-1.0
0
200
400
600
800
1000
1200
1400

FIGURE 21.2

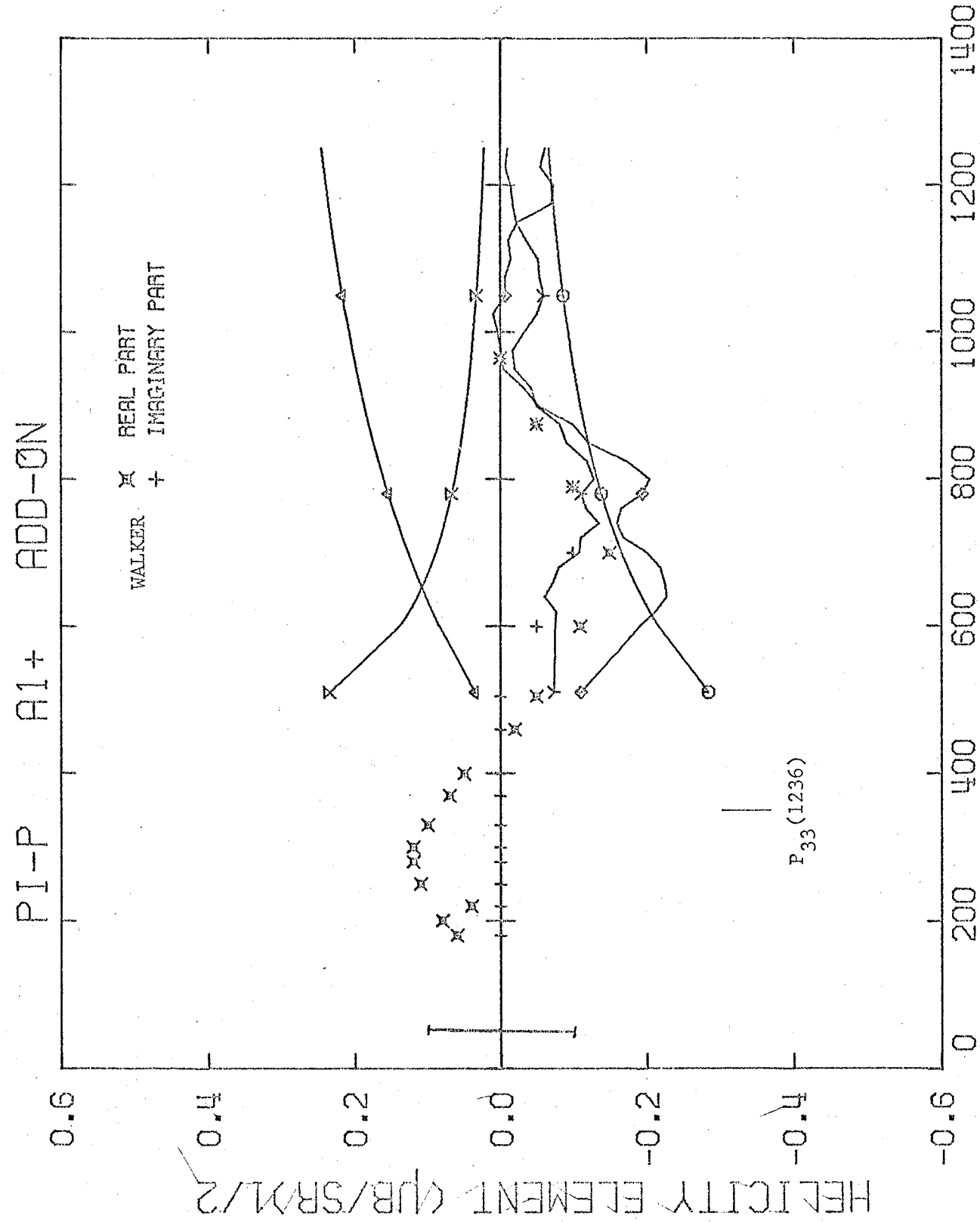
PI-P A1+ ADD-ON
WALKER
REAL PART
IMAGINARY PART
$P_{33}(1236)$
HELICITY ELEMENT (UB/SR/ML/2
LAB PHOTON ENERGY (MEV)
0.6
0.4
0.2
0.0
-0.2
-0.4
-0.6
0
200
400
600
800
1000
1200
1400

FIGURE 21.3

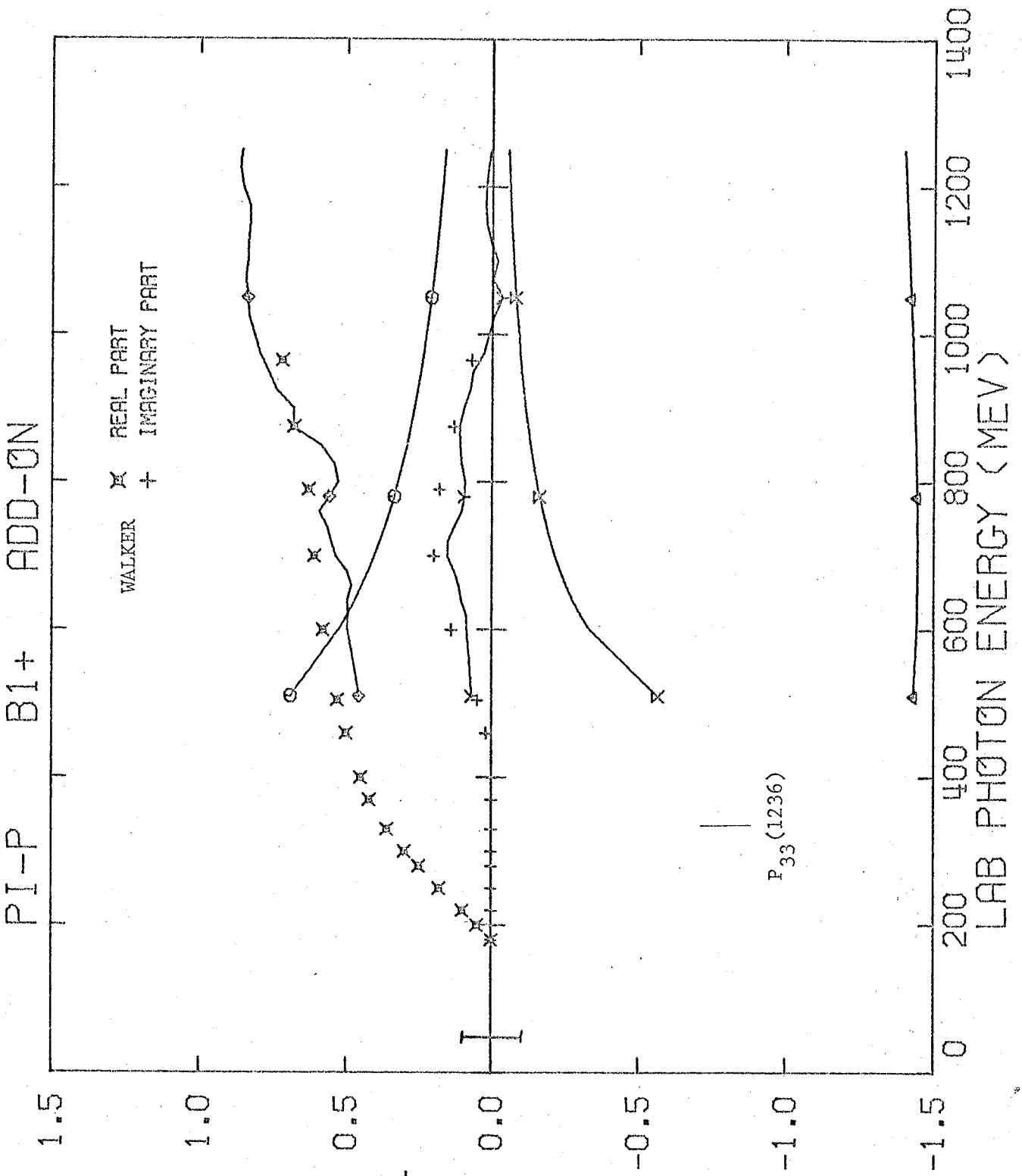
PI-P B1+ ADD-ON
WALKER
REAL PART
IMAGINARY PART
$P_{33}(1236)$
HELICITY ELEMENT (UB/SR)1/2
LAB PHOTON ENERGY (MEV)
1.5
1.0
0.5
0.0
-0.5
-1.0
-1.5
0
200
400
600
800
1000
1200
1400

FIGURE 21.4

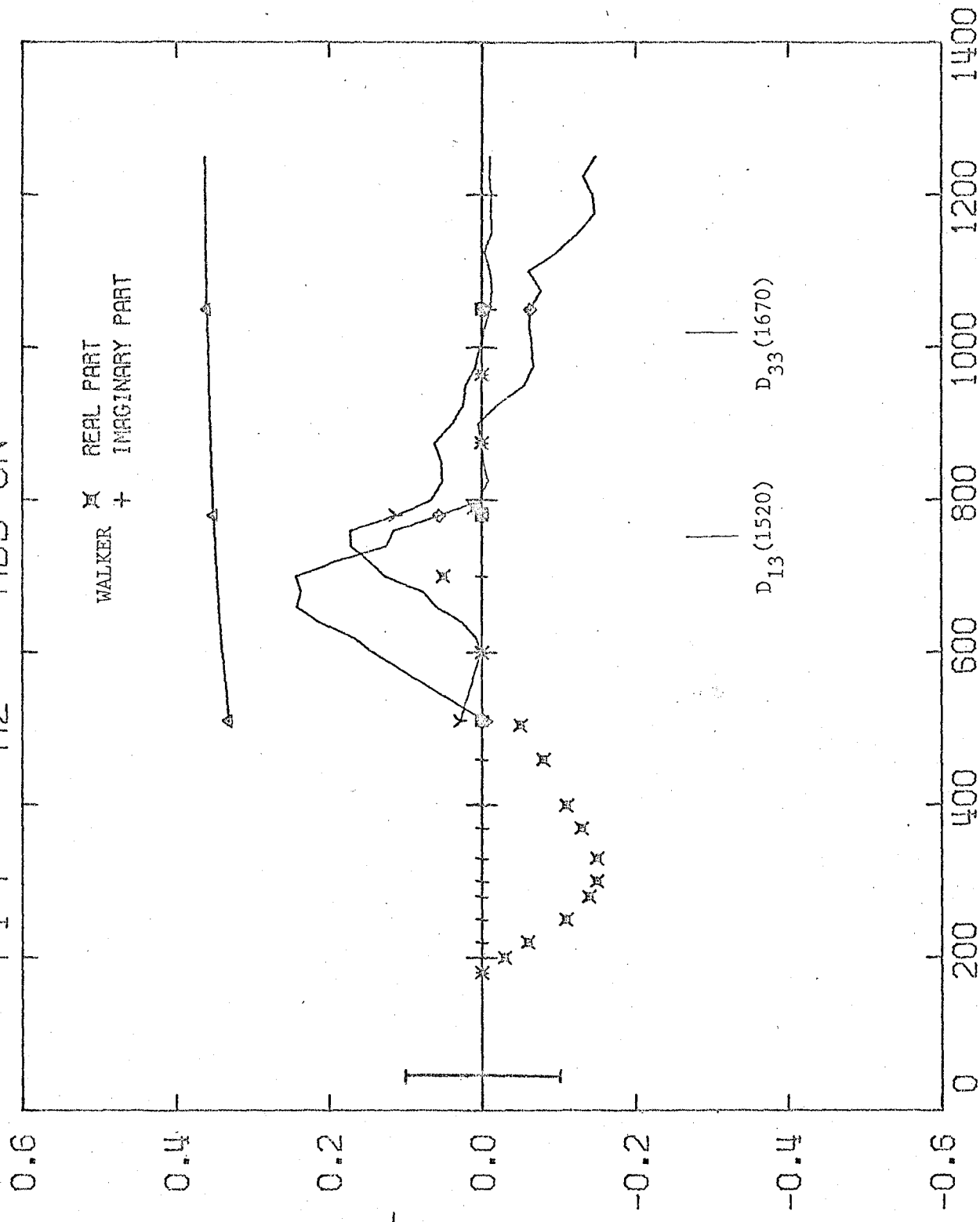
PI-P A2- ADD-ON
WALKER
REAL PART
IMAGINARY PART
$D_{13}(1520)$
$D_{33}(1670)$
HELICITY ELEMENT (UB/SR)1/2
LAB PHOTON ENERGY (MEV)
0.6
0.4
0.2
0.0
-0.2
-0.4
-0.6
0
200
400
600
800
1000
1200
1400

FIGURE 21.5

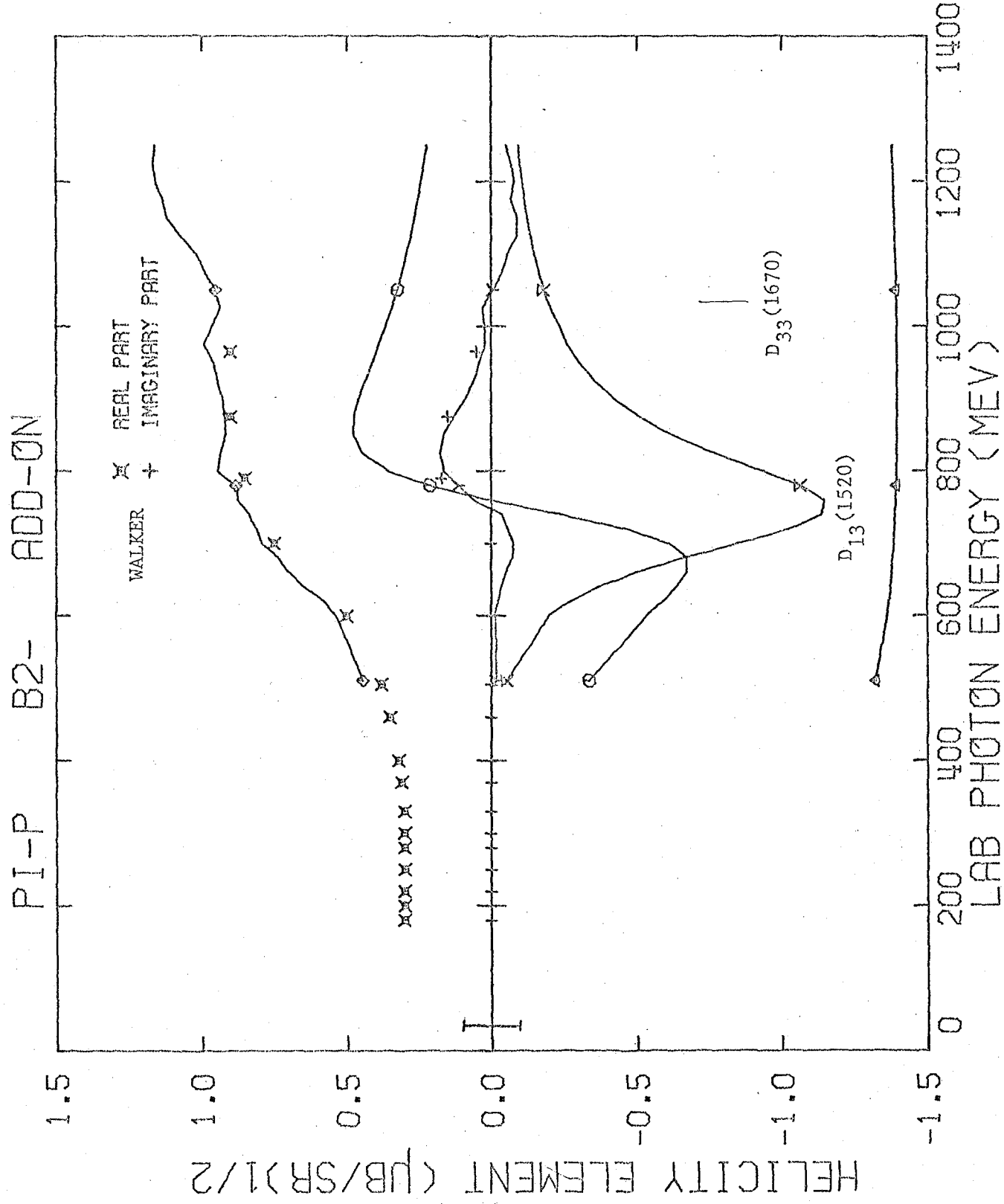
PI-P B2- ADD-ON
WALKER
REAL PART
IMAGINARY PART
$D_{33}(1670)$
$D_{13}(1520)$
HELICITY ELEMENT (UB/SR)1/2
LAB PHOTON ENERGY (MEV)
1.5
1.0
0.5
0.0
-0.5
-1.0
-1.5
0
200
400
600
800
1000
1200
1400

FIGURE 21.6

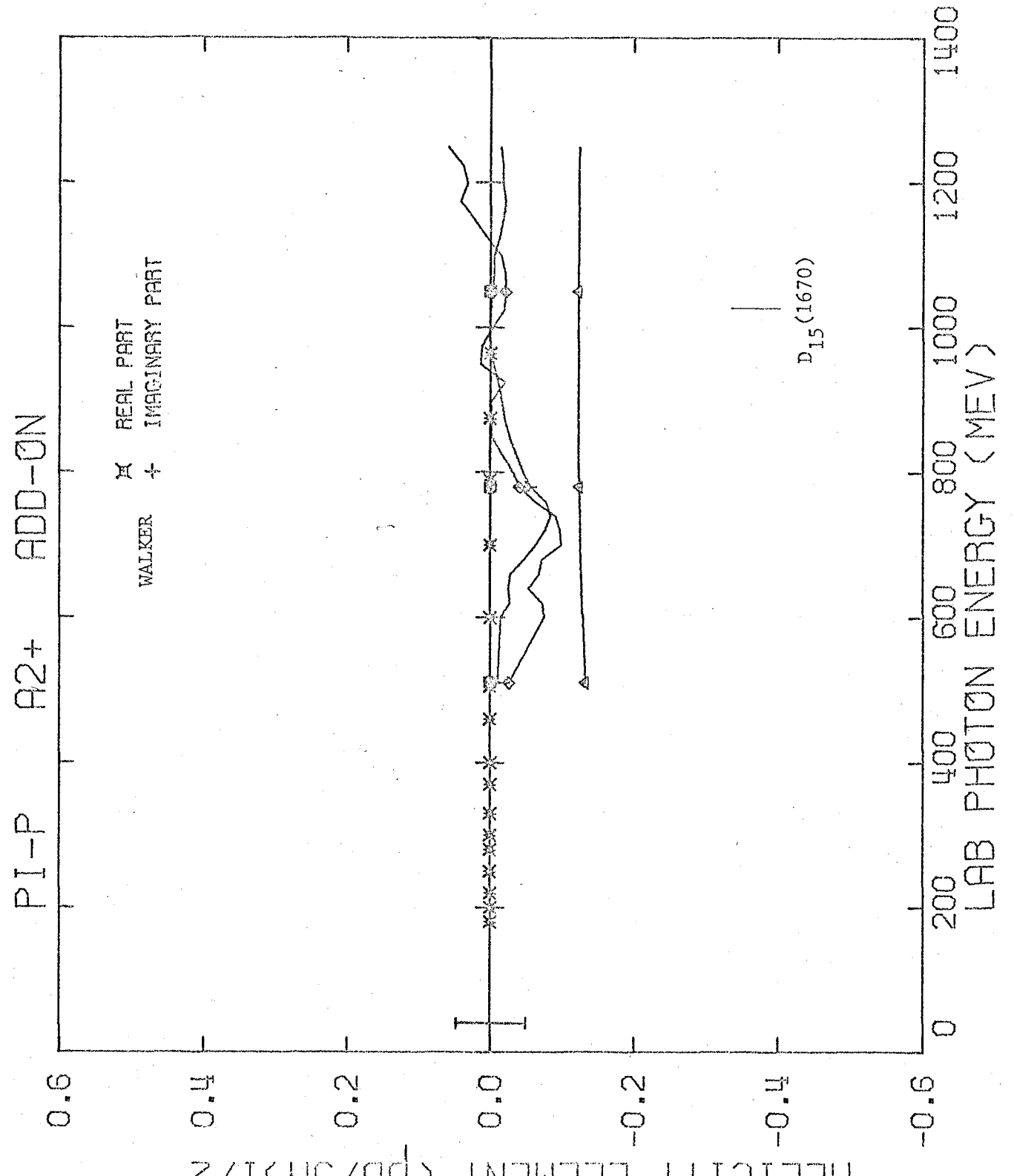
PI-P A2+ ADD-ON
WALKER
REAL PART
IMAGINARY PART
$D_{15}(1670)$
HELICITY ELEMENT (UB/SR)1/2
LAB PHOTON ENERGY (MEV)
0.6
0.4
0.2
0.0
-0.2
-0.4
-0.6
0
200
400
600
800
1000
1200
1400

FIGURE 21.7

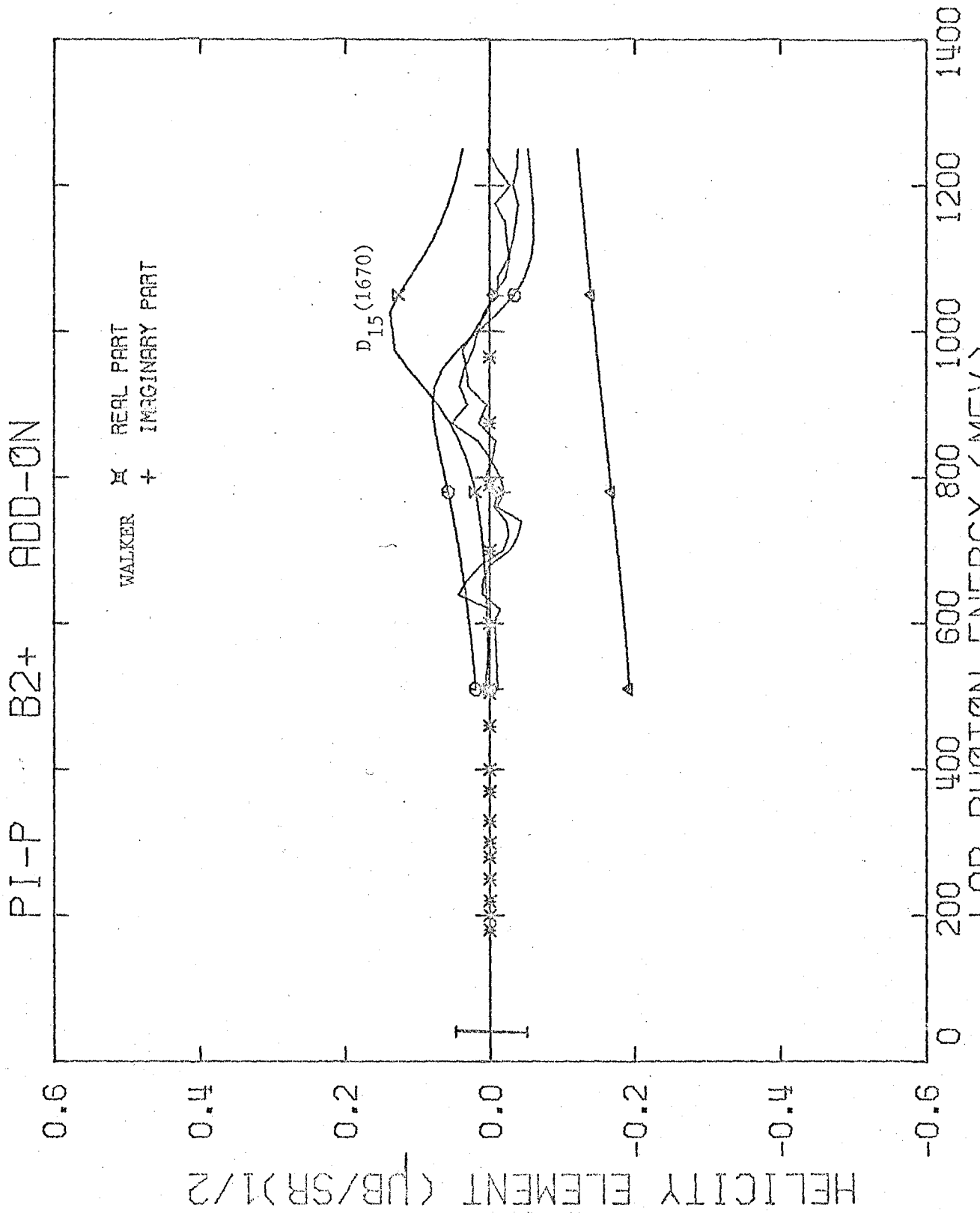
PI-P B2+ ADD-ON
WALKER
REAL PART
IMAGINARY PART
$D_{15}(1670)$
HELICITY ELEMENT (UB/SR)1/2
LAB PHOTON ENERGY (MEV)
0.6
0.4
0.2
0.0
-0.2
-0.4
-0.6
0
200
400
600
800
1000
1200
1400

FIGURE 21.8

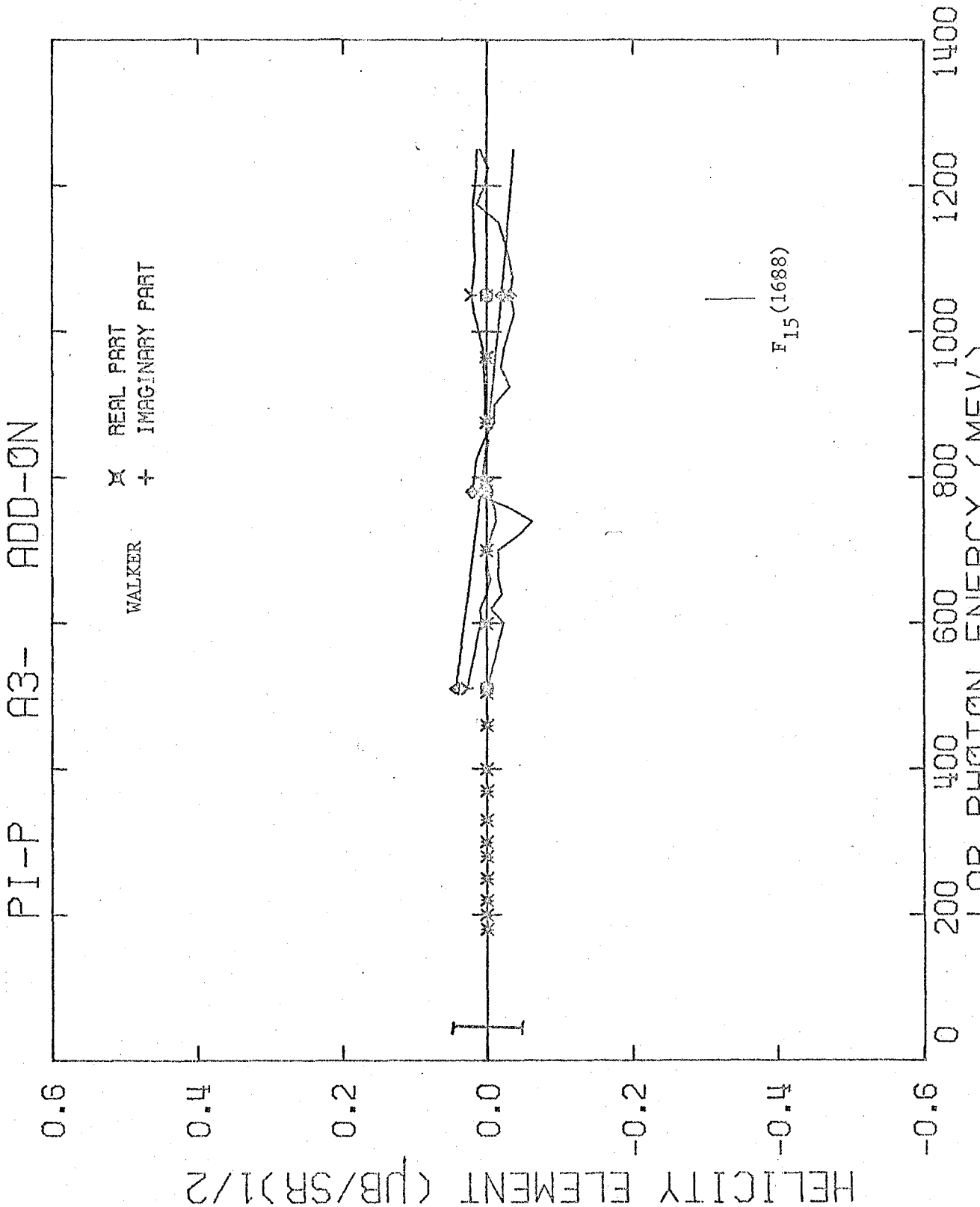
PI-P A3- ADD-ON
WALKER
REAL PART
IMAGINARY PART
$F_{15}(1688)$
HELICITY ELEMENT (UB/SR)1/2
LAB PHOTON ENERGY (MEV)
0.6
0.4
0.2
0.0
-0.2
-0.4
-0.6
0
200
400
600
800
1000
1200
1400

FIGURE 21.9

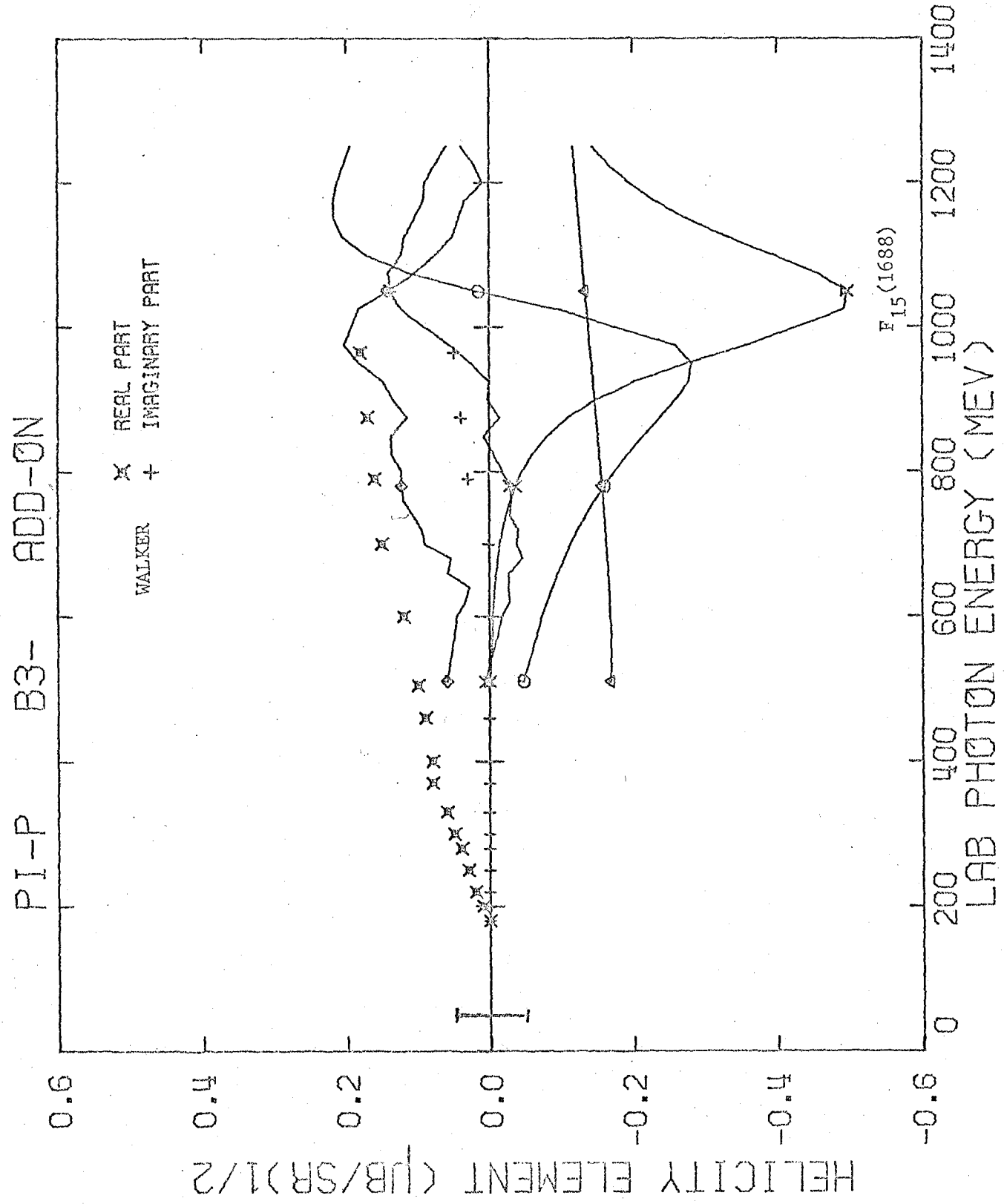
PI-P B3- ADD-ON
WALKER
REAL PART
IMAGINARY PART
$F_{15}(1688)$
HELICITY ELEMENT (UB/SR)1/2
LAB PHOTON ENERGY (MEV)
0.6
0.4
0.2
0.0
-0.2
-0.4
-0.6
0
200
400
600
800
1000
1200
1400

FIGURE 21.10

Finally, this π^- fit seems to want to reduce the amplitude of the B_{3-} resonant element (Figure 21.10) which corresponds to the $F_{15}(1688)$ resonance, helicity 3/2 component. The quark model (1) predicts that this resonant element is zero, and it is interesting to note that the fit is pushing the B_{3-} amplitude in the right direction to agree with the model. However, the amplitude apparently does not go completely to zero. The smallness of the $F_{15}(1688)$ in this analysis appears to be directly related to the smallness of the π^- cross section compared to the π^+ cross section at $k_\gamma^{lab} = 1000$ MeV.

The A_{1-} add-on element (Figure 21.2) wants to add a significant imaginary part in the region of the $P_{11}(1470)$ resonance. However, the real part of the add-on amplitude does not have the correct behavior for a negative resonance amplitude, and thus a resonance interpretation of the add-on amplitude is dubious. I have set the initial value of the P_{11} resonance to -0.250 instead of zero as in Walker's paper. Walker had the same problem with the P_{11} and he noted that the A_{1-} resonant amplitude was poorly determined for π^- photoproduction. In any case, despite my insertion of the resonance and along with an already negative add-on amplitude, this fit wants to add even more negative imaginary part.

There seems to be very little resonant behavior for the A_{2+} and B_{2+} helicity elements (Figures 21.7 and 21.8). Thus, I leave the amplitudes for the $D_{15}(1670)$ resonance at Walker's values.

Furthermore, the data are too poor to determine any definite amplitudes for the $S_{31}(1650)$, $D_{33}(1670)$, and $S_{11}(1700)$ all of which were left out of Walker's analysis.

I have done a final fit with changes to the resonances as given in Table 9. Plots of the add-on and of the total helicity elements which resulted from the fit are given in Appendix IX. The cross sections produced by this fit are the curves plotted through the final angular distributions (Figure 11) of this π^- experiment.

The fitted proton polarizations are plotted at 90° for comparison with the data in Figure 22 while the fitted beam asymmetries and experimental beam asymmetry data at 90° are plotted in Figure 23. The fit to the asymmetries is very good while the fit to the polarizations is as good as can be expected with the poor consistency of the data. It should be noted that the smoothness of the polarization and asymmetry fits is due to the fact that interpolated smooth values of data were used at each energy of the fit.

TABLE 9

Resonance	$I\ J^P$	Designation	Helicity Element	A^+ Walker	A^+ This Fit	A° Walker	A^- Walker	A^- This Fit
$\Delta(1236)$ $\Gamma=120$	$\frac{3}{2}\ \frac{3}{2}^+$	P_{33}	A_{1+}	1.000		1.414	1.000	
			B_{1+}	-2.430		-3.430	-2.430	
$N(1470)$ $\Gamma=230$	$\frac{1}{2}\ \frac{1}{2}^+$	P_{11}	A_{1-}	-0.250	-0.400	0.177	0.	?
$N(1520)$ $\Gamma=120$	$\frac{1}{2}\ \frac{3}{2}^-$	D_{13}	A_{2-}	-0.200		0.140	0.	0.300
			B_{2-}	-1.320		0.940	-1.150	
$N(1535)$ $\Gamma=120$	$\frac{1}{2}\ \frac{1}{2}^-$	S_{11}	A_{0+}	-0.650	?	0.460	-0.800	+0.250 (1520 MeV)
$\Delta(1650)$ $\Gamma=150$	$\frac{3}{2}\ \frac{1}{2}^-$	S_{31}	A_{0+}	0.		0.	0.	
$N(1670)$ $\Gamma=140$	$\frac{1}{2}\ \frac{5}{2}^-$	D_{15}	A_{2+}	0.		0.	0.	
			B_{2+}	0.141		-0.100	0.141	
$\Delta(1670)$ $\Gamma=225$	$\frac{3}{2}\ \frac{3}{2}^-$	D_{33}	A_{2-}	0.		0.	0.	
			B_{2-}	0.		0.	0.	
$N(1688)$ $\Gamma=125$	$\frac{1}{2}\ \frac{5}{2}^+$	F_{15}	A_{3-}	0.		0.	0.	
			B_{3-}	-0.600	-0.500	0.425	-0.500	-0.200
$N(1700)$ $\Gamma=250$	$\frac{1}{2}\ \frac{1}{2}^-$	S_{11}	A_{0+}	0.		0.	0.	

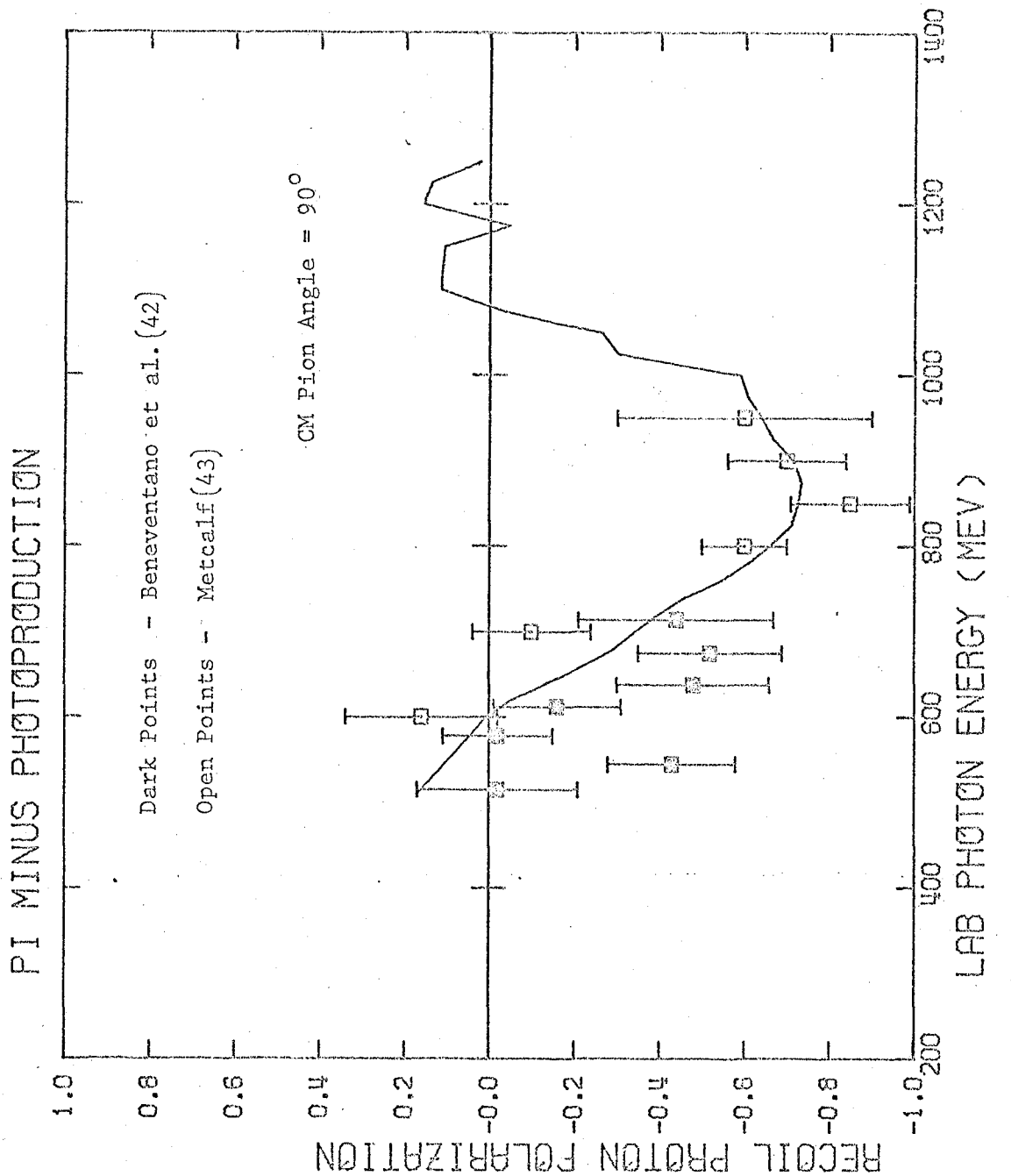
PI MINUS PHOTOPRODUCTION
Dark Points - Beneventano et al.(42)
Open Points - Metcalf(43)
CM Pion Angle = 90°
RECOIL PROTON POLARIZATION
LAB PHOTON ENERGY (MEV)
1.0
0.8
0.6
0.4
0.2
-0.0
-0.2
-0.4
-0.6
-0.8
-1.0
200
400
600
800
1000
1200
1400

FIGURE 22

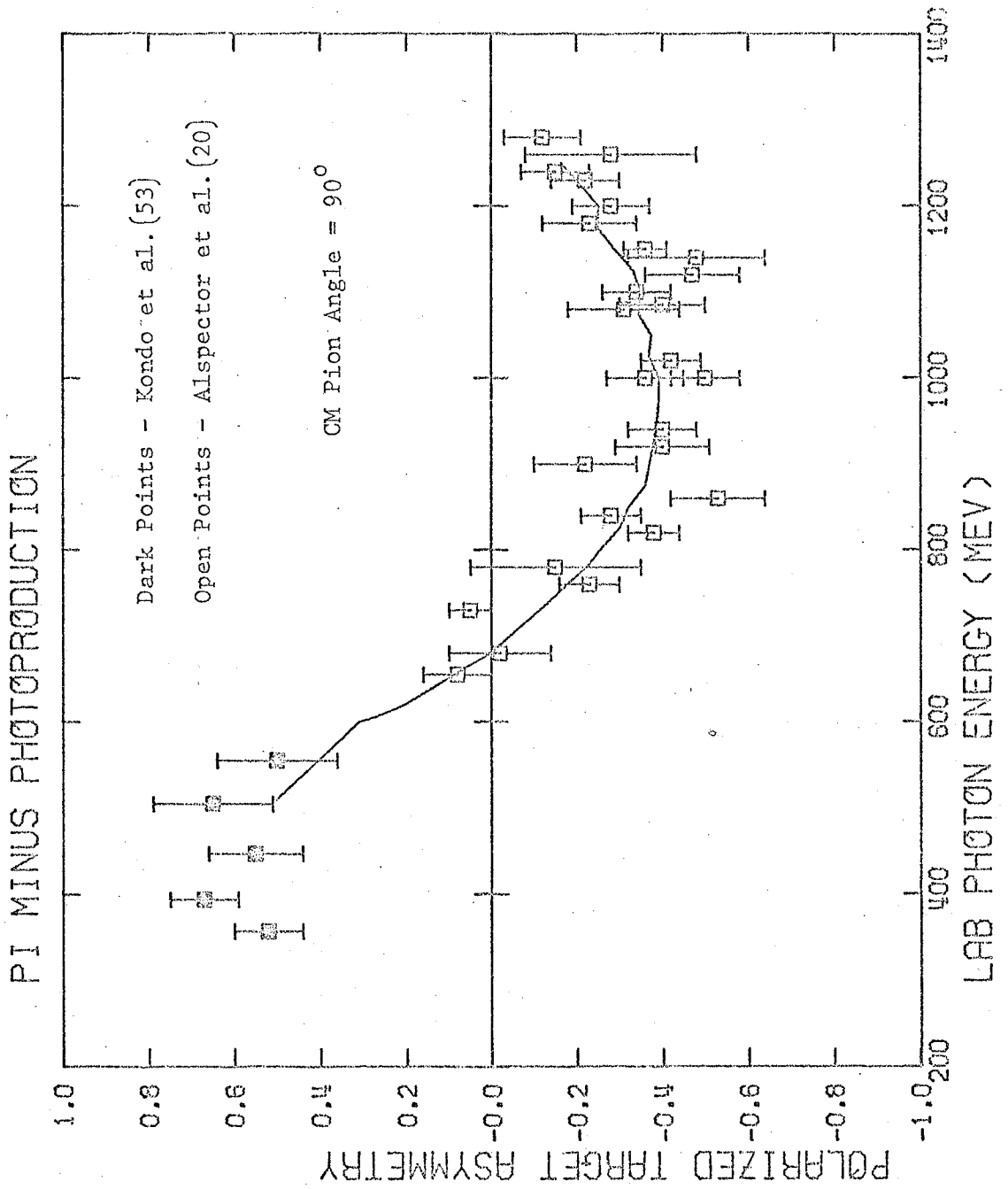
PI MINUS PHOTOPRODUCTION
Dark Points - Kondo et al.(53)
Open Points - Alspector et al.(20)
CM Pion Angle = 90°
POLARIZED TARGET ASYMMETRY
LAB PHOTON ENERGY (MEV)
1.0
0.8
0.6
0.4
0.2
-0.0
-0.2
-0.4
-0.6
-0.8
-1.0
200
400
600
800
1000
1200
1400

FIGURE 23

a) The zero degree cross section.

The zero degree cross section obtained from this fit and the one obtained from a Moravcsik fit (Figure 13) are almost identical. The main characteristic of the zero degree cross section for π^- photoproduction is the sharp dropoff at $k_\gamma^{lab} = 700$ MeV. A possible explanation for this sharp dropoff is the interference of a positive resonance (real part) with a positive background (real part) or of a negative resonance with a negative background. While this may be partially the case, my final fit seems to indicate that most of the dropoff is due to the add-on (background) elements. This clouds the physical interpretation of the 0° behavior of the cross section. Figure 24 is a plot of the total helicity amplitude H_2 (see Appendix V for the definition of the helicity amplitudes H_i) at 0° and of its various components. The total real and imaginary parts (square and "x") both have the above behavior at 700 MeV, although the behavior is not so striking in the amplitude as it is in the cross section. The interference (sum) of all the resonant components of the helicity 1/2 elements ($A_{\ell\pm}$) produces the resonant component (real and imaginary parts) of H_2 (octogon and "cradle" curves) which has a slight dropoff effect. The interference of all the add-on components of the helicity elements produces the greatest dropoff, especially in the real part ("diamond" curve).

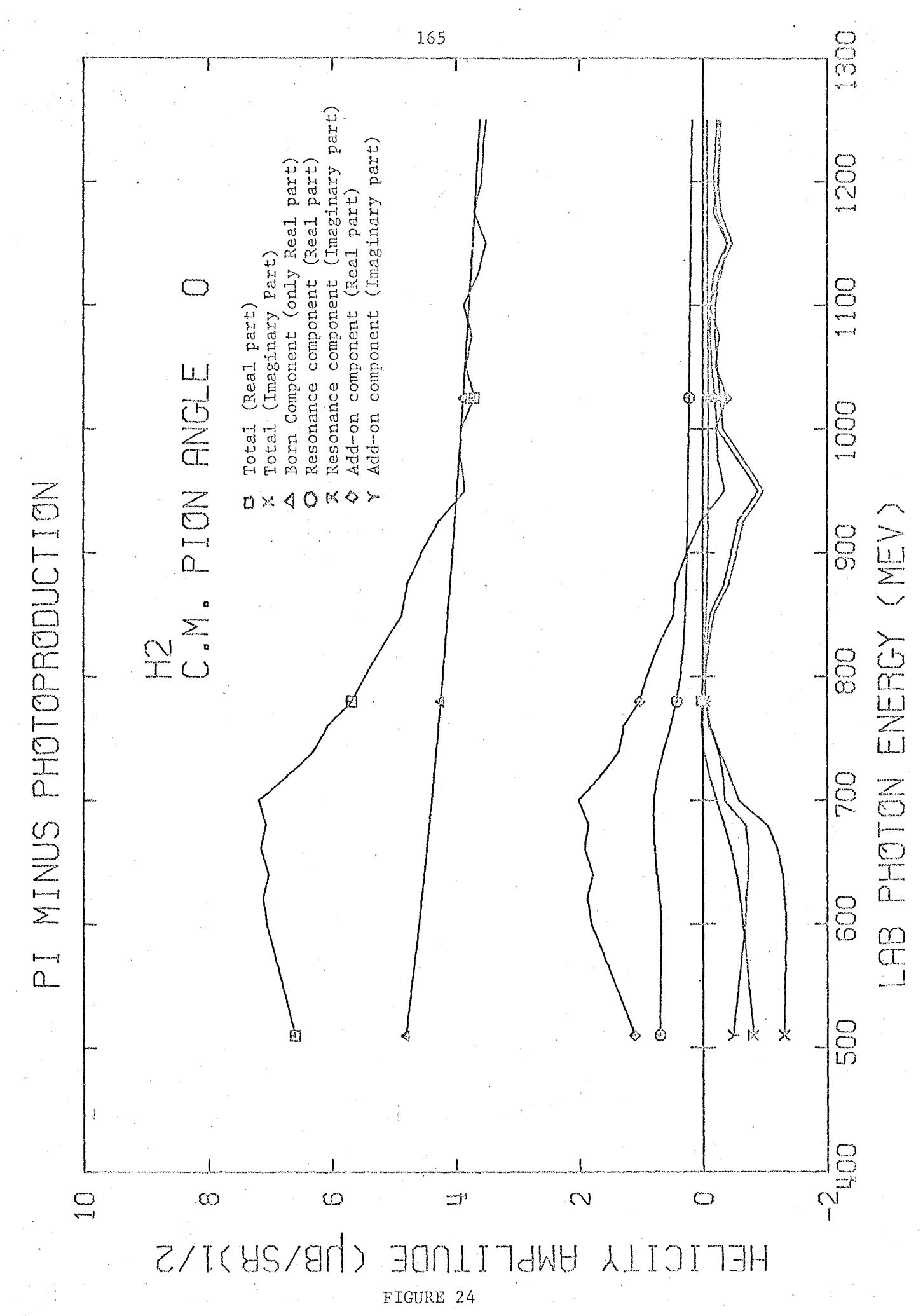
PI MINUS PHOTOPRODUCTION
H2
C.M. PION ANGLE 0
Total (Real part)
Total (Imaginary Part)
Born Component (only Real part)
Resonance component (Real part)
Resonance component (Imaginary part)
Add-on component (Real part)
Add-on component (Imaginary part)
HELICITY AMPLITUDE (UB/SR)1/2
LAB PHOTON ENERGY (MEV)
10
8
6
4
2
0
-2
400
500
600
700
800
900
1000
1100
1200
1300

FIGURE 24

It should not be surprising that the main component of the real part of H_2 at 0^o is that due to the Born approximation (triangles) which is characterized by a forward peak.

b) The deuterium cross section.

After fitting what we hope are the true neutron cross sections, we can calculate what the deuterium cross section should be from the final state model of Chew and Lewis (45). The relationship between the deuterium cross section, neutron cross section, "spin-flip" cross section, and "spin-non-flip" cross section (see Appendix V) is illustrated in Figure 25. The spin-non-flip cross section goes to zero at forward and backward angles while the spin-flip cross section approaches the neutron cross section at these angles. The deuterium cross section is reduced at forward angles and gradually merges with the neutron cross section at about 60^o. A comparison of the deuterium cross section calculated from the fit and the deuterium experimental cross section data at 10^o is given in Figure 26. The agreement is excellent except at the lowest energies. This leads to the conclusion that (at least above 650 MeV) the "ratio" cross sections are probably a good approximation to the true neutron cross sections. Also, most of the final state effects seem to be accounted for by the Pauli exclusion principle.

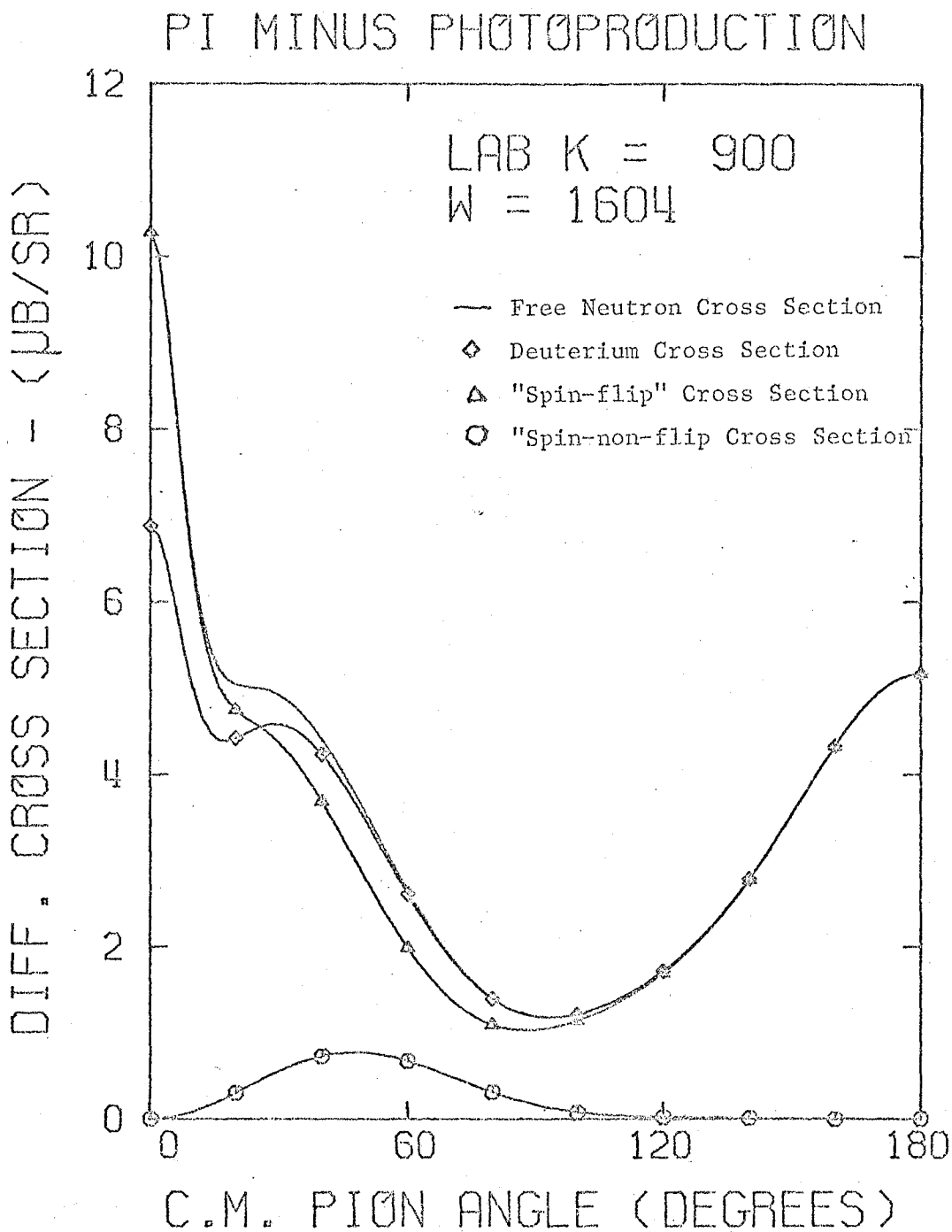
PI MINUS PHOTOPRODUCTION
LAB K = 900
W = 1604
Free Neutron Cross Section
Deuterium Cross Section
"Spin-flip" Cross Section
"Spin-non-flip Cross Section
DIFF. CROSS SECTION - (UB/SR)
C.M. PION ANGLE (DEGREES)
0
2
4
6
8
10
12
0
60
120
180

FIGURE 25

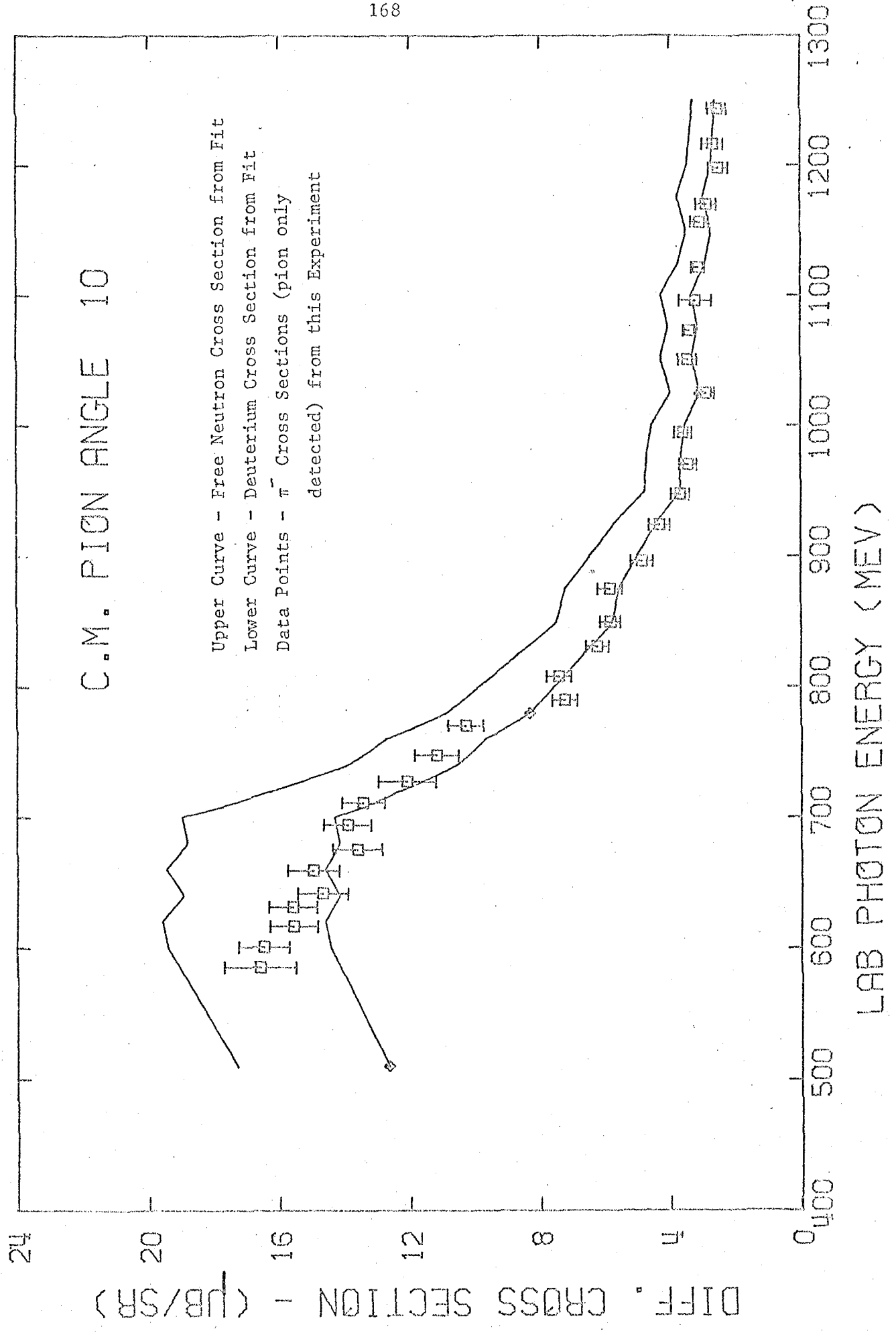
PI MINUS PHOTOPRODUCTION
C.M. PION ANGLE 10
Upper Curve - Free Neutron Cross Section from Fit
Lower Curve - Deuterium Cross Section from Fit
Data Points - π⁻ Cross Sections (pion only detected) from this Experiment
DIFF. CROSS SECTION - (UB/SR)
LAB PHOTON ENERGY (MEV)
0
4
8
12
16
20
24
400
500
600
700
800
900
1000
1100
1200
1300

FIGURE 26

2. π^+ Photoproduction.

I have also done a preliminary fit of π^+ photoproduction from 425 MeV to 1269 MeV using the data listed in Table 7. Since the data for this reaction had been fairly comprehensive at the time of Walker's analysis, I did not expect much change in the resonance parameters. However, as with the π^- analysis, there were some striking effects (Fig. 27) mainly due to the addition of new polarization and target asymmetry data.

The most interesting effect was in the A_{1-} amplitude at the energy corresponding to the $P_{11}(1470)$ resonance. The add-on imaginary part had a large hump of amplitude equal to the initial resonance amplitude (-0.250). The real part of the add-on element had the correct behavior for a negative resonance but with a much smaller amplitude. I have thus increased the P_{11} amplitude to -0.400 which is enough to cancel the behavior of the real add-on amplitude.

The only other definite resonant behavior was in the B_{3-} element, corresponding to the $F_{15}(1688)$ resonance, helicity 3/2 component. A small decrease in this amplitude was indicated; I have changed the value from -.600 to -.500.

There are two other possible cases of resonant behavior in the add-on elements. One is the significant deviation

FIGURE 27

INITIAL FIT OF ADD-ON HELICITY ELEMENTS (BACKGROUND) FOR π^+ PHOTOPRODUCTION

There are ten graphs for the ten lowest order partial waves A_{0+}, A_{1-}, A_{1+}, B_{1+}, A_{2-}, B_{2-}, A_{2+}, B_{2+}, A_{3-}, B_{3-}. Refer to Table 8 (page 143) for the properties of these helicity elements. Refer to Table 9 (page 161) for a list of resonances and their associated helicity elements. Refer to page 148 for key to symbols on graphs.

Artificial errors assigned to the Walker helicity elements are shown on the left of each graph. They are ±.1 for the j = 1/2 elements, and ±.05 for the j = 3/2 and j = 5/2 elements.

The energies used in the fit were as follows: 425, 450, 475, 500, 525, 550, 603, 635, 663, 698, 733, 772, 813, 857, 902, 977, 1002, 1028, 1056, 1102, 1131, 1174, 1204, 1235, and 1269 MeV.

The experiments used in this fit are listed in Table 7.

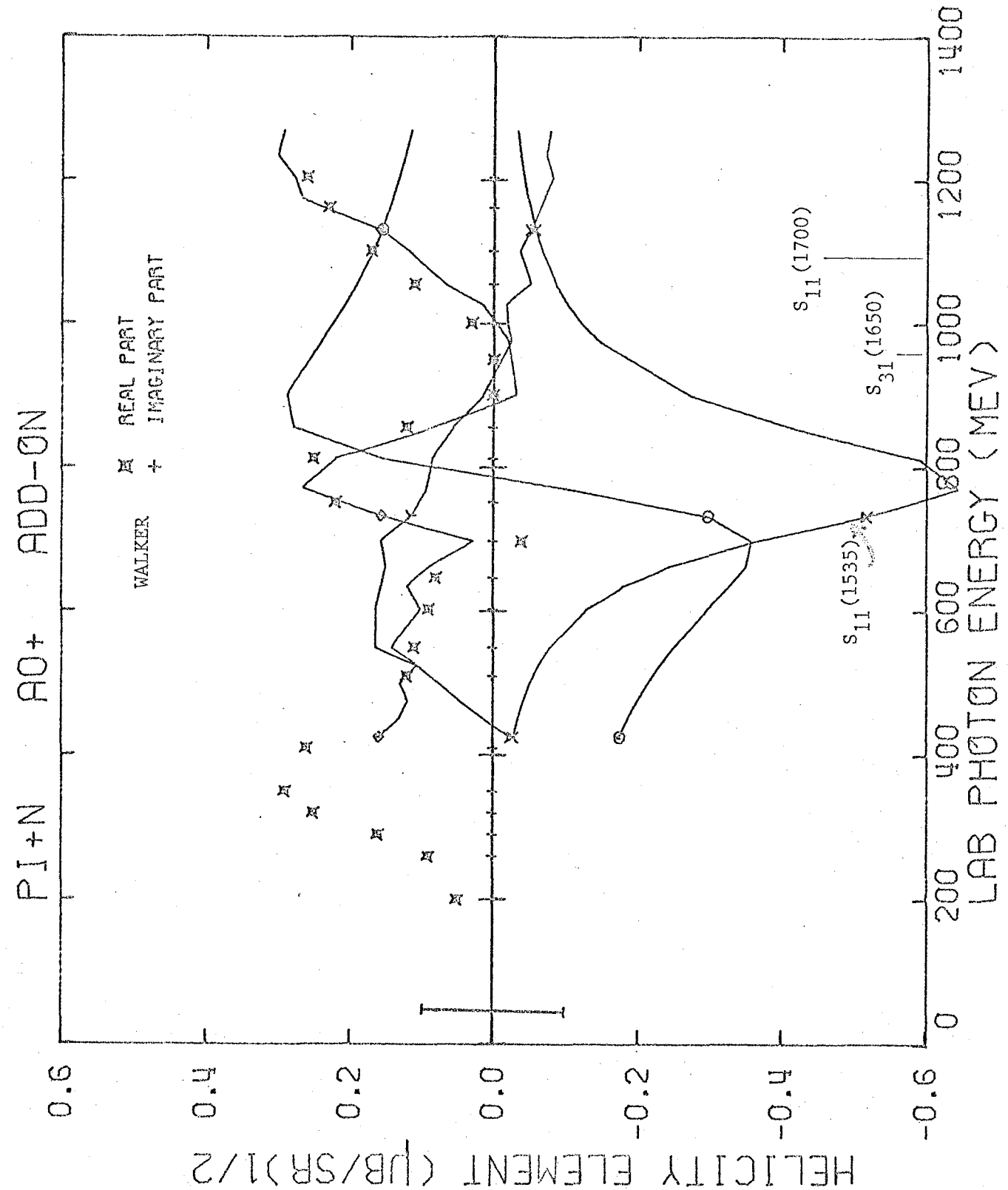
PI+N A0+ ADD-ON
WALKER
REAL PART
IMAGINARY PART
$S_{11}(1700)$
$S_{31}(1650)$
$S_{11}(1535)$
HELICITY ELEMENT (UB/SR)1/2
LAB PHOTON ENERGY (MEV)
0.6
0.4
0.2
0.0
-0.2
-0.4
-0.6
0
200
400
600
800
1000
1200
1400

FIGURE 27.1

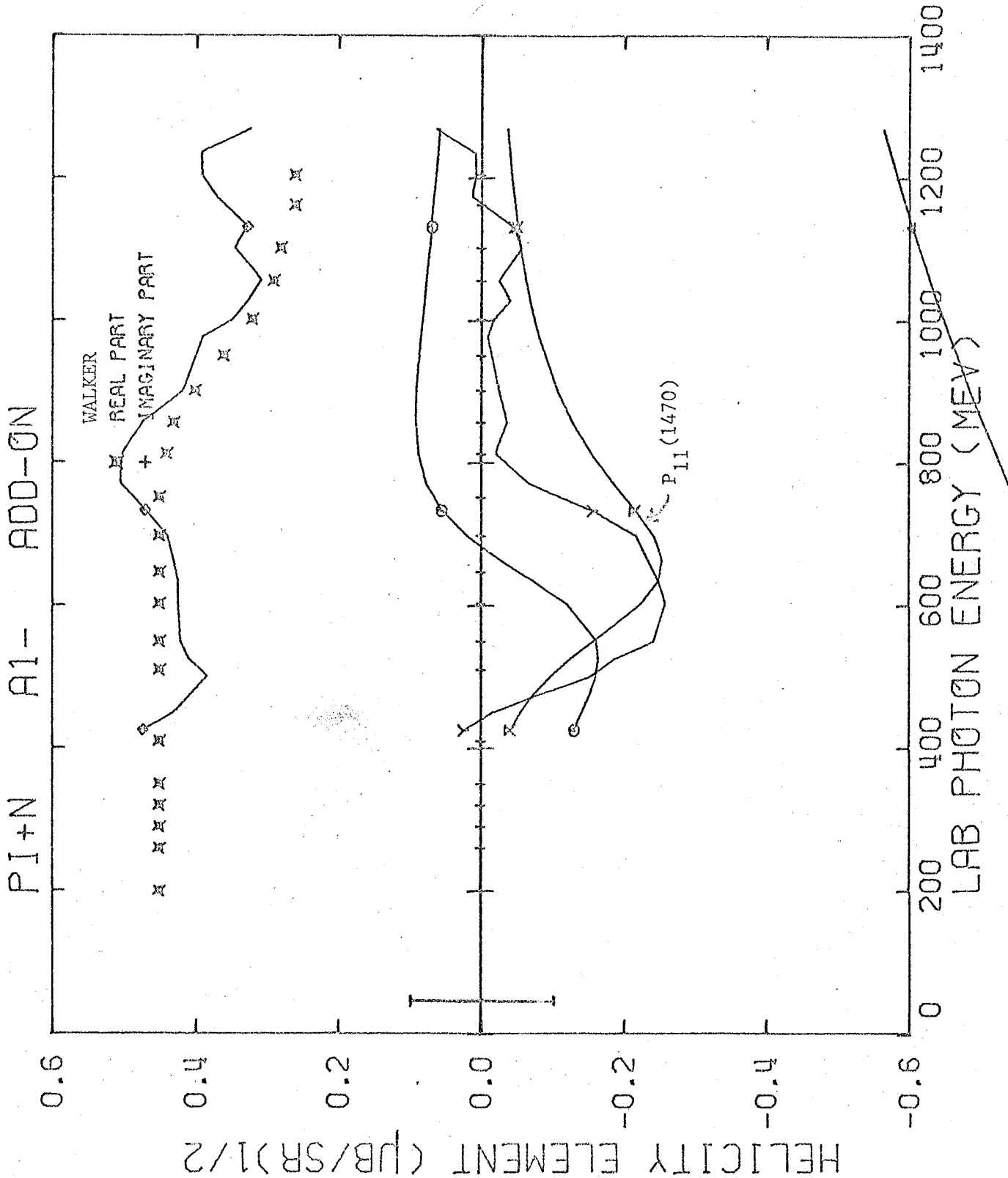
PI+N A1- ADD-ON
WALKER
REAL PART
IMAGINARY PART
$P_{11}(1470)$
HELICITY ELEMENT (UB/SR)1/2
LAB PHOTON ENERGY (MEV)
0.6
0.4
0.2
0.0
-0.2
-0.4
-0.6
0
200
400
600
800
1000
1200
1400

FIGURE 27.2

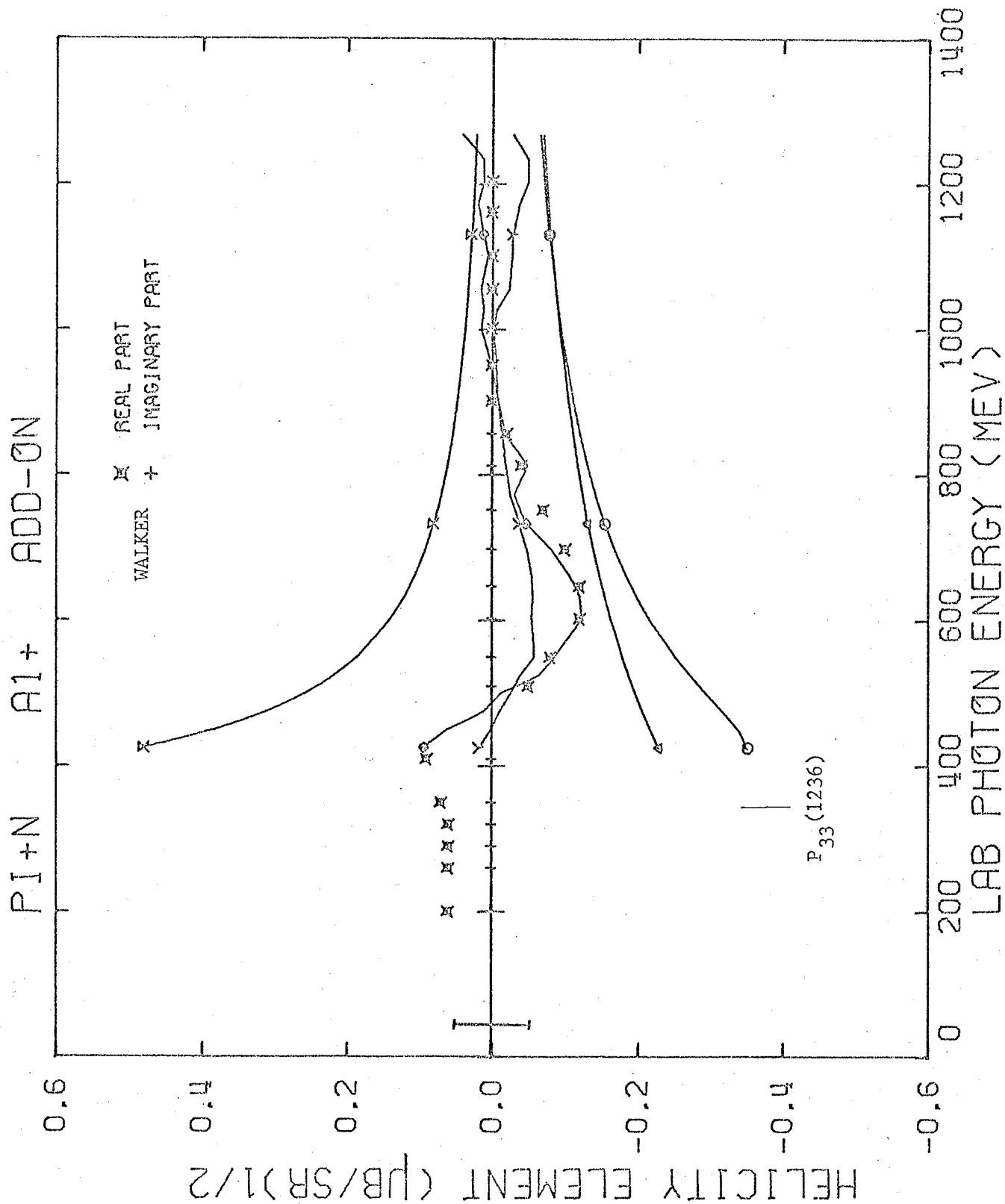
PI+N A1+ ADD-ON
REAL PART
IMAGINARY PART
WALKER
$P_{33}(1236)$
HELICITY ELEMENT (UB/SR)1/2
LAB PHOTON ENERGY (MEV)
0.6
0.4
0.2
0.0
-0.2
-0.4
-0.6
0
200
400
600
800
1000
1200
1400

FIGURE 27.3

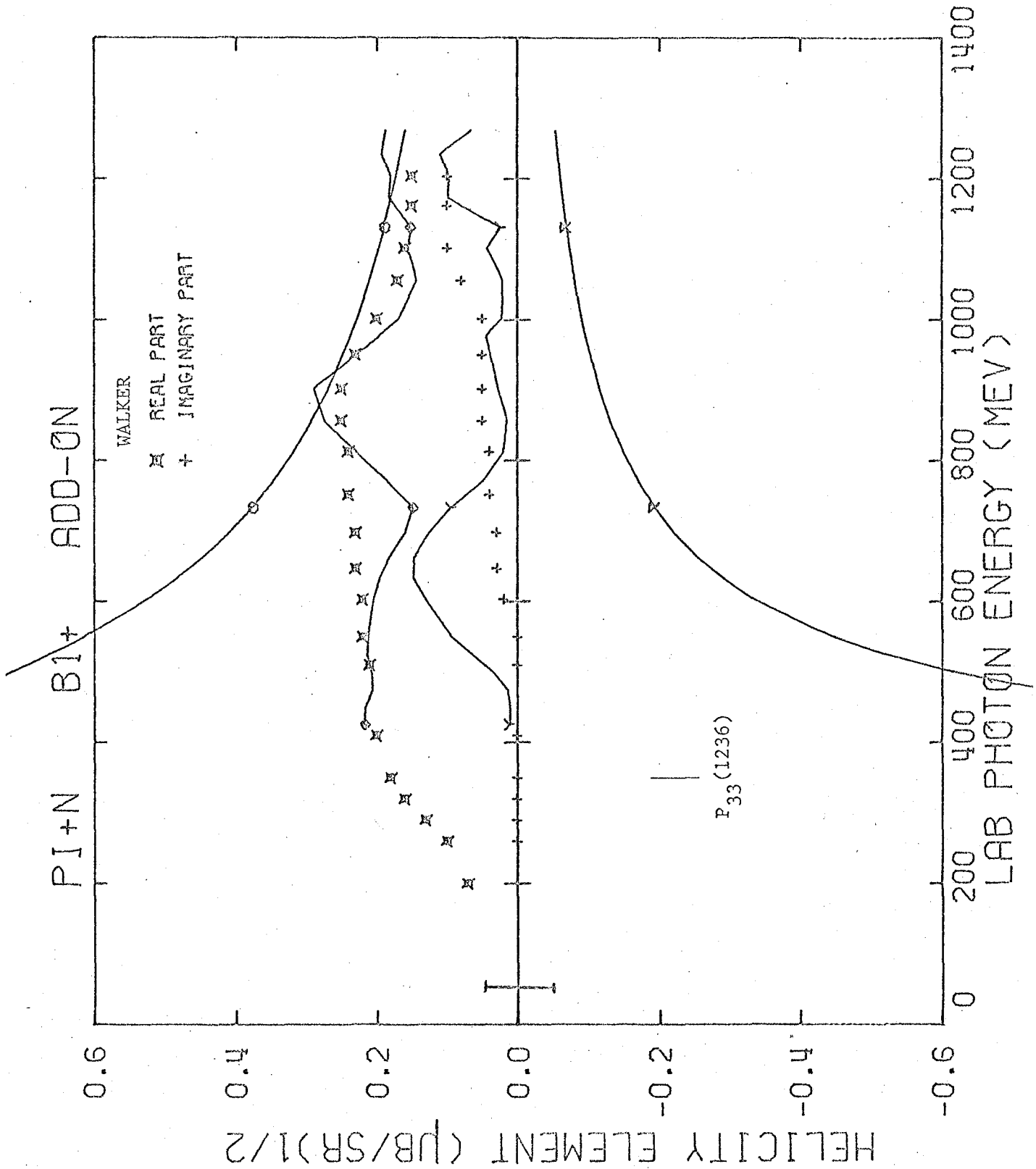
PI+N B1+ ADD-ON
WALKER
REAL PART
IMAGINARY PART
$P_{33}(1236)$
HELICITY ELEMENT (UB/SR)1/2
LAB PHOTON ENERGY (MEV)
0.6
0.4
0.2
0.0
-0.2
-0.4
-0.6
0
200
400
600
800
1000
1200
1400

FIGURE 27.4

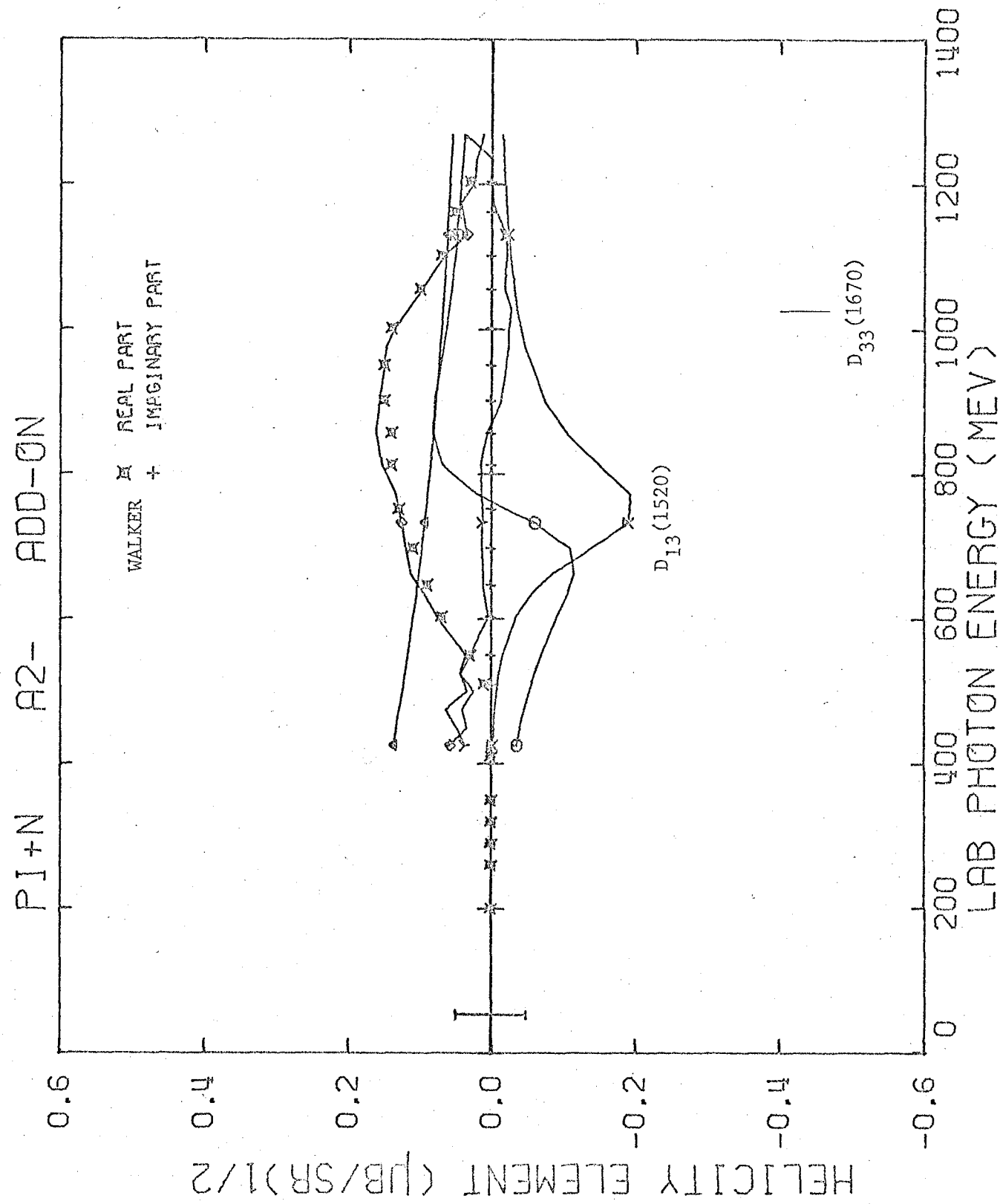
PI+N A2- ADD-ON
WALKER
REAL PART
IMAGINARY PART
$D_{13}(1520)$
$D_{33}(1670)$
HELICITY ELEMENT (UB/SR)1/2
LAB PHOTON ENERGY (MEV)
0.6
0.4
0.2
0.0
-0.2
-0.4
-0.6
0
200
400
600
800
1000
1200
1400

FIGURE 27.5

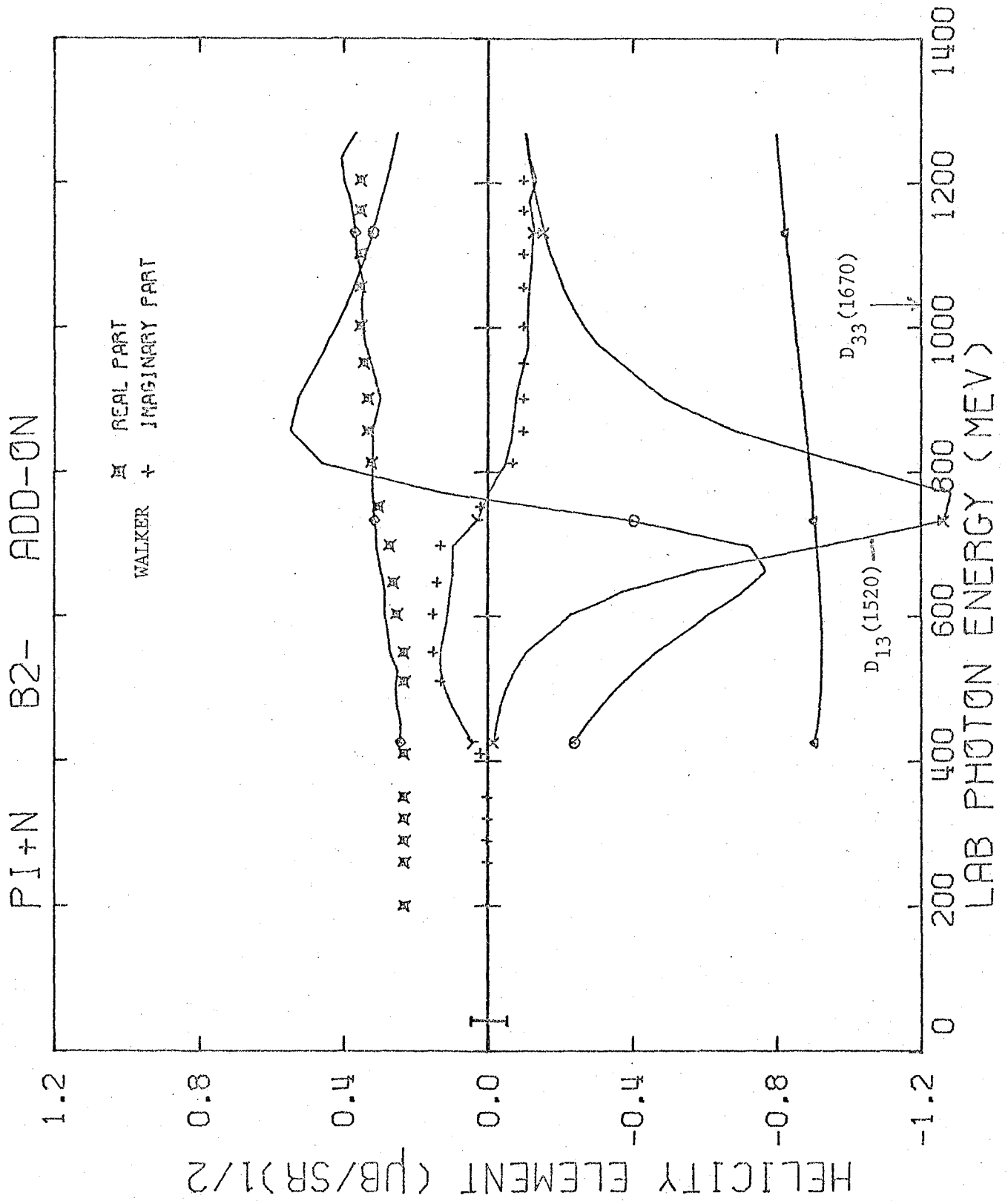
PI+N B2- ADD-ON
WALKER
REAL PART
IMAGINARY PART
$D_{33}(1670)$
$D_{13}(1520)$
HELICITY ELEMENT (UB/SR)1/2
LAB PHOTON ENERGY (MEV)
1.2
0.8
0.4
0.0
-0.4
-0.8
-1.2
0
200
400
600
800
1000
1200
1400

FIGURE 27.6

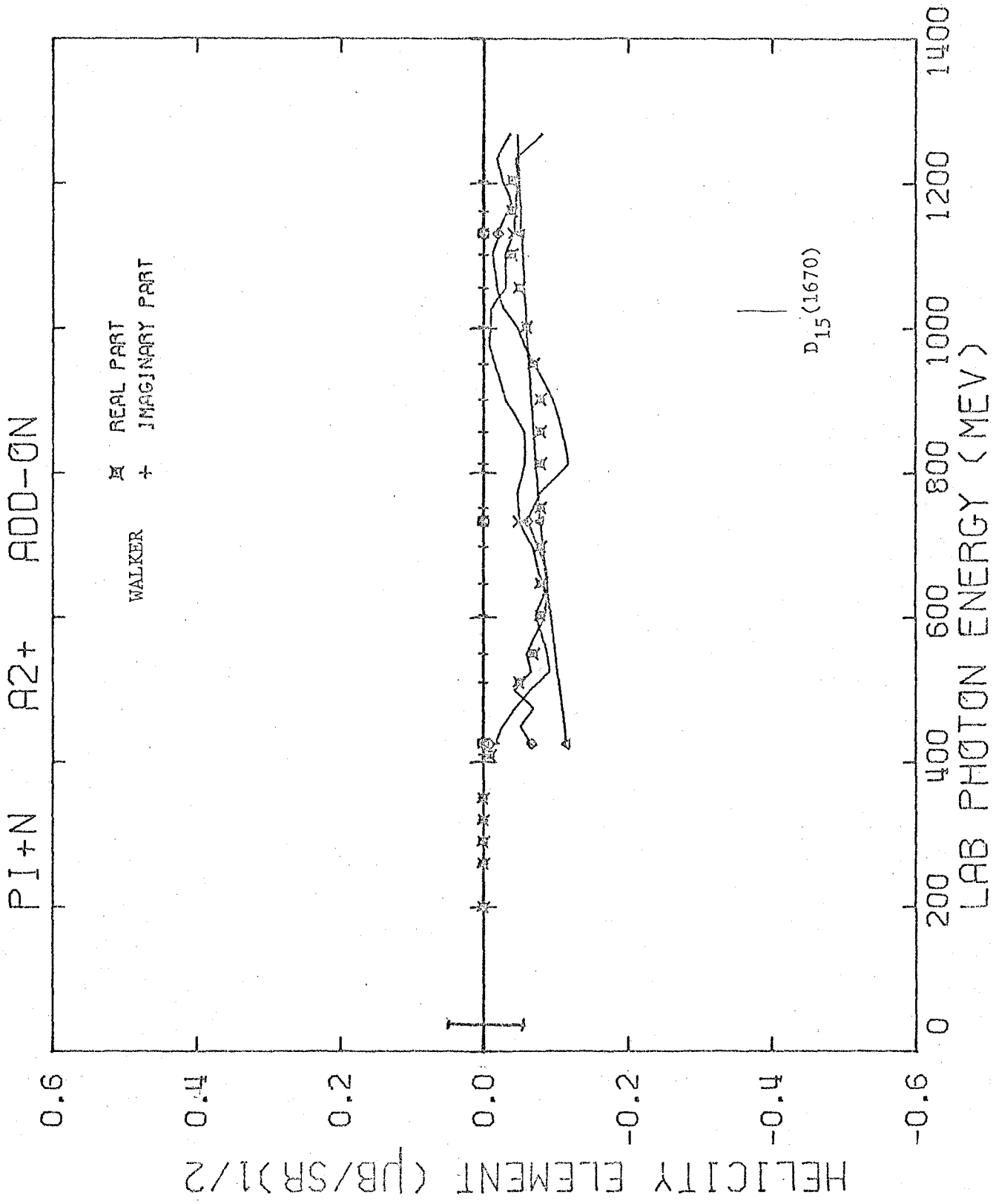
PI+N A2+ ADD-ON
WALKER
REAL PART
IMAGINARY PART
$D_{15}(1670)$
HELICITY ELEMENT (UB/SR)1/2
LAB PHOTON ENERGY (MEV)
0.6
0.4
0.2
0.0
-0.2
-0.4
-0.6
0
200
400
600
800
1000
1200
1400

FIGURE 27.7

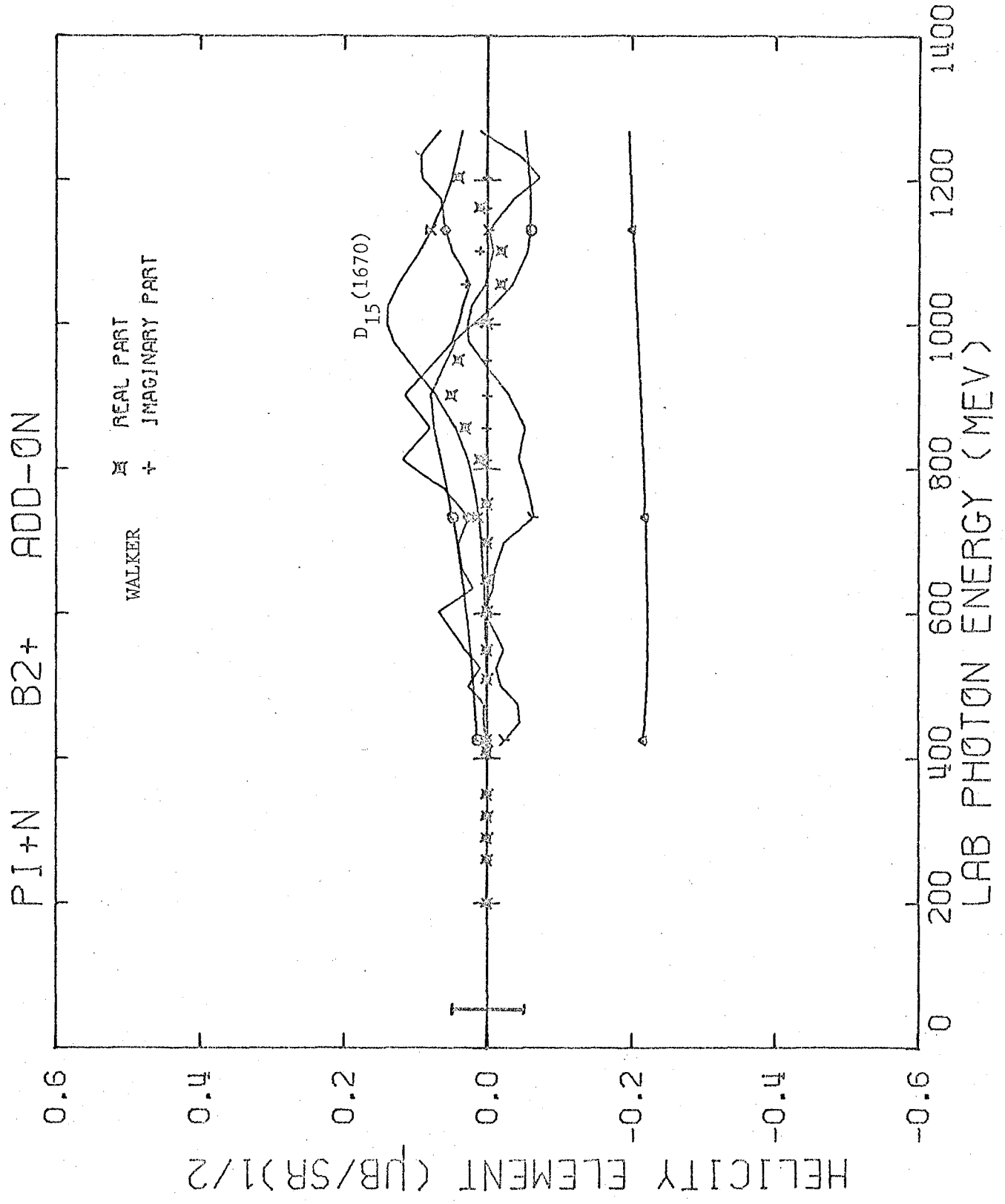
PI+N B2+ ADD-ON
WALKER
REAL PART
IMAGINARY PART
$D_{15}(1670)$
HELICITY ELEMENT (UB/SR)1/2
LAB PHOTON ENERGY (MEV)
0.6
0.4
0.2
0.0
-0.2
-0.4
-0.6
0
200
400
600
800
1000
1200
1400

FIGURE 27.8

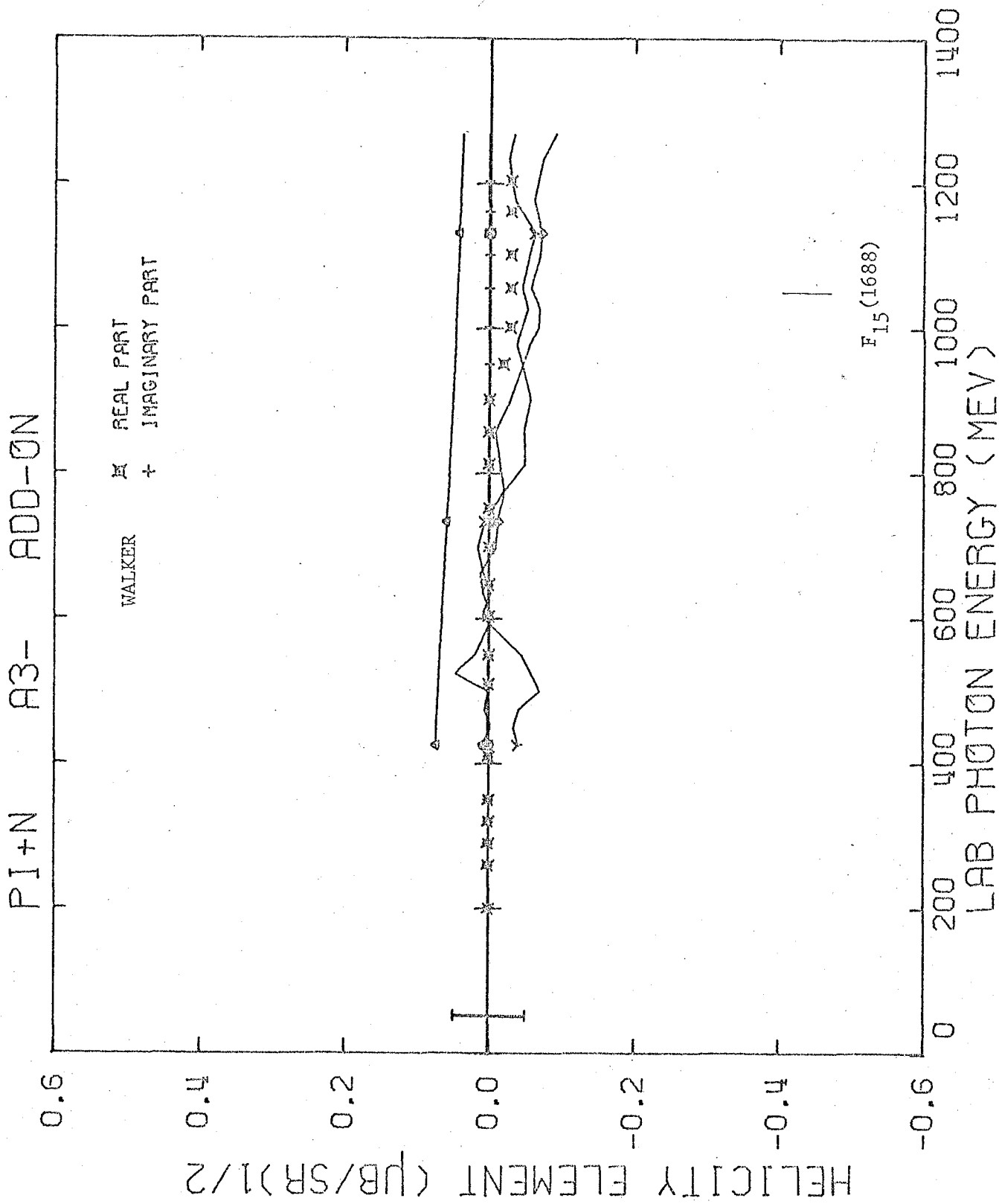
PI+N A3- ADD-ON
WALKER
REAL PART
IMAGINARY PART
$F_{15}(1688)$
HELICITY ELEMENT (UB/SR)1/2
LAB PHOTON ENERGY (MEV)
0.6
0.4
0.2
0.0
-0.2
-0.4
-0.6
0
200
400
600
800
1000
1200
1400

FIGURE 27.9

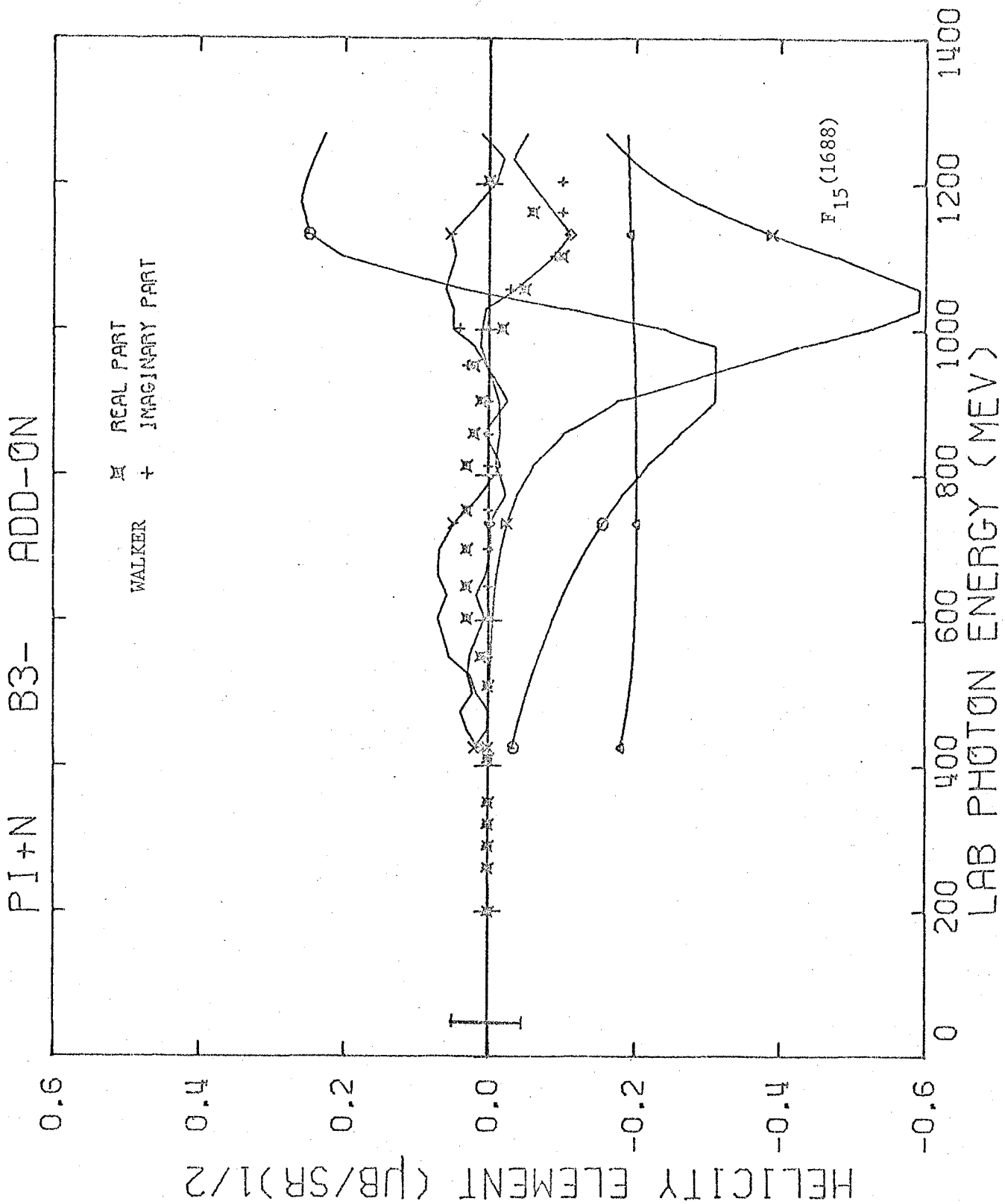
PI+N B3- ADD-ON
WALKER
REAL PART
IMAGINARY PART
$F_{15}(1688)$
HELICITY ELEMENT (UB/SR)1/2
LAB PHOTON ENERGY (MEV)
0.6
0.4
0.2
0.0
-0.2
-0.4
-0.6
0
200
400
600
800
1000
1200
1400

FIGURE 27.10

of the imaginary part of the A_{0+} element at an energy somewhat below that of the $S_{11}(1535)$ resonance. The presence of the jagged real part in Walker's solution, which was inserted to reproduce the cusp effect seen in the 0^{o} and 180^{o} data at the η threshold, makes the search for resonant behavior very difficult. Even so, it seems that a slight resonant behavior of the real add-on part is indicated, since the fitted solution is greater than Walker's solution below the center of the imaginary (add-on) hump, and the fitted solution is less than Walker's above the center of the hump. However, the differences are very small and probably do not justify changing the value of the resonance.

There may also be a slight resonant behavior in the B_{2+} element, corresponding to the $D_{15}(1670)$ resonance, helicity 3/2 component. There appears to be an imaginary background, with a slight resonant hump beneath the D_{15}. The "inverse" behavior of the imaginary part is not reassuring, however.

Unfortunately, there are several places where humps seem to be needed to fit the data but where no resonances are known to occur. At about 600 MeV photon energy, many of the elements have a hump in the real or imaginary parts. I have not had time to investigate this phenomenon fully and cannot make a statement as to its cause. I can only say that in

my final fit, where the humps are included, the fit and the data agree very well.

I have obtained a final fit of the π^+ reaction where I have used the altered values of the P_{11} and F_{15} given above. Plots of this fit (add-on and total helicity elements) may be found in Appendix IX.

The final fit to the available polarizations and asymmetries is shown in Figures 28 - 31. The agreement is not as good as in the π^- case, but is within the error bars.

Again, as in the π^- case, we can calculate the expected π^+ cross section from deuterium using the model of Chew and Lewis. A comparison of this calculation with the deuterium π^+ data at 10° (Figure 32) shows fair agreement. Thus it seems that most of the final state effects are due to the Pauli exclusion principle.

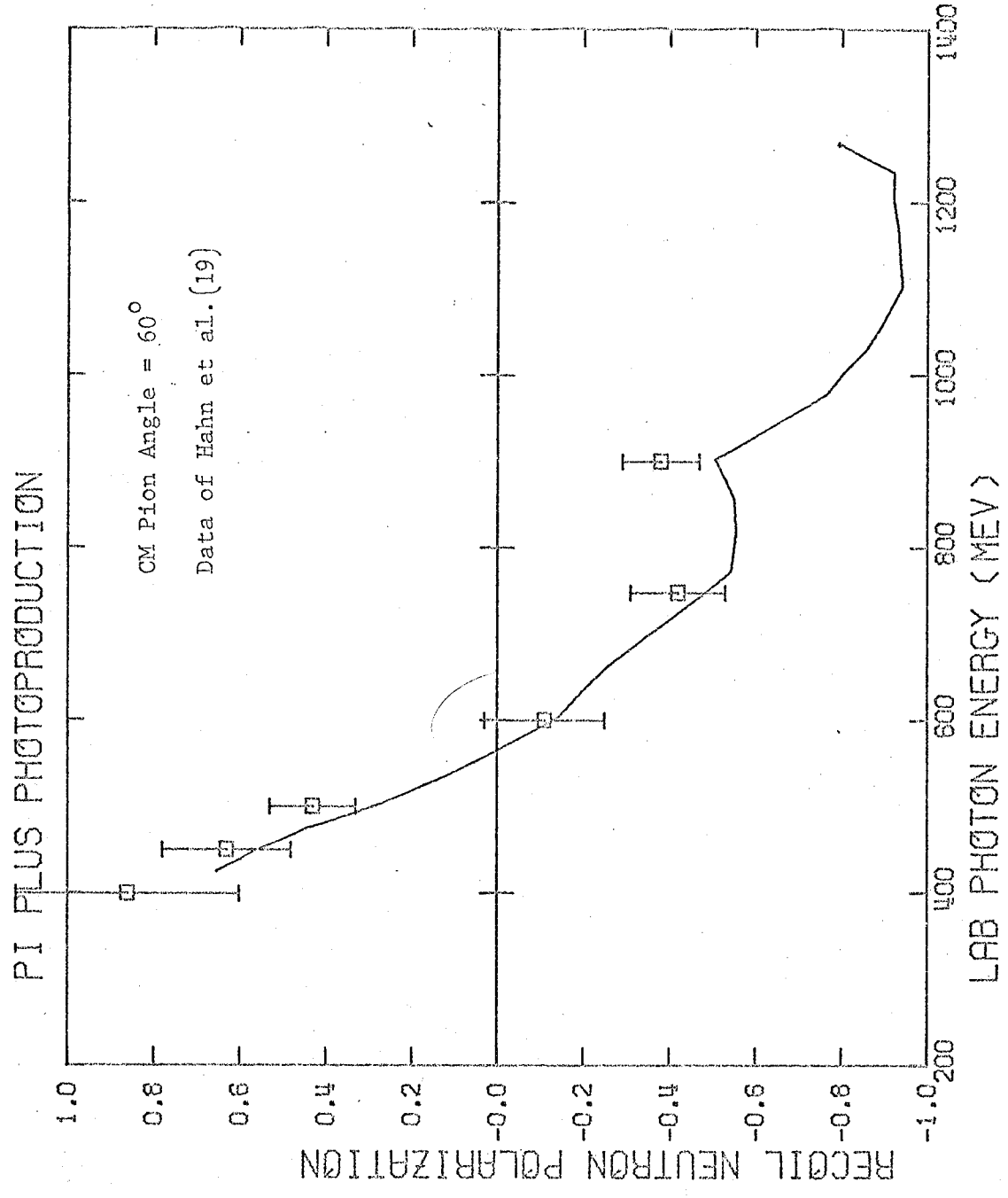
PI PLUS PHOTOPRODUCTION
CM Pion Angle = 60°
Data of Hahn et al.(19)
RECOIL NEUTRON POLARIZATION
LAB PHOTON ENERGY (MEV)
1.0
0.8
0.6
0.4
0.2
-0.0
-0.2
-0.4
-0.6
-0.8
-1.0
200
400
600
800
1000
1200
1400

FIGURE 28

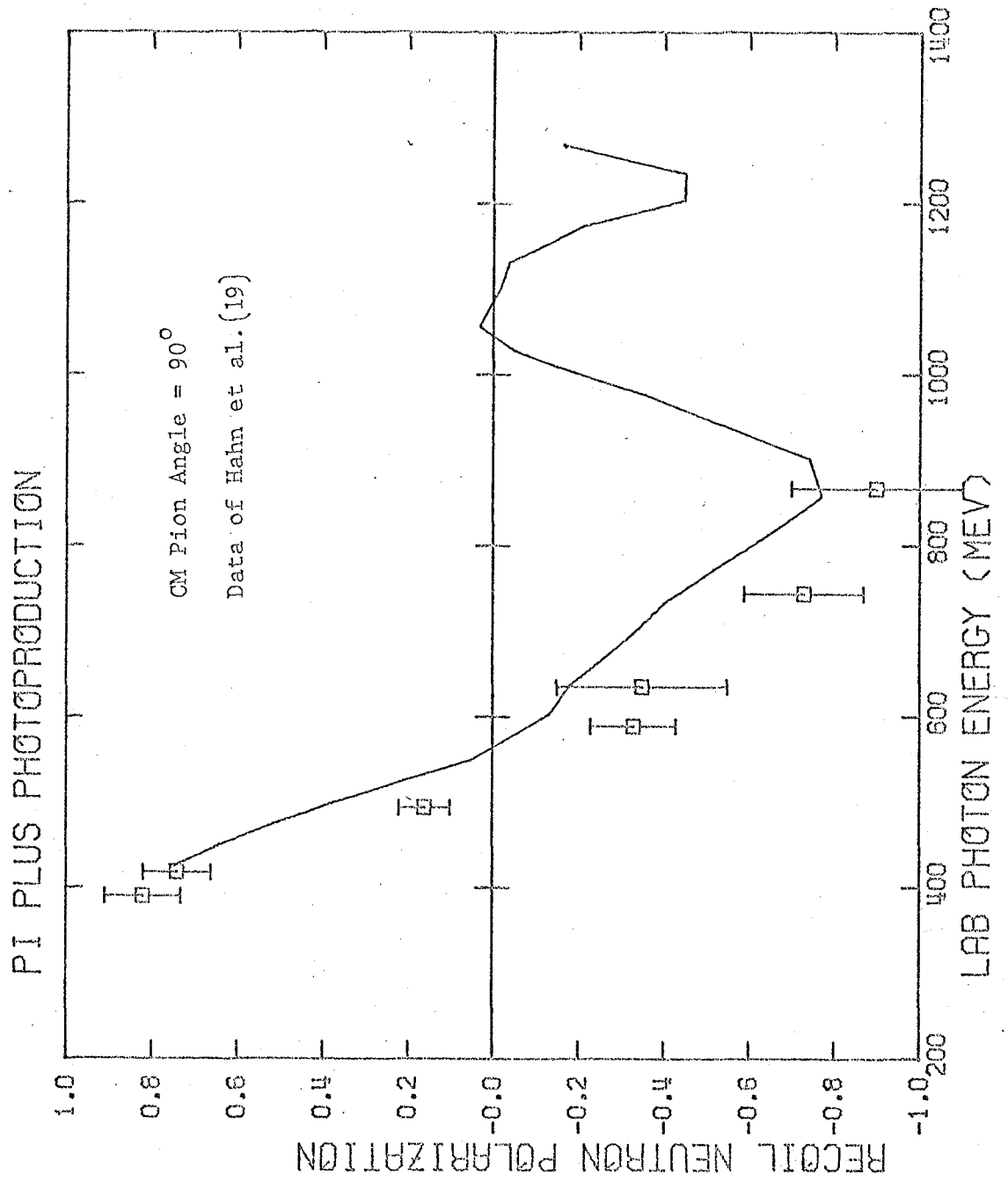
PI PLUS PHOTOPRODUCTION
CM Pion Angle = 90°
Data of Hahn et al.(19)
RECOIL NEUTRON POLARIZATION
LAB PHOTON ENERGY (MEV)
1.0
0.8
0.6
0.4
0.2
-0.0
-0.2
-0.4
-0.6
-0.8
-1.0
200
400
600
800
1000
1200
1400

FIGURE 29

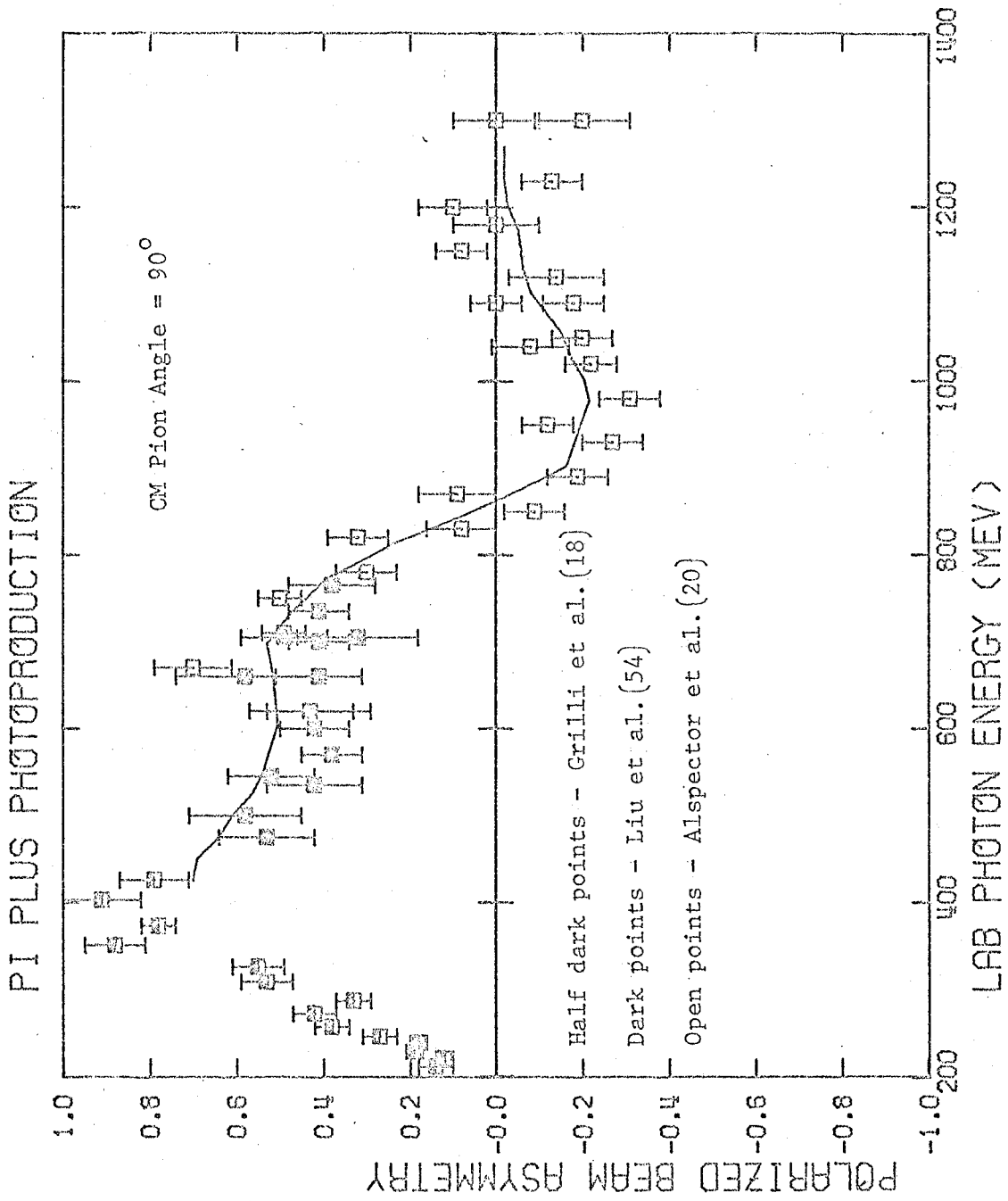
PI PLUS PHOTOPRODUCTION
CM Pion Angle = 90°
Half dark points - Grilli et al.(18)
Dark points - Liu et al.(54)
Open points - Alspector et al.(20)
POLARIZED BEAM ASYMMETRY
LAB PHOTON ENERGY (MEV)
1.0
0.8
0.6
0.4
0.2
-0.0
-0.2
-0.4
-0.6
-0.8
-1.0
200
400
600
800
1000
1200
1400

FIGURE 30

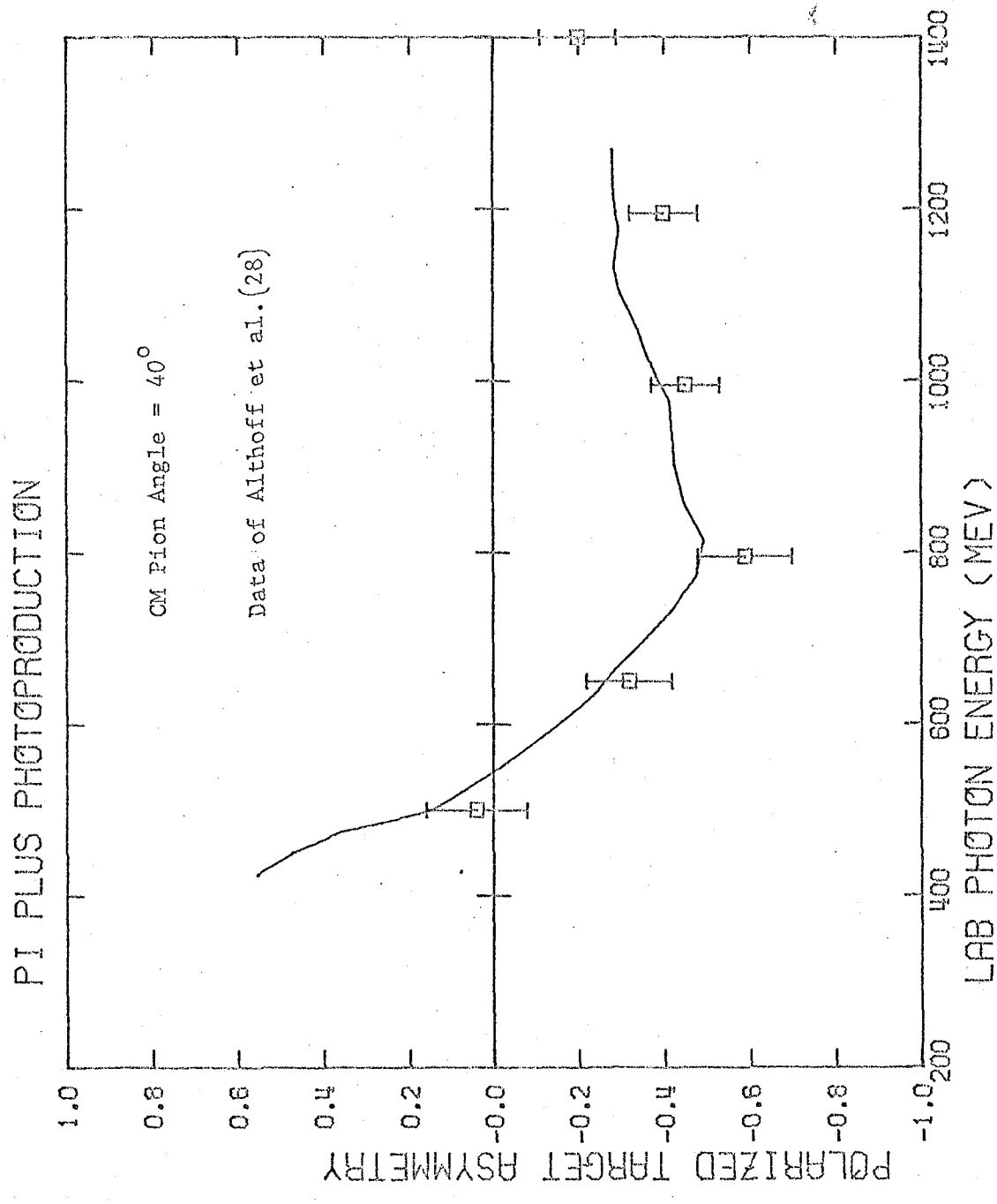
PI PLUS PHOTOPRODUCTION
CM Pion Angle = 40°
Data of Althoff et al.(28)
POLARIZED TARGET ASYMMETRY
LAB PHOTON ENERGY (MEV)
1.0
0.8
0.6
0.4
0.2
-0.0
-0.2
-0.4
-0.6
-0.8
-1.0
200
400
600
800
1000
1200
1400

FIGURE 31

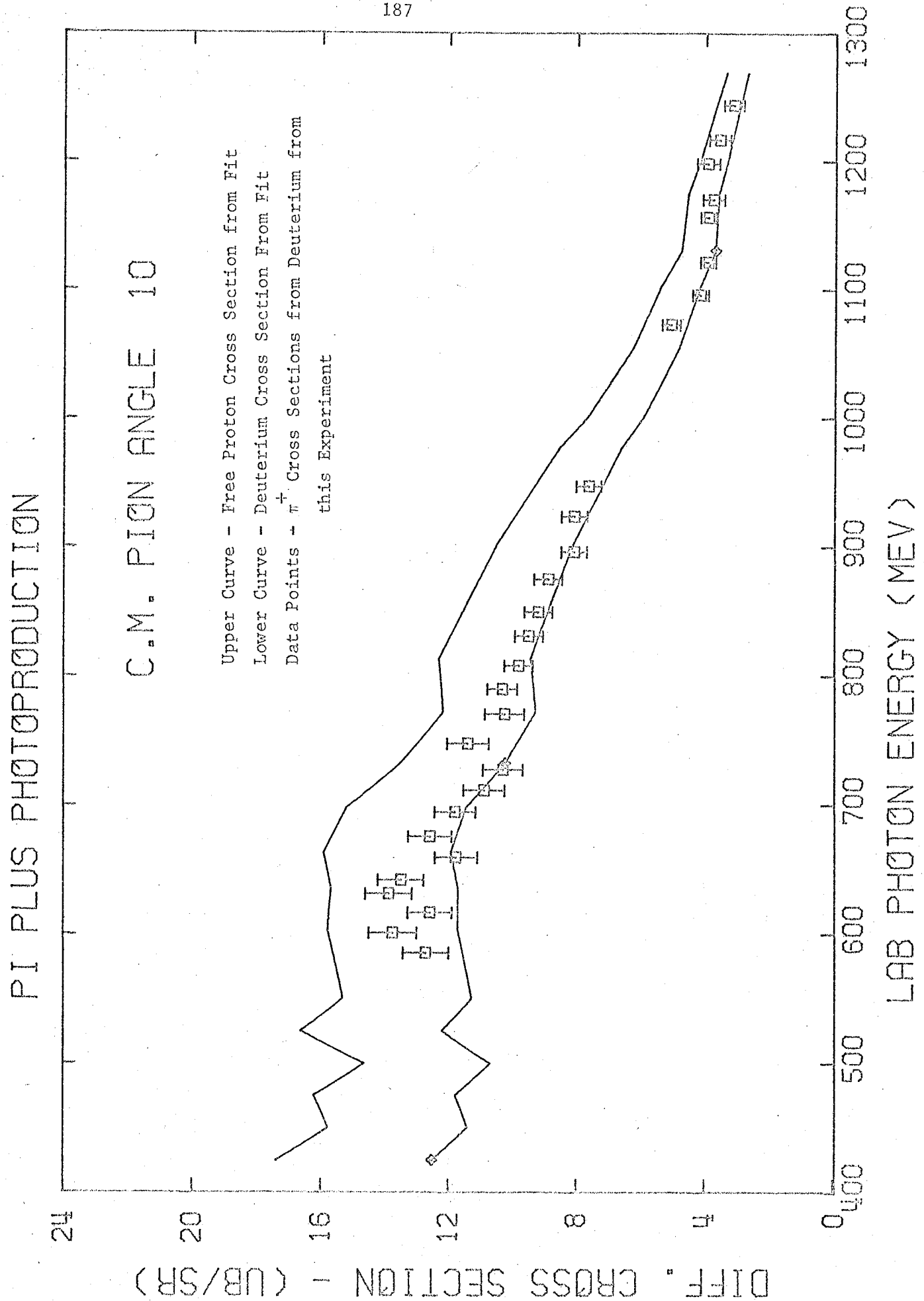
PI PLUS PHOTOPRODUCTION
C.M. PION ANGLE 10
Upper Curve - Free Proton Cross Section from Fit
Lower Curve - Deuterium Cross Section From Fit
Data Points - π^+ Cross Sections from Deuterium from this Experiment
DIFF. CROSS SECTION - (UB/SR)
LAB PHOTON ENERGY (MEV)
0
4
8
12
16
20
24
400
500
600
700
800
900
1000
1100
1200
1300

FIGURE 32

D. Discussion of results for the $S_{11}(1535)$ resonance.

As shown above (page 149), the amplitude for the $S_{11}(1535)$ resonance in π^- photoproduction seems to want to go to zero or perhaps even to positive values. In a "final" fit, I have set the resonance amplitude to +0.25 and the energy to 1520 (page 251) to remove most of the resonant behavior in the real part of the fitted add-on element. The imaginary part of the fitted add-on element still wants to go positive at energies below the resonance energy. This behavior may be due to wrong values for energy, width, or amplitude of the resonance, or may be unrelated to resonance behavior. Obviously, more work needs to be done on this problem.

In any case, whatever the final values of the resonance parameters for the S_{11}, my initial analysis (Figure 21.1, page 149) shows that a large negative amplitude is unlikely. Now the final results of Walker's analysis give amplitudes of -0.65 and -0.80 for the S_{11} in π^+ and π^- photoproduction respectively. (Table 9) These amplitudes are roughly in agreement with the quark model and imply that the S_{11} is excited mainly by isovector photons (see eqn. I.1, page 3). However, if the π^- amplitude is wrong and should be changed to zero or positive value, this would imply a significant amount of isoscalar excitation.

It is interesting to note that the S_{11} has been predicted to be mainly isoscalar from the results of η photoproduction experiments. (57)

PART VI

CONCLUSIONS

1) The reaction $\gamma n \rightarrow \pi^- p$ has a much smaller cross section than $\gamma p \rightarrow \pi^+ n$ in the third resonance region (1000 MeV photon energy). A partial wave analysis of the π^- reaction indicates that this is mainly due to weaker excitation of the $F_{15}(1688)$, helicity 3/2 resonance. This resonance appears to have a finite amplitude, however, in disagreement with a quark model prediction of zero.

2) The above partial wave analysis favors a positive amplitude for the $S_{11}(1535)$ resonance in π^- photoproduction, in disagreement with previous analyses and with a quark model prediction. The positive amplitude seems to be required to fit the new polarization and asymmetry data. The present analysis may indicate the S_{11} resonance is excited by isoscalar photons, in agreement with the results of Anderson and Prepost (57) in η photoproduction.

3) The status of the $P_{11}(1470)$ resonance in pion photoproduction is still indefinite although there appear to be large humps in the imaginary parts of the corresponding helicity elements.

4) Final state effects in the deuterium cross section seem to be mostly accounted for by the Pauli exclusion principle.

5) Partial wave analysis of photoproduction in the low energy region ($k_\gamma^{lab} < 1.5$ GeV) is still presenting difficulties due to lack of data. Especially needed are polarization and asymmetry data at many angles and energies. In the analysis of π^- photoproduction presented in this paper, the effects of a few new asymmetry and polarization data points were very large.

APPENDICES

APPENDIX I

NOTES ON KINEMATICS

A brief explanation of some kinematical quantities is necessary for the interpretation of tables and graphs.

The measured reaction is $\gamma d \rightarrow \pi^- pp$, which has a three-body final state. From this, we extract cross section information about the reaction $\gamma n \rightarrow \pi^- p$ and express our results in terms of kinematical quantities defined for the two-body final state.

Define as four-momenta k, p_d, q, p_r, and p_s for the incoming photon, the target deuteron, the outgoing pion, the "recoil" proton, and the "spectator" proton respectively. Then the equation of four-momentum conservation is:

$$k + p_d = q + p_r + p_s \qquad (1.1)$$

To express the kinematics in terms of the two-body reaction of interest, we define the CM total energy W of the (π^-, recoil p) system by:

$$W^2 = (q + p_r)^2 \qquad (1.2)$$

Now, if the target neutron in deuterium were on the mass shell, there would be no ambiguity in the definition of the photon energy k' in the neutron rest system for the two-body reaction. That is, for a free neutron:

$$k'(\text{free neutron rest system}) = \frac{W^2 - M_n^2}{2M_n} \qquad (1.3)$$

where M_n is the rest mass of the neutron; and k' and W are uniquely related. This is the relation between the lab photon energy and the CM total energy in single pion photoproduction reactions with a hydrogen target, where M_n is replaced by M_p. However, because the neutron is bound, this relation is no longer true for a deuterium target with W defined as above.

In order to compare our π^- photoproduction results with experiments using hydrogen targets (since the results of these experiments are usually given in terms of lab photon energy and CM pion angle measured from the photon beam line), we define an artificial photon energy k' given by equation 1.3. It is this photon energy which is given in the tables and graphs and which is (perhaps confusingly) called the "lab photon energy". However, only the CM total energy W of the two-body final state has definite physical meaning, and the value of k' should be considered mainly as a means of defining W by equation 1.3.

It should be noted, however, that in the partial wave analysis of π^- photoproduction, the values of k' given in the tables and graphs have been treated as photon energies in the free nucleon rest frame.

APPENDIX II

BEAM ENERGY MONITORING

The total energy in the bremsstrahlung beam passing through the deuterium target for each data run was measured indirectly with a Wilson type quantameter[58,59]. The quantameter could not be placed in the beam line during data runs where the particle detected in the spectrometer came off at a small lab angle ($<15^{o}$), due to the interference of the spectrometer with the beam line. To make for efficiency, at the sacrifice of some accuracy, the quantameter was not used at all during data runs. Rather the relative beam energy was measured by several secondary monitors during data runs, and these were then intercalibrated with the quantameter during special "monitor" runs taken inbetween the data runs. The quantameter, which could be pushed in and out of the beam line, was located just upstream of the deuterium target (Figure 2). A description of the monitors and the specific monitoring procedure follows.

A. Wilson quantameter - primary monitor.

The Wilson quantameter is a closed chamber consisting of 12 plates of copper, each 1 cm. thick, and separated by gaps alternating between 1 and 2 cm. in length. The chamber was (initially) filled with a gas mixture of 95% argon, 5% carbon dioxide at a total pressure ≈800 mm. Hg. at a temperature

=20° C. The amount of material is enough to almost completely absorb the beam. The beam energy is calculated by measuring the ionization of the gas caused by the electron-photon shower generated mainly in the copper plates. The plates are alternately held at ground potential and a negative high voltage. The electrons from ionization are collected at the grounded plates and the total charge collected is measured by an electronic integrator. If we know the amount of energy loss per ion pair formed in the gas and the ratio of energy loss in Cu to energy loss in the gas, we can theoretically calculate the total energy contained in the beam, given the ionization of the gas. (58)

1. Calibration constant of the (south) quantameter.

The theoretical calculation described above gives for this quantameter:

$$U_Q = (4.80 \pm 0.15) \times 10^{18} \text{ MeV/coulomb}$$

of ionization electrons collected. This number has been given for a pressure of 800 mm. Hg. and temperature 20° C.

This constant has been measured twice for our quantameter in an electron beam at Stanford by comparing the quantameter to a Faraday cup. The results were:

In 1960 $U_Q = (4.73 \pm 0.07) \times 10^{18}$ MeV/coulomb

In 1966 $U_Q = (4.78 \pm 0.14) \times 10^{18}$ MeV/coulomb

where both numbers have been corrected to 800 mm. Hg. and 20° C. (60)

Gomez et al. (59) suggest that the accuracy of the

experimental numbers is not good enough to justify using them and that the theoretical value should be used instead.

Thus the calibration constant used in this experiment was $U_Q = (4.80 \pm 0.15) \times 10^{18}$ MeV/coulomb at P = 800 mm. Hg. and T = 20° C.

2. Leakage of gas.

If the ratio $T(^{\circ}K)/P$ were constant for the quantameter, the above calibration constant would be valid for the experiment. A change in this ratio indicates a leakage of gas (PV=nRT). A slow leakage has been observed, and the ratio $T(^{\circ}K)/P$ was seen to change at a rate of +1.53% per year over the course of this experiment (one year). (Figure 33) If the mixture of gasses remained the same, it might be expected that the ionization of the gas per unit input beam energy would be simply proportional to the gas density, or equivalently, to P/T.

Indeed, we have made this assumption in the calculation of beam energy for this experiment. The above calibration constant then becomes:

$$C_Q = (13.10 \pm 0.41) \times 10^{18} \text{ MeV/coulomb per } T/P$$

or $U_Q = C_Q \times T/P$ where the units of T are $^{\circ}K$ and the units of P are mm. Hg.

It is unfortunate that the calibration of the quantameter has not been checked since 1966. However, this quantameter has been known to leak gas in the past while the two calibration measurements mentioned above, separated by 6 years, were consistent

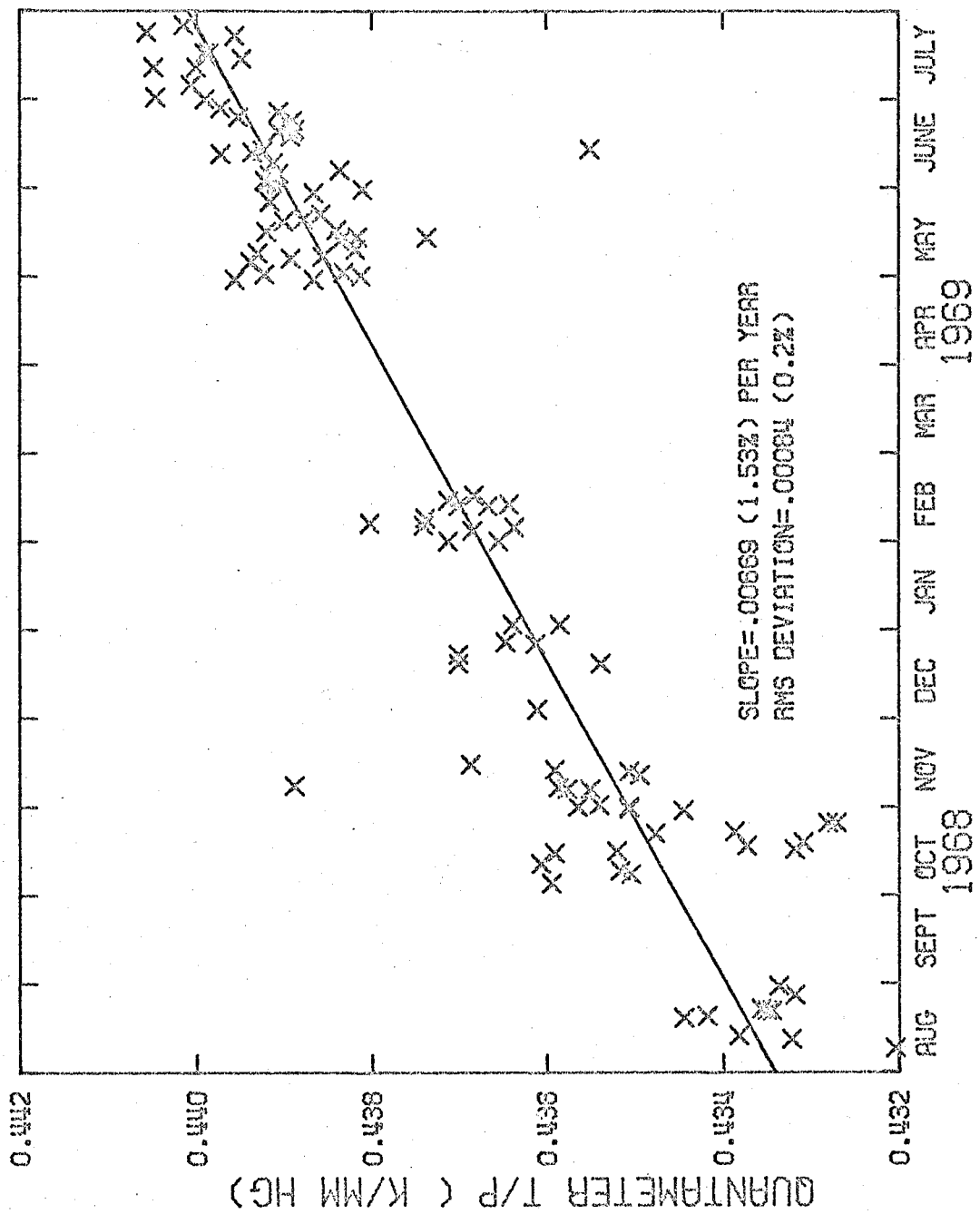
QUANTAMETER T/P (K/MM HG)
0.442
0.440
0.438
0.436
0.434
0.432
AUG
SEPT
OCT
NOV
DEC
JAN
FEB
MAR
APR
MAY
JUNE
JULY
1968
1969
SLOPE=.00669 (1.53%) PER YEAR
RMS DEVIATION=.00084 (0.2%)

FIGURE 33

with theory within experimental error. Therefore I believe that it is safe to continue to use the theoretical constant.

3. Temperature and pressure.

The pressure (in mm. Hg.) of the gas inside the quantameter is read off a gauge which is part of the quantameter unit. The temperature of the gas is assumed to be the same as the temperature of a Centigrade thermometer which is put in good thermal contact with the metal case. Even if there is a long adjustment time between gas and case (room) temperature, the statistical scattering caused by possibly erroneous temperature readings causes an error in T/P of the order of only 0.2%, because the absolute temperature is used in the ratio. The pressure gauge on the quantameter is assumed to be operating correctly.

B. Secondary monitors.

Five secondary monitors were used in this experiment to determine the relative beam total energy during data runs. Three of these were also active during monitor runs when the Wilson quantameter was in the beam line for intercalibration.

1. 40 MHz probe.

The 40 MHz probe is a device to monitor the relative circulating electron current in the synchrotron. It was gated to sense the current at a time immediately before the electron beam was dumped (converted to an external bremsstrahlung beam

by the internal tantalum target ("radiator")). It operated during both data runs and monitor runs. Assuming that the full beam is "dumped", this monitor should give a good indication of the relative beam energy.

2. TC1 (thin chamber).

TC1 was a thin (mylar) walled ionization chamber filled with an inert gas which was placed in the path of the photon beam, whose energy it monitored by the small ionization of the gas. It was located immediately downstream of the primary Pb collimator through which the photon beam exited from the synchrotron. Ionized electrons were collected and fed to a current integrator whose output (counter and meter) was proportional to the charge collected, and thus to the amount of ionization. TC1 was active during both monitor and data runs.

3. TC2 (thin chamber).

TC2 was another thin walled ionization chamber similar to TC1 and was located downstream of the UCLA hydrogen target and just upstream of the last sweeping magnet. This monitor was active during both monitor and data runs.

4. MT (monitor telescope).

The monitor telescope consisted of two scintillation counters located below the deuterium target and surrounded by lead brick shielding. The counters were physically set in a telescopic arrangement (one below the other) and electronically connected in coincidence in order to detect reaction products

moving straight down from the target, thus providing another relative monitor of the beam total energy. Since the deuterium target was located downstream of the Wilson quantameter, this monitor was inactive during monitor runs.

5. BC (beam catcher).

The beam catcher is another ionization chamber where an electron-photon shower is generated in a few copper plates. Directly behind this chamber is the termination of the beam line. This monitor, being downstream of the quantameter, was not active during monitor runs. Also it could not be used during data runs in which the high momentum magnetic spectrometer (HEMA or OUTR) blocked the beam line. As with TC1 and TC2, the current output of this monitor was integrated and the relative charge read off on a counter and meter. A brief description of the current integrators and integrator calibrator follows.

C. Current integrators, integrator calibrator.

The current pulses collected by the various ionization chambers were fed into current integrators whose outputs gave the relative charge collected in units of BIP's (beam integrator pulses). Whole BIP's were read off a counter (scaler) and fractions of a BIP were read off a meter. One BIP is the charge collected in the integrator by a fixed capacitance which has been charged to a fixed voltage (Q=CV).

The integrator used by the Wilson quantameter was calibrated in coulombs/BIP by the integrator calibrator, which was a circuit rack containing an extremely precise capacitance which is pulse discharged from a fixed voltage value which has been precisely measured with a null voltmeter with standard reference cell. The coulombs/pulse delivered by this calibrator during our experiment was

$$C/Pulse = 503.75 \times 10^{-10} \pm 0.25\% \quad \text{(on the 50 volt setting)}$$

The combination of quantameter calibration constant, integrator calibrator constant, and integrator calibration constant gives the useful constant:

$$\frac{MeV}{BIP} = \frac{MeV}{Coulomb} \times \frac{Coulombs}{Calibrator\ pulse} \times \frac{Calibrator\ pulses}{Integrator\ BIP} \qquad (3.1)$$

which for our experiment was roughly 11×10^{12} MeV/BIP for the integrator used with the quantameter.

D. Specific program for calculation of total beam energy

The total beam energy passing through the deuterium target for a given data run was calculated using the following formula:

$$MeV\ (data\ run) = \frac{MeV}{QBIP} \times (QBIP's)_{avg} \qquad (3.2)$$

where MeV/QBIP is the energy per BIP of the quantameter integrator as calculated in equation 3.1, and $(QBIP's)_{avg}$ is as given in equation 3.3. The MeV/QBIP was calculated once a day or after a synchrotron endpoint change.

$(QBIP's)_{avg}$ is defined by:

$$(QBIP's)_{avg} = \frac{1}{3} \times \left[\left(\frac{QBIP's}{TC1\text{-}BIP} \right)_S \times (TC1\text{-}BIP's)_D + \left(\frac{QBIP's}{TC2\text{-}BIP} \right)_S \times (TC2\text{-}BIP's)_D + \left(\frac{QBIP's}{40\ MHz} \right)_S \times (40\ MHz\ scaler)_D \right] \qquad (3.3)$$

where the subscript S means that an average is taken over the two monitor runs surrounding the data run, and D refers to quantities measured during the data run.

An estimate of the standard deviation in the quantity $(QBIP's)_{avg}$ due to variations of the three secondary monitors from the average was obtained by plotting the differences $\left((QBIP's)_{via\ TC1} - (QBIP's)_{avg}\right)$, $\left((QBIP's)_{via\ TC2} - (QBIP's)_{avg}\right)$, and $\left((QBIP's)_{via\ 40\ MHz} - (QBIP's)_{ave}\right)$, where $(QBIP's)_{via\ x}$ is the appropriate term in equation 3.3. An example of this is given in Figure 34 . The standard deviation varies from slightly less than 1% to about 2%. This error is a statistical error which, however, is not included in the statistical error given for the final data.

In several cases, one of the monitors TC1, TC2, or 40 MHz gave wild results and was not included in the average.

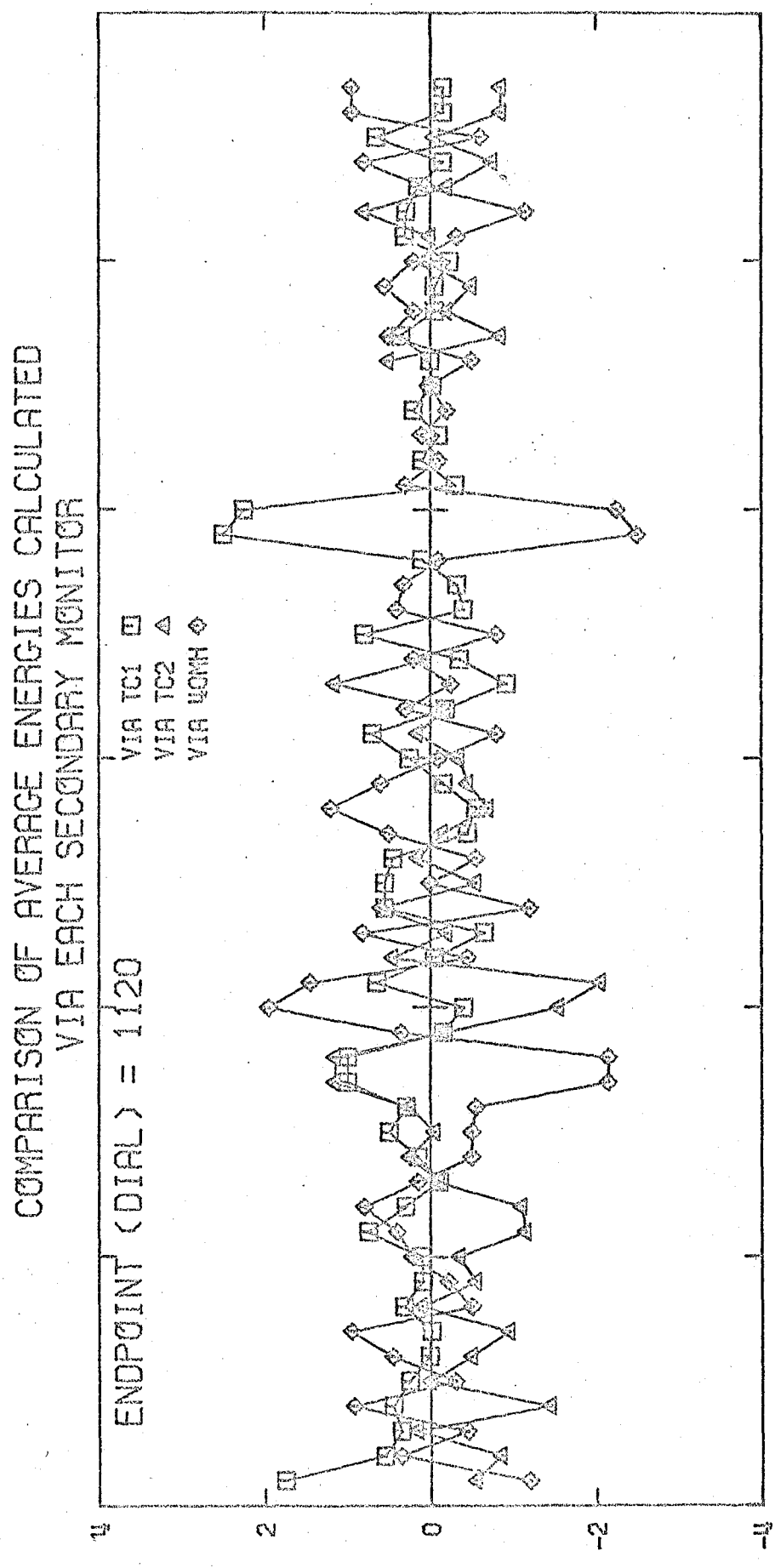
COMPARISON OF AVERAGE ENERGIES CALCULATED
VIA EACH SECONDARY MONITOR
ENDPOINT (DIAL) = 1120
VIA TC1
VIA TC2
VIA WDMM
% DEVIATION FROM AVERAGE ENERGY
4
2
0
-2
-4
DATA RUNS

FIGURE 34

APPENDIX III

EXPERIMENTAL APPARATUS

A. Spectrometers and counters

At each data point, a magnetic spectrometer was used to identify one of the outgoing charged particles and to measure its vector momentum. Two magnetic spectrometers with a total of three possible configurations were available for this task. A low momentum spectrometer, or low energy magnet (LEM) was used to measure particle momenta up to 600 MeV/c. A high energy magnet (HEMA) could measure momenta up to 1200 MeV/c; and by means of extensions to the HEMA frame, another configuration (OUTR for "outrigger") was possible which extended the maximum allowable momentum to 1650 MeV/c.

Both spectrometers were set in frames which could be rotated around the deuterium target assembly. The maximum allowable lab angles for the various configurations were 148° for the LEM, 55° for the HEMA and 39° for the OUTR. Figure 2 shows one possible position for the spectrometers in the experimental area.

1) HEMA and OUTR

A schematic diagram of the counters in the high momentum spectrometer (side view) is given in Figure 35. A central particle trajectory is shown which originates at the deuterium

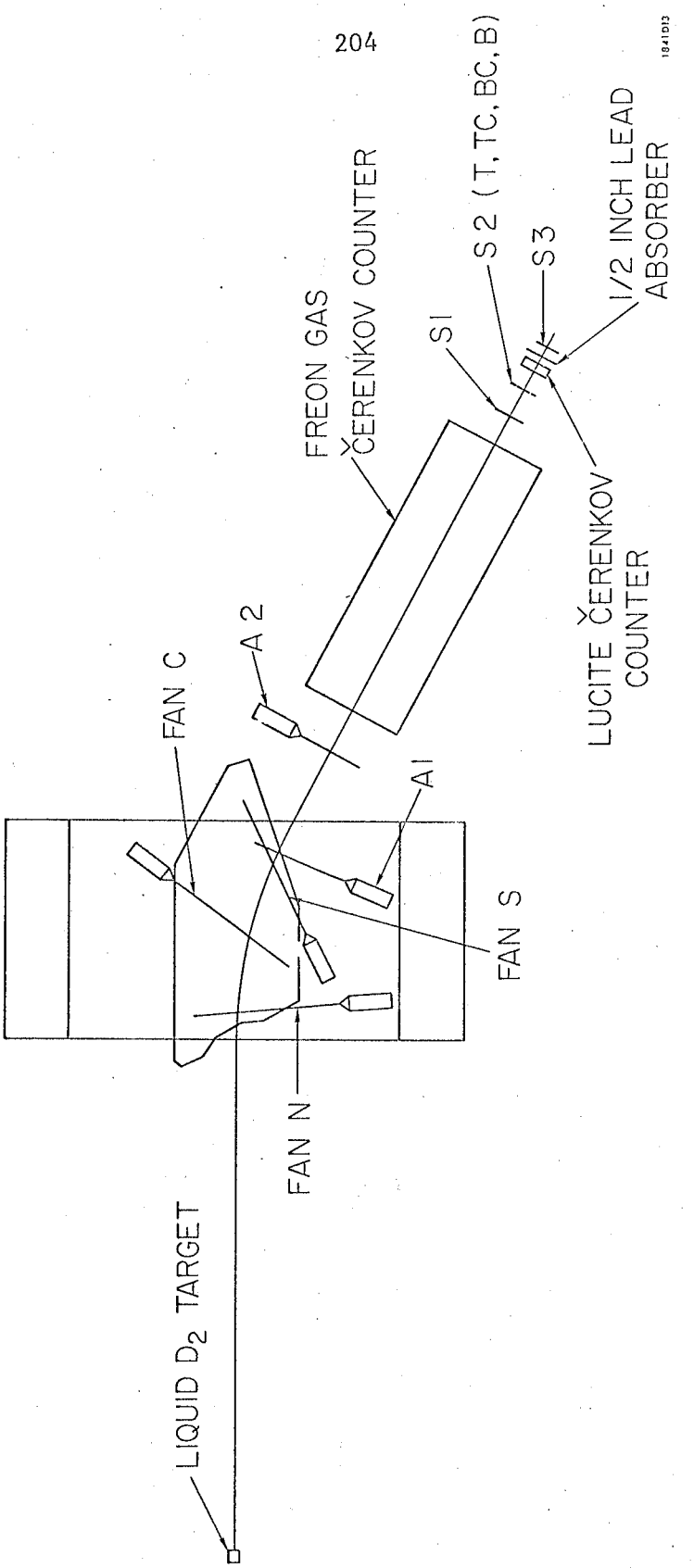
1841013
FREON GAS ČERENKOV COUNTER
S2 (T, TC, BC, B)
S3
1/2 INCH LEAD ABSORBER
S1
LUCITE ČERENKOV COUNTER
A2
FAN C
A1
FAN S
FAN N
LIQUID D_2 TARGET

FIGURE 35

target, passes between the pole faces of the magnet, and is there bent downward to pass through the various scintillation counters and Cerenkov counters. A set of three FAN counters (scintillation counters) were set against the inner sides of the pole faces of the magnet to veto particles which scattered off the pole faces and went through the rest of the system. A particle event was defined by a five-fold coincidence between the counters A1, A2, S1, S2, and S3 along with a veto from the FAN's. The four-channel hodoscope S2 defined the momentum channels of the spectrometer.

The horizontal aperture (perpendicular to the plane of the diagram) of the spectrometer was defined by the counter A1 whose angular width was 0.0158 radians or about 0.9^{o} at the deuterium target. The vertical aperture was roughly 0.1 radians or about 6^{o} at the target.

The momentum calibration and aperture measurements were made by F. Wolverton(61). A summary of the acceptance properties of the HEMA and OUTR configurations for each momentum channel is given in Table 10 and Table 11. For each channel, the momentum spread ($\Delta P/P_{o}$) was about 2.5%.

Particle identification was accomplished by means of the two Cerenkov counters FC and LC. A suitable combination of triggers of FC and LC was used to distinguish between

TABLE 10

HEMA Acceptance Properties

12 × 2.75 inch aperture counter

1.18 inch momentum counters

Momentum Channel	Mean Q	$\Delta\beta$ radians	ΔQ	$\Delta\beta\Delta Q$ radians	$\Delta\theta$ radians	$\Delta\Omega$ steradians	$\Delta Q\Delta\Omega$ steradians
T	0.0423	0.1022	0.0266	0.00272	0.0158	1.614×10^{-3}	4.30×10^{-5}
TC	0.0138	0.1026	0.0252	0.00258	0.0158	1.620×10^{-3}	4.08×10^{-5}
BC	-0.0129	0.1030	0.0239	0.00246	0.0158	1.628×10^{-3}	3.89×10^{-5}
B	-0.0380	0.1033	0.0228	0.00236	0.0158	1.633×10^{-3}	3.73×10^{-5}

$Q = (P - P_o)/P_o$ where P_o is the central momentum of the spectrometer

$\Delta\beta$ = vertical aperture

$\Delta\theta$ = horizontal aperture

$\Delta\Omega$ = total angular acceptance

TABLE 11

OUTR Acceptance Properties

12 × 2.75 inch aperture counter

1.18 inch momentum counters

Momentum Channel	Mean Q	$\Delta\beta$ radians	ΔQ	$\Delta\beta\Delta Q$ radians	$\Delta\theta$ radians	$\Delta\Omega$ steradians	$\Delta Q\Delta\Omega$ steradians
T	0.0292	0.0913	0.0199	0.00182	0.0164	1.497×10^{-3}	2.98×10^{-5}
TC	0.0080	0.0914	0.0189	0.00173	0.0164	1.499×10^{-3}	2.84×10^{-5}
BC	-0.0122	0.0915	0.0182	0.00167	0.0164	1.501×10^{-3}	2.74×10^{-5}
B	-0.0316	0.0916	0.0178	0.00163	0.0164	1.503×10^{-3}	2.67×10^{-5}

electrons, pions, and protons. Muons and pions gave the same set of triggers and no attempt was made to distinguish between them, since it was assumed that all muons came from pion decays.

The Freon Cerenkov counter (FC) consisted of a large gas-filled box with phototube to collect Cerenkov light from particles moving at a speed greater than 0.999c. Since no pion or proton detected by the spectrometer ever reached this speed, FC was triggered only on electrons (or positrons). For electrons causing a particle trigger ($A1 \cdot A2 \cdot S1 \cdot S2 \cdot S3 \cdot \overline{FAN}$), the detection efficiency of FC was very high, averaging around 99.7%. Measurements of this efficiency were made (periodically during the experiment) in a pure electron beam generated by placing a pinhole Pb collimeter in the photon beam while the magnet was placed at 0^{o}.

Low energy electrons which might not trigger FC, were absorbed by a 1/2 inch slab of lead placed downstream of LC.

The Lucite Cerenkov counter (LC) consisted of a Lucite slab with a phototube attached at each end. A combination of the effects of the index of refraction of Lucite and of the optical path to the phototubes gave the counter a threshold

of 0.9c. Since all pions and electrons measured by HEMA and OUTR were above this threshold, LC was triggered on these particles. However, due to losses (the optical system was not perfect) the pion (and electron) efficiency of LC averaged only about 98.5%. This number was measured by setting the magnetic field of the spectrometer so as to detect only negatively charged particles, thus eliminating protons.

Unfortunately, LC had a non-zero proton efficiency which was probably due to "knock-on" electrons and perhaps some scintillation due to low energy protons. The efficiency ranged from 0.7% to 4%. To measure this efficiency, an almost pure proton beam was generated by setting the synchrotron endpoint below the energy necessary to produce pions of a given momentum in the spectrometer while still allowing protons of this momentum. Also, time of flight restrictions were imposed to reduce pion contamination. Nevertheless, due to smearing, all pions could not be eliminated. A comparison was made between a pulse height spectrum produced by this beam and that of a pion beam in order to subtract out any remaining pion contamination.

2) LEM

A schematic of the low energy magnet counter system is given in Figure 36. A particle trigger was defined by the

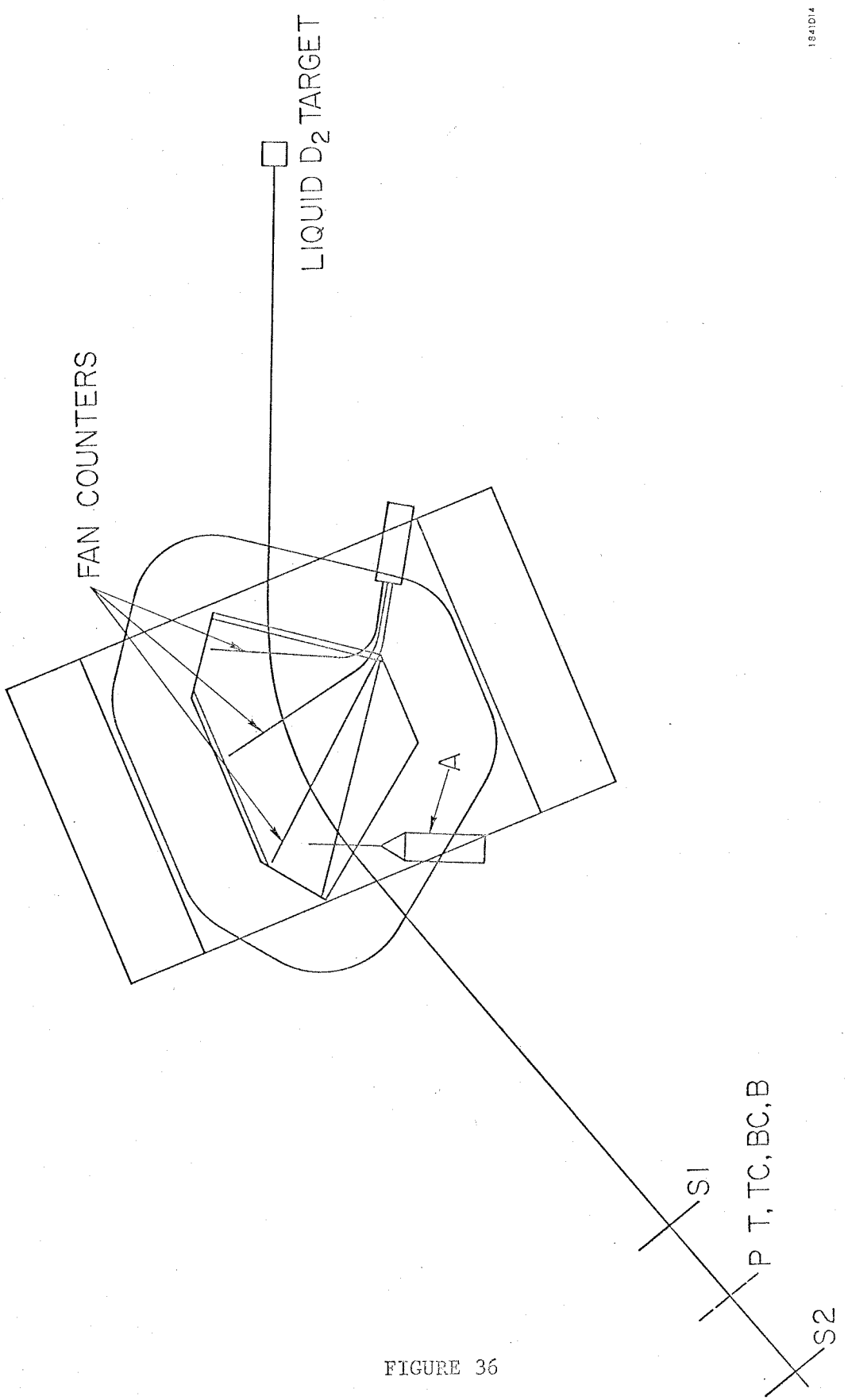

FIGURE 36

four-fold concidence of A, S1, P, and S2, along with a veto from the FAN counters. The P counter was a four-channel hodoscope which defined the momentum channels of the spectrometer.

The horizontal aperture was defined by A whose angular width was 0.0289 radians or about 1.7^{o} at the deuterium target. The vertical aperture of the magnet system was about 0.11 radians or about 6^{o} at the target.

The LEM was calibrated by H. Thiessen(62) for a 7-momentum channel hodoscope P. We have replaced Thiessen's 7-channel counter with a 4-channel counter. A recalculation of the acceptance parameters for the new momentum channels, using the field map measurements of Thiessen, was done by P. Walden(44) and a summary of the new LEM acceptances is given in Table 12. For each channel, the momentum spread ($\Delta P/P_o$) was about 2.6%

In the LEM, particle identification was accomplished by means of pulse height discrimination in counters S1 and S3 along with time of flight restrictions. Proton energies in the LEM were much lower than the energy for minimum ionization, and the larger proton pulse heights were easily distinguished from pion pulse heights. The separation, however, was not perfect; and at best settings of pulse height discriminators, the pion efficiency averaged 99.6% while the proton efficiency hovered near 1%.

TABLE 12

LEM Acceptance Properties

9.5 × 2.75 inch aperture counter

1.25 inch momentum counters

Momentum Channel	Mean Q	$\Delta\beta$ radians	ΔQ	$\Delta\beta\Delta Q$ radians	$\Delta\theta$ radians	$\Delta\Omega$ steradians	$\Delta Q\Delta\Omega$ steradians
T	0.0384	0.1120	0.0262	0.00294	0.0289	3.24×10^{-3}	8.49×10^{-5}
TC	0.0112	0.1120	0.0250	0.00280	0.0289	3.24×10^{-3}	8.10×10^{-5}
BC	-0.0147	0.1120	0.0239	0.00268	0.0289	3.24×10^{-3}	7.74×10^{-5}
B	-0.0394	0.1120	0.0229	0.00257	0.0289	3.24×10^{-3}	7.43×10^{-5}

$Q = (P - P_o)/P_o$ where P_o is the central momentum of the spectrometer

$\Delta\beta$ = vertical aperture $\Delta\Omega$ = total angular acceptance

$\Delta\theta$ = horizontal aperture

The LEM was unable to distinguish pions from electrons. At the start of the experiment, we were not worried about this defect, since we assumed that the electron rates were negligible at the large lab angles at which the LEM was used. However, during the experiment, we observed a discontinuous jump between the HEMA cross sections and the LEM cross sections which we now believe to be due to electron-positron contamination in the LEM results. A further discussion of this problem is given in Section IV.C.

B. The recoil counter

The recoil counter was used to detect the recoil proton p_r (from the reaction $\gamma d \rightarrow \pi^- p_r p_s$) while the spectrometer was used to detect the pion. At backward pion angles, however, the arrangement was reversed with the proton being detected by the spectrometer (HEMA or OUTR) while the pion was detected in the "recoil" counter. The recoil counter was designed to accept about 50% of the recoil particles associated with a particle in the spectrometer.

Figure 37 shows the structure and dimensions of this counter. The actual aperture is defined by the small counter RC. The three counters RB, RL, and RR were used to define a coincidence with RC and to crudely indicate any left-right

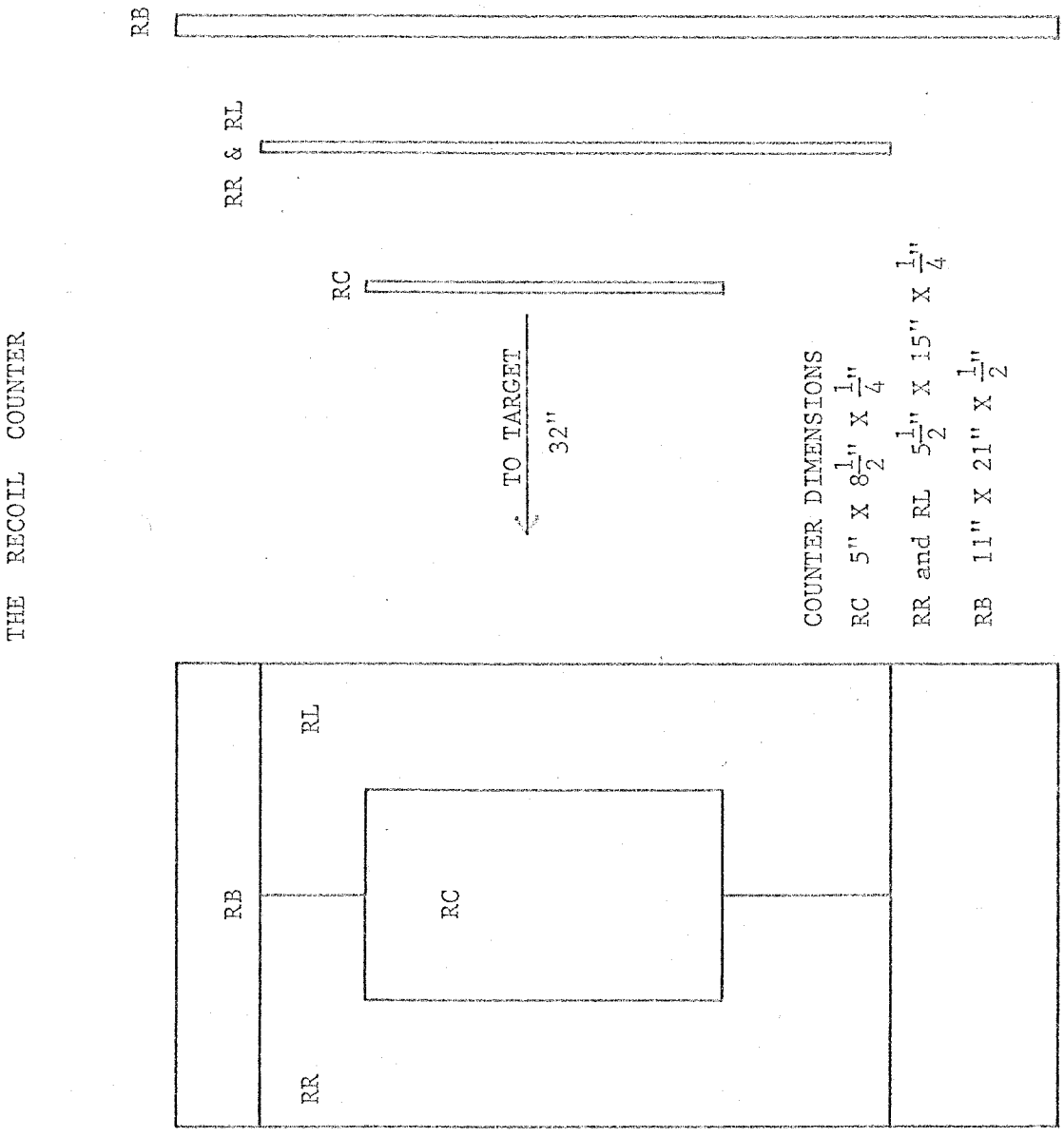
THE RECOIL COUNTER
RB
RR & RL
RC
TO TARGET
32"
COUNTER DIMENSIONS
RC 5" X 8 1/2" X 1/4"
RR and RL 5 1/2" X 15" X 1/4"
RB 11" X 21" X 1/2"
RB
RL
RC
RR

FIGURE 37

asymmetry in the distribution of recoils. The recoil counter system was set up and moveable in angle on a circular track of 32 inch radius surrounding the deuterium target.

C. Electronics

Schematics of the HEMA, LEM, and recoil electronics are given in Figures 38, 39, and 40 respectively.

In general, for the spectrometers, a fast coincidence of about 5 nanoseconds was required between the counters defining a particle trigger. This fast coincidence is produced in the coincidence circuit module labelled "S" in the HEMA and LEM diagrams. Actually, due to the fact that this module could physically take only four inputs, the final particle trigger was obtained in the module PAR·$\overline{\text{FAN}}$ whose inputs were a fast (5ns) pulse from S and slower (longer) pulses (10 ns) from FAN (veto) and from A2 (HEMA).

Particle identification was then made by the slower electronics (50 ns pulse lengths). In the HEMA electronics, the various combinations of LC and FC and their vetos were fed into the coincidence circuits π, p, e, and X. The X coincidence circuit identified a normally impossible situation where FC was triggered and LC was not. Counts in this circuit were due purely to the inefficiencies of the Cerenkov counters.

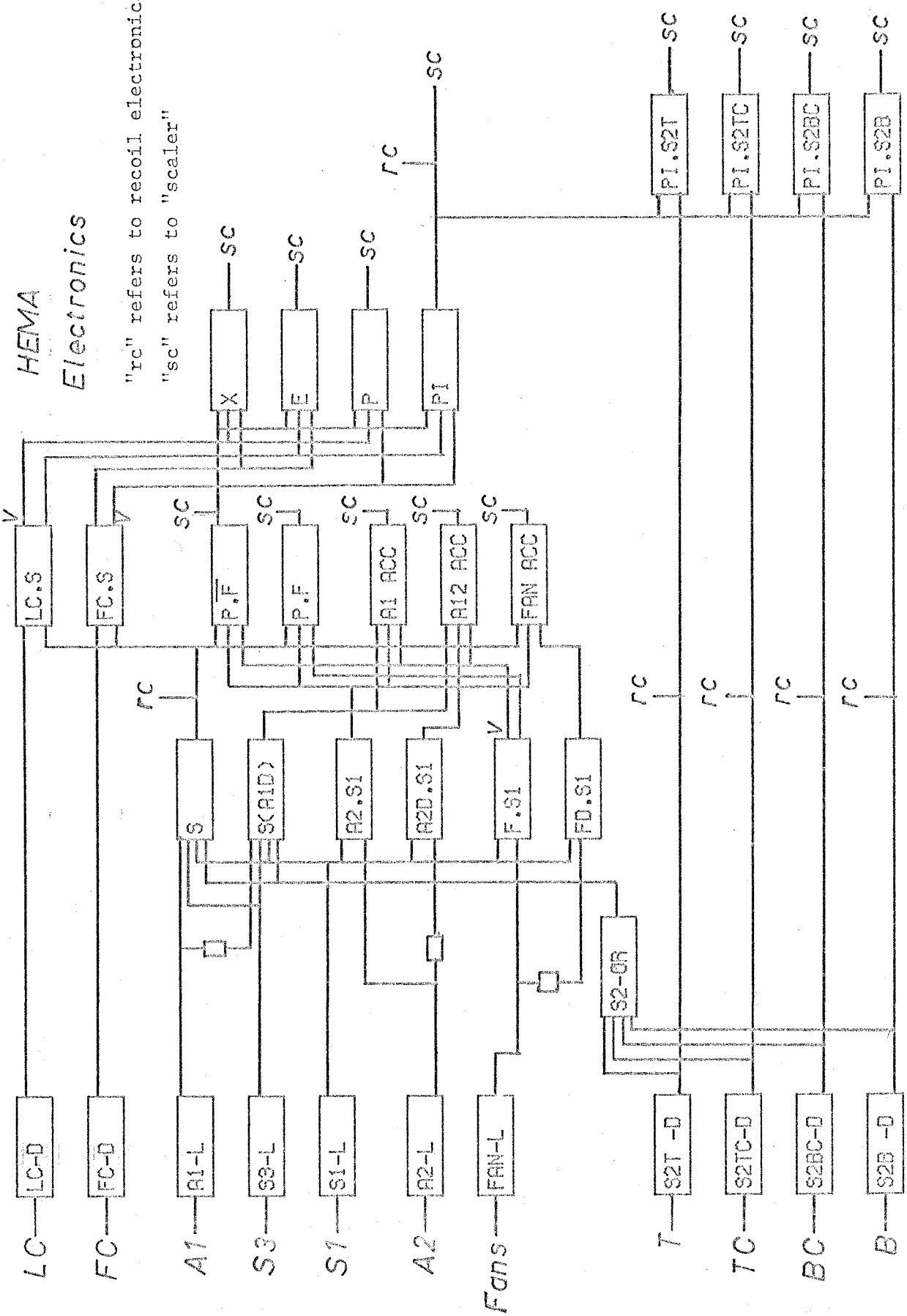
HEMA
Electronics
"rc" refers to recoil electronics
"sc" refers to "scaler"
LC.S
FC.S
X
E
P
PI
P.F
P.F
A1 ACC
A12 ACC
FAN ACC
S
S(A1D)
A2.S1
A2D.S1
F.S1
FD.S1
S2-GR
PI.S2T
PI.S2TC
PI.S2BC
PI.S2B
LC-D
FC-D
A1-L
S3-L
S1-L
A2-L
FAN-L
S2T -D
S2TC-D
S2BC-D
S2B -D
LC
FC
A1
S3
S1
A2
Fans
T
TC
BC
B

FUGURE 38

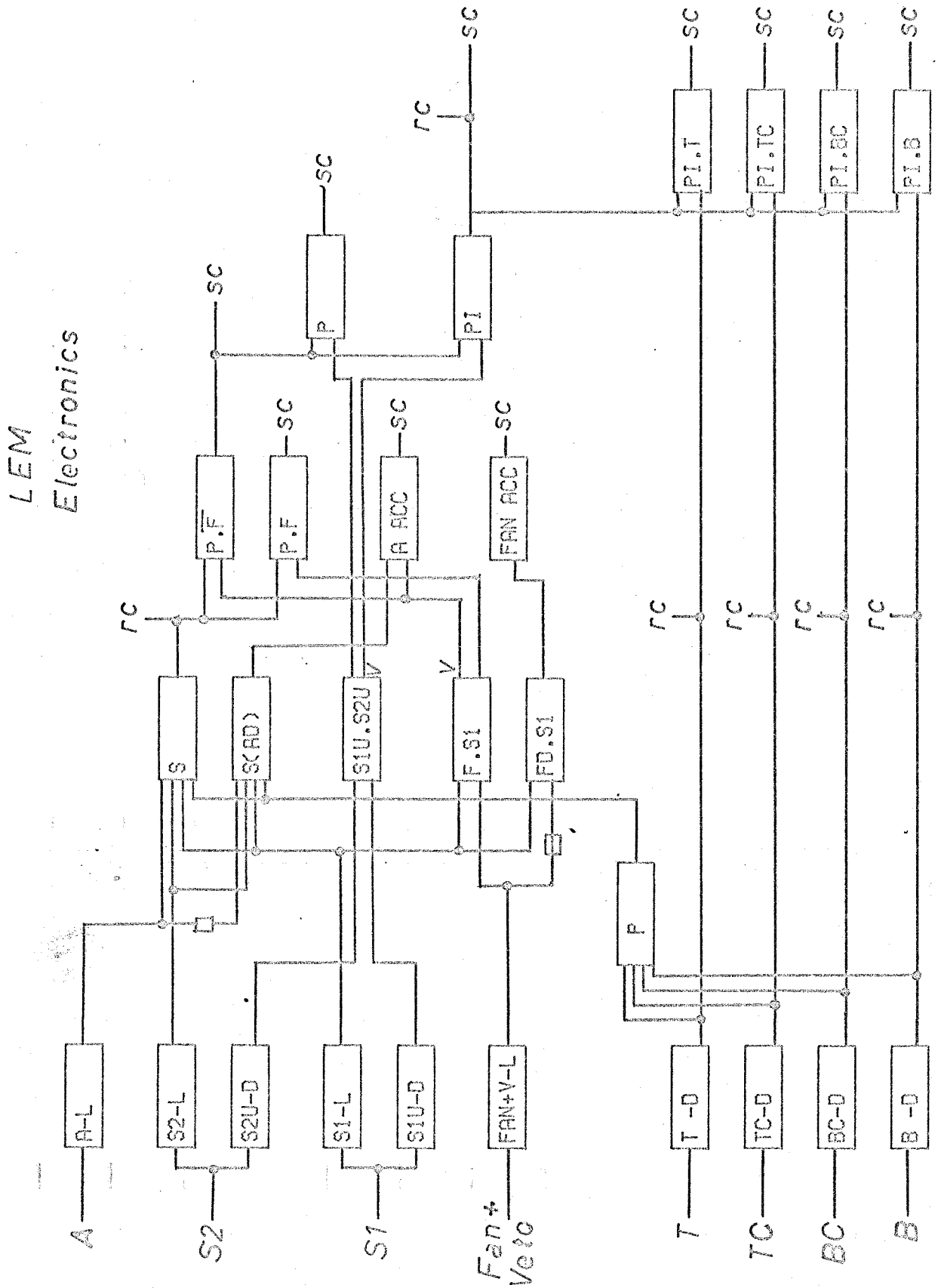
LEM
Electronics
sc
rc
P
PI
P.F̄
P.F
A ACC
FAN ACC
PI.T
PI.TC
PI.BC
PI.B
S
S(AD)
S1U.S2U
F.S1
FD.S1
A-L
S2-L
S2U-D
S1-L
S1U-D
FAN+V-L
T-D
TC-D
BC-D
B-D
A
S2
S1
Fan + Velo
T
TC
BC
B

FIGURE 39

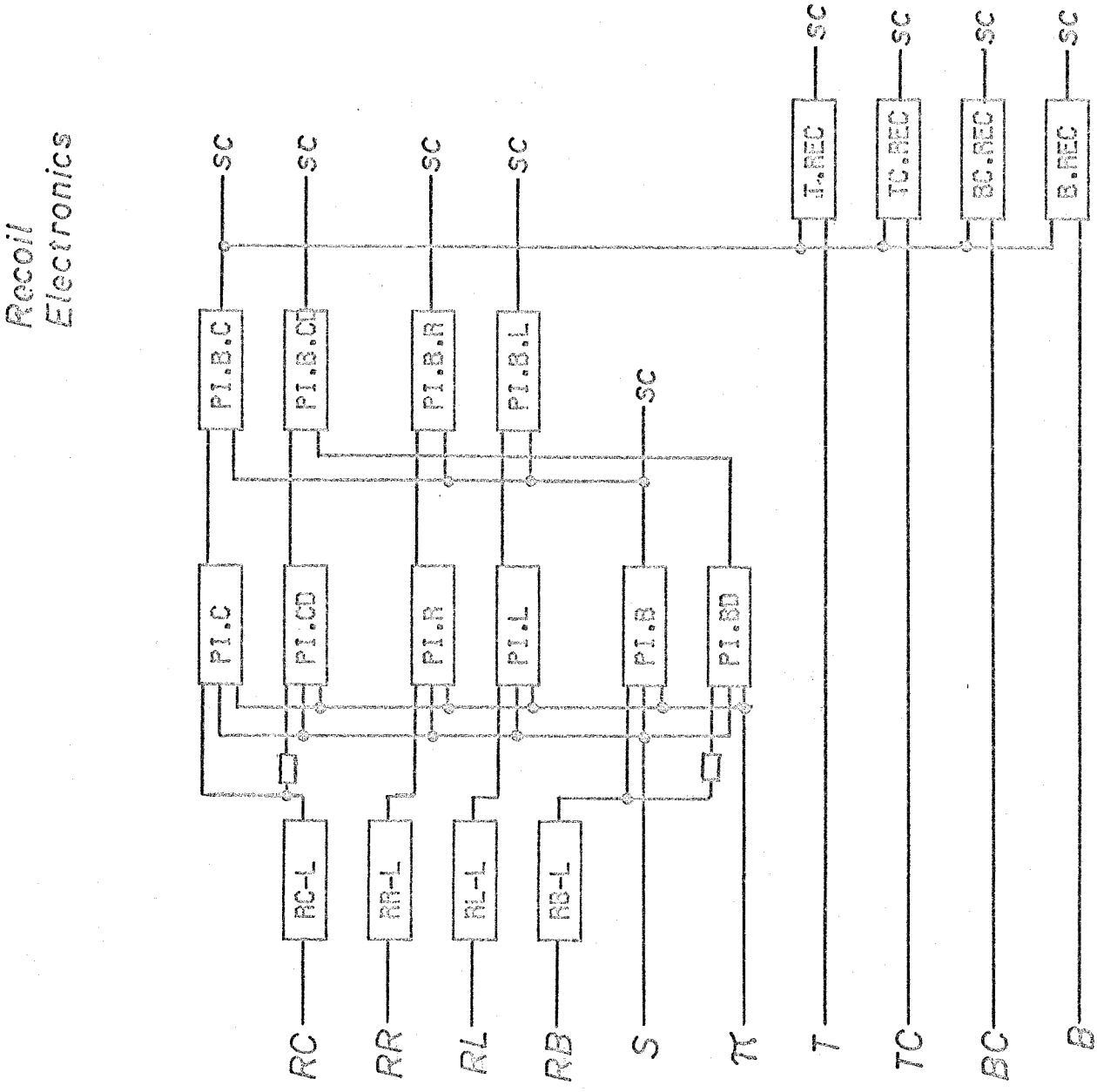
Recoil
Electronics
SC
P1.B.C
P1.B.CD
P1.B.R
P1.B.L
P1.C
P1.CD
P1.R
P1.L
P1.B
P1.BD
RC-L
RR-L
RL-L
RB-L
T.REC
TC.REC
BC.REC
B.REC
RC
RR
RL
RB
S
T
TC
BC
B

FIGURE 40

In the LEM electronics, the coincidence signal and veto signal from the circuit S1U·S2U were fed into the p and π coincidence circuits. As electrons were not distinguished from pions, there was no separate electron circuit.

Finally, the π signal (or the p signal for the reverse recoil setup) was put in coincidence with the 4 momentum channels to obtain the π (or p) counts in each channel.

If the recoil counter was used, the signals S (fast), π (or p), and the 4 momentum channels were put in coincidence with the final recoil signal B·C to obtain the number of events in each momentum channel for which a recoil particle was observed.

To monitor FAN triggers and various accidentals rates, appropriate coincidences were defined. A problem with the definition of A1 and A1·A2 accidentals is mentioned in Section IV.F.

The reduction of scaler counts to true particle rates using counter efficiencies and accidentals corrections was done by P. Walden and is completely described in Appendix 10 of his Ph.D. thesis(44).

APPENDIX IV

THE HULTHEN WAVE FUNCTION

A useful representation of the deuteron ground state is given by the Hulthen wave function:

$$u_i(\rho) = \left(\frac{\alpha}{2\pi(1 - \alpha\rho_1)}\right)^{\frac{1}{2}} \frac{(e^{-\alpha\rho} - e^{-\beta\rho})}{\rho} \tag{4.1}$$

where $\alpha = 45.69$ MeV

$\beta = 275.74$ MeV

$\rho_1 = 0.0088177\ \text{MeV}^{-1} = 1.74$ fermi

ρ_1 is the neutron-proton effective range and is related to α and β by the normalization condition:

$$\rho_1 = \frac{4}{(\alpha + \beta)} - \frac{1}{\beta} \tag{4.2}$$

The corresponding momentum-space wave function is:

$$c(k) = \left(\frac{\alpha}{\pi^2(1 - \alpha\rho_1)}\right)^{\frac{1}{2}} \frac{(\beta^2 - \alpha^2)}{(\alpha^2 + k^2)(\beta^2 + k^2)} \tag{4.3}$$

The momentum (magnitude) probability density is then $= 4\pi k^2 |c(k)|^2$. This last function is plotted in Figure 3 . The curve peaks at about 50 MeV/c which is then the most likely internal nucleon momentum.

The deuteron form factor then is given by:

$$F(k) = \int \exp(i\vec{k}\cdot\vec{\rho})\ u_i^2(\rho)\ d^3\rho \tag{4.4}$$

$$= \frac{1}{1 - \alpha\rho_1}\left(\frac{2\alpha}{k}\right)\left[\tan^{-1}(k/2\alpha) - \tan^{-1}(k/2\beta) - 2\tan^{-1}(k/(\alpha+\beta))\right]$$

APPENDIX V

NOTATION AND HELICITY FORMALISM FOR PARTIAL WAVE ANALYSIS

All variables are in the center of momentum (CM) system.

Particle four-momenta: see Figure 41.

$k = (k,\vec{k})$ incident photon

$p_1 = (E_1,\vec{p}_1)$ initial (target) nucleon (note $\vec{p}_1 = -\vec{k}$)

$q = (\omega,\vec{q})$ outgoing pion

$p_2 = (E_2,\vec{p}_2)$ final (recoil) nucleon (note $\vec{p}_2 = -\vec{q}$)

M_1 = mass of initial nucleon

m = mass of outgoing pion

M_2 = mass of final nucleon

W = CM total energy

$\theta = \theta_\pi^{CM}$ = angle between $\vec{q}$ and $\vec{k}$

Units used in theoretical formulas:

$\hbar = 1$

$c = 1$

Unit of energy = 1 GeV

Unit of cross section = 1 GeV^{-2}

Units used in graphs and numerical tables:

Unit of cross section = 1 microbarn (μb) = 10^{-30} cm^2

Unit of helicity amplitudes = $(1\ \mu b)^{\frac{1}{2}}$

Conversion of GeV^{-2} to μb:

1 GeV^{-2} = 389.5 μb

Variables in CM Frame

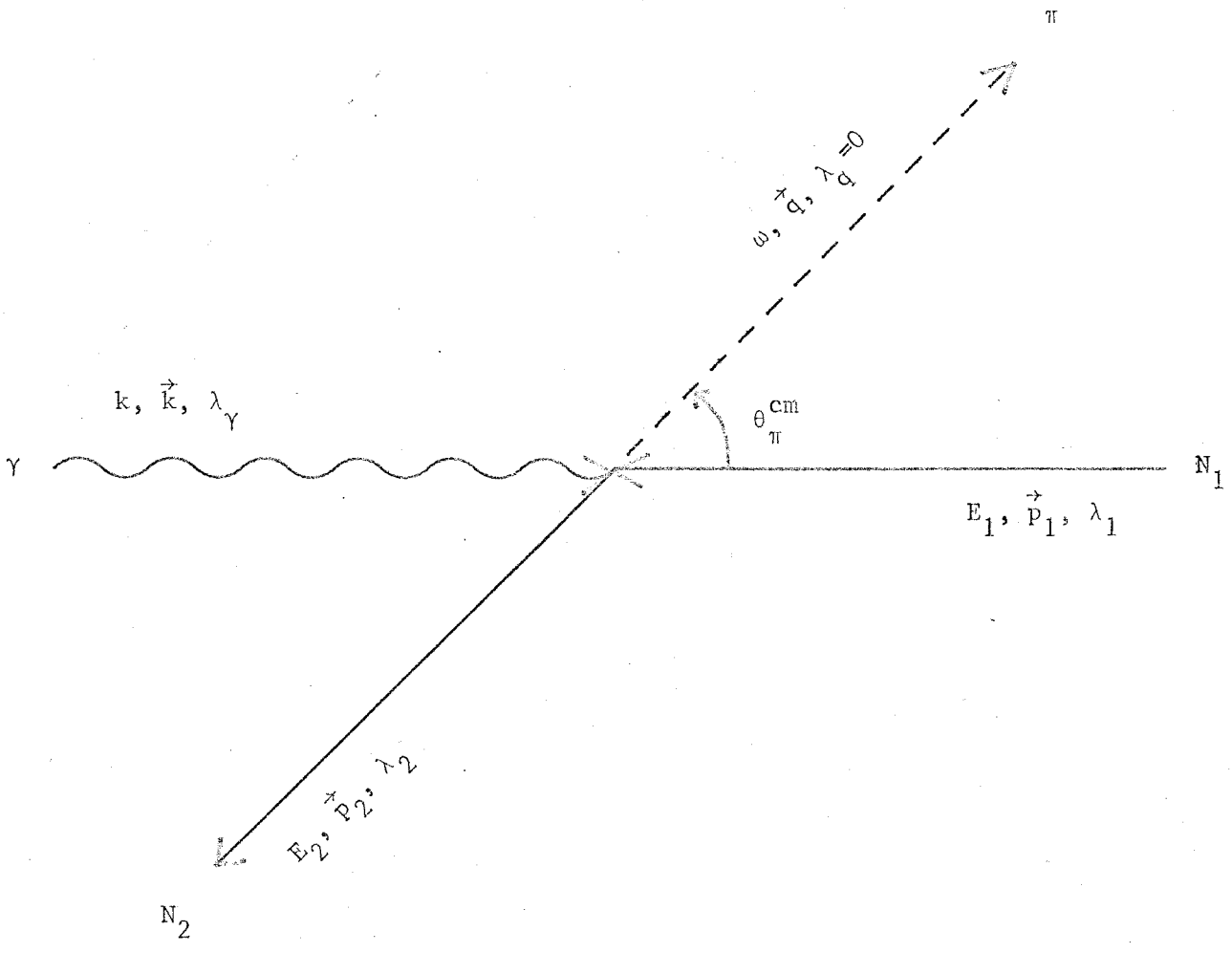

FIGURE 41

Particle helicities: (in the CM system)

(Helicity is defined as the particle spin component in the direction of motion.)

$\lambda_k = \pm 1$ = photon helicity

$\lambda_1 = \pm\frac{1}{2}$ = helicity of initial nucleon

$\lambda_q = 0$ = helicity of pion

$\lambda_2 = \pm\frac{1}{2}$ = helicity of final nucleon

$\lambda \equiv \lambda_k - \lambda_1 = \pm 3/2, \pm 1/2$ = total initial helicity (along $\vec{k}$)

$\mu \equiv \lambda_q - \lambda_2 = \pm 1/2$ = total final helicity (along $\vec{q}$)

Definition of <u>helicity amplitude</u> $A_{\mu\lambda}(\theta,\phi)$: Walker[3]

initial states labeled by $\lambda = 3/2, 1/2, -1/2, -3/2$
$\theta = 0, \phi = 0$

final states labeled by $\mu = 1/2, -1/2$
θ, ϕ

A is defined in terms of the S matrix by:

$$S = 1 + i(2\pi)^4 \delta^4(P_f - P_i) (8\pi WN) A \qquad (5.1)$$

where $N \equiv (2k\ 2E_1\ 2\omega\ 2E_2)^{-\frac{1}{2}}$ and P_f and P_i are the total final and initial four-momenta.

The <u>cross-section formula</u> is ($M \equiv 8\pi WNA$) :

$$v_{rel}\, d\sigma = |M|^2 (2\pi)^4 \delta^4(P_f - P_i) \frac{d^3q}{(2\pi)^3} \frac{d^3p_2}{(2\pi)^3} \qquad (5.2)$$

This reduces to:

$$\left(\frac{d\sigma}{d\Omega}\right)^{CM}_{\mu\lambda}(\theta,\phi) = \frac{q}{k} |A_{\mu\lambda}(\theta,\phi)|^2 \qquad (5.3)$$

There are 8 amplitudes $A_{\mu\lambda}$ corresponding to the 4 possible values of λ and the 2 possible values of μ. However, by parity symmetry, only 4 of these amplitudes are independent [63]. That is:

$$A_{-\mu,-\lambda}(\theta,\phi) = -e^{i(\lambda-\mu)(\pi-2\phi)} A_{\mu\lambda}(\theta,\phi) \qquad (5.4)$$

Definition of the helicity amplitudes $H_i(\theta,\phi)$

Let H_1, H_2, H_3, H_4 be the 4 independent helicity amplitudes for photon helicity $\lambda_k = +1$ defined by the matrix:

$$A(\lambda_k=+1) \equiv \begin{pmatrix} A_{1/2,3/2} & A_{1/2,1/2} \\ A_{-1/2,3/2} & A_{-1/2,1/2} \end{pmatrix} = \begin{pmatrix} H_1 & H_2 \\ H_3 & H_4 \end{pmatrix} \qquad (5.5)$$

Note that H_1 and H_3 have initial helicity 3/2 while H_2 and H_4 have initial helicity 1/2.

Formulas for differential cross section, polarization, beam asymmetry, and target asymmetry (from Walker [3]).

Setting $\phi = 0$, we have:

$$\sigma(\theta) \equiv \left(\frac{d\sigma}{d\Omega}\right)^{CM}(\theta) = \frac{1}{2}\frac{q}{k}\sum_{fi}\sum|A_{fi}(\theta)|^2 = \frac{1}{2}\frac{q}{k}\,\mathrm{Tr}(A^\dagger A)$$

$$= \frac{1}{2}\frac{q}{k}\sum_{i=1}^{4}|H_i(\theta)|^2 \qquad (5.6)$$

$$\text{Polarization } \vec{P}\cdot(\hat{k}\times\hat{q}) = \frac{1}{2}\frac{q}{k}\frac{1}{\sigma(\theta)}\,\mathrm{Tr}(A^\dagger\sigma_y A)$$

$$= -\frac{q}{k}\frac{1}{\sigma(\theta)}\,\mathrm{Im}(H_1H_3^*-H_2H_4^*) \qquad (5.7)$$

where σ_y is the y Pauli spin matrix. The above results hold for both $\lambda_k = +1$ and -1.

Polarized photon asymmetry

$$\Sigma(\theta) = \frac{\sigma_\perp - \sigma_\parallel}{\sigma_\perp + \sigma_\parallel} = \frac{q}{k}\frac{1}{\sigma(\theta)} \mathrm{Re}(H_1 H_4^* - H_2 H_3^*) \qquad (5.8)$$

where $\sigma_\perp$ is the cross section for linearly polarized photons with electric vector perpendicular to the reaction plane and $\sigma_\parallel$ for photons with electric vector parallel to the reaction plane.

Polarized target asymmetry

$$T(\theta) = \frac{\sigma_+ - \sigma_-}{\sigma_+ + \sigma_-} = \frac{q}{k}\frac{1}{\sigma(\theta)} \mathrm{Im}(H_1 H_2^* - H_3 H_4^*) \qquad (5.9)$$

where σ_+ and σ_- are the differential cross sections for target nucleons polarized + and - along the direction $\hat{k} \times \hat{q}$.

CGLN amplitudes - relationship to helicity amplitudes

The CGLN[51] amplitudes F_1, F_2, F_3, F_4 determine the photoproduction amplitude A by the formula:

$$iA(\vec{\varepsilon}) = i\,\vec{\sigma}\cdot\vec{\varepsilon}\,F_1 + \vec{\sigma}\cdot\hat{q}\;\vec{\sigma}\cdot(\hat{k}\times\vec{\varepsilon})\,F_2 + i\,\vec{\sigma}\cdot\hat{k}\;\hat{q}\cdot\vec{\varepsilon}\,F_3 + i\,\vec{\sigma}\cdot\hat{q}\;\hat{q}\cdot\vec{\varepsilon}\,F_4 \qquad (5.10)$$

where $\vec{\sigma}$ are the Pauli spin matrices and $\vec{\varepsilon}$ is the photon polarization vector. For photon spin defined along the direction of motion $\hat{k}$ $(=\hat{z})$, (helicity = ± 1) we have:

$$\vec{\varepsilon} = \vec{\varepsilon}_\pm = \mp (1/\sqrt{2})\ (\hat{x} \pm i\hat{y}) \qquad (5.11)$$

The helicity amplitudes may be written in terms of the CGLN amplitudes:

$$
\begin{aligned}
H_1(\theta,\phi) &= -(1/\sqrt{2})\, e^{i\phi} \sin\theta \cos\tfrac{1}{2}\theta \,(F_3 + F_4) \\
H_2(\theta,\phi) &= \sqrt{2} \cos\tfrac{1}{2}\theta \left[(F_2 - F_1) + \tfrac{1}{2}(1 - \cos\theta)\,(F_3 - F_4)\right] \\
H_3(\theta,\phi) &= (1/\sqrt{2})\, e^{2i\phi} \sin\theta \sin\tfrac{1}{2}\theta \,(F_3 - F_4) \\
H_4(\theta,\phi) &= \sqrt{2}\, e^{i\phi} \sin\tfrac{1}{2}\theta \left[(F_1 + F_2) + \tfrac{1}{2}(1 + \cos\theta)\,(F_3 + F_4)\right]
\end{aligned}
\tag{5.12}
$$

Chew and Lewis amplitudes - "spin-flip" and "spin-non-flip" cross sections

The Chew and Lewis (45) amplitudes $\vec{K}$ and L may be given by:

$$
iA(\vec{\varepsilon}) = i\,(-1/\sqrt{2})\,\left(\vec{\sigma}\cdot\vec{K}(\vec{\varepsilon}) + L(\vec{\varepsilon})\right) \tag{5.13}
$$

where $\vec{K}$ is the spin-flip amplitude and L is the spin-non flip amplitude. For photon polarization $\vec{\varepsilon} = \vec{\varepsilon}_+$ we have:

$$
\begin{aligned}
K_x &= F_1 - \cos\theta\, F_2 - \sin^2\theta \cos\phi\, e^{i\phi} F_4 \\
K_y &= i\, F_1 - i \cos\theta\, F_2 + \sin^2\theta \sin\phi\, e^{i\phi} F_4 \\
K_z &= \sin\theta\, e^{i\phi} F_2 + \sin\theta\, e^{i\phi} F_3 + \cos\theta \sin\theta\, e^{i\phi} F_4 \\
L &= -\sin\theta\, e^{i\phi} F_2
\end{aligned}
\tag{5.14}
$$

The "spin-non-flip" cross section is proportional to $\left(|L|^2\right)_{ave}$. Specifically, at $\phi = 0$, we have:

$$
\sigma(\theta)_{snf} = \frac{1}{2}\frac{q}{k} \sin^2\theta\, |F_2|^2 \tag{5.15}
$$

In terms of helicity amplitudes, this is:

$$\sigma(\theta)_{snf} = \frac{1}{4}\frac{q}{k}\left|H_1(\theta)\cos\tfrac{1}{2}\theta + H_2(\theta)\sin\tfrac{1}{2}\theta - H_3(\theta)\sin\tfrac{1}{2}\theta + H_4(\theta)\cos\tfrac{1}{2}\theta\right|^2 \qquad (5.16)$$

$$\sigma(\theta)_{sf} = \sigma(\theta) - \sigma(\theta)_{snf} \qquad (5.17)$$

Deuterium cross section

The deuterium cross section, obtained by assuming a simple 2-nucleon wave function for the deuteron and using the impulse approximation (45) is:

$$\sigma(\theta)_{deut} = \left(1 - (1/3)\ F(D) \right) \sigma(\theta)_{sf} + \left(1 - F(D) \right) \sigma(\theta)_{snf} \qquad (5.18)$$

where D is the lab nuclear recoil momentum and F(D) is the deuteron form factor given by

$$F(D) = \int \exp(i\vec{D}\cdot\vec{\rho})\ u_i^2(\vec{\rho})\ d^3\rho \qquad (5.19)$$

where $u_i(\vec{\rho})$ is the Hulthen wave function for the deuteron (see Appendix IV).

APPENDIX VI

PARTIAL WAVE AMPLITUDES

The helicity amplitudes may be decomposed into states of definite total angular momentum, definite initial and final total helicity. The following equation defines the helicity coefficients $A^j_{\mu\lambda}$:

$$A_{\mu\lambda}(\theta,\phi) = \sum_j A^j_{\mu\lambda} \ (2j + 1) \ d^j_{\lambda\mu}(\theta) \ e^{i(\lambda-\mu)\phi} \qquad (6.1)$$

where the functions $(2j + 1) \ d^j_{\lambda\mu}(\theta) \ e^{i(\lambda-\mu)\phi}$ are orthogonal and normalized to 4π when integrated over all solid angles. The d functions are described in Jacob and Wick(63). I use the definition given in Equation 18 of Walker(3).

The total cross section may be expressed very simply in terms of the helicity coefficients:

$$\sigma_T = 2\pi \frac{q}{k} \sum_j \sum_\mu \sum_\lambda (2j + 1) \ |A^j_{\mu\lambda}|^2 \qquad (6.2)$$

where the sum goes over only positive values of λ.

Helicity elements are defined as the linear combinations of the helicity coefficients which have definite initial state total helicity and definite final state parity, thus corresponding to a definite final state orbital angular momentum. These elements are formed by taking sums and differences of coefficients with final total helicity μ $= +\frac{1}{2}$ and $-\frac{1}{2}$. Define the helicity elements $A_{\ell\pm}$ and $B_{\ell\pm}$:

$$A_{n+} = -(1/\sqrt{2})\ (A^{j}_{1/2,1/2} + A^{j}_{-1/2,1/2})$$

$$A_{(n+1)-} = (1/\sqrt{2})\ (A^{j}_{1/2,1/2} - A^{j}_{-1/2,1/2})$$

$$B_{n+} = \left(\frac{2}{n(n+2)}\right)^{1/2} (A^{j}_{1/2,3/2} + A^{j}_{-1/2,3/2}) \qquad (6.3)$$

$$B_{(n+1)-} = -\left(\frac{2}{n(n+2)}\right)^{1/2} (A^{j}_{1/2,3/2} - A^{j}_{-1/2,3/2})$$

$A_{\ell\pm}$ refers to initial helicity 1/2, orbital angular momentum ℓ, and total angular momentum $j = \ell \pm 1/2$. $B_{\ell\pm}$ refers to initial helicity 3/2, orbital angular momentum ℓ, and total angular momentum $j = \ell \pm 1/2$. The orbital angular momentum ℓ refers to the final pion-nucleon system. The parity of this system is $-(-1)^{\ell}$ where the initial minus sign is due to the negative parity of the pion.

Finally, the helicity amplitudes may be expressed in terms of the helicity elements as follows:

$$H_1(\theta,\phi) = (1/\sqrt{2})\ e^{i\phi} \sin\theta \cos\tfrac{1}{2}\theta \sum_{n=1}^{\infty} (B_{n+} - B_{(n+1)-})\ (P''_n - P''_{n+1})$$

$$H_2(\theta,\phi) = \sqrt{2} \cos\tfrac{1}{2}\theta \sum_{n=0}^{\infty} (A_{n+} - A_{(n+1)-})\ (P'_n - P'_{n+1}) \qquad (6.4)$$

$$H_3(\theta,\phi) = (1/\sqrt{2})\ e^{2i\phi} \sin\theta \sin\tfrac{1}{2}\theta \sum_{n=1}^{\infty} (B_{n+} + B_{(n+1)-})\ (P''_n + P''_{n+1})$$

$$H_4(\theta,\phi) = \sqrt{2}\ e^{i\phi} \sin\tfrac{1}{2}\theta \sum_{n=0}^{\infty} (A_{n+} + A_{(n+1)-})\ (P'_n + P'_{n+1})$$

where the d functions have been expressed in terms of sums and differences of derivatives of Legendre polynomials.

The contributions of each helicity element to the four helicity amplitudes H_i are shown in Figure 42. Note that at 0^o, the only non-zero helicity amplitude is H_2 and that at 180^o, the only non-zero helicity amplitude is H_4. Only the $A_{\ell\pm}$ helicity elements contribute at 0^o and 180^o because of the conservation of angular momentum.

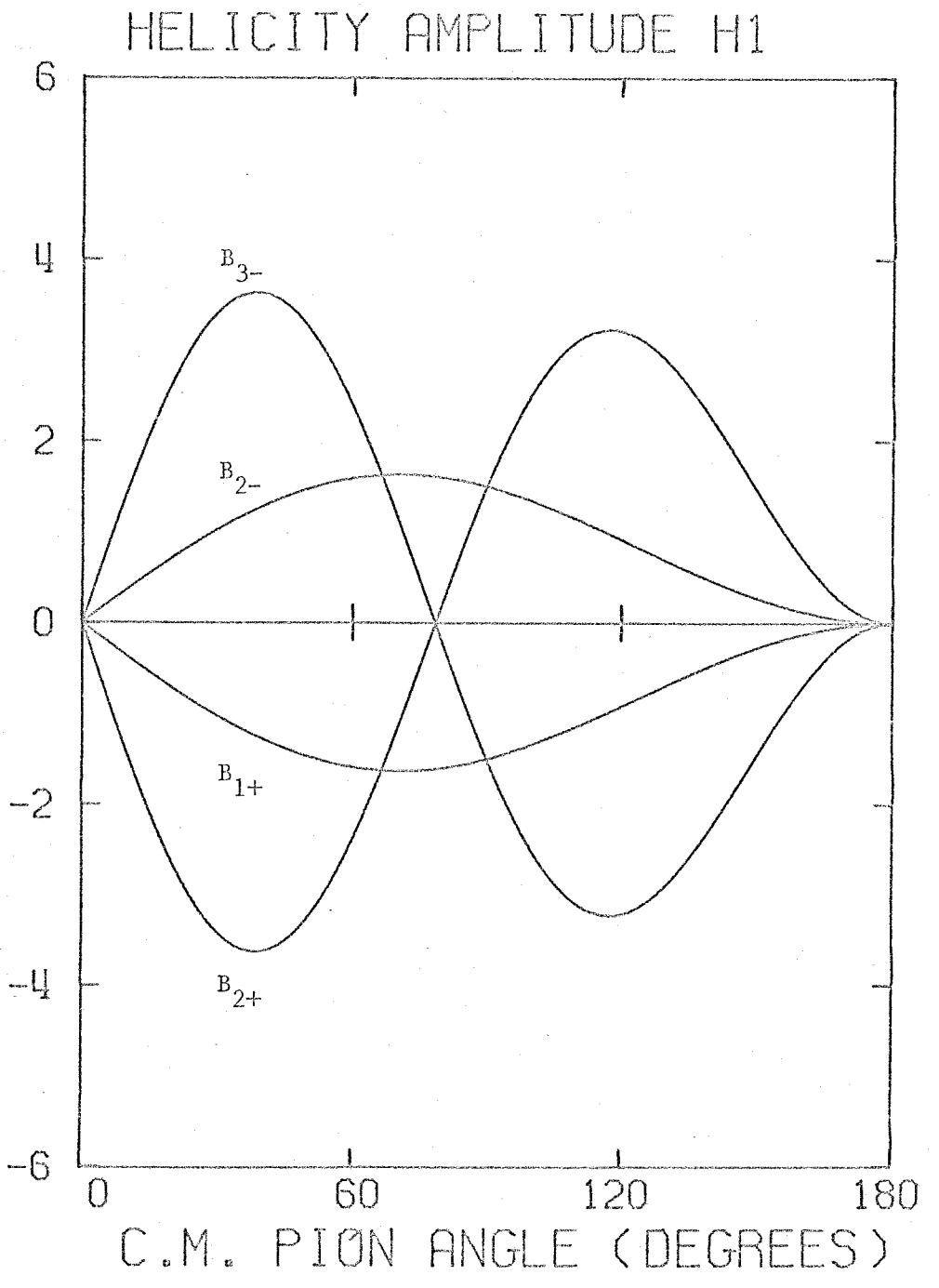
HELICITY AMPLITUDE H1
6
4
2
0
-2
-4
-6
B_{3-}
B_{2-}
B_{1+}
B_{2+}
0
60
120
180
C.M. PION ANGLE (DEGREES)

FIGURE 42.1

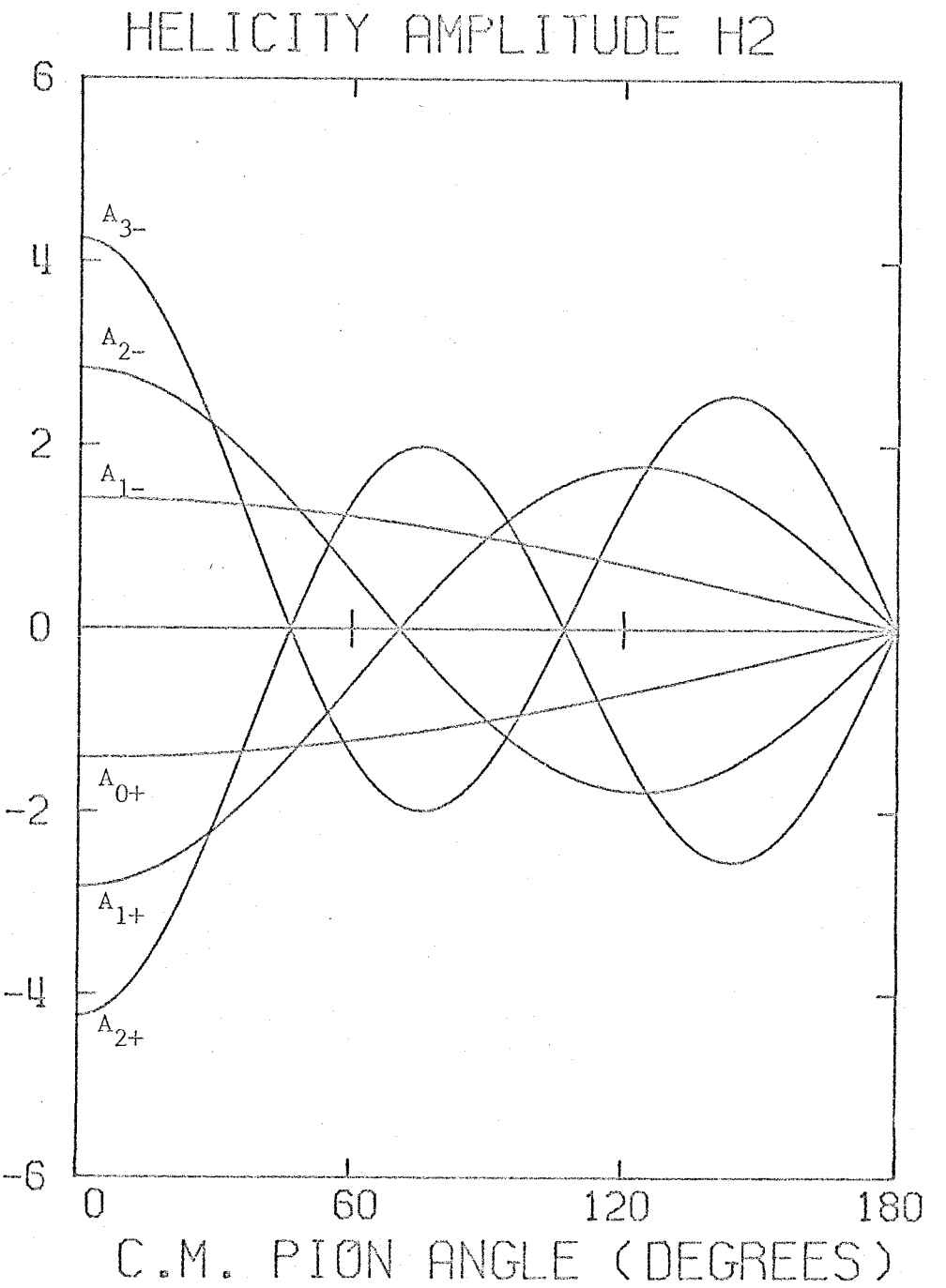
HELICITY AMPLITUDE H2
6
4
2
0
-2
-4
-6
A3-
A2-
A1-
A0+
A1+
A2+
0
60
120
180
C.M. PION ANGLE (DEGREES)

FIGURE 42.2

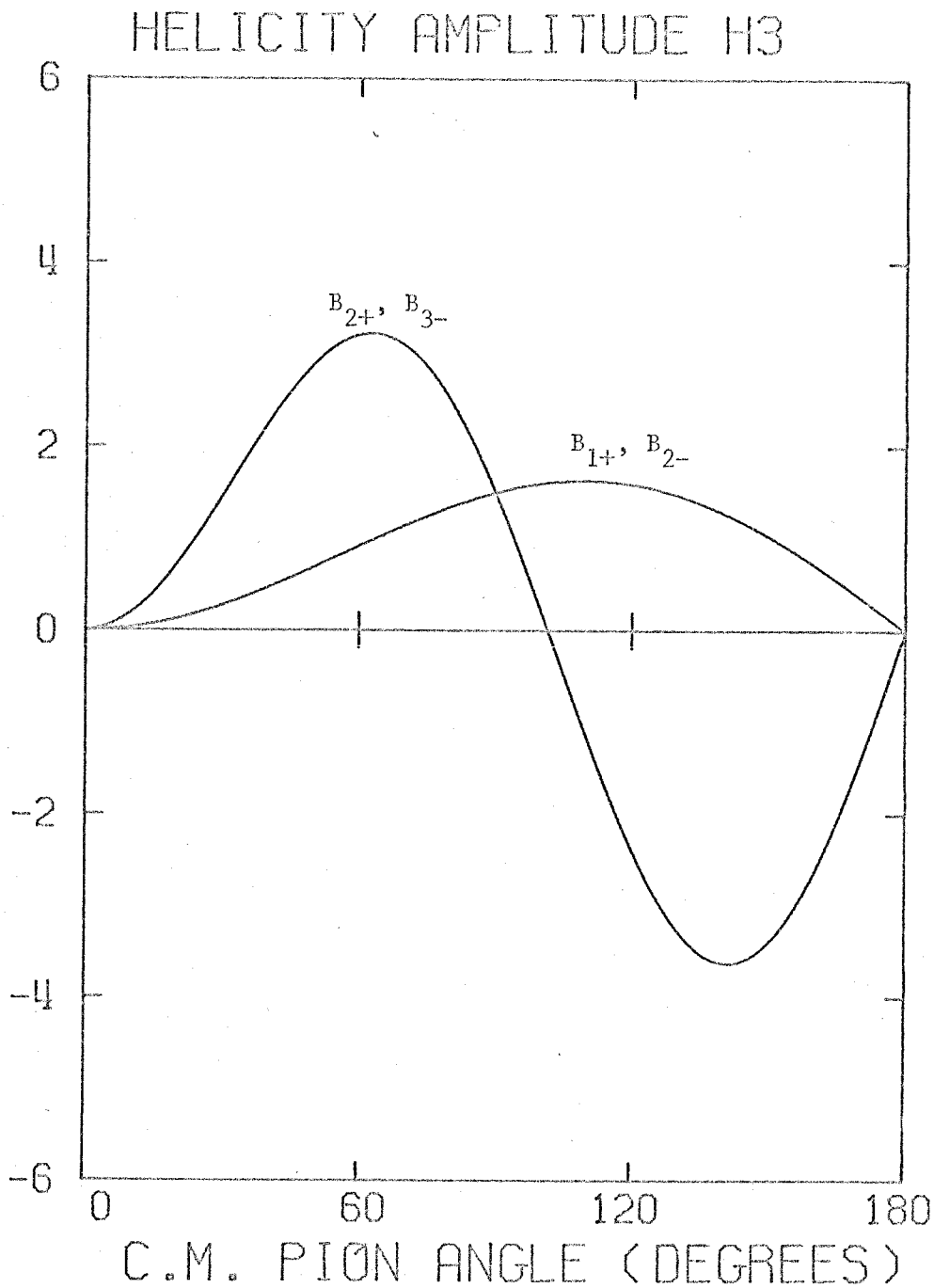
HELICITY AMPLITUDE H3
6
4
2
0
-2
-4
-6
B_{2+}, B_{3-}
B_{1+}, B_{2-}
0
60
120
180
C.M. PION ANGLE (DEGREES)

FIGURE 42.3

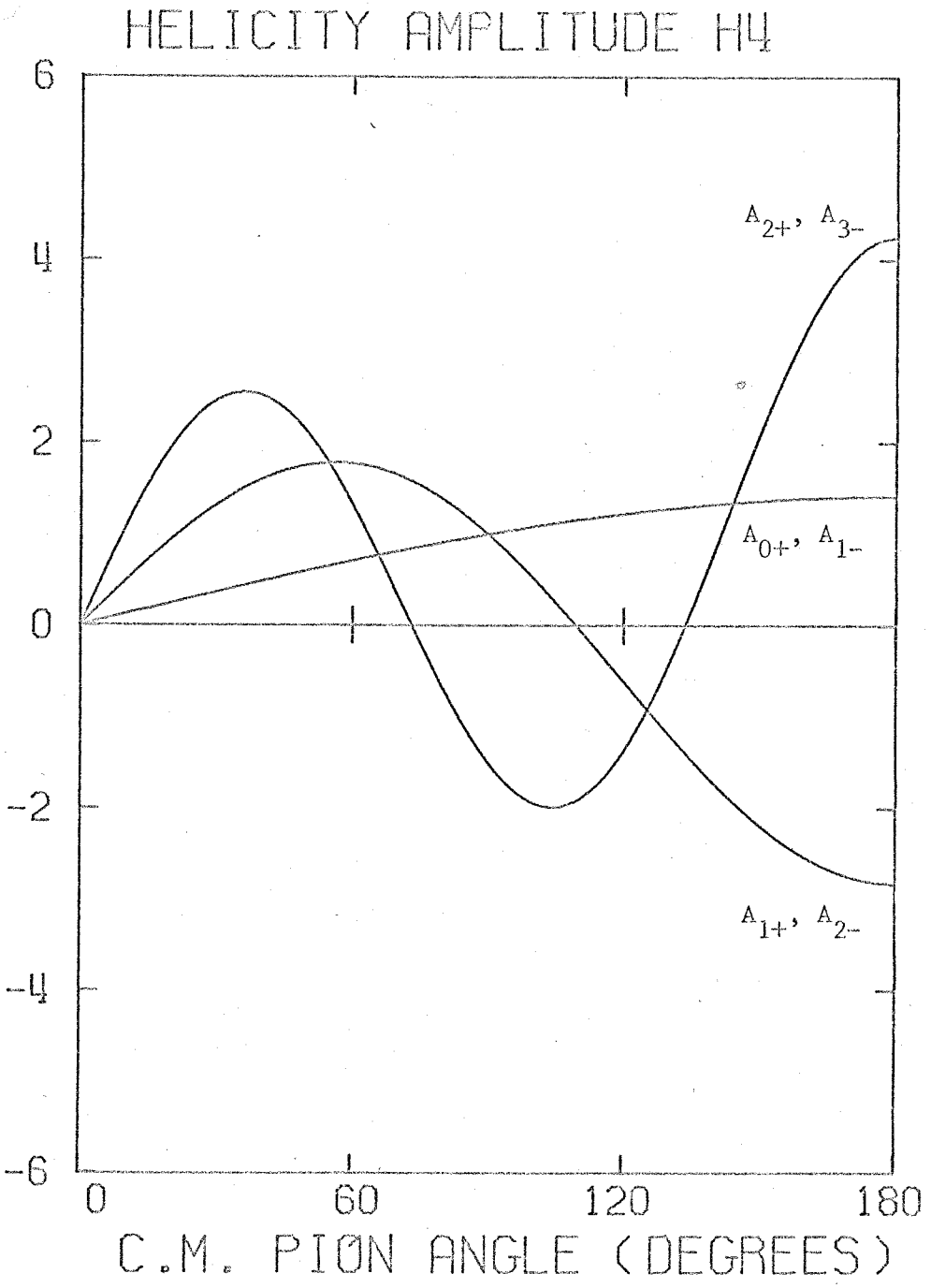
HELICITY AMPLITUDE H4
6
4
2
0
-2
-4
-6
0
60
120
180
C.M. PION ANGLE (DEGREES)
A_{2+}, A_{3-}
A_{0+}, A_{1-}
A_{1+}, A_{2-}

FIGURE 42.4

APPENDIX VII

BORN TERMS AND RESONANCES

A. Born terms.

The Feynman diagrams for the Born approximation are shown in Figure 43. G_π is the pion-nucleon coupling constant for the particular reaction. The couplings are:

$$G_{\pi^+} = -G_{\pi^-} = -\sqrt{2}\, G_{\pi^o p} = \sqrt{2}\, G_{\pi^o n} = \sqrt{2}\, G \qquad (7.1)$$

where $G^2/4\pi = 14.7$. $e^2/4\pi$ is the electromagnetic coupling constant and is equal to $1/137.036$. $\varepsilon_\pi = -1$, 0, or +1 for coupling to a π^-, π^o, or π^+ respectively. ε_1 and ε_2 each equal 0 or 1 for coupling to a neutron or a proton respectively. μ_1 and μ_2 each separately equal -1.913 or +1.793 for magnetic coupling to a neutron or proton respectively.

For convenience in the following formulas, define $Z_1 = (E_1 + M_1)^{\frac{1}{2}}$ and $Z_2 = (E_2 + M_2)^{\frac{1}{2}}$. The Born approximation for electric coupling e is given in terms of the CGLN amplitudes (see Appendix V) by:

$$F_1 = -\frac{eG_\pi}{4\pi}\frac{Z_1 Z_2}{W+M_1}\left(\frac{\varepsilon_1}{2W} + \frac{k\varepsilon_2}{u - M_2^2}\right)$$

$$F_2 = \frac{eG_\pi}{4\pi}\frac{qZ_1}{Z_2(W+M_1)}\left(\frac{\varepsilon_1}{2W} + \frac{k\varepsilon_2}{u - M_2^2}\right) \qquad (7.2)$$

$$F_3 = \frac{eG_\pi}{4\pi}\frac{qkZ_2}{WZ_1}\left(\frac{\varepsilon_\pi}{t - m_\pi^2} - \frac{\varepsilon_2}{u - M_2^2}\right)$$

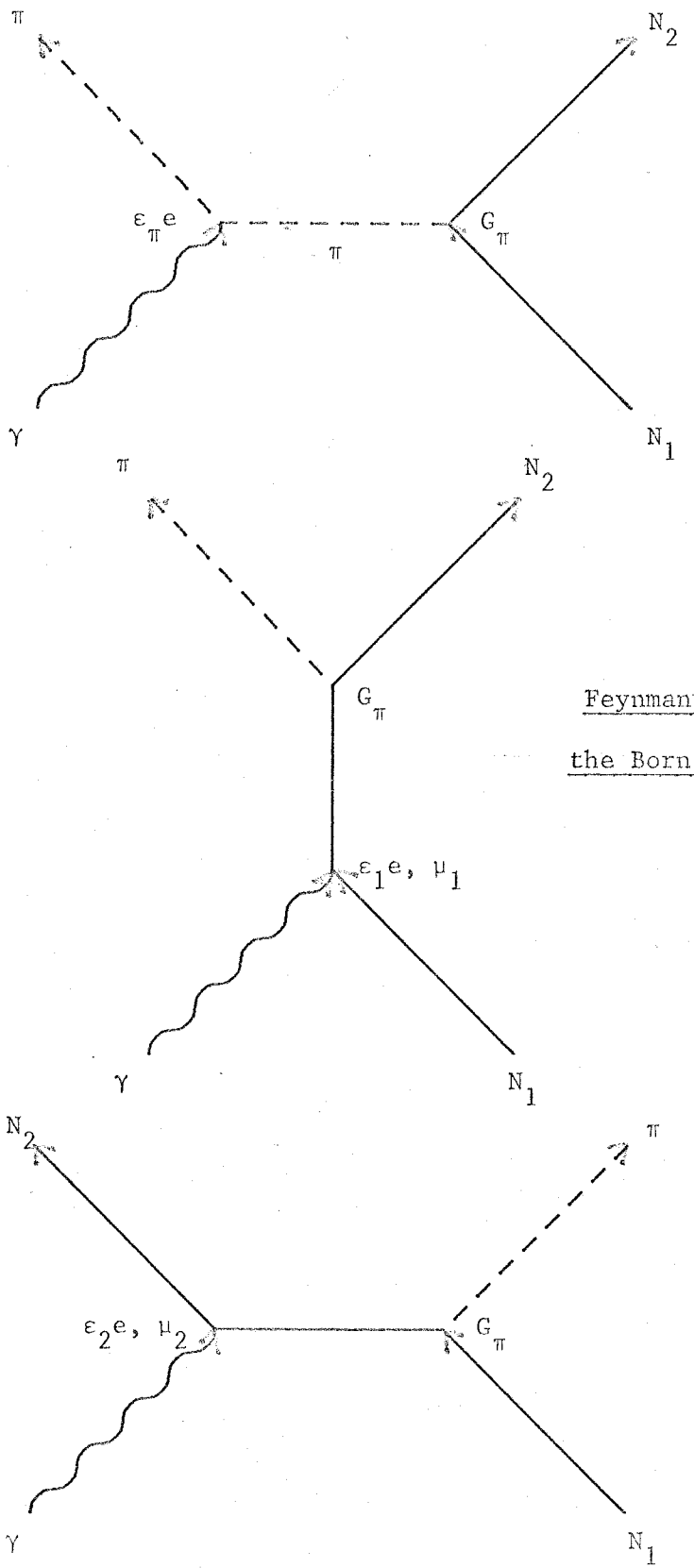

Feynman Diagrams for the Born Approximation

FIGURE 43

$$F_4 = -\frac{eG_\pi}{4\pi}\frac{q^2 Z_1}{WZ_2}\left(\frac{\varepsilon_\pi}{t - m_\pi^2} - \frac{\varepsilon_2}{u - M_2^2}\right)$$

where $W^2 = s$, and s, t, and u are the Mandelstam variables given by:

$$\begin{aligned} s &= (k + p_1)^2 = (q + p_2)^2 \\ t &= (k - q)^2 = (p_1 - P_2)^2 \\ u &= (k - p_2)^2 = (q - p_1)^2 \end{aligned} \tag{7.3}$$

The Born approximation for the anomalous magnetic moment terms is:

$$\begin{aligned} F_1 &= \frac{eG_\pi}{4\pi}\frac{kZ_2}{4WZ_1}\left(\frac{\mu_1}{M_1} - \frac{\mu_2 Z_1^2}{kM_2} - \frac{2\mu_2(W + M_1)}{u - M_2^2}\right) \\ F_2 &= \frac{eG_\pi}{4\pi}\frac{qk}{4WZ_1Z_2}\left(\frac{\mu_1 Z_1^2}{M_1 k} - \frac{\mu_2}{M_2} + \frac{2\mu_2(W + M_1)}{u - M_2^2}\right) \\ F_3 &= -\frac{eG_\pi}{4\pi}\frac{\mu_2 qk}{2WM_2}\frac{Z_2}{Z_1}\frac{W + M_1}{u - M_2^2} \\ F_4 &= -\frac{eG_\pi}{4\pi}\frac{\mu_2 qk}{2WM_2}\frac{q}{Z_1Z_2}\frac{W + M_1}{u - M_2^2} \end{aligned} \tag{7.4}$$

B. Resonances.

The resonant amplitude in Walker's model(3) is given by:

$$A(W) = A(W_o)\left(\frac{k_o q_o}{kq}\right)^{\frac{1}{2}} \frac{W_o \Gamma^{\frac{1}{2}} \Gamma_\gamma^{\frac{1}{2}}}{s_o - s - iW_o\Gamma} \tag{7.5}$$

where

$$\Gamma = \Gamma_o \left(\frac{q}{q_o}\right)^{2\ell+1} \left(\frac{q_o^2 + X^2}{q^2 + X^2}\right)^{\ell}$$

$$\Gamma_\gamma = \Gamma_o \left(\frac{k}{k_o}\right)^{2j_\gamma} \left(\frac{k_o^2 + X^2}{k^2 + X^2}\right)^{j_\gamma} \tag{7.6}$$

where W_o is the central energy, and k_o, q_o, and s_o are the values of k, q, and s at $W = W_o$. The resonance parameters are:

a) the central energy W_o

b) the width Γ_o

c) the amplitude $A(W_o)$ (of the imaginary part at the central energy)

d) the angular momentum ℓ

e) the photon angular momentum j_γ (not really a definite quantity for helicity elements)

f) the parameter X which gives a cutoff for large k or q .

Typical behavior of the real and imaginary parts of a resonance is shown in Figure 44.

Typical Behavior of a Resonance

The parameters here are:

W_o = 1520 MeV (photon energy = 760 MeV)

Γ_o = 120 MeV

$A(W_o)$ = +1.00

ℓ = 2, j_γ = 1, and X = 0.350

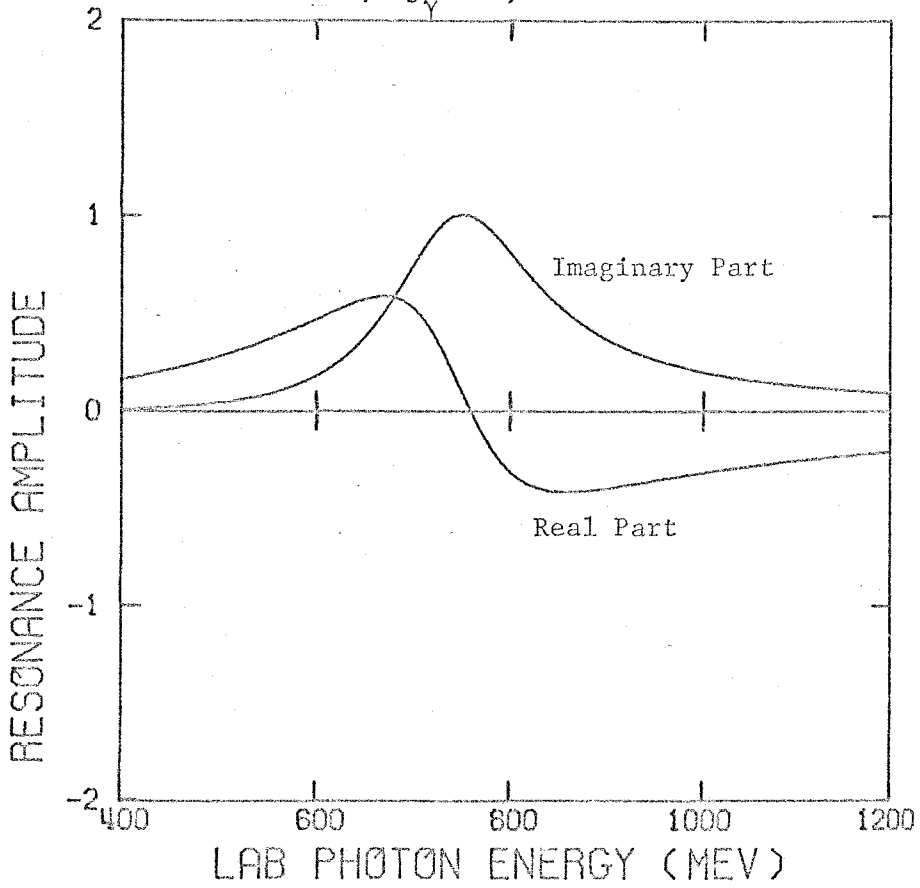

FIGURE 44

APPENDIX VIII

FITTING PROCEDURE

We are trying to fit cross sections, polarizations, and asymmetries with the parameters $A_{\ell\pm}$, $B_{\ell\pm}$ the add-on helicity elements. Or in the case of the "all energy" fits, we use as parameters the resonance amplitudes, widths, energies, and the polynomial coefficients which specify the smooth energy dependence of the add-on elements.

The cross sections etc. are quadratic in the A and B helicity elements and are also non-linear in the resonance parameters. Thus a simple least squares fit, which requires the fitting functions to be linear in the parameters, will not work. I will describe two methods for obtaining a fit when the fitting functions are non-linear. I will then write down the actual algorithm used in my analysis, which is a combination of the two fitting methods.

A. Possible fitting methods.

1) Linearization of fitting functions

It is possible to linearize the fitting functions by expanding them in a Taylor's series in the parameters. However, neglecting the non-linear terms should be expected to work only when the zero-order parameters are already close to the final solution. After the fitting function is linearized, we then go through the procedure of minimizing χ^2, which is the weighted sum of squares of the deviations of the data points

from the fitting function. Let us go through this procedure.

First, define:

$x_i \equiv$ i'th experimental data value (cross section, etc.) where $i = 1,2,\ldots,n$

$\sigma_i \equiv$ error of the i'th experimental data point

$f_i(a_1,a_2,\ldots,a_m) \equiv f_i \equiv$ value of the fitting function at the i'th data point where $i = 1,2,\ldots,n$ and $a_1,a_2,\ldots,a_m$ are the m parameters (eg. helicity elements or resonance parameters) being determined by the fit.

$f_i(a_1^o,a_2^o,\ldots,a_m^o) \equiv f_i(0) \equiv$ value of the fitting function for the zero-order (initial) set of parameters.

Now expand f_i around the point $(a_1^o,a_2^o,\ldots,a_m^o)$.

$$f_i = f_i(0) + \sum_{j=1}^{m} \frac{\partial f_i}{\partial a_j}(0)\cdot(a_j - a_j^o) + \frac{1}{2}\sum_{j=1}^{m}\sum_{k=1}^{m} \frac{\partial^2 f_i}{\partial a_j \partial a_k}(0) \times (a_j - a_j^o)\cdot(a_k - a_k^o) + \cdots\cdots \qquad (8.1)$$

where (0) after the derivatives means that these derivatives are evaluated at the point $(a_1^o,a_2^o,\ldots,a_m^o)$.

Define $\delta a_j = (a_j - a_j^o)$

Now form χ^2 :

$$\chi^2 \equiv \sum_{i=1}^{n} \frac{1}{\sigma_i^2} (x_i - f_i)^2$$

$$= \sum_{i=1}^{n} \frac{1}{\sigma_i^2} \left(x_i - f_i(0) - \sum_{j=1}^{m} \frac{\partial f_i}{\partial a_j}(0) \cdot \delta a_j \right. \tag{8.2}$$

$$\left. - \sum_{j=1}^{m} \sum_{k=1}^{m} \frac{1}{2} \frac{\partial^2 f_i}{\partial a_j \partial a_k}(0) \cdot \delta a_j \delta a_k - \cdots \right)^2$$

To minimize, take the derivative with respect to each parameter and set equal to zero:

$$\frac{\partial \chi^2}{\partial a_\ell} = \sum_{i=1}^{n} \frac{1}{\sigma_i^2} \cdot 2 \left(x_i - f_i(0) - \sum_{j=1}^{m} \frac{\partial f_i}{\partial a_j}(0) \cdot \delta a_j \right.$$

$$\left. - \sum_{j=1}^{m} \sum_{k=1}^{m} \frac{1}{2} \frac{\partial^2 f_i}{\partial a_j \partial a_k}(0) \cdot \delta a_j \delta a_k - \cdots \right) \cdot \left(- \frac{\partial f_i}{\partial a_\ell}(0) \right. \tag{8.3}$$

$$\left. - \sum_{j=1}^{m} \frac{\partial^2 f_i}{\partial a_j \partial a_\ell}(0) \cdot \delta a_j - \cdots \right)$$

where use has been made of the fact that $\frac{\partial^2 f_i}{\partial a_j \partial a_\ell}(0)$ is symmetric in j and ℓ.

Now gather terms in 1, δa, δa^2, ...

$$\frac{\partial \chi^2}{\partial a_\ell} = 0$$

$$= \left(\sum_{i=1}^{n} \frac{2}{\sigma_i^2} (x_i - f_i(0)) \cdot \left(- \frac{\partial f_i}{\partial a_\ell}(0)\right) \right)$$

$$+ \sum_{j=1}^{m} \left(\sum_{i=1}^{n} \frac{2}{\sigma_i^2} \left(\frac{\partial f_i}{\partial a_j}(0) \frac{\partial f_i}{\partial a_\ell}(0) - (x_i - f_i(0)) \right.\right.$$

$$\left.\left. \times \frac{\partial^2 f_i}{\partial a_j \partial a_\ell}(0) \right) \right) \cdot \delta a_j + \cdots \qquad (8.4)$$

This can be written:

$$0 = - A_\ell + \sum_{j=1}^{m} B_{\ell j} \delta a_j + \sum_{j=1}^{m} \sum_{k=1}^{m} C_{\ell jk} \delta a_j \delta a_k + \cdots \qquad (8.5)$$

Approximation: assume that we are close to the final solution and that we can neglect the δa^2 (and all higher order) terms in comparison with the δa terms. Then we have:

$$A_\ell = \sum_{j=1}^{m} B_{\ell j} \delta a_j \qquad \text{for } \ell = 1,2,\ldots,m \qquad (8.6)$$

where

$$A_\ell = \sum_{i=1}^{n} \frac{2}{\sigma_i^2} (x_i - f_i(0)) \cdot \frac{\partial f_i}{\partial a_\ell}(0) \qquad (8.7)$$

$$B_{\ell j} = \sum_{i=1}^{n} \frac{2}{\sigma_i^2} \left(\frac{\partial f_i}{\partial a_j}(0) \frac{\partial f_i}{\partial a_\ell}(0) - (x_i - f_i(0)) \frac{\partial^2 f_i}{\partial a_j \partial a_\ell}(0) \right)$$

In matrix notation, the equation is:

$$\vec{A} = B\,\vec{\delta a} \tag{8.8}$$

The solution is:

$$\vec{\delta a} = B^{-1}\,\vec{A} \tag{8.9}$$

which can be obtained by inverting the symmetric matrix B. The δa's obtained in this solution do not necessarily give a minimum in χ^2 as we did not solve the exact equation 8.5. However, we hope that we have moved closer to the minimum and that we might reach it in a few more iterations. For each iteration we start with the a_j's obtained as a solution to the previous iteration.

2) Gradient method

In the case that the solution to the above linearization method does not converge, we have probably started with parameters which are too far away from the true final values, and thus the approximations (linearization) will not work.

Another kind of fitting procedure which requires χ^2 to decrease and is good when we are far from the minimum (but not so good when we approach the minimum) is called the "gradient search". Instead of trying to move directly to the minimum (as the linearization procedure tries),

the gradient search tries to move towards the minimum along the direction of steepest descent of χ^2, ie. along the negative of the gradient of χ^2.

The changes of the parameters along the negative gradient are proportional to $-\frac{\partial \chi^2}{\partial a_j}$. It is only necessary to choose a small enough proportionality factor λ to insure that the changing of the parameters by $\delta a_j = \lambda(-\frac{\partial \chi^2}{\partial a_j})$ will cause χ^2 to decrease.

B. Actual fitting procedure used.

My fitting procedure is a combination of methods 1) and 2) described above. To do this, I relate the solution via the gradient method to the solution via the linearization method. The gradient solution is:

$$\delta a_j = \lambda(-\frac{\partial \chi^2}{\partial a_j}) \tag{8.10}$$

Now for λ very small, δa_j is also very small. Then from equations 8.4, 8.5, and 8.7, we have:

$$\frac{\partial \chi^2}{\partial a_j} \simeq -A_j \tag{8.11}$$

and equation 8.10 reduces to:

$$\delta a_j = \lambda A_j \tag{8.12}$$

Now the solution to the linearization method (equation 8.9) may be written:

$$\delta a_j = \sum_{k=1}^{m} (B^{-1})_{jk} A_k \tag{8.13}$$

where $j = 1,2,\ldots,m$. We can almost resurrect the form of equation 8.12 by taking only the diagonal terms of 8.13 and inserting λ. This gives:

$$\delta a_j = (B^{-1})_{jj} \lambda A_j \tag{8.14}$$

It turns out that using equation 8.14 to find a set of parameters which cause a decrease in χ^2 works almost as well as using equation 8.12 (8.10) directly. The scale factors $(B^{-1})_{jj}$ have little effect. This fact makes it very easy to write an algorithm which will combine the gradient search and the linearization method. In the algorithm, I solve the matrix equation

$$\vec{A} = C\,\vec{\delta a} \tag{8.15}$$

for the δa's where the matrix C is defined:

$$C_{\ell j} \equiv \begin{cases} B_{\ell j} \cdot (1+\gamma) & \text{for } \ell = j \\ B_{\ell j} & \text{for } \ell \neq j \end{cases} \tag{8.16}$$

where A and B are given by equations 8.7 and γ is a parameter

whose value determines whether the fitting method is closer to a gradient search or to the linearization procedure. If γ is very small compared to one, $C \simeq B$ and the solution is the same as for the linearization method. If γ is large compared to one, the diagonal elements of B predominate and the solution is the same as for equation 8.14 (the modified gradient search) with $\lambda \simeq 1/\gamma$. I use the following algorithm which is described by Bevington(64).

Algorithm for fit:

1) Compute χ^2 due to the initial set of parameters.
2) Start initially with $\gamma = 1/9$
3) Compute $\delta\vec{a}$ using equation 8.15 with the present choice of γ.
4) Compute χ^2 from the latest parameters $(a_j + \delta a_j)$ and latest choice of γ.
5) If $\chi^2(\vec{a} + \delta\vec{a}) > \chi^2(\vec{a})$, increase γ by a factor of 3 and go to step 3 .
6) If $\chi^2(\vec{a} + \delta\vec{a}) < \chi^2(\vec{a})$, decrease γ by a factor of 3, consider $\vec{a}' = \vec{a} + \delta\vec{a}$ to be the new starting point, and go to step 3 .
7) If in step 6, the change in parameters becomes smaller than the error of the fit, the iteration procedure has converged and take $\vec{a}$ as the final solution.

Finally, in the linearization formulas, I have found it practical to drop the second derivatives in the $B_{\ell j}$ (equation 8.7).

APPENDIX IX

FINAL HELICITY ELEMENT FITS

1) Add-on Elements - π^- Photoproduction - Figure 45

2) Total Elements - π^- Photoproduction - Figure 46

3) Add-on Elements - π^+ Photoproduction - Figure 47

4) Total Elements - π^+ Photoproduction - Figure 48

FIGURE 45

FINAL FIT OF ADD-ON HELICITY
ELEMENTS FOR π^- PHOTOPRODUCTION

See page 148 for key to symbols.

In this fit, the resonances have been changed as follows:

$S_{11}(1535)$, amplitude -0.800
$\longrightarrow$ $S_{11}(1520)$, amplitude +0.25 (page 251)

$D_{13}(1520)$, amplitude 0.000 $\longrightarrow$ +0.300 (page 255)
helicity 1/2

$F_{15}(1688)$, amplitude -0.500 $\longrightarrow$ -0.200 (page 260)
helicity 3/2

See Table 9, page 161, for complete summary of resonance changes.

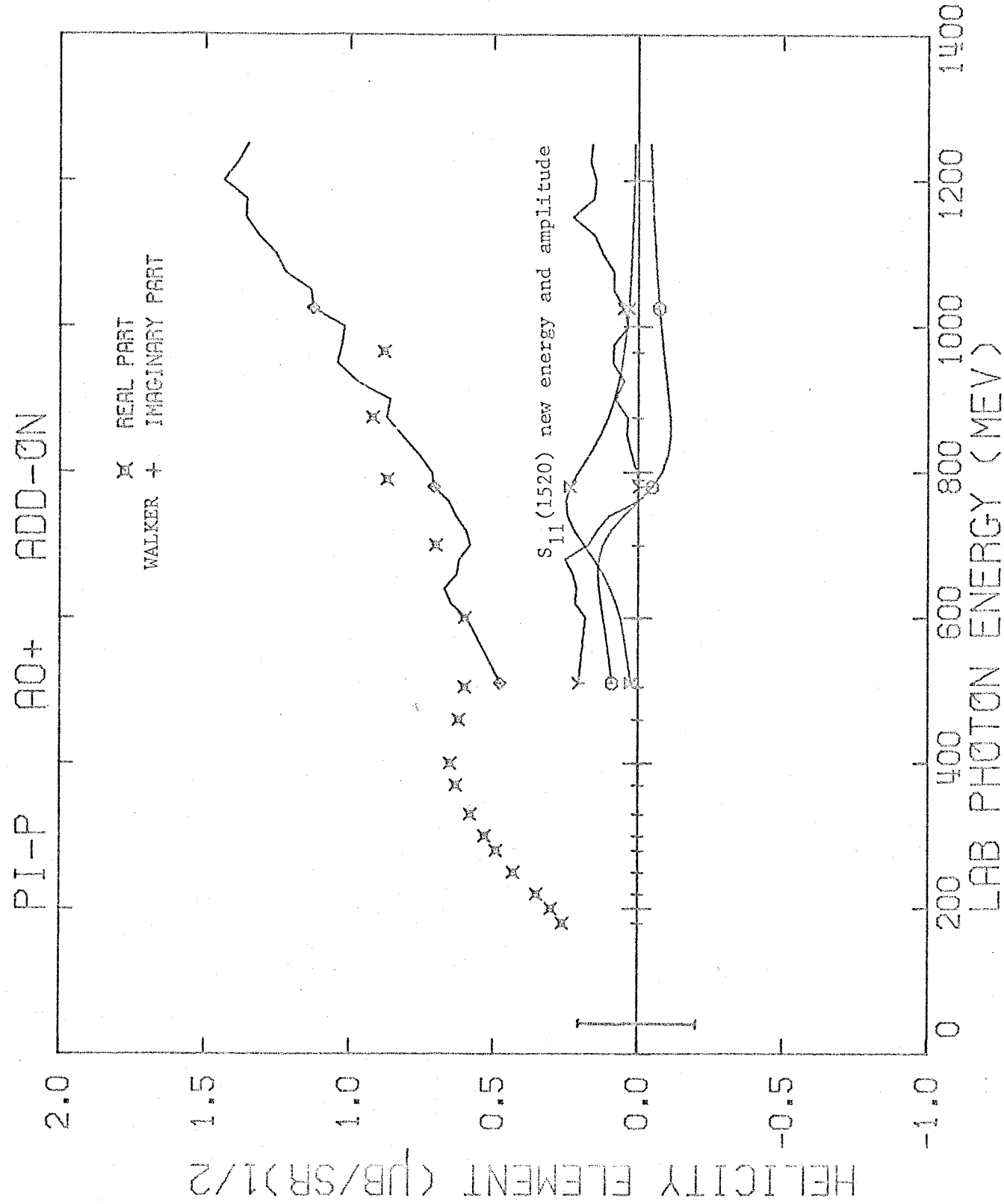
PI-P A0+ ADD-ON
REAL PART
WALKER + IMAGINARY PART
S_{11}(1520) new energy and amplitude
HELICITY ELEMENT (UB/SR)1/2
2.0
1.5
1.0
0.5
0.0
-0.5
-1.0
0
200
400
600
800
1000
1200
1400
LAB PHOTON ENERGY (MEV)

FIGURE 45.1

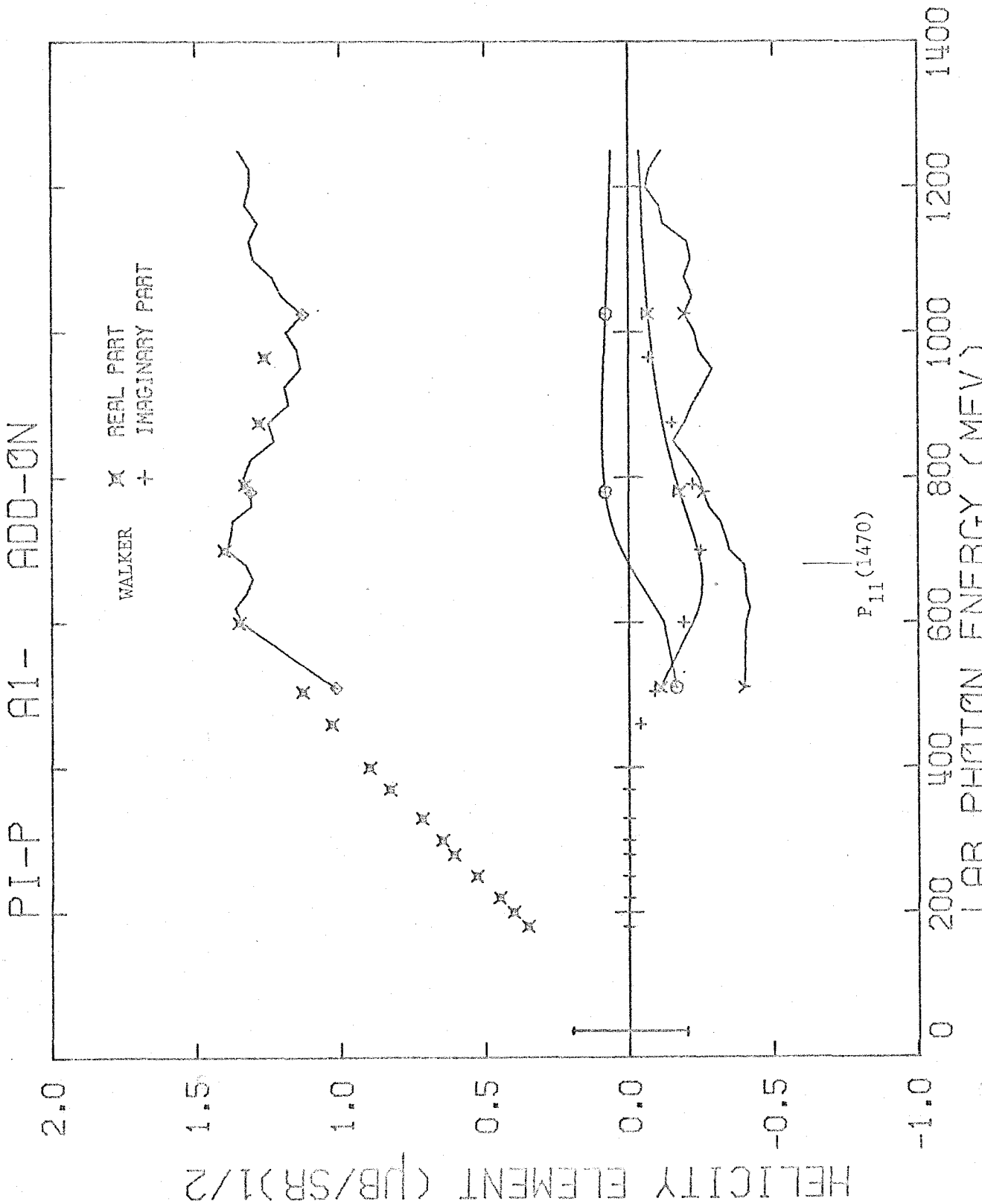
PI-P A1- ADD-ON
WALKER
REAL PART
IMAGINARY PART
$P_{11}(1470)$
HELICITY ELEMENT (UB/SR)1/2
LAB PHOTON ENERGY (MEV)
2.0
1.5
1.0
0.5
0.0
-0.5
-1.0
0
200
400
600
800
1000
1200
1400

FIGURE 45.2

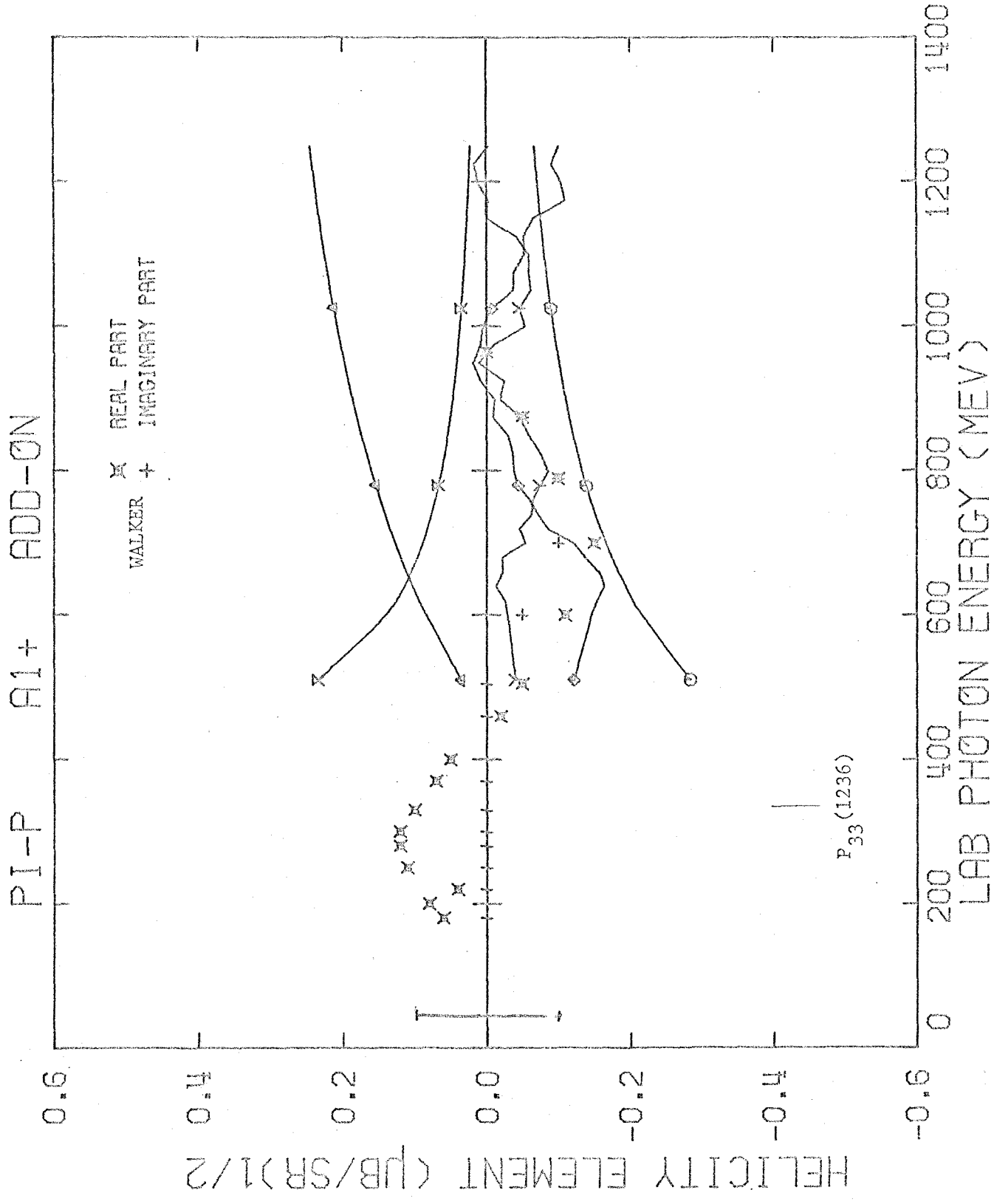
PI-P A1+ ADD-ON
WALKER
REAL PART
IMAGINARY PART
$P_{33}(1236)$
HELICITY ELEMENT (UB/SR)1/2
LAB PHOTON ENERGY (MEV)
0.6
0.4
0.2
0.0
-0.2
-0.4
-0.6
0
200
400
600
800
1000
1200
1400

FIGURE 45.3

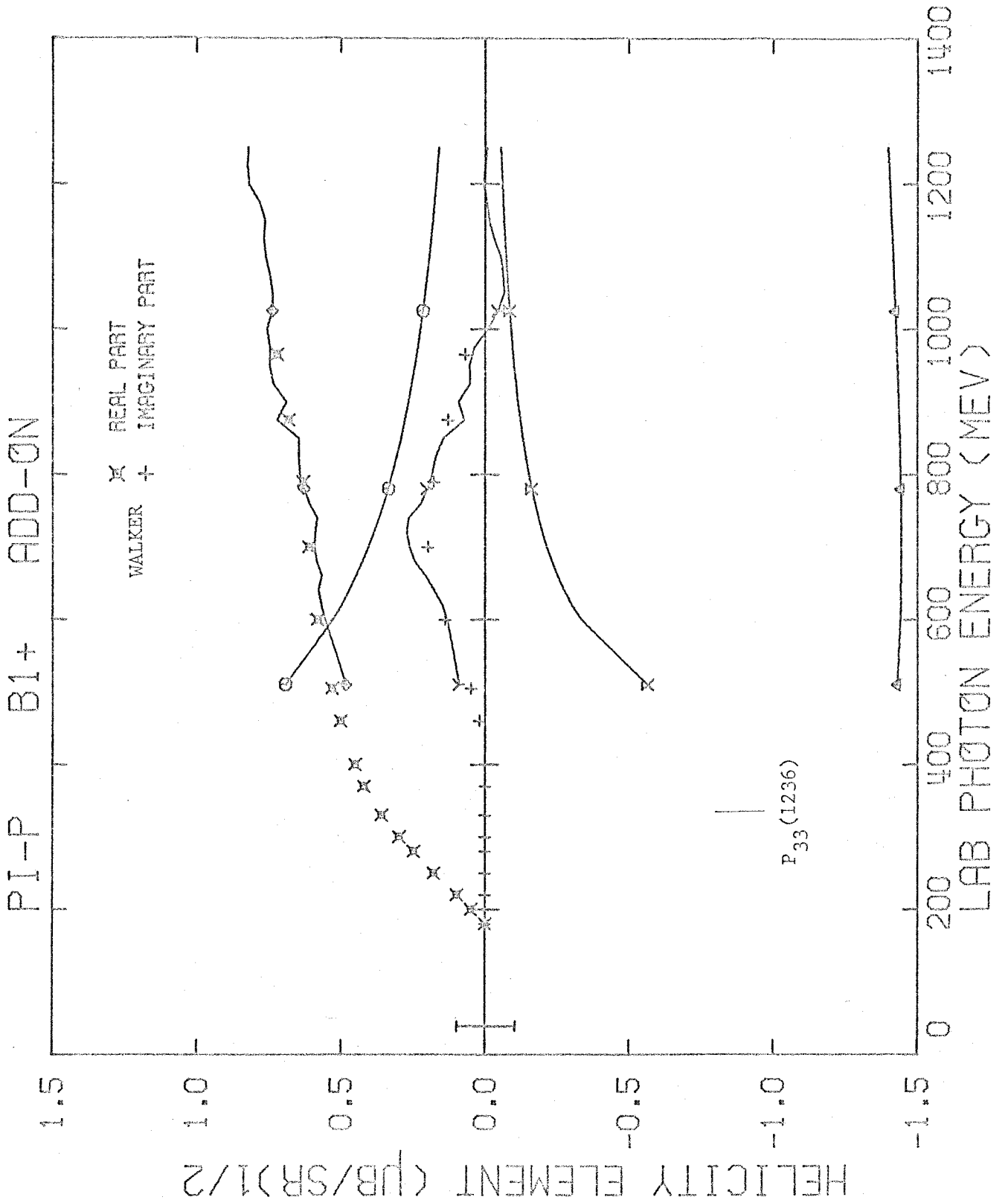
PI-P B1+ ADD-ON
WALKER
REAL PART
IMAGINARY PART
$P_{33}(1236)$
HELICITY ELEMENT (UB/SR)1/2
LAB PHOTON ENERGY (MEV)
1.5
1.0
0.5
0.0
-0.5
-1.0
-1.5
0
200
400
600
800
1000
1200
1400

FIGURE 45.4

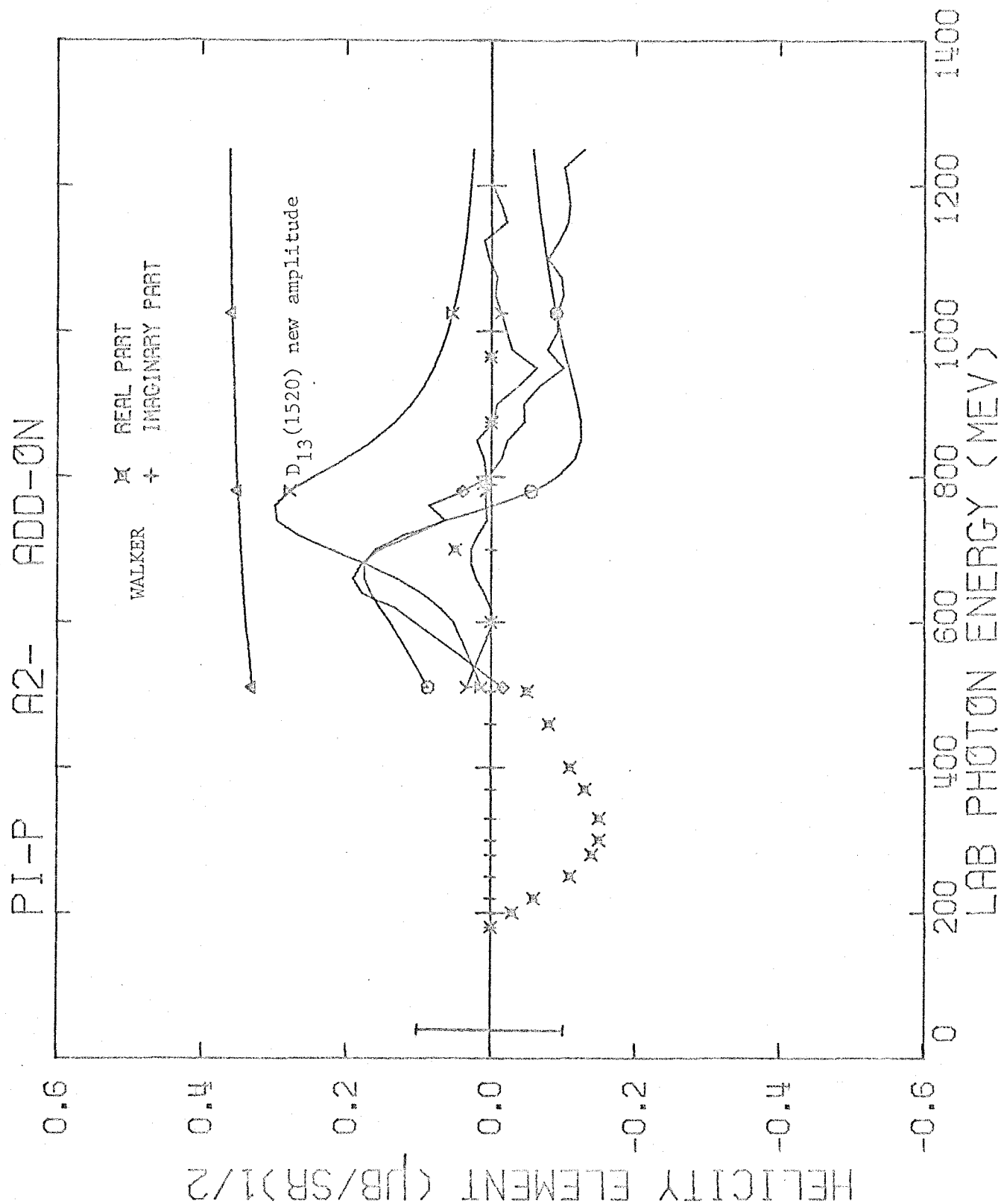
PI-P A2- ADD-ON
WALKER
REAL PART
IMAGINARY PART
D_{13}(1520) new amplitude
HELICITY ELEMENT (UB/SR)1/2
LAB PHOTON ENERGY (MEV)
0.6
0.4
0.2
0.0
-0.2
-0.4
-0.6
0
200
400
600
800
1000
1200
1400

FIGURE 45.5

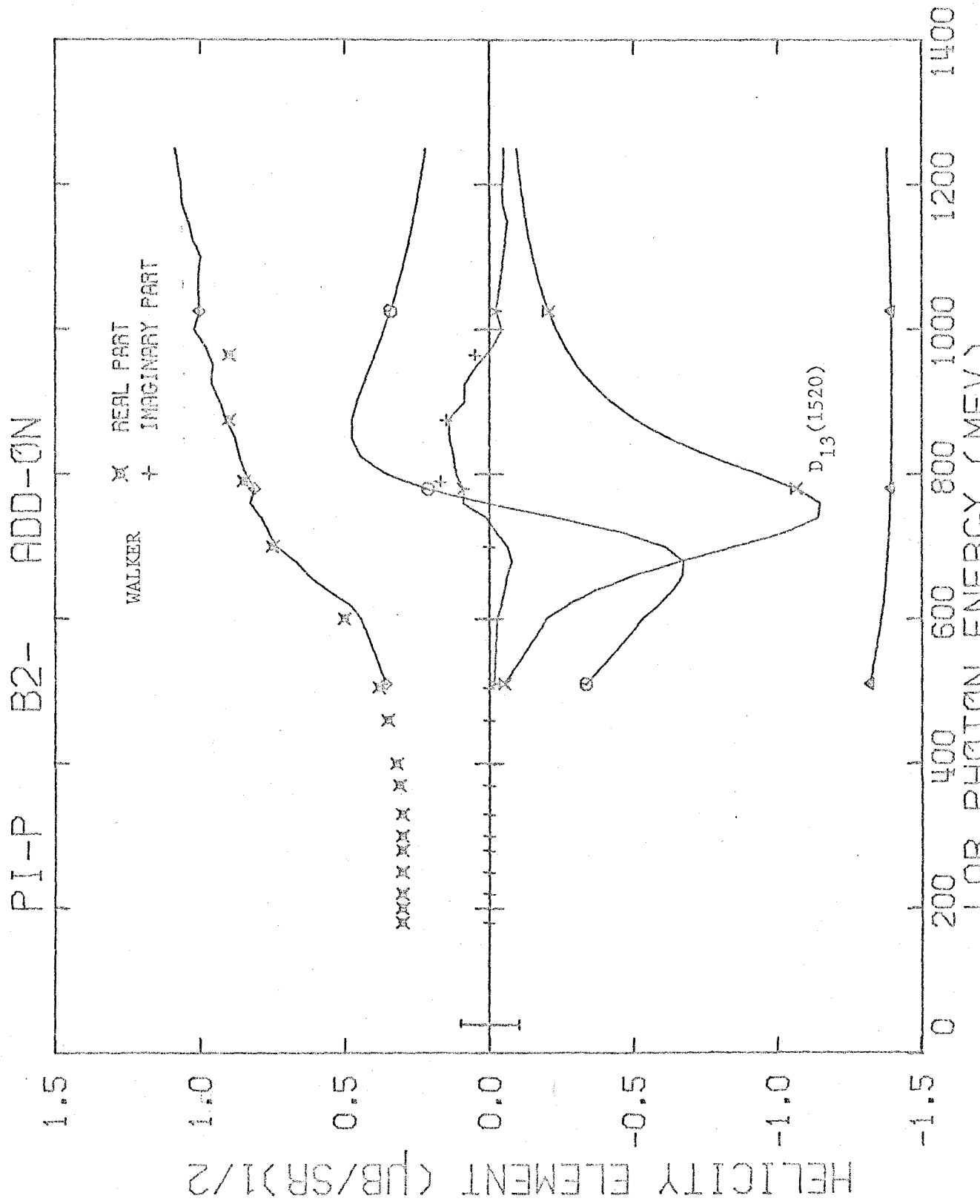
PI-P B2- ADD-ON
WALKER
REAL PART
IMAGINARY PART
$D_{13}(1520)$
HELICITY ELEMENT (UB/SR)1/2
LAB PHOTON ENERGY (MEV)
1.5
1.0
0.5
0.0
-0.5
-1.0
-1.5
0
200
400
600
800
1000
1200
1400

FIGURE 45.6

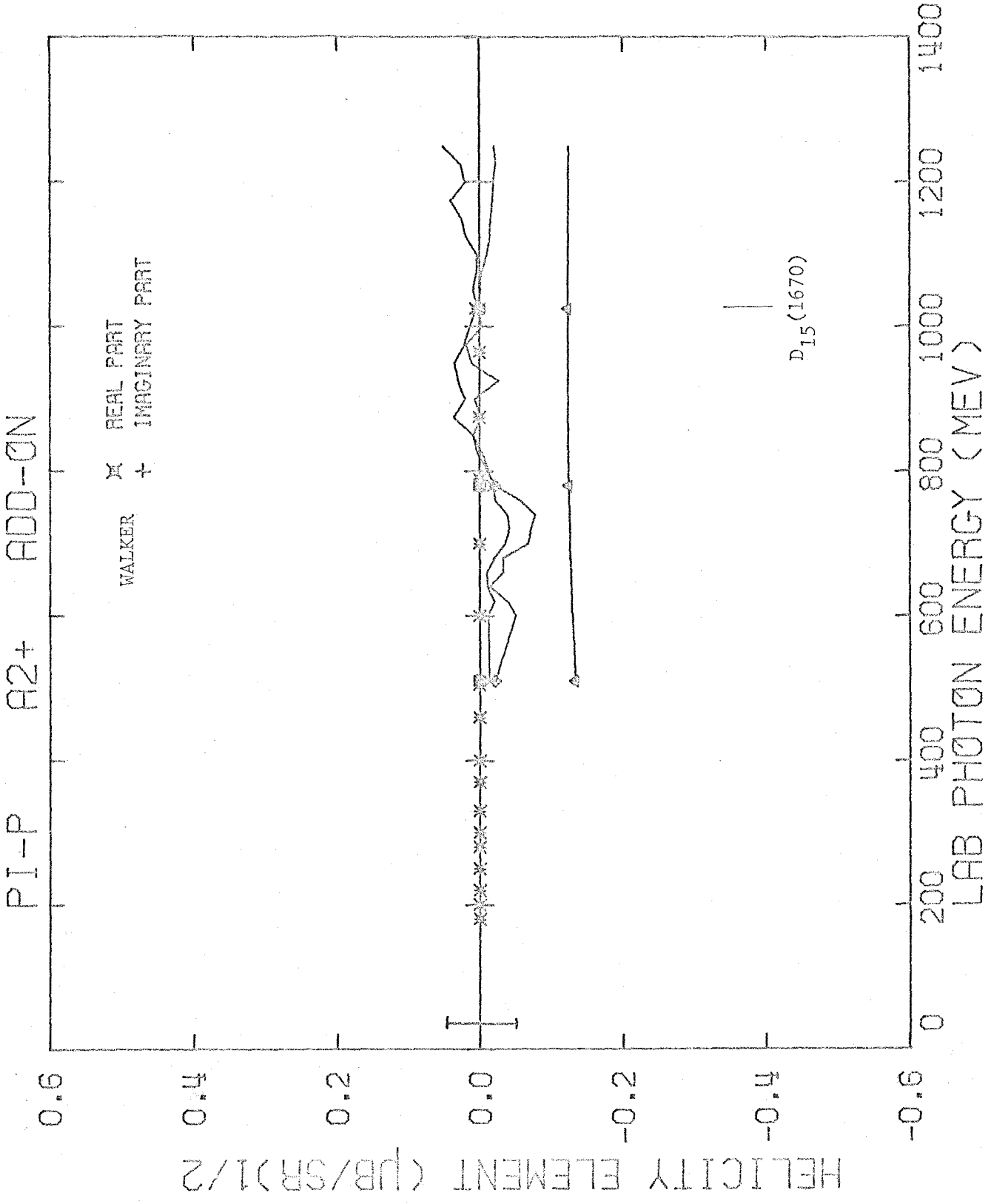
PI-P A2+ ADD-ON
WALKER
REAL PART
IMAGINARY PART
$D_{15}(1670)$
HELICITY ELEMENT (UB/SR)1/2
LAB PHOTON ENERGY (MEV)
0.6
0.4
0.2
0.0
-0.2
-0.4
-0.6
0
200
400
600
800
1000
1200
1400

FIGURE 45.7

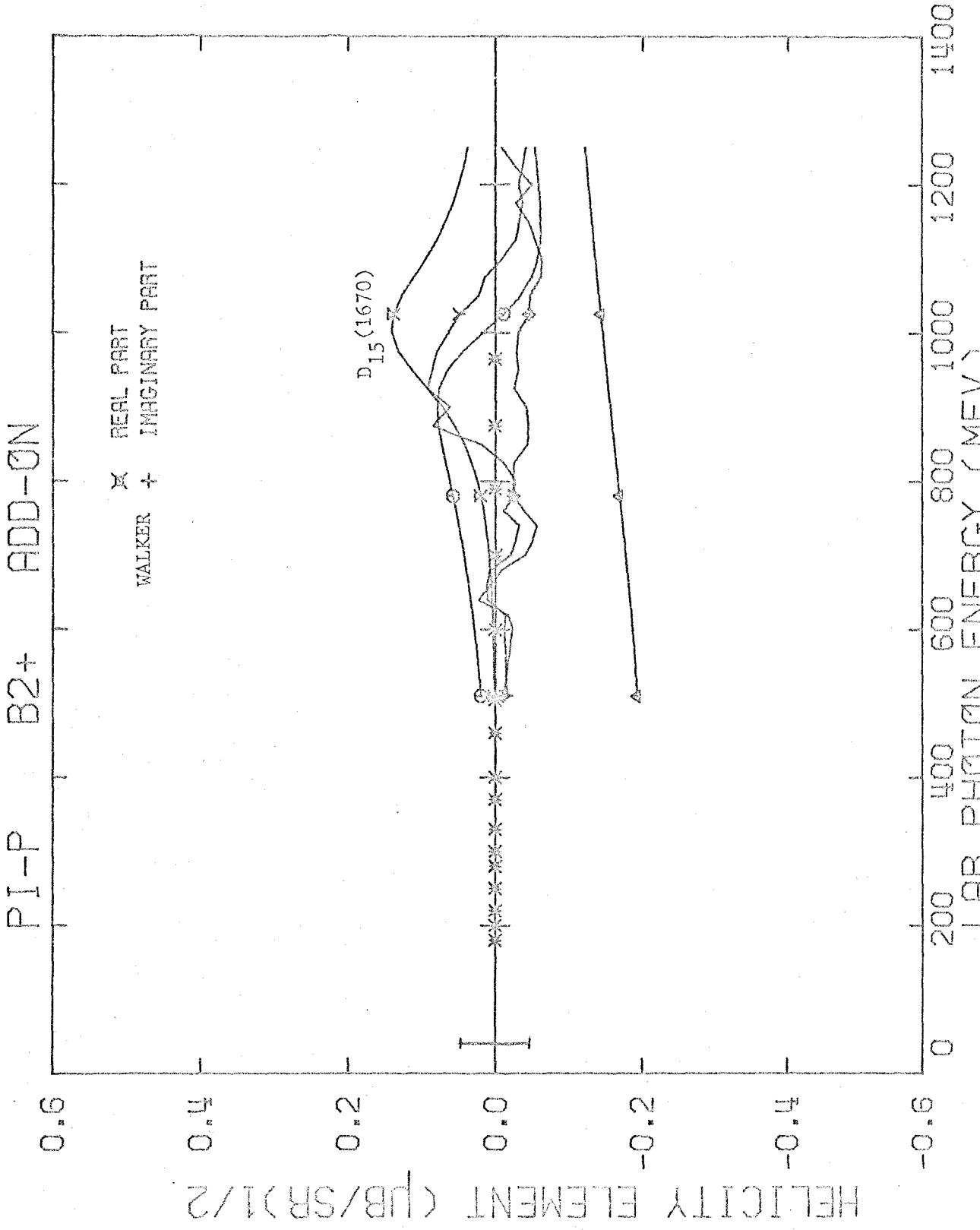
PI-P B2+ ADD-ON
REAL PART
WALKER + IMAGINARY PART
$D_{15}(1670)$
HELICITY ELEMENT (UB/SR)1/2
LAB PHOTON ENERGY (MEV)
0.6
0.4
0.2
0.0
-0.2
-0.4
-0.6
0
200
400
600
800
1000
1200
1400

FIGURE 45.8

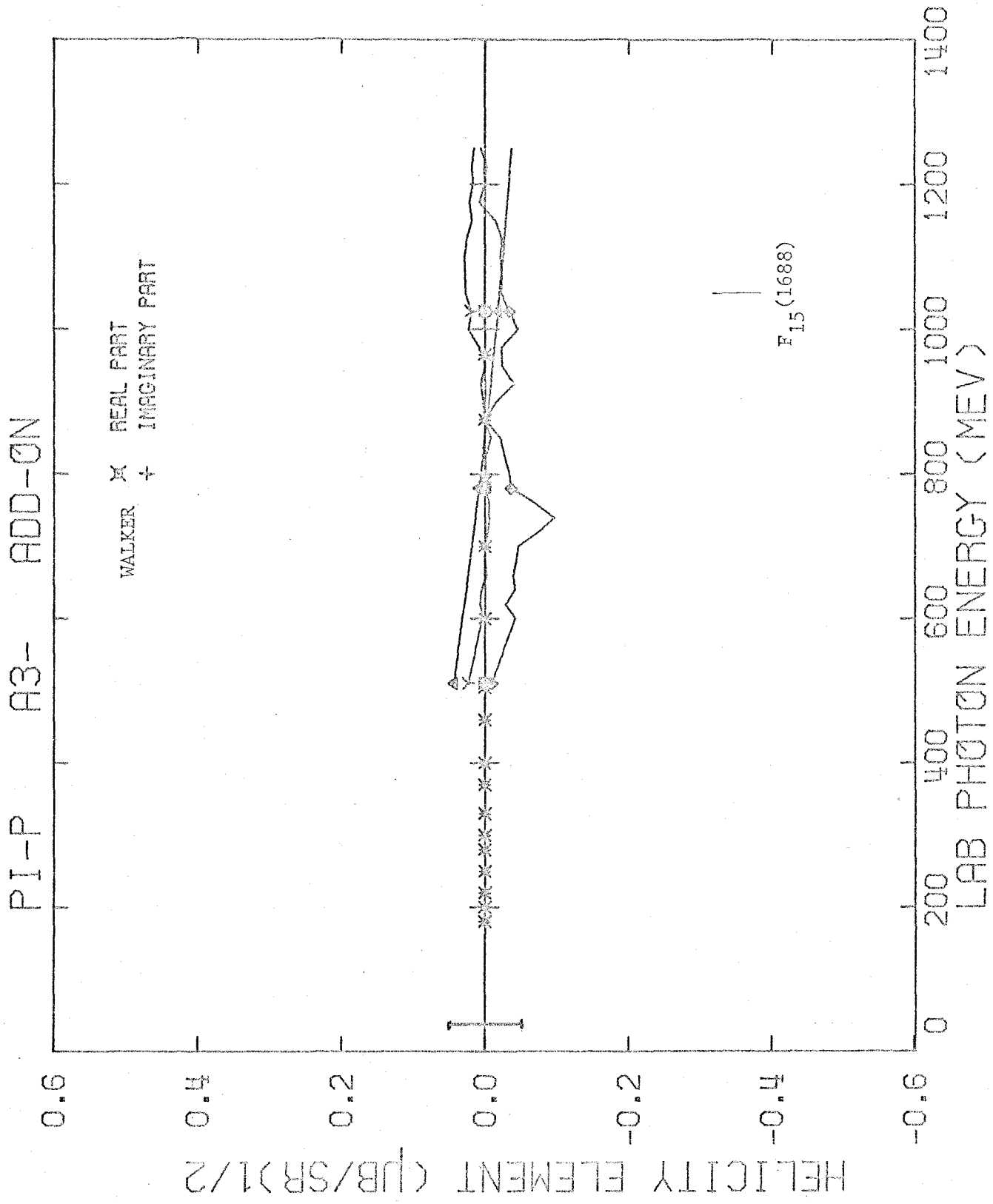
PI-P A3- ADD-ON
WALKER
REAL PART
IMAGINARY PART
$F_{15}(1688)$
HELICITY ELEMENT (UB/SR)1/2
LAB PHOTON ENERGY (MEV)
0.6
0.4
0.2
0.0
-0.2
-0.4
-0.6
0
200
400
600
800
1000
1200
1400

FIGURE 45.9

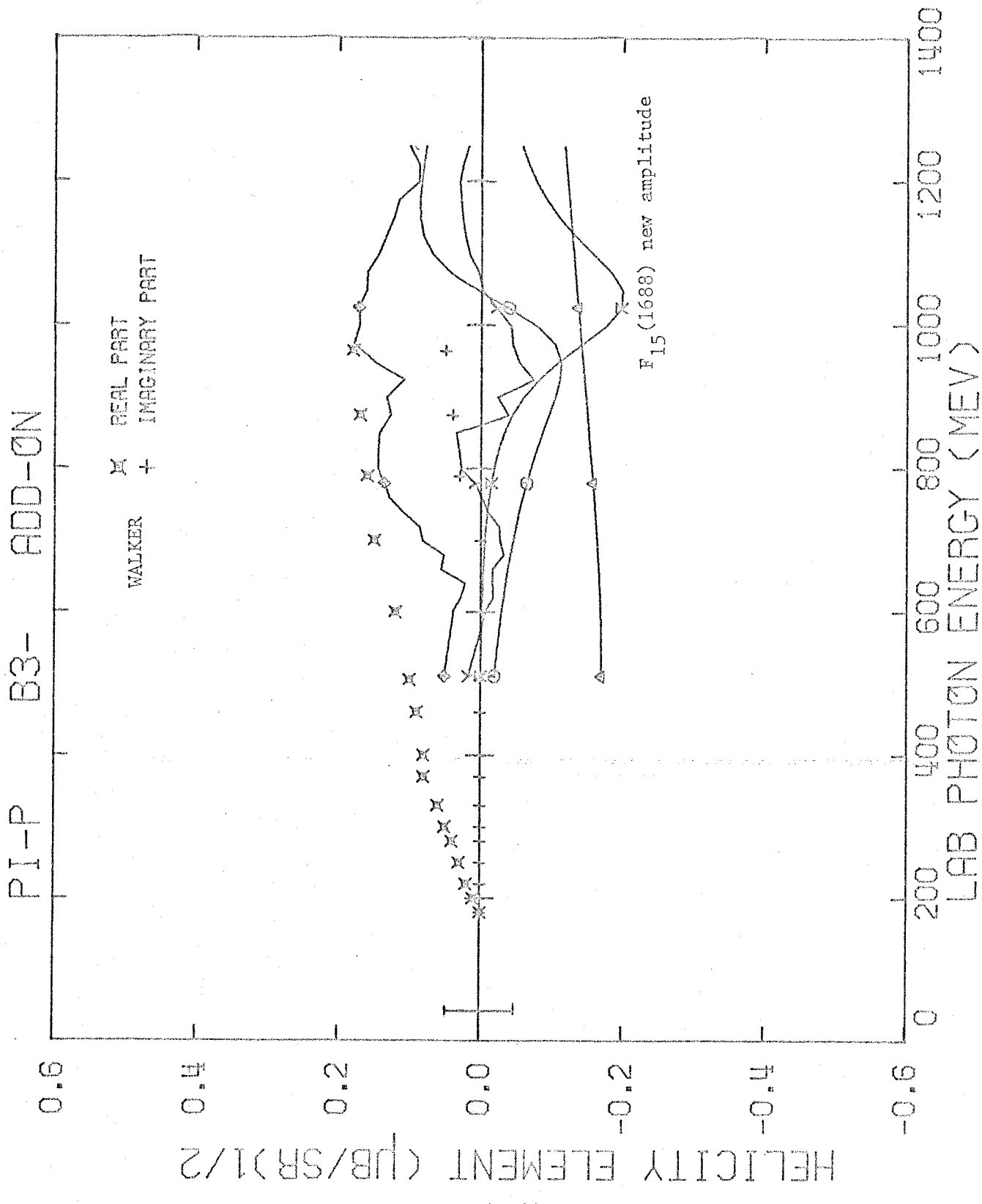
PI-P B3- ADD-ON
WALKER
REAL PART
IMAGINARY PART
$F_{15}(1688)$ new amplitude
HELICITY ELEMENT (UB/SR)1/2
LAB PHOTON ENERGY (MEV)
0.6
0.4
0.2
0.0
-0.2
-0.4
-0.6
0
200
400
600
800
1000
1200
1400

FIGURE 45.10

FIGURE 46

TOTAL HELICITY ELEMENTS FROM

FINAL FIT OF π^- PHOTOPRODUCTION

The final total (Born part + resonance part + add-on part) helicity elements (plotted curves) are compared with Walker's total helicity elements (plotted points).

The curves are identified by □ for the real part and by ✕ for the imaginary part of the total helicity element.

Note that there has been a very large change in the imaginary parts of the A_{0+} and A_{1-} helicity amplitudes (pages 262 and 263).

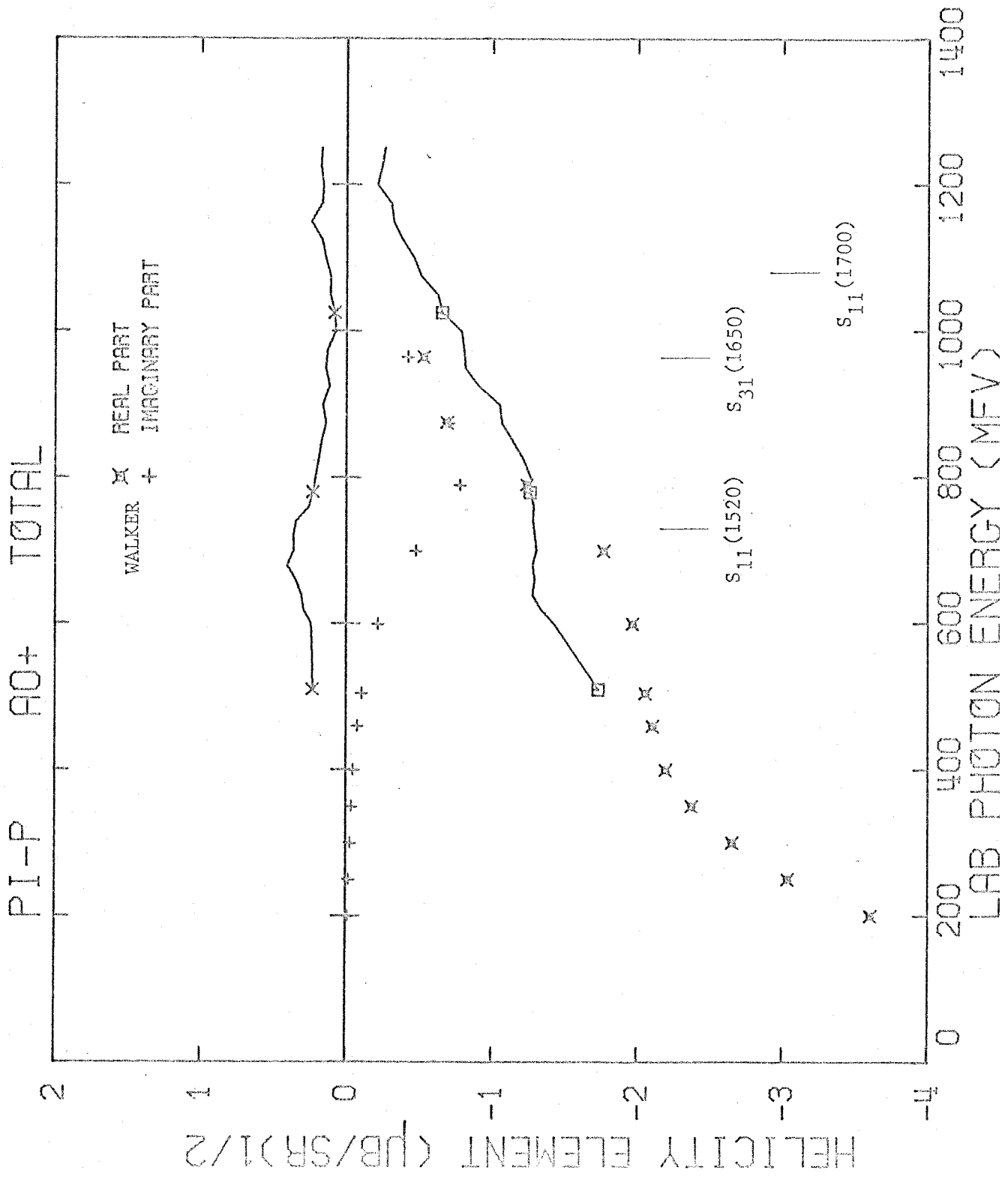
PI-P A0+ TOTAL
WALKER
REAL PART
IMAGINARY PART
$S_{11}(1520)$
$S_{31}(1650)$
$S_{11}(1700)$
HELICITY ELEMENT (UB/SR)1/2
LAB PHOTON ENERGY (MEV)
2
1
0
-1
-2
-3
-4
0
200
400
600
800
1000
1200
1400

FIGURE 46.1

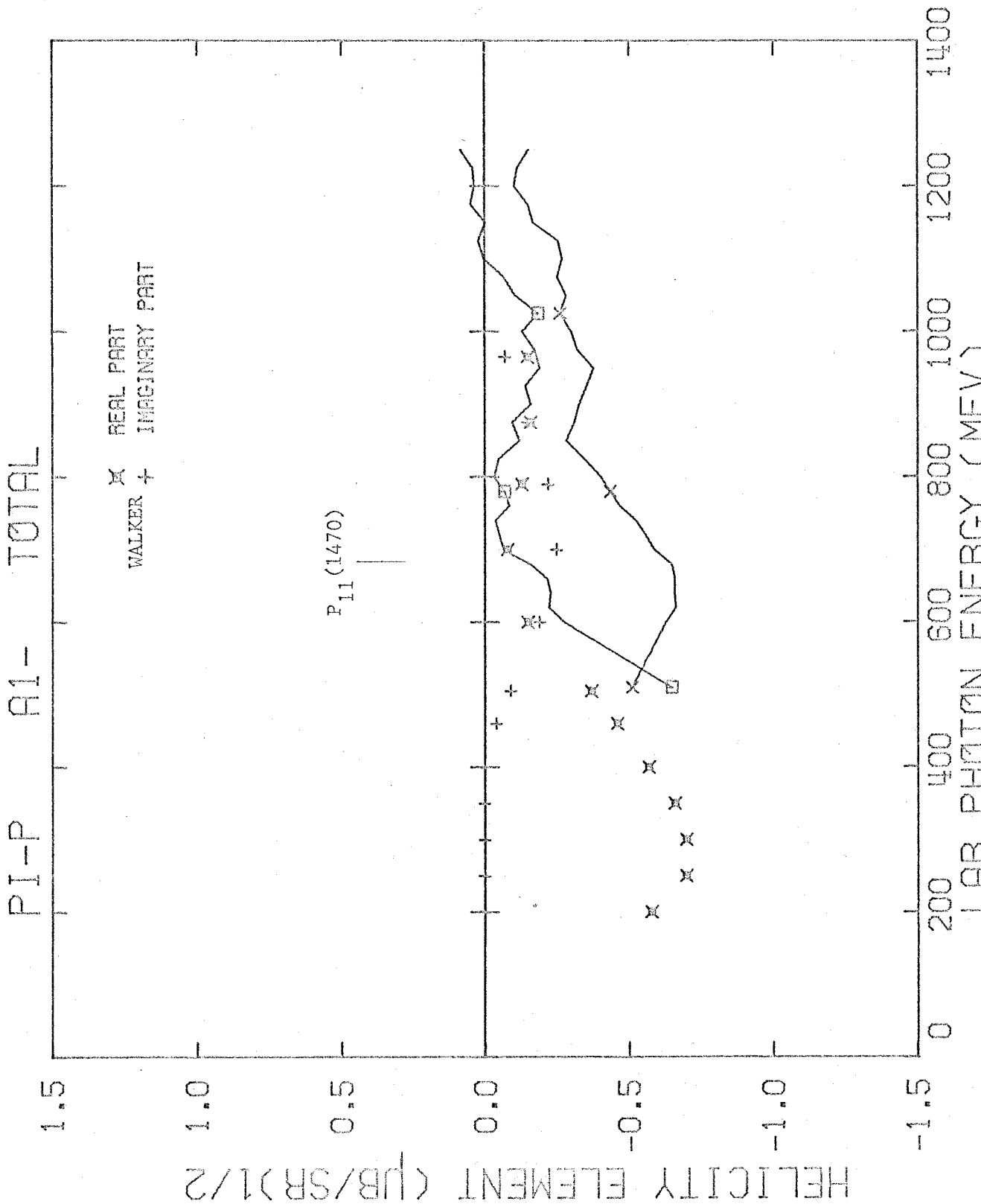
PI-P A1- TOTAL
WALKER
REAL PART
IMAGINARY PART
$P_{11}(1470)$
HELICITY ELEMENT (UB/SR)1/2
LAB PHOTON ENERGY (MEV)
1.5
1.0
0.5
0.0
-0.5
-1.0
-1.5
0
200
400
600
800
1000
1200
1400

FIGURE 46.2

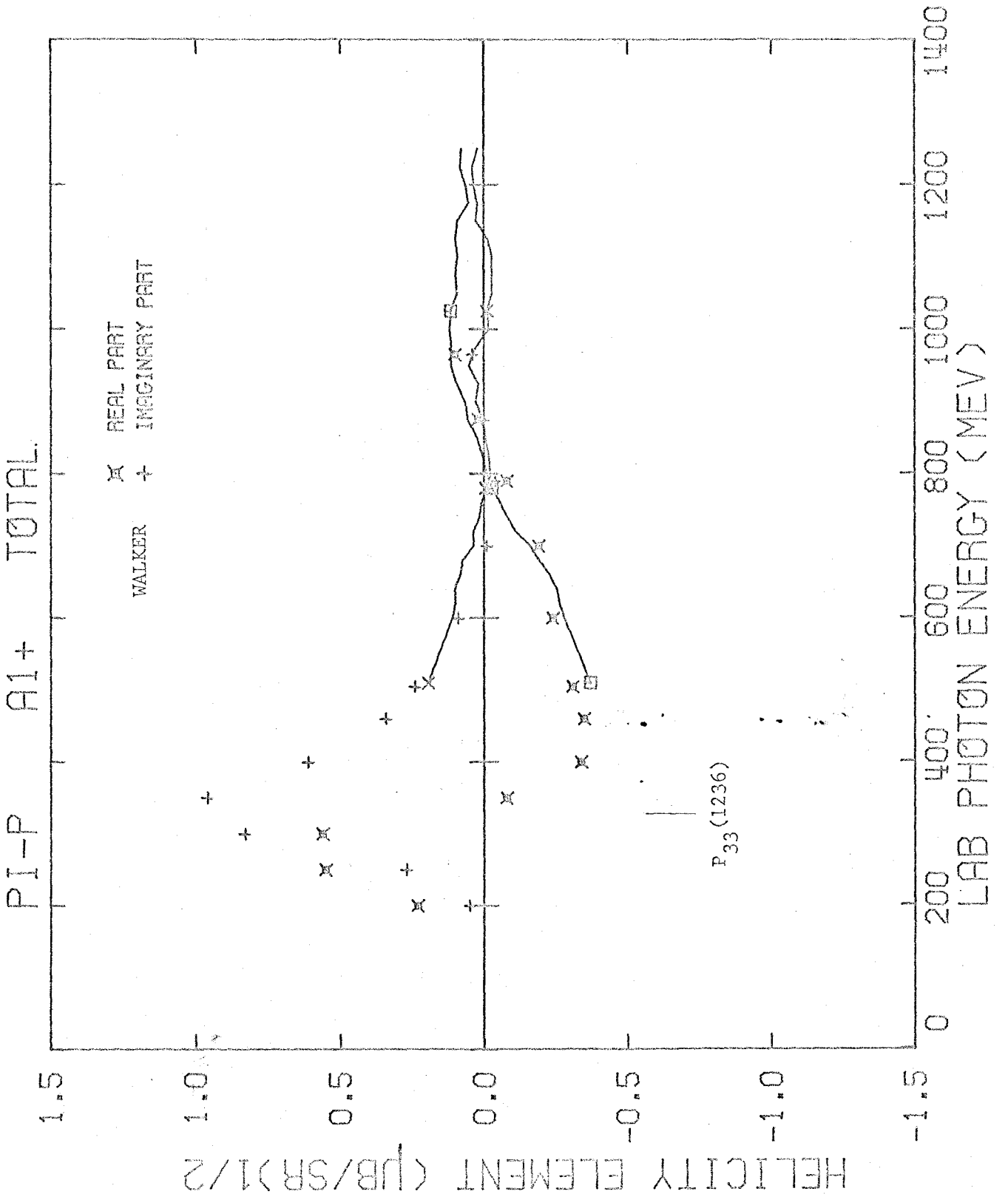
PI-P A1+ TOTAL
WALKER
REAL PART
IMAGINARY PART
$P_{33}(1236)$
HELICITY ELEMENT (UB/SR)1/2
LAB PHOTON ENERGY (MEV)
1.5
1.0
0.5
0.0
-0.5
-1.0
-1.5
0
200
400
600
800
1000
1200
1400

FIGURE 46.3

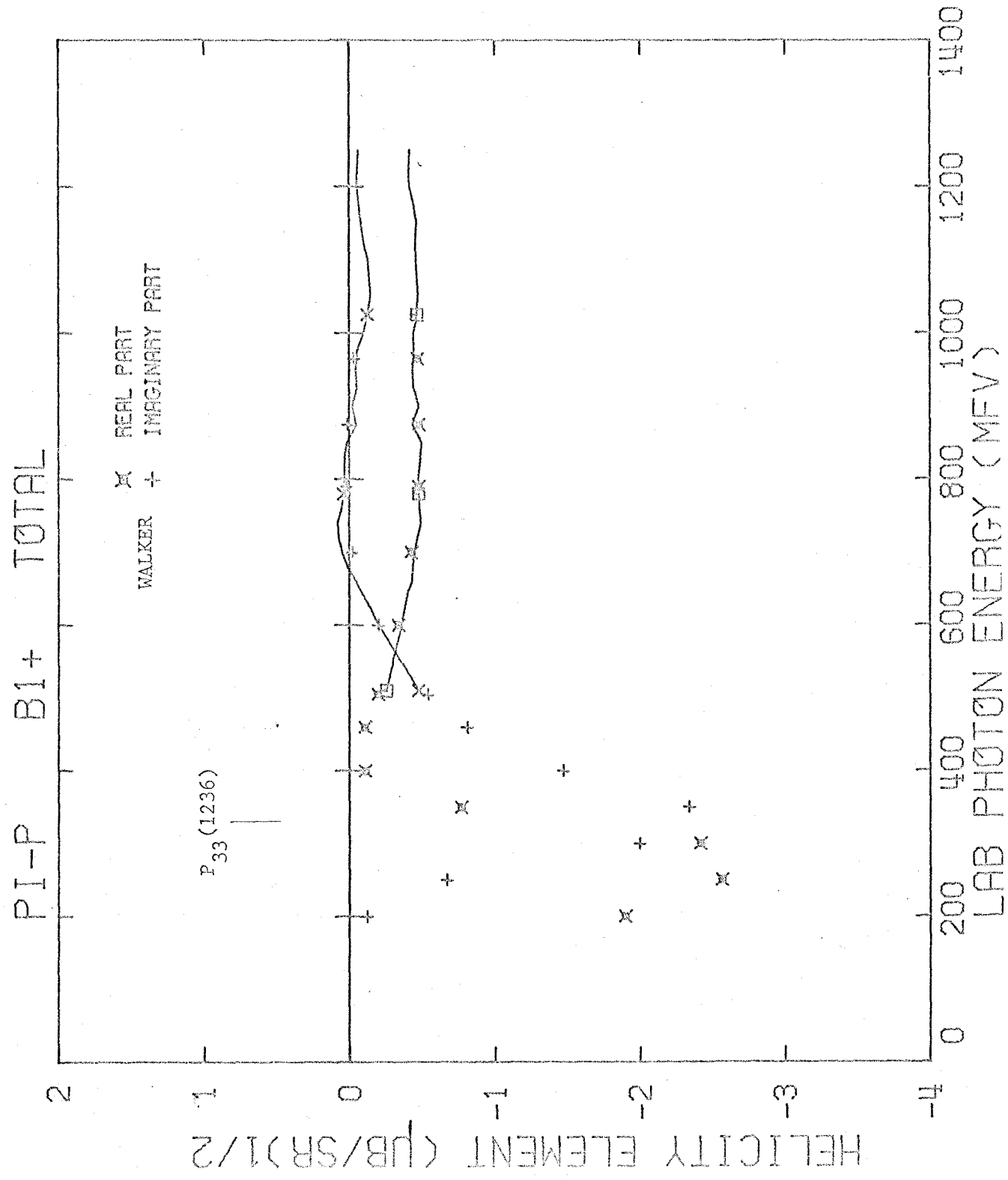
PI-P B1+ TOTAL
REAL PART
WALKER + IMAGINARY PART
$P_{33}(1236)$
HELICITY ELEMENT (UB/SR)1/2
LAB PHOTON ENERGY (MEV)
2
1
0
-1
-2
-3
-4
0
200
400
600
800
1000
1200
1400

FIGURE 46.4

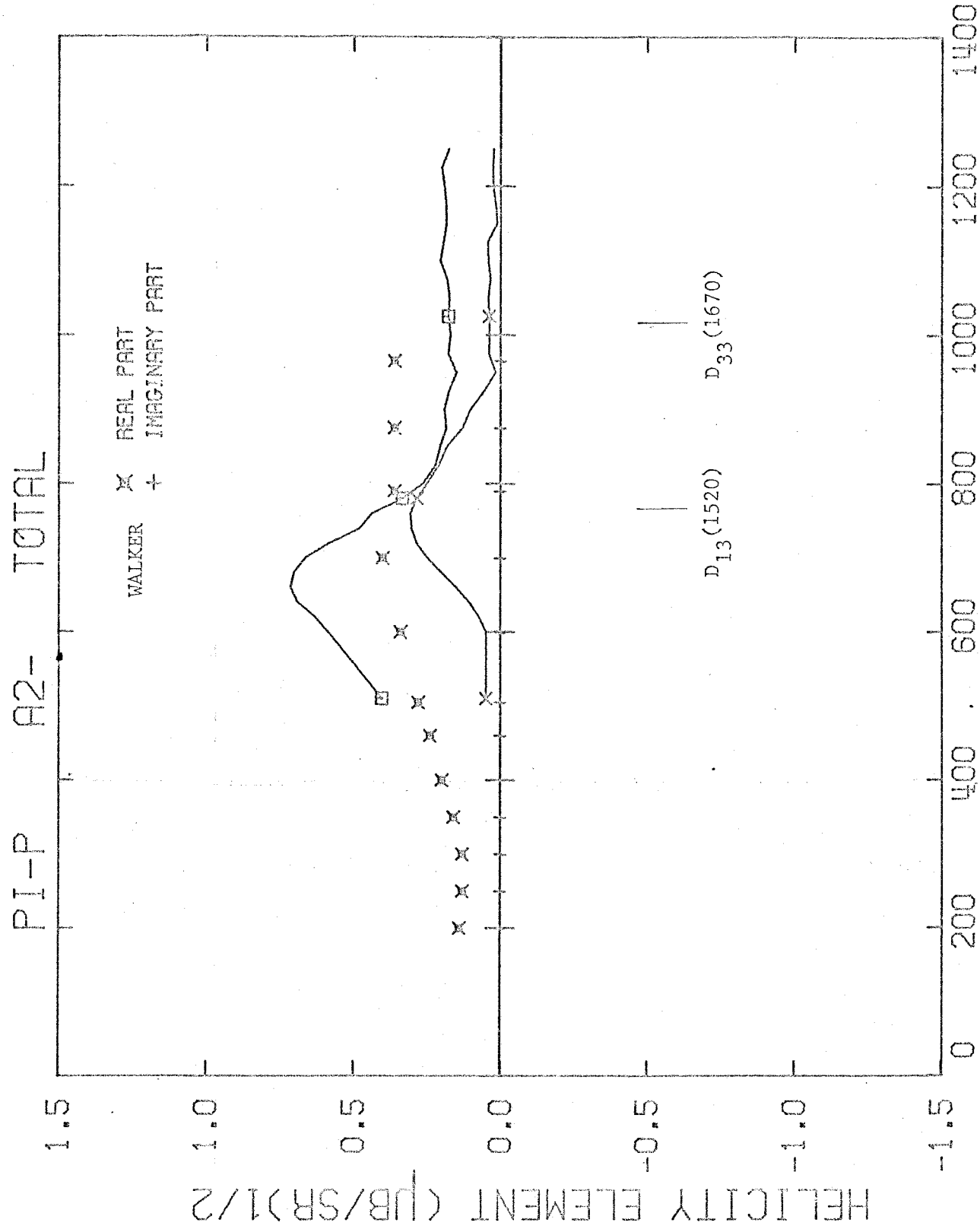
PI-P A2- TOTAL
WALKER
REAL PART
IMAGINARY PART
$D_{13}(1520)$
$D_{33}(1670)$
HELICITY ELEMENT (UB/SR)1/2
LAB PHOTON ENERGY (MEV)
1.5
1.0
0.5
0.0
-0.5
-1.0
-1.5
0
200
400
600
800
1000
1200
1400

FIGURE 46.5

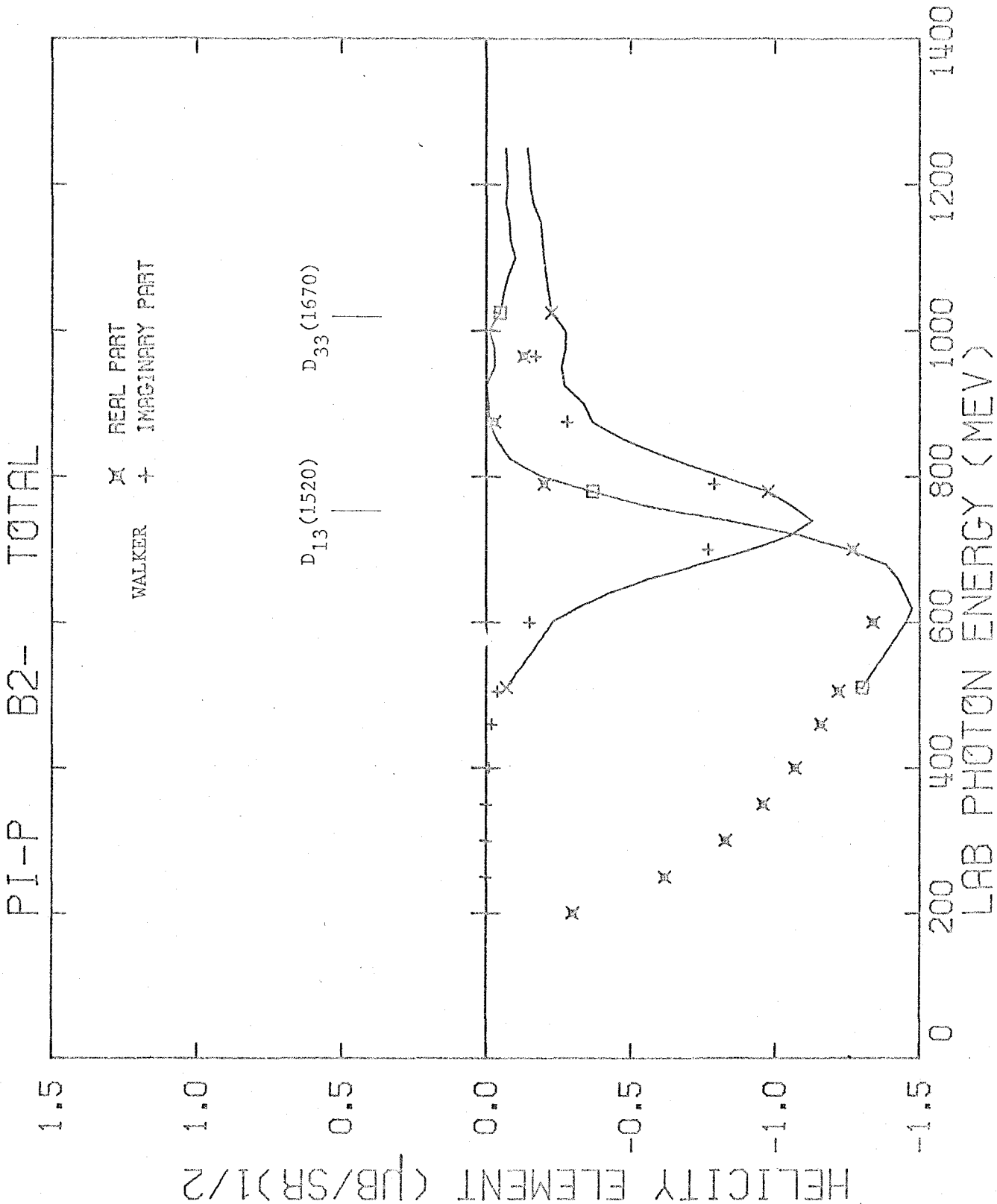
PI-P B2- TOTAL
WALKER
REAL PART
IMAGINARY PART
$D_{13}(1520)$
$D_{33}(1670)$
HELICITY ELEMENT (UB/SR)1/2
LAB PHOTON ENERGY (MEV)
1.5
1.0
0.5
0.0
-0.5
-1.0
-1.5
0
200
400
600
800
1000
1200
1400

FIGURE 46.6

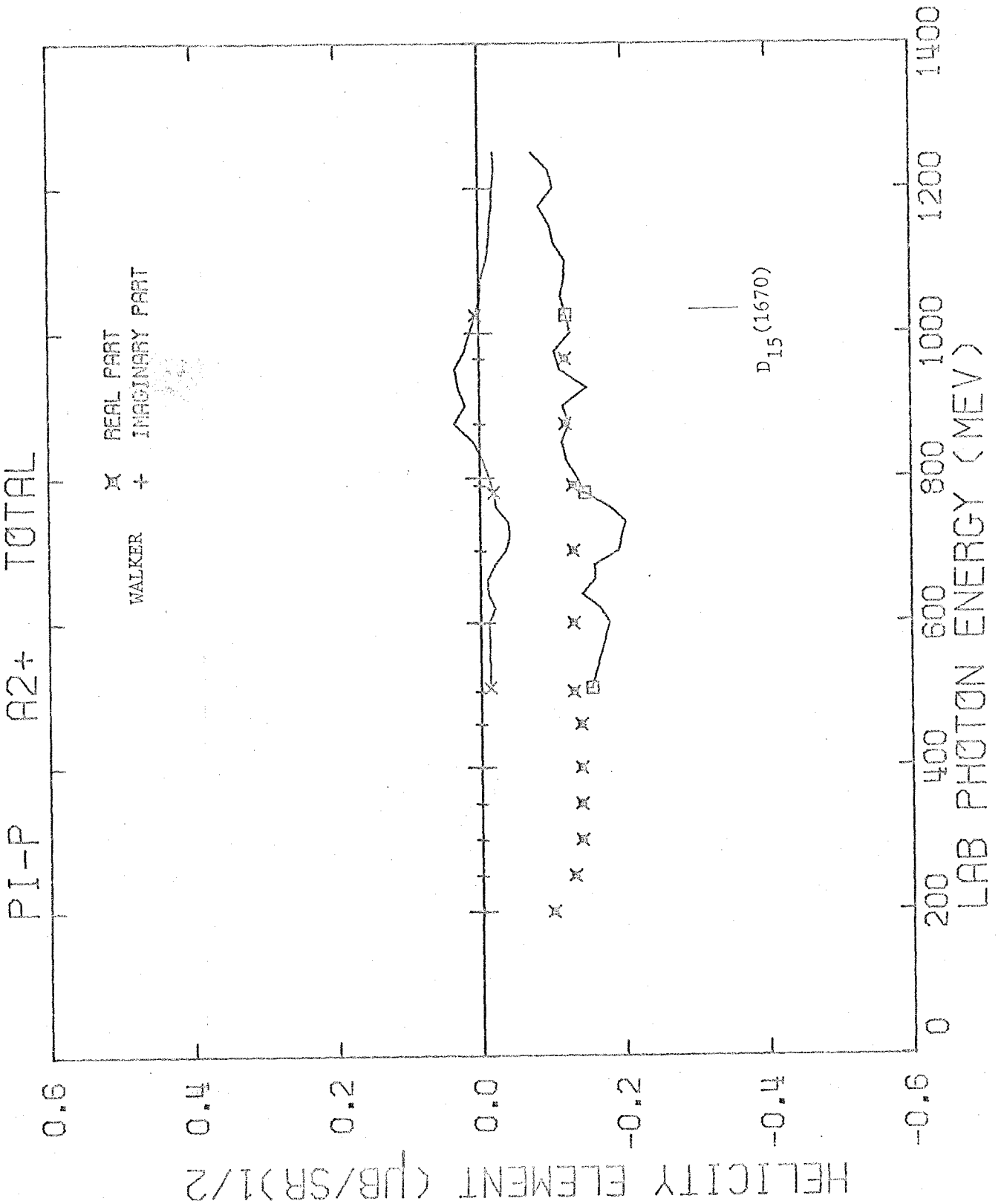
PI-P A2+ TOTAL
REAL PART
IMAGINARY PART
WALKER
$D_{15}(1670)$
HELICITY ELEMENT (UB/SR)1/2
LAB PHOTON ENERGY (MEV)
0.6
0.4
0.2
0.0
-0.2
-0.4
-0.6
0
200
400
600
800
1000
1200
1400

FIGURE 46.7

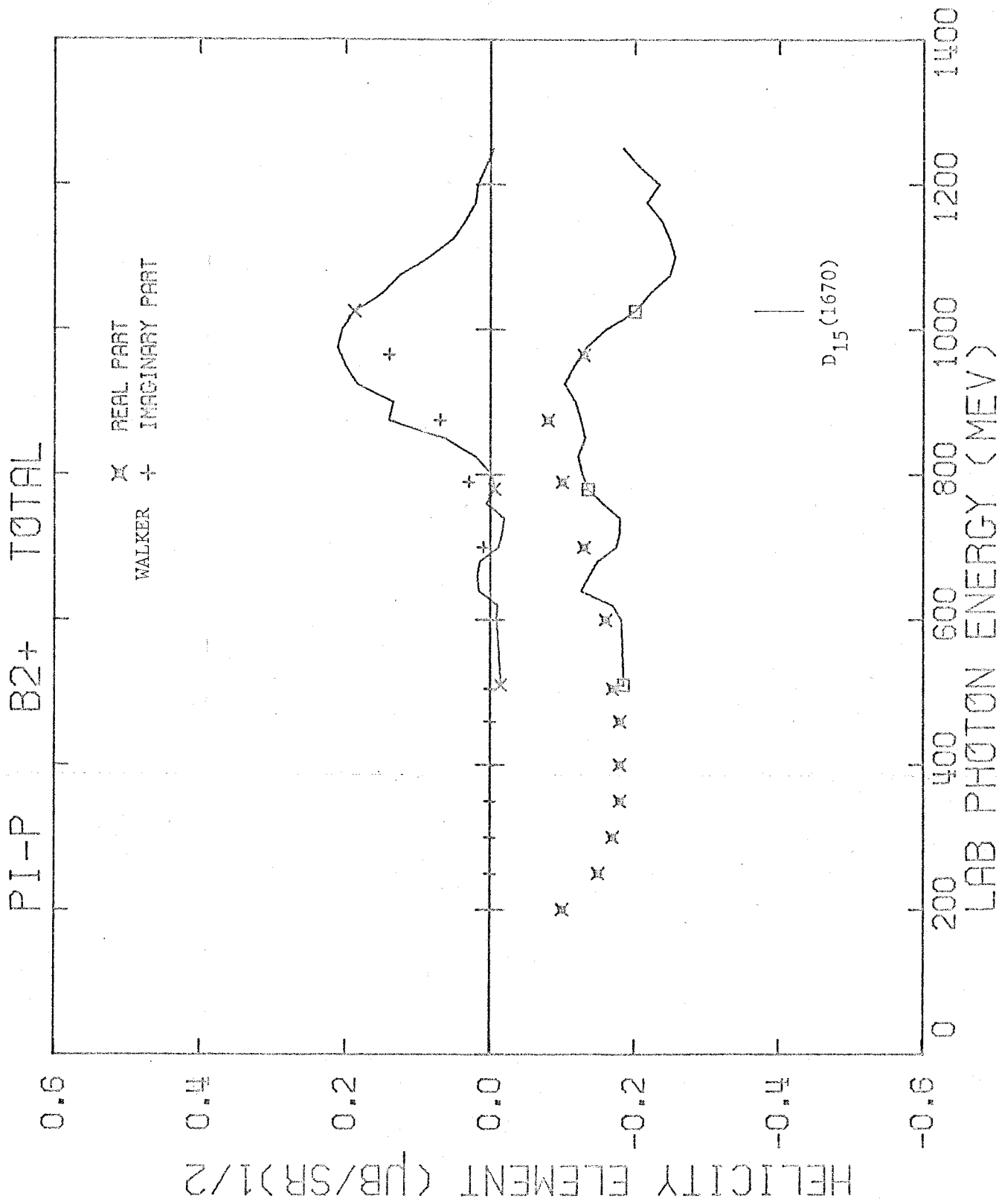
PI-P B2+ TOTAL
WALKER
REAL PART
IMAGINARY PART
$D_{15}(1670)$
HELICITY ELEMENT (UB/SR)1/2
LAB PHOTON ENERGY (MEV)
0.6
0.4
0.2
0.0
-0.2
-0.4
-0.6
0
200
400
600
800
1000
1200
1400

FIGURE 46.8

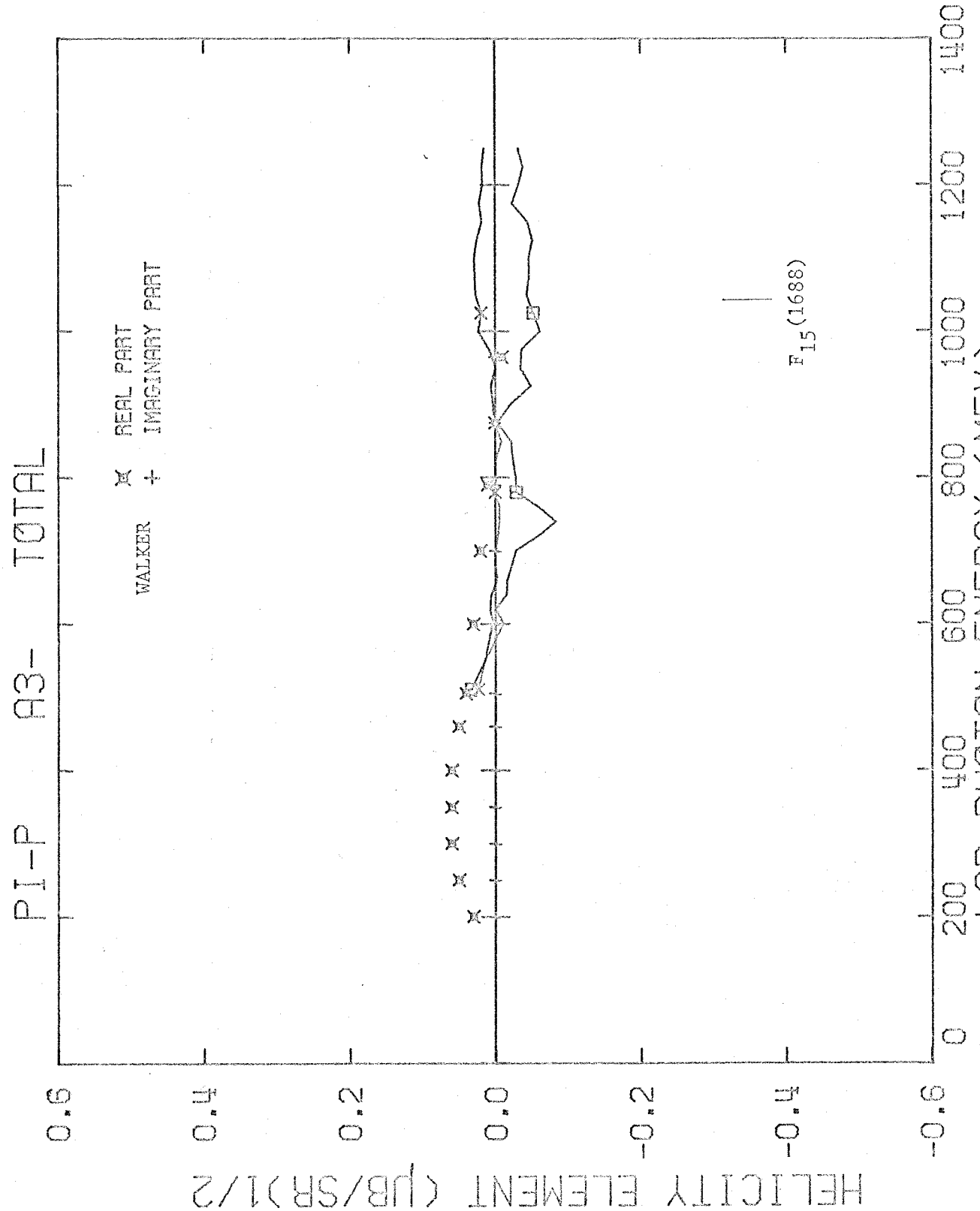
PI-P A3- TOTAL
WALKER
X REAL PART
+ IMAGINARY PART
F15(1688)
HELICITY ELEMENT (UB/SR)1/2
LAB PHOTON ENERGY (MEV)
0.6
0.4
0.2
0.0
-0.2
-0.4
-0.6
0
200
400
600
800
1000
1200
1400

FIGURE 46.9

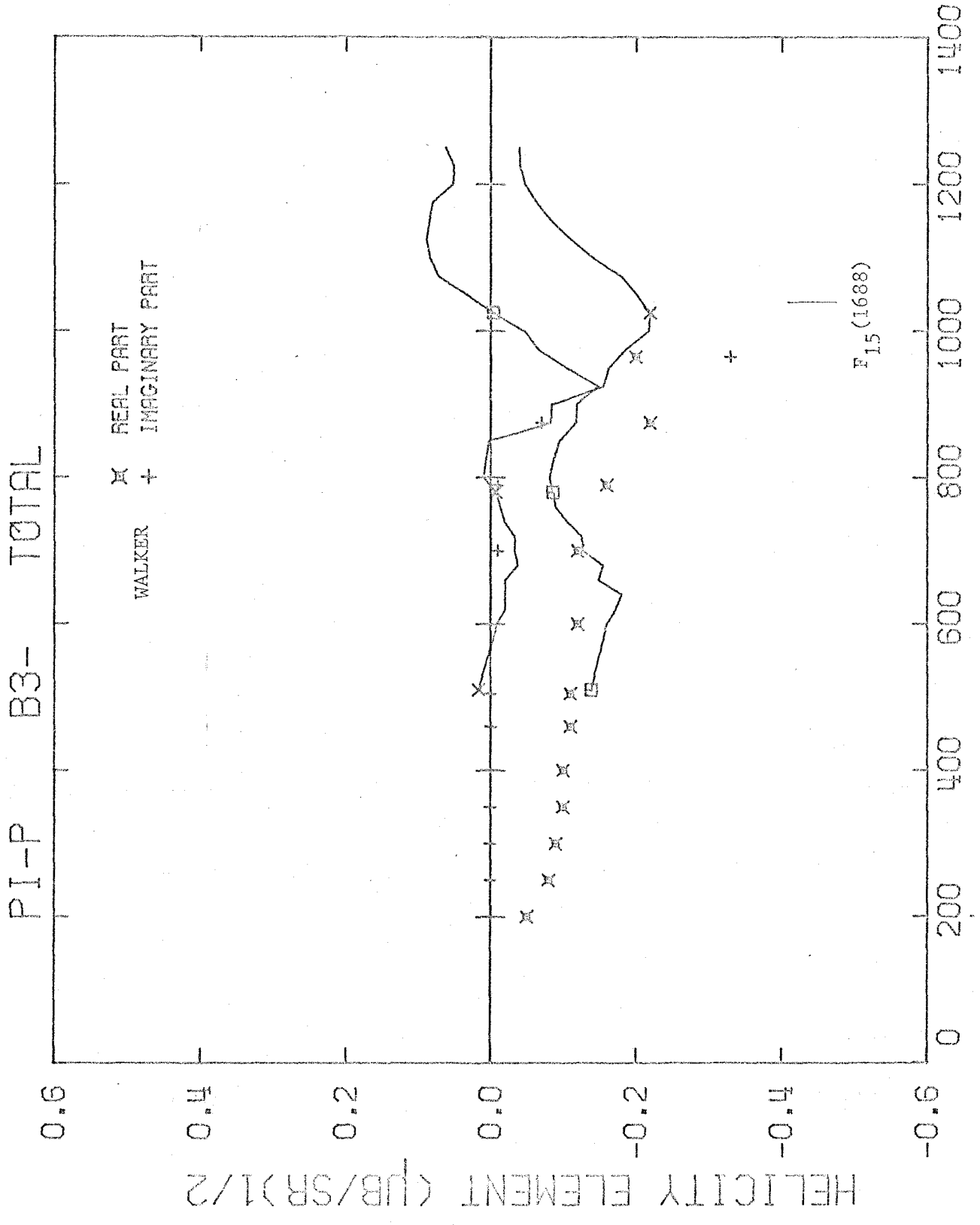
PI-P B3- TOTAL
WALKER
REAL PART
IMAGINARY PART
$F_{15}(1688)$
HELICITY ELEMENT (UB/SR)1/2
0.6
0.4
0.2
0.0
-0.2
-0.4
-0.6
0
200
400
600
800
1000
1200
1400

FIGURE 46.10

FIGURE 47

FINAL FIT OF ADD-ON HELICITY ELEMENTS FOR π^+ PHOTOPRODUCTION

See page 148 for key to symbols and explanation of curves.

In this fit the resonances have been changed as follows:

$P_{11}(1470)$, amplitude -0.250 ⟶ -0.400

$F_{15}(1688)$, amplitude -0.600 ⟶ -0.500
helicity 3/2

See Table 9, page 161, for complete summary of resonance changes.

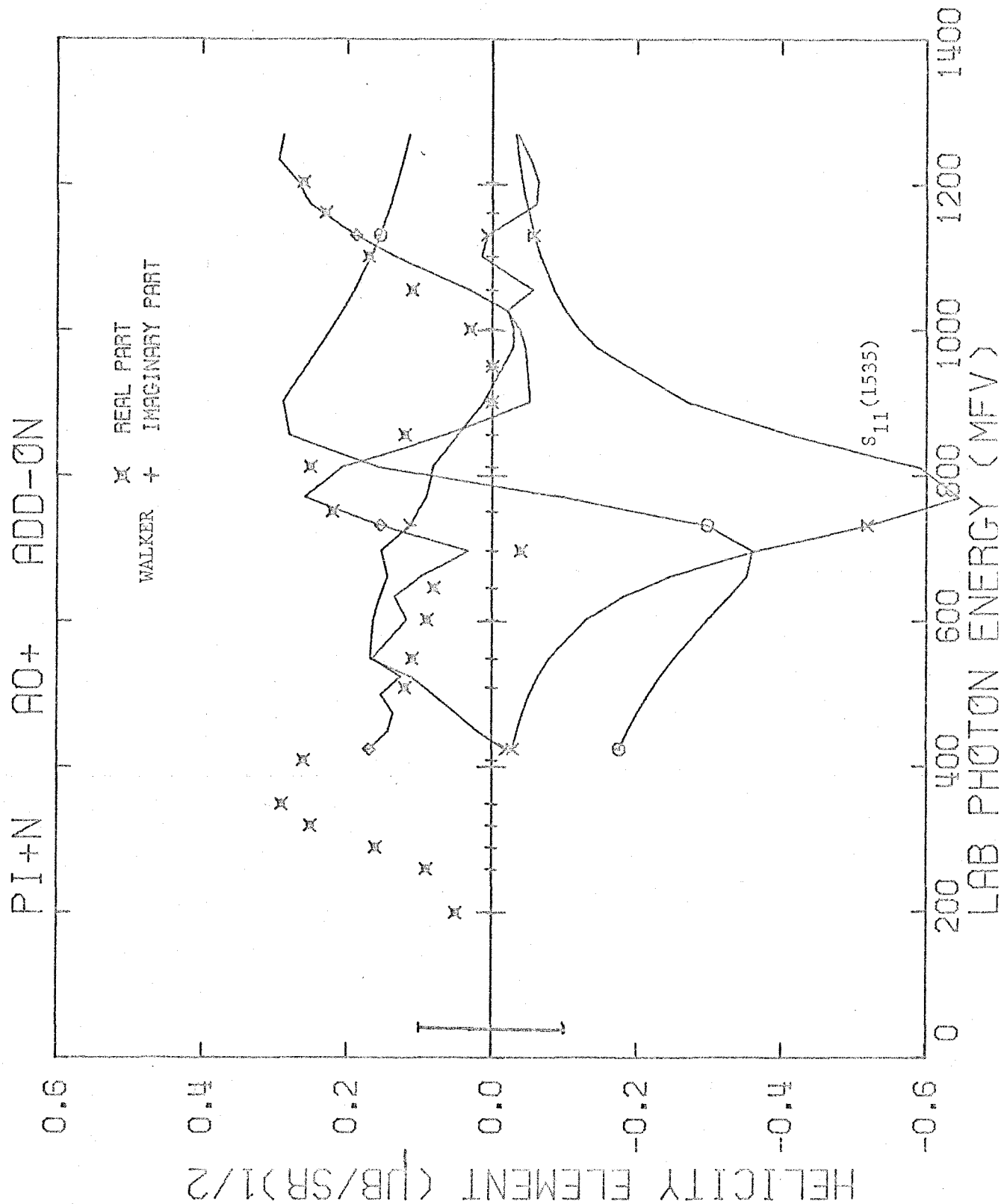
PI+N A0+ ADD-ON
REAL PART
WALKER + IMAGINARY PART
$S_{11}(1535)$
LAB PHOTON ENERGY (MEV)
HELICITY ELEMENT (UB/SR)1/2
0
200
400
600
800
1000
1200
1400
0.6
0.4
0.2
0.0
-0.2
-0.4
-0.6

FIGURE 47.1

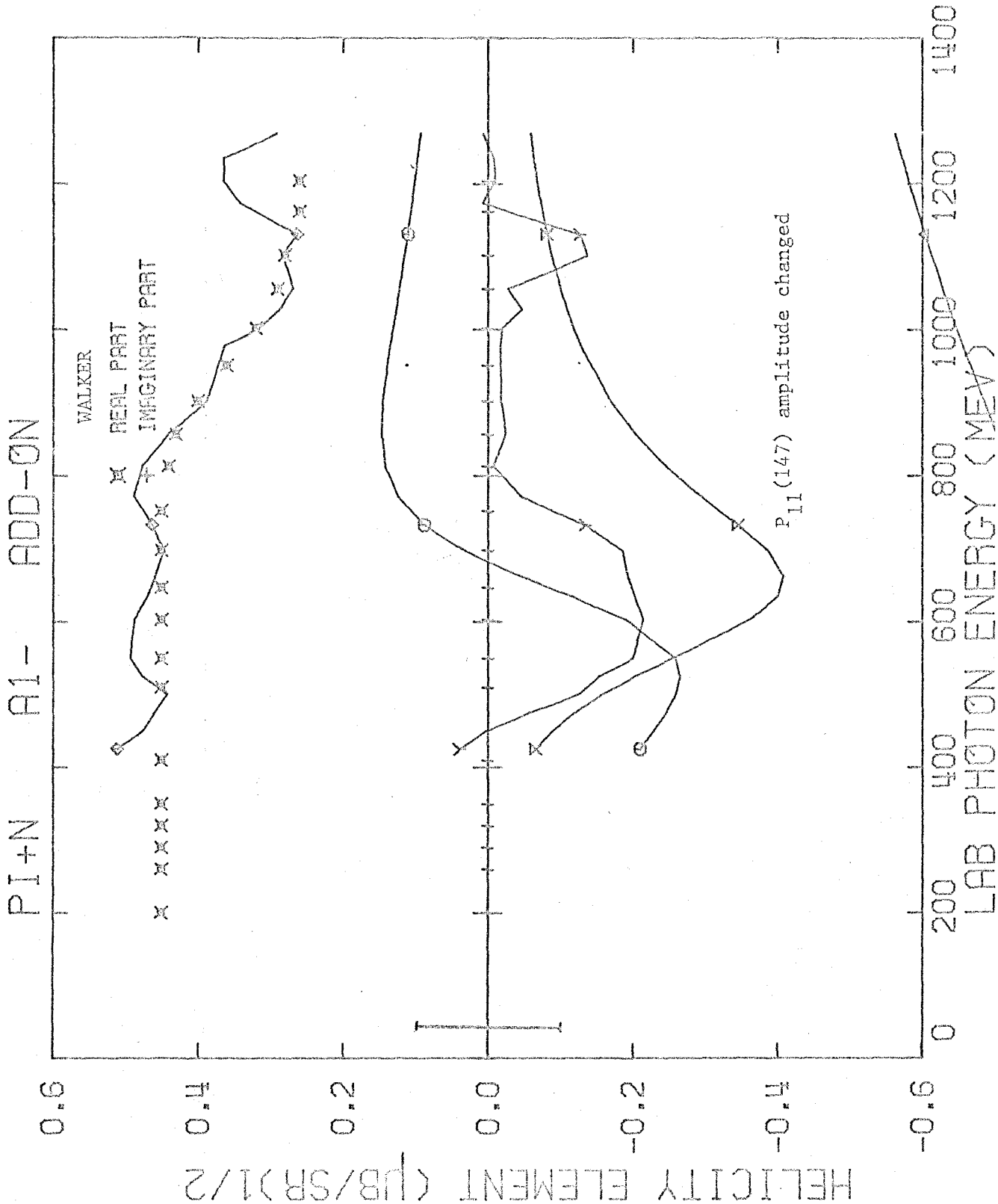
PI+N A1- ADD-ON
WALKER
REAL PART
IMAGINARY PART
$P_{11}(147)$ amplitude changed
HELICITY ELEMENT (μB/SR)1/2
LAB PHOTON ENERGY (MEV)
0.6
0.4
0.2
0.0
-0.2
-0.4
-0.6
0
200
400
600
800
1000
1200
1400

FIGURE 47.2

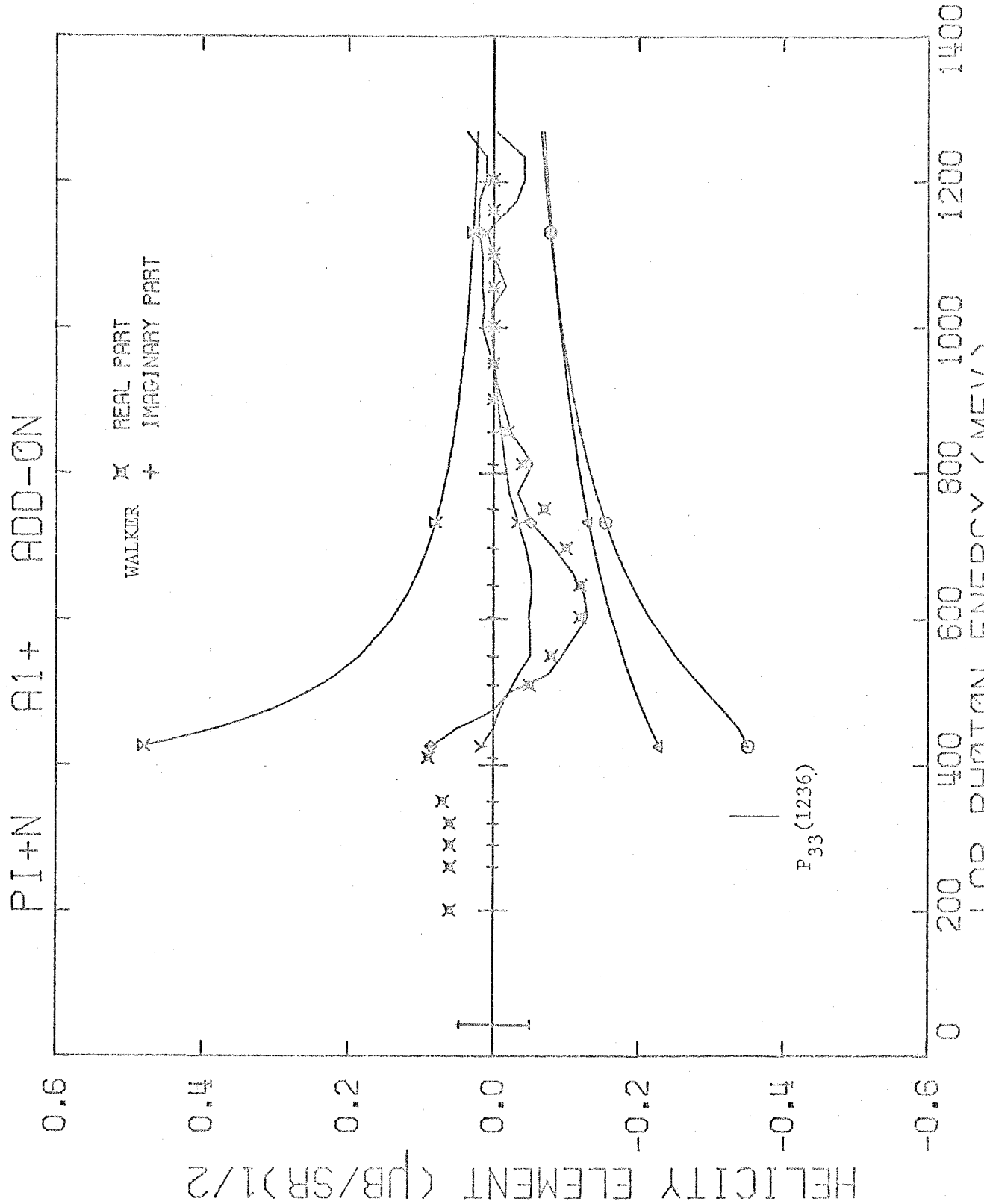
PI+N A1+ ADD-ON
WALKER
REAL PART
IMAGINARY PART
$P_{33}(1236)$
HELICITY ELEMENT (UB/SR)1/2
LAB PHOTON ENERGY (MEV)
0.6
0.4
0.2
0.0
-0.2
-0.4
-0.6
0
200
400
600
800
1000
1200
1400

FIGURE 47.3

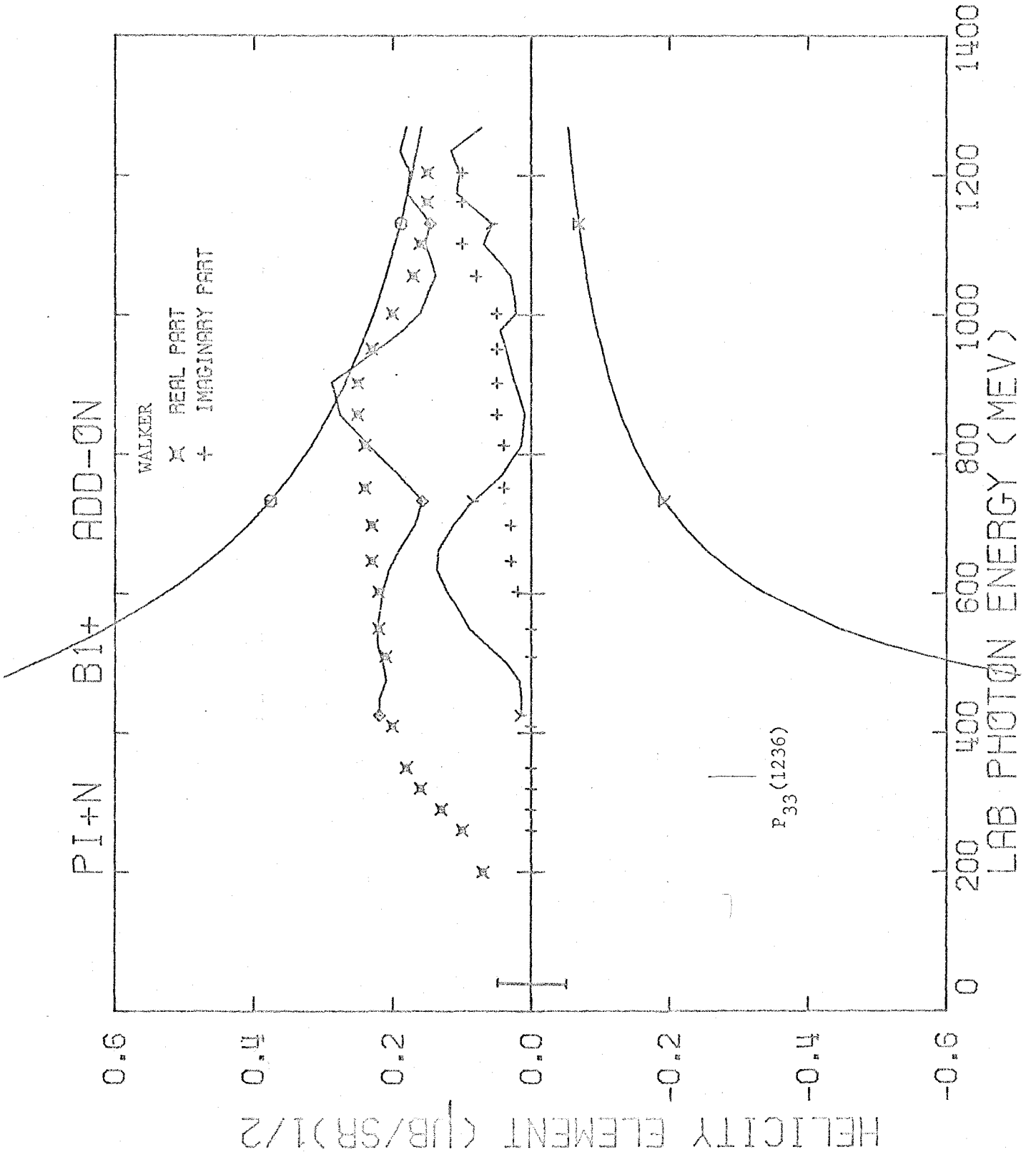
PI+N B1+ ADD-ON
WALKER
REAL PART
IMAGINARY PART
$P_{33}(1236)$
HELICITY ELEMENT (|B/SR|)1/2
LAB PHOTON ENERGY (MEV)
0.6
0.4
0.2
0.0
-0.2
-0.4
-0.6
0
200
400
600
800
1000
1200
1400

FIGURE 47.4

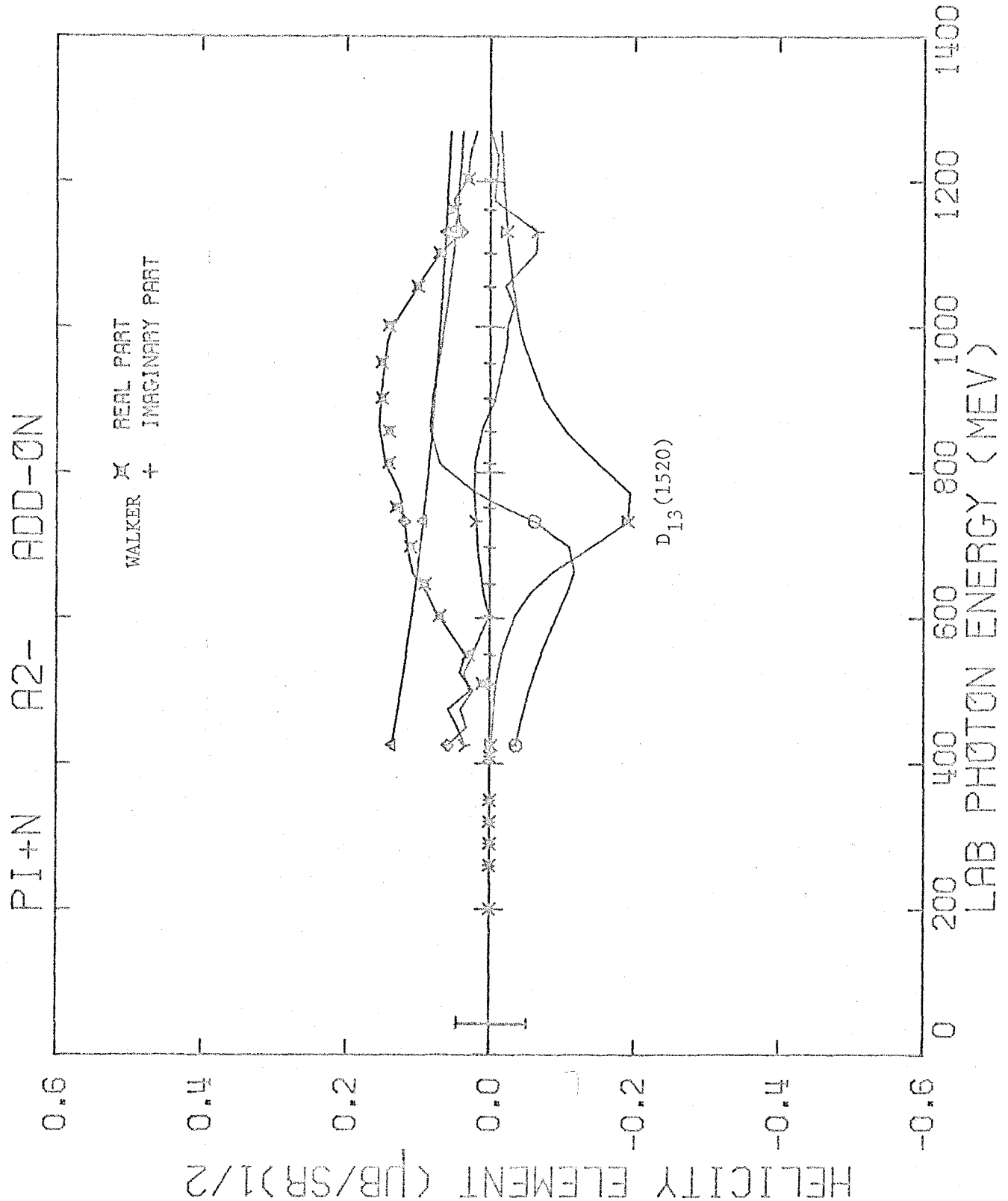
PI+N A2- ADD-ON
WALKER
REAL PART
IMAGINARY PART
$D_{13}(1520)$
HELICITY ELEMENT (UB/SR)1/2
LAB PHOTON ENERGY (MEV)
0.6
0.4
0.2
0.0
-0.2
-0.4
-0.6
0
200
400
600
800
1000
1200
1400

FIGURE 47.5

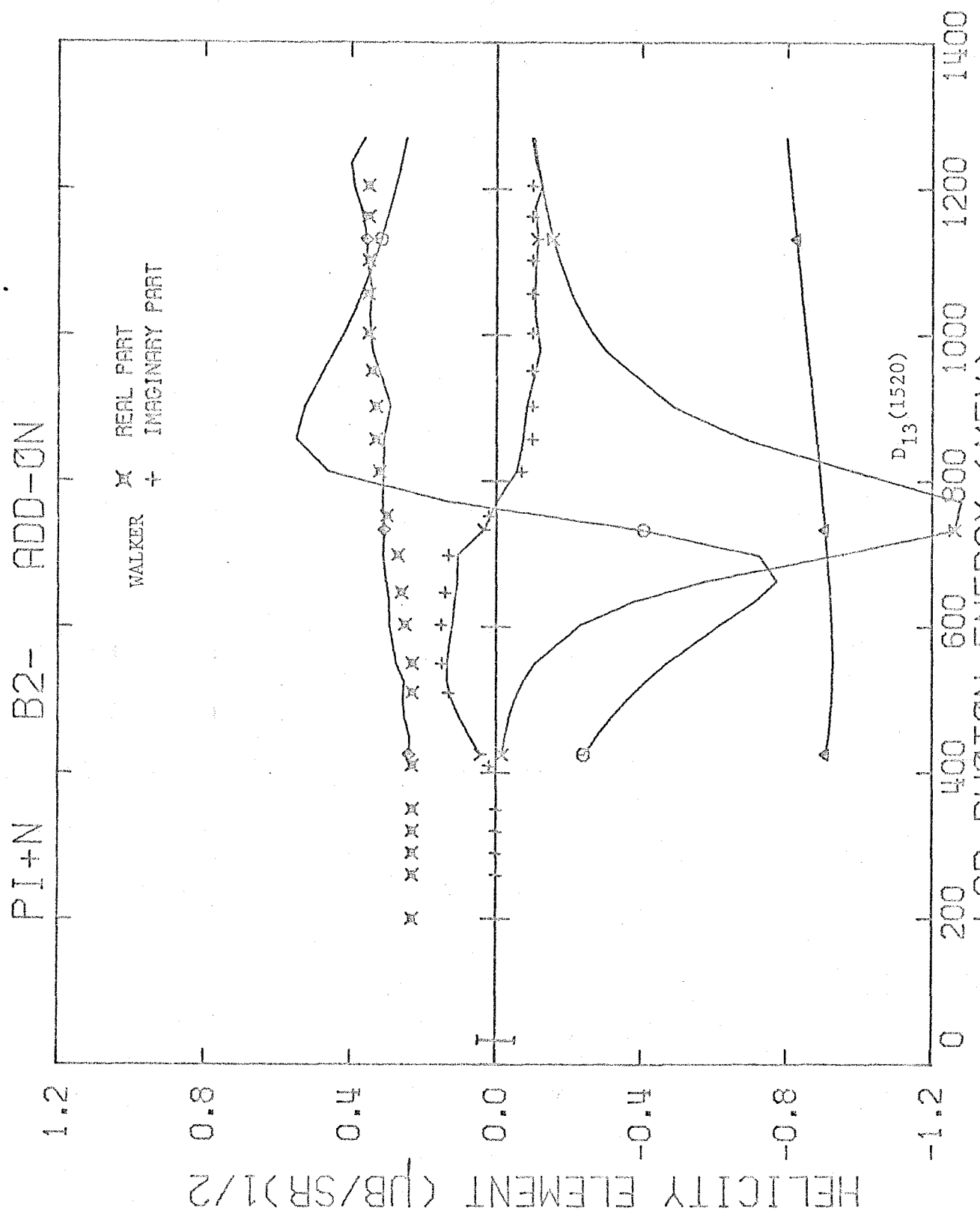
PI+N B2- ADD-ON
WALKER
REAL PART
IMAGINARY PART
$D_{13}(1520)$
HELICITY ELEMENT (UB/SR)1/2
LAB PHOTON ENERGY (MEV)
1.2
0.8
0.4
0.0
-0.4
-0.8
-1.2
0
200
400
600
800
1000
1200
1400

FIGURE 47.6

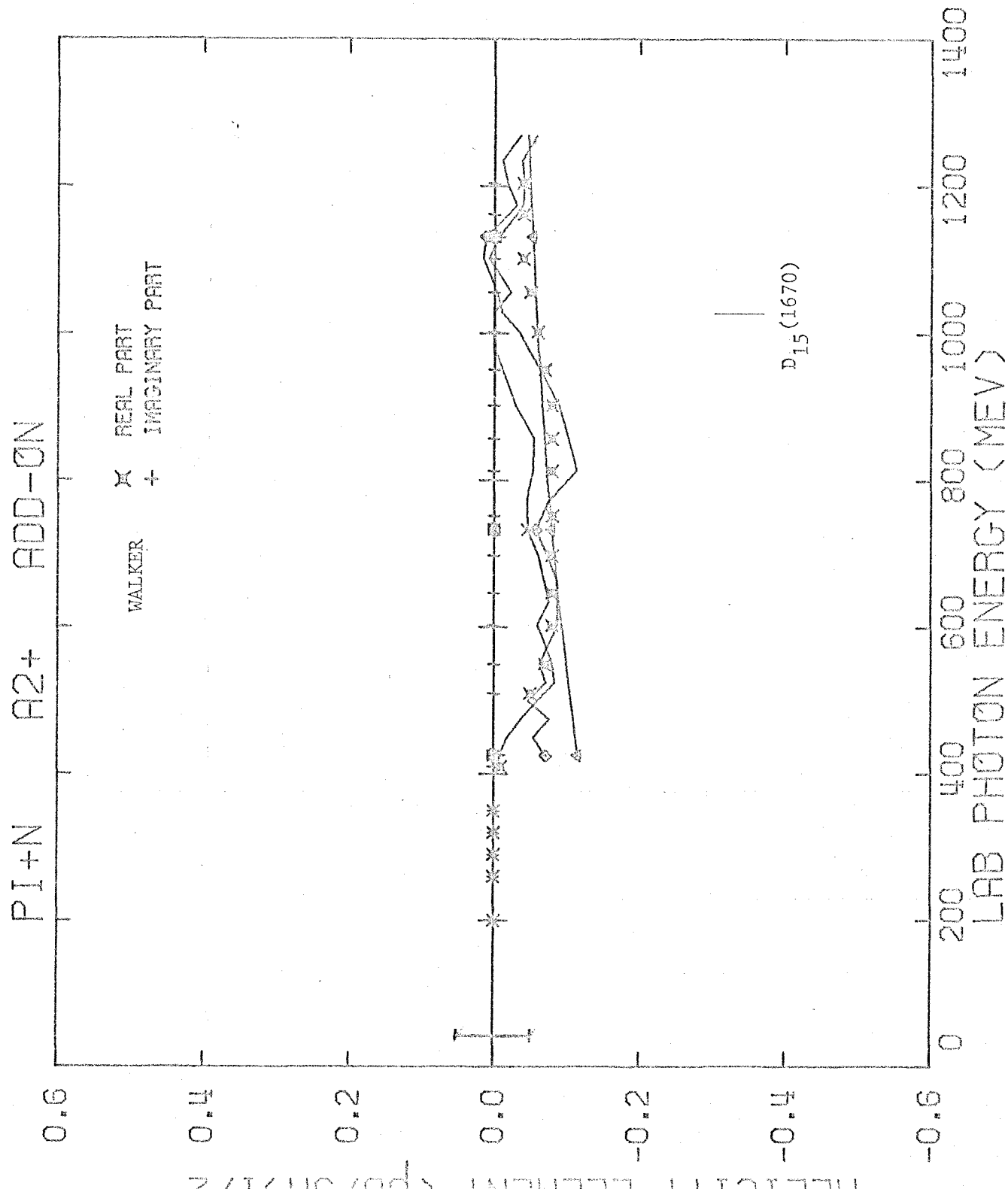
PI+N A2+ ADD-ON
WALKER
REAL PART
IMAGINARY PART
$D_{15}(1670)$
HELICITY ELEMENT (UB/SR)1/2
LAB PHOTON ENERGY (MEV)
0.6
0.4
0.2
0.0
-0.2
-0.4
-0.6
0
200
400
600
800
1000
1200
1400

FIGURE 47.7

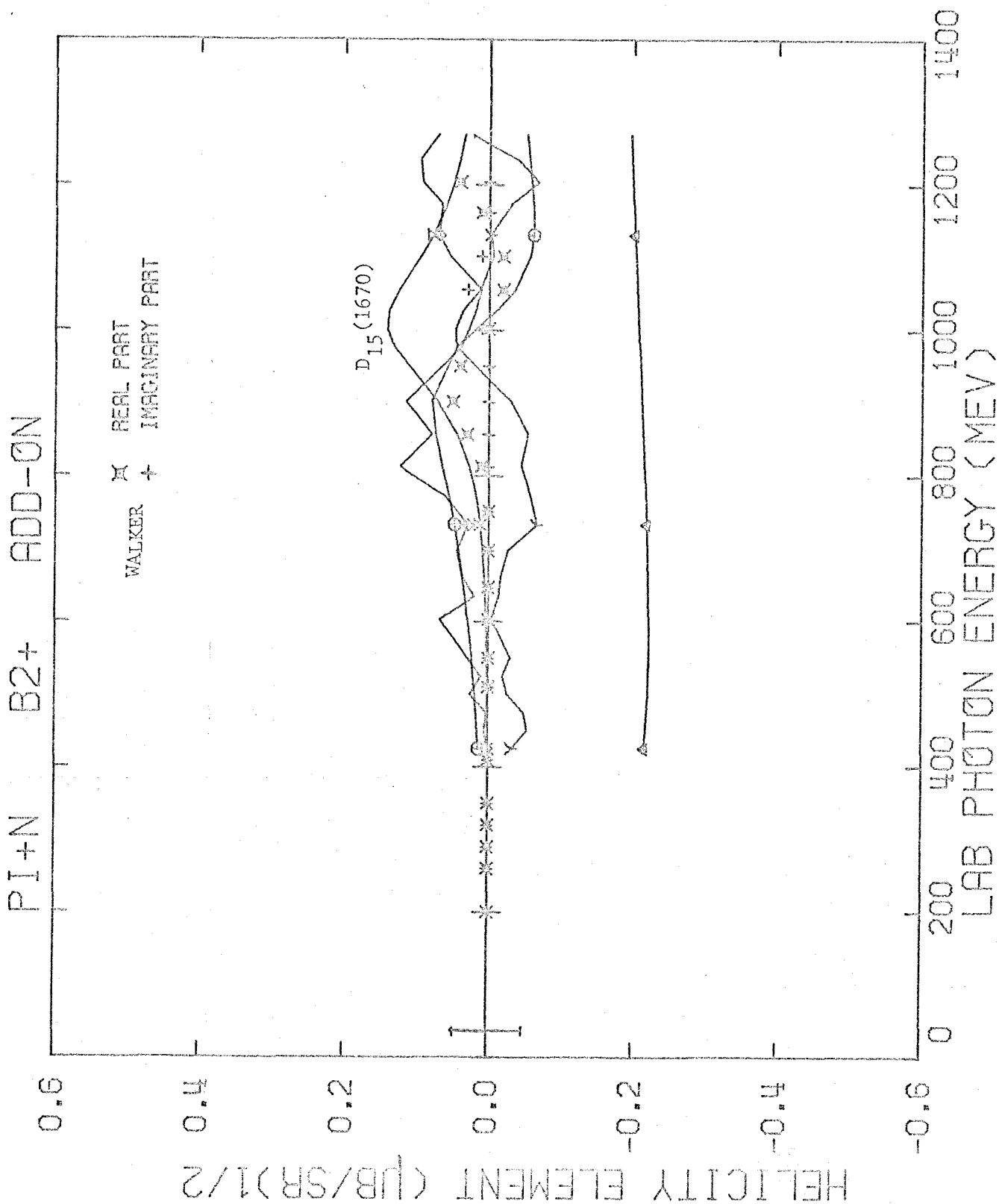
PI+N B2+ ADD-ON
WALKER
REAL PART
IMAGINARY PART
$D_{15}(1670)$
HELICITY ELEMENT (UB/SR)1/2
LAB PHOTON ENERGY (MEV)
0.6
0.4
0.2
0.0
-0.2
-0.4
-0.6
0
200
400
600
800
1000
1200
1400

FIGURE 47.8

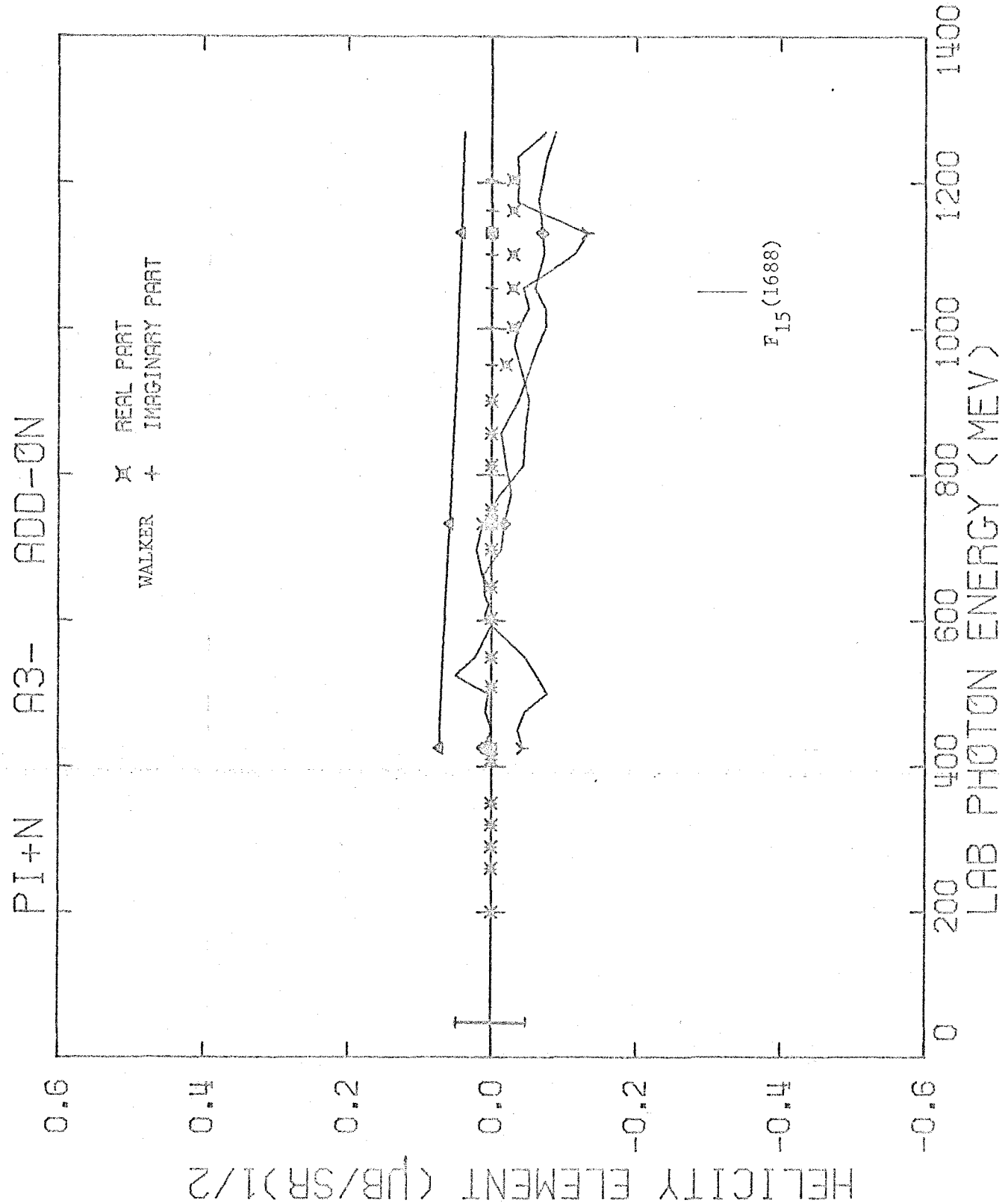
PI+N A3- ADD-ON
WALKER
REAL PART
IMAGINARY PART
$F_{15}(1688)$
HELICITY ELEMENT (UB/SR)1/2
LAB PHOTON ENERGY (MEV)
0.6
0.4
0.2
0.0
-0.2
-0.4
-0.6
0
200
400
600
800
1000
1200
1400

FIGURE 47.9

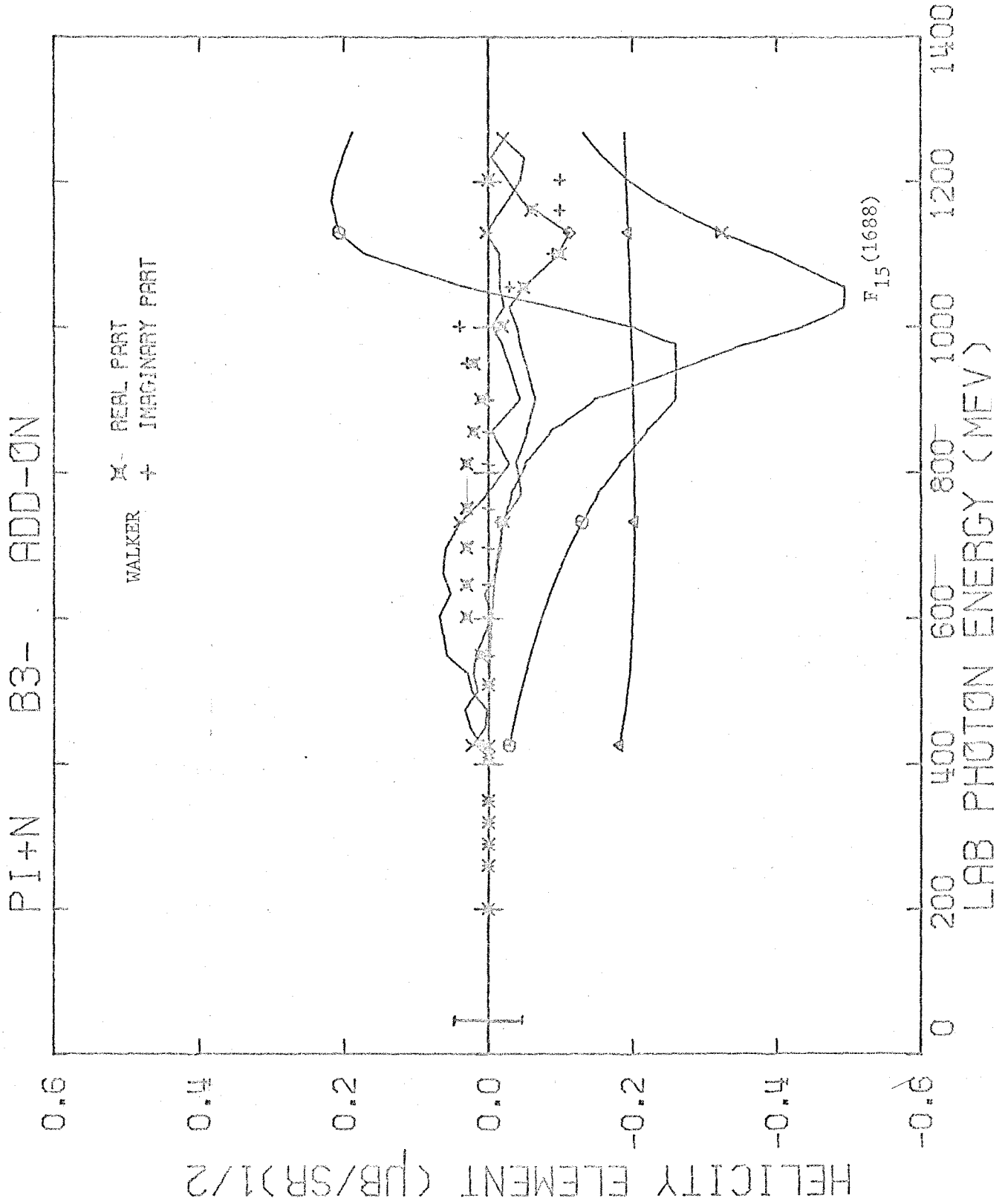
PI+N B3- ADD-ON
WALKER
REAL PART
IMAGINARY PART
$F_{15}(1688)$
HELICITY ELEMENT (UB/SR)1/2
LAB PHOTON ENERGY (MEV)
0.6
0.4
0.2
0.0
-0.2
-0.4
-0.6
0
200
400
600
800
1000
1200
1400

FIGURE 47.10

FIGURE 48

TOTAL HELICITY ELEMENTS FROM

FINAL FIT OF π^+ PHOTOPRODUCTION

The final total fitted helicity elements (plotted curves) are compared with Walker's total helicity elements (plotted points).

The curves are identified by ☐ for the real part and by ✕ for the imaginary part.

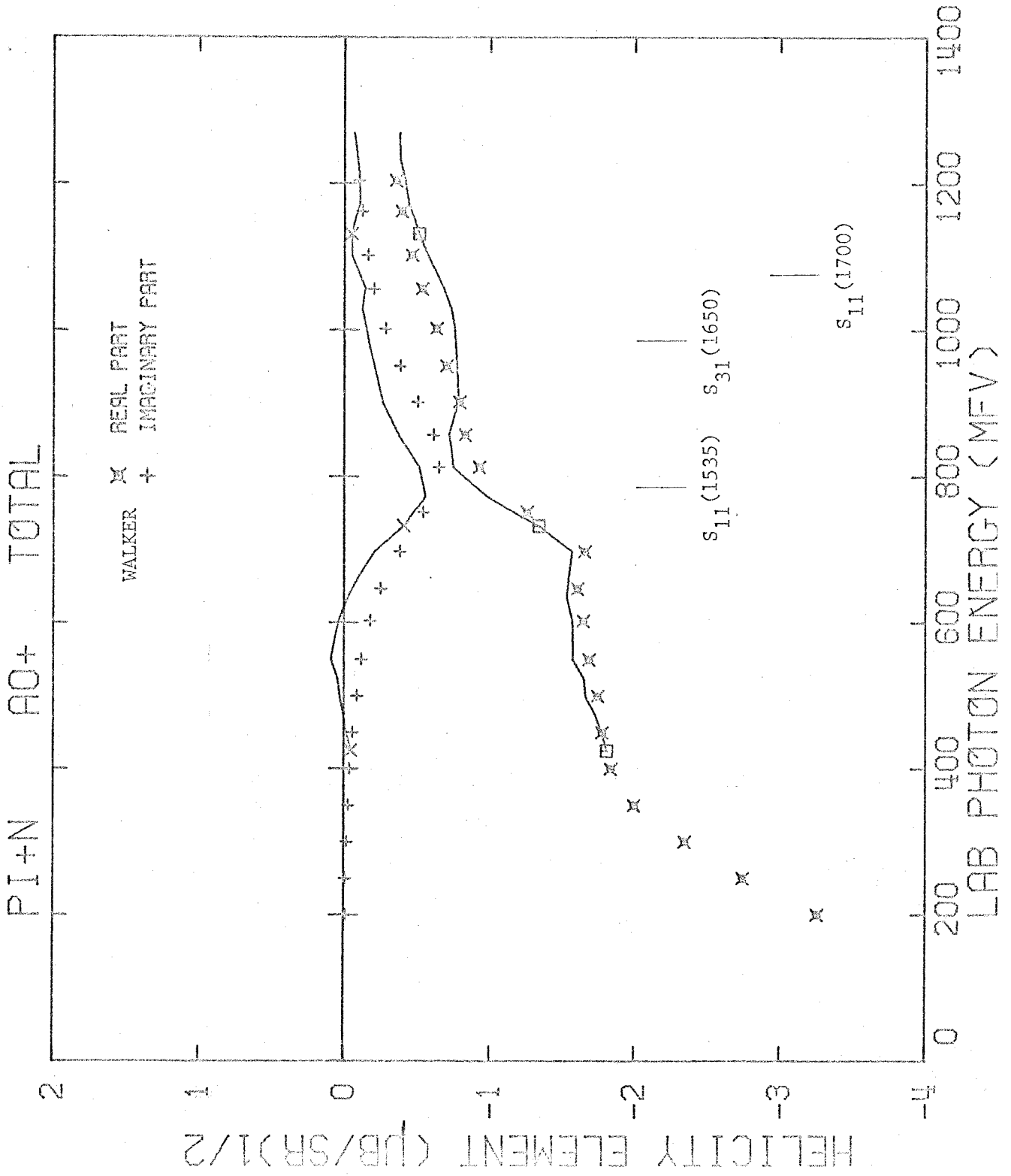
PI+N AO+ TOTAL
WALKER
REAL PART
IMAGINARY PART
$S_{11}(1535)$
$S_{31}(1650)$
$S_{11}(1700)$
HELICITY ELEMENT (UB/SR)1/2
LAB PHOTON ENERGY (MEV)
2
1
0
-1
-2
-3
-4
0
200
400
600
800
1000
1200
1400

FIGURE 48.1

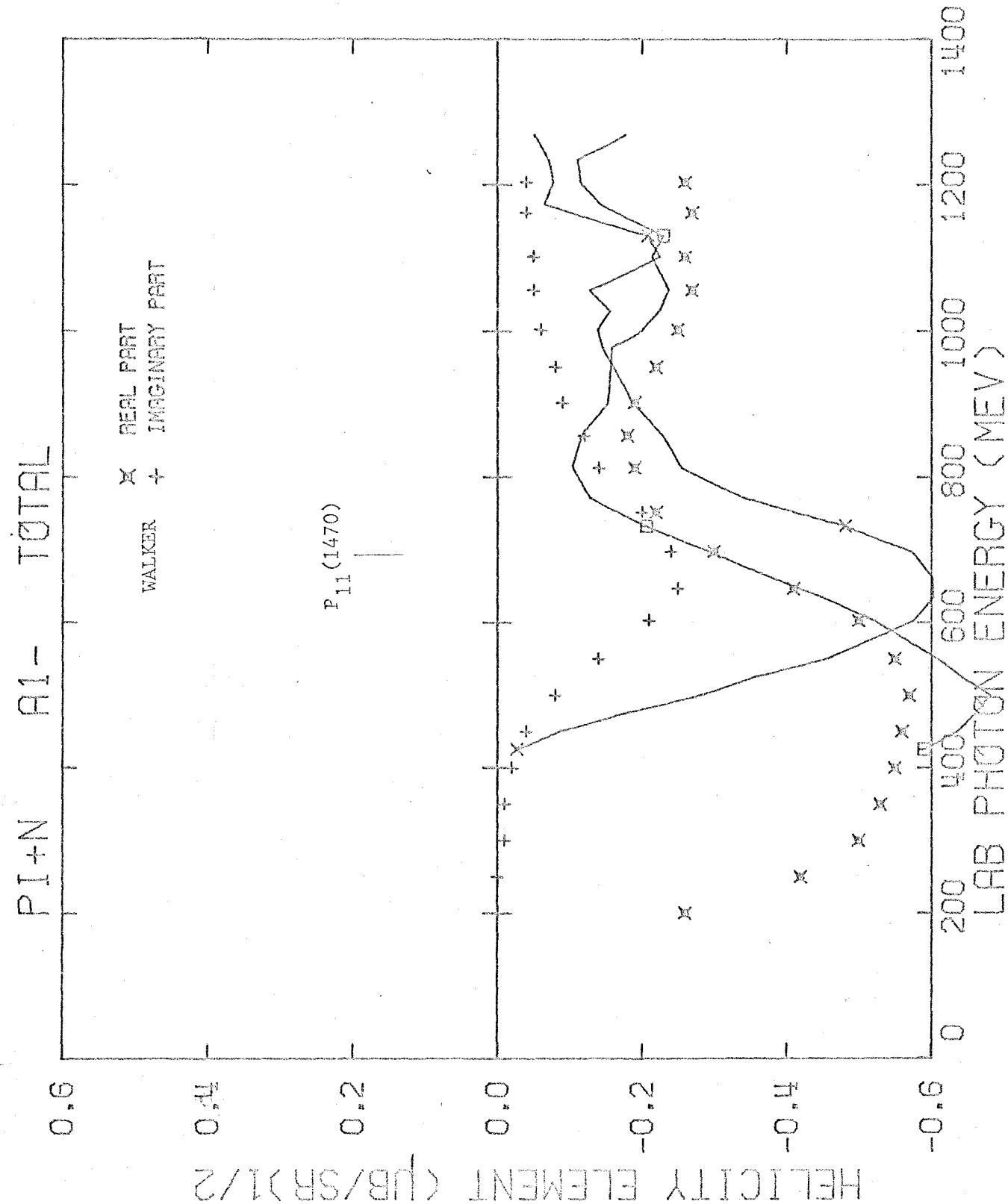
PI+N A1- TOTAL
WALKER
REAL PART
IMAGINARY PART
$P_{11}(1470)$
HELICITY ELEMENT (UB/SR)1/2
LAB PHOTON ENERGY (MEV)
0.6
0.4
0.2
0.0
-0.2
-0.4
-0.6
0
200
400
600
800
1000
1200
1400

FIGURE 48.2

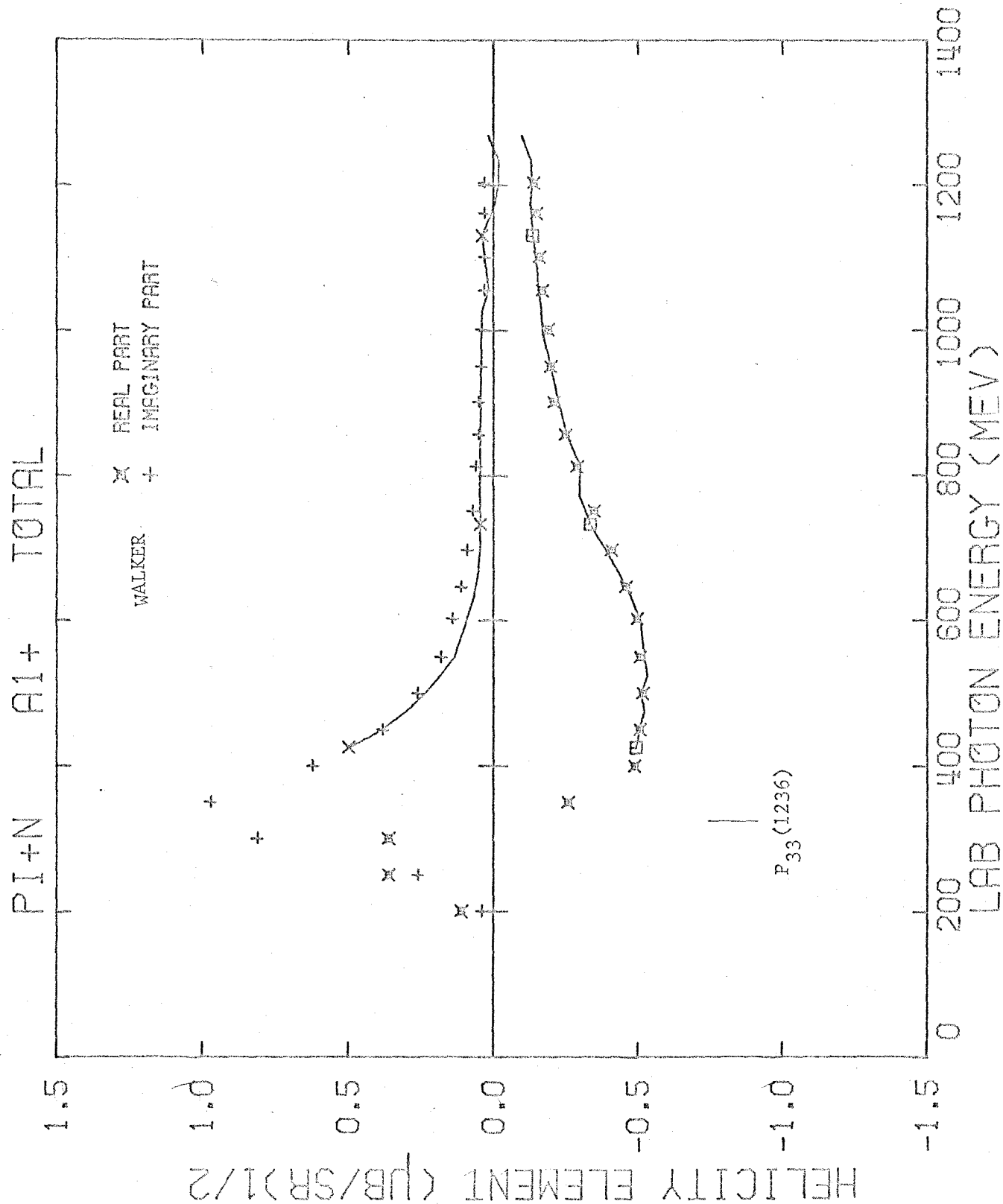
PI+N A1+ TOTAL
WALKER
REAL PART
IMAGINARY PART
$P_{33}(1236)$
HELICITY ELEMENT (UB/SR)1/2
LAB PHOTON ENERGY (MEV)
1.5
1.0
0.5
0.0
-0.5
-1.0
-1.5
0
200
400
600
800
1000
1200
1400

FIGURE 48.3

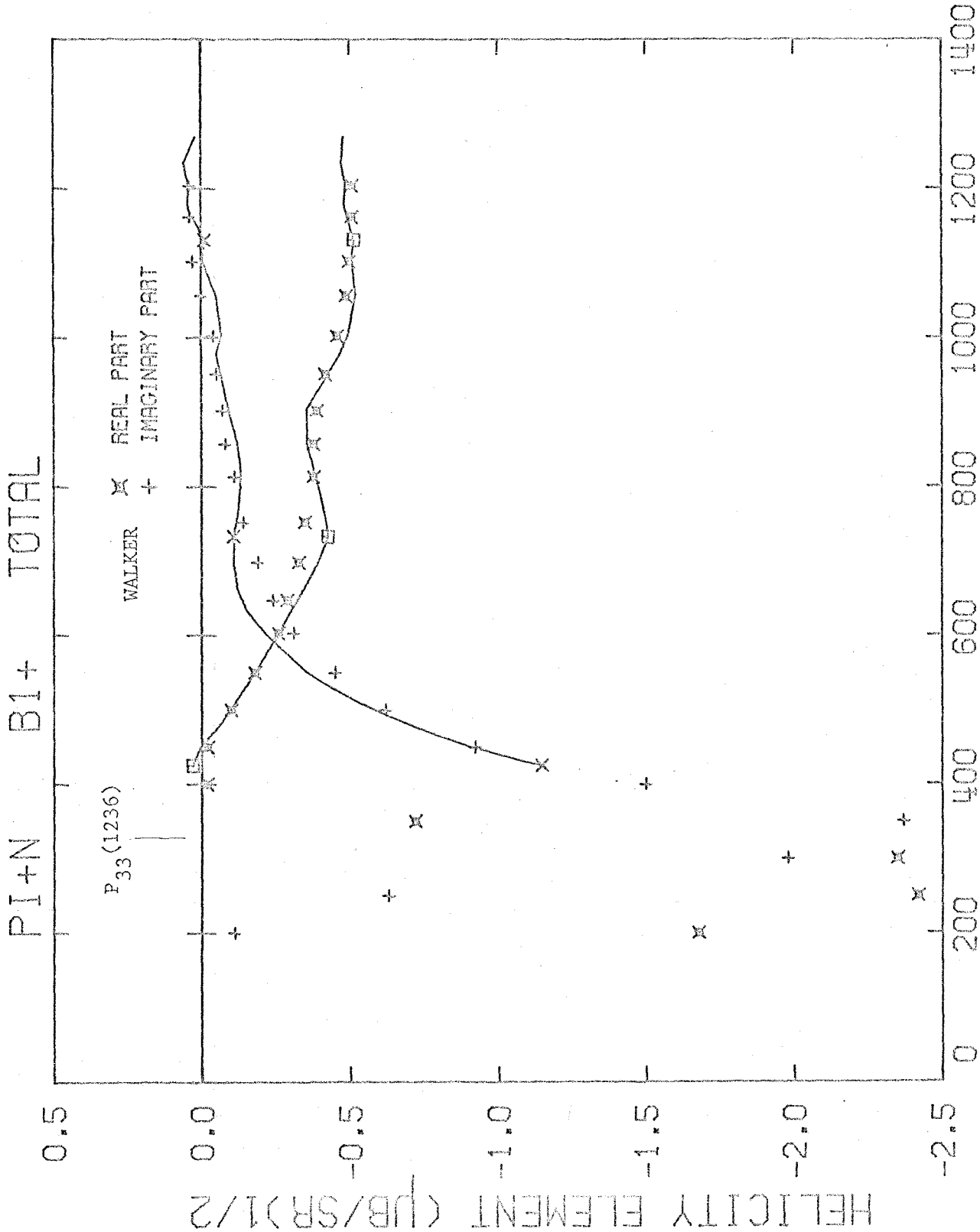
PI+N B1+ TOTAL
WALKER
REAL PART
IMAGINARY PART
$P_{33}(1236)$
LAB PHOTON ENERGY (MEV)
0
200
400
600
800
1000
1200
1400
HELICITY ELEMENT (UB/SR)1/2
0.5
0.0
-0.5
-1.0
-1.5
-2.0
-2.5

FIGURE 48.4

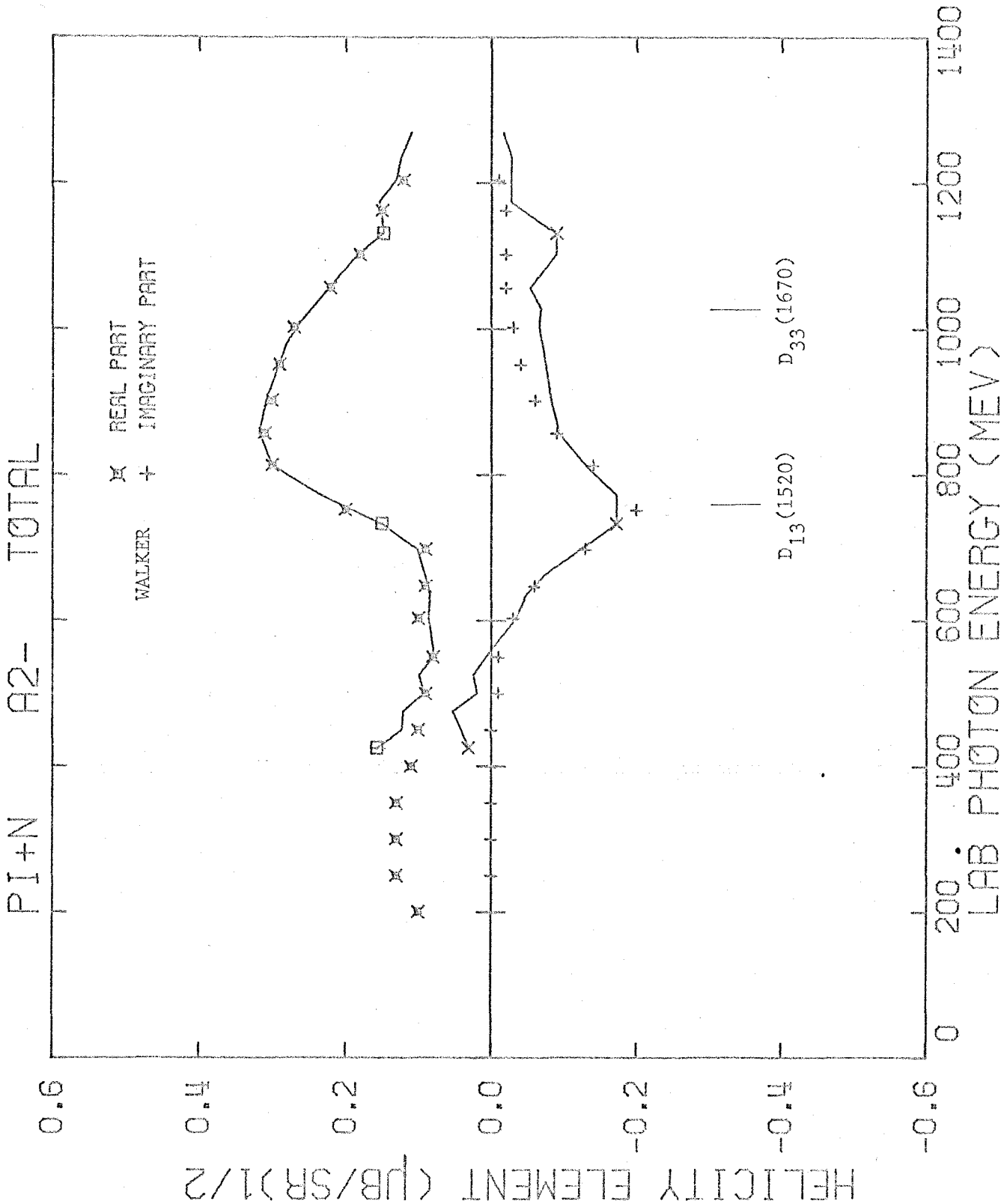
PI+N A2- TOTAL
WALKER
REAL PART
IMAGINARY PART
$D_{13}(1520)$
$D_{33}(1670)$
HELICITY ELEMENT (UB/SR)1/2
LAB PHOTON ENERGY (MEV)
0.6
0.4
0.2
0.0
-0.2
-0.4
-0.6
0
200
400
600
800
1000
1200
1400

FIGURE 48.5

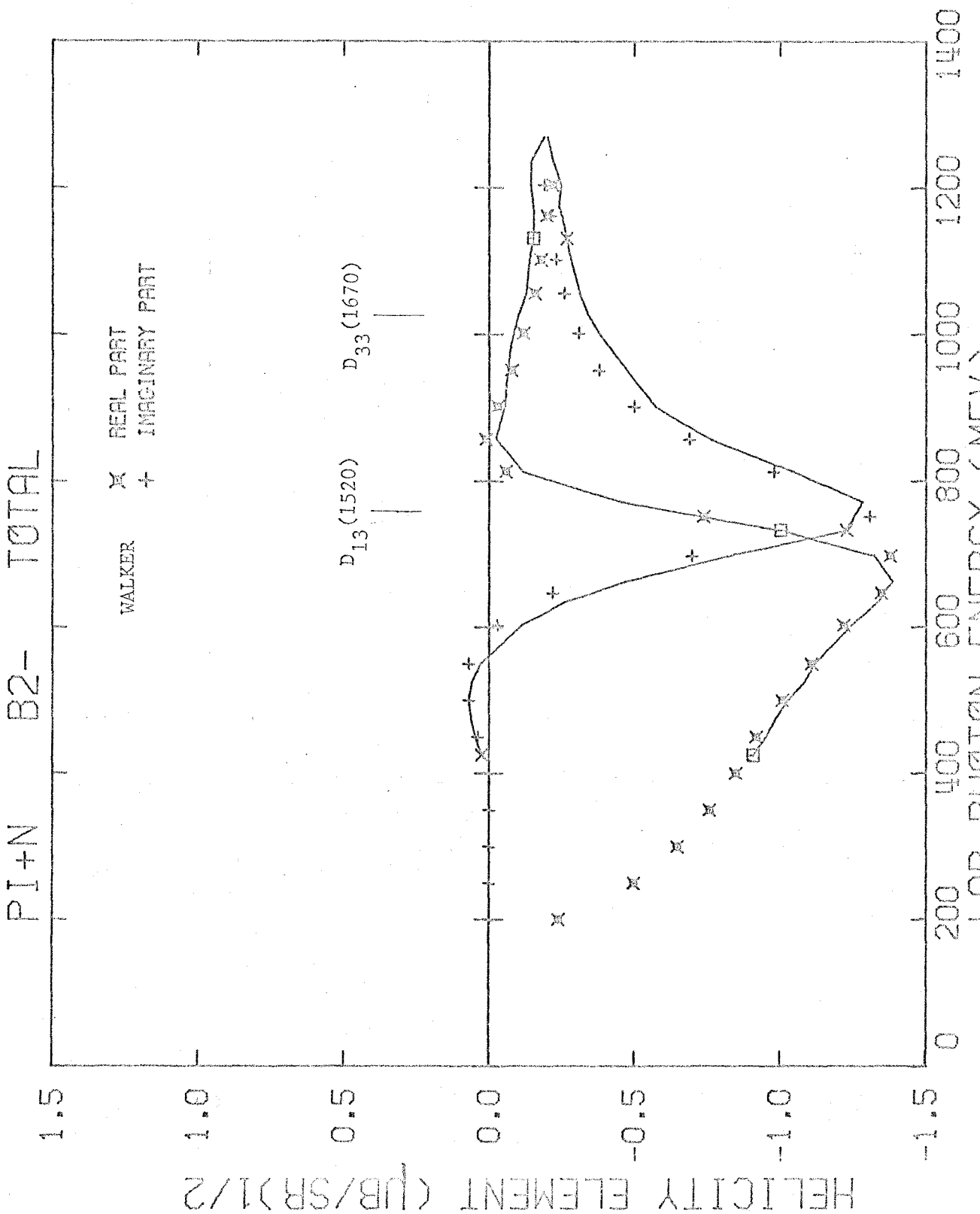
PI+N B2- TOTAL
WALKER
REAL PART
IMAGINARY PART
$D_{13}(1520)$
$D_{33}(1670)$
HELICITY ELEMENT (UB/SR)1/2
LAB PHOTON ENERGY (MEV)
1.5
1.0
0.5
0.0
-0.5
-1.0
-1.5
0
200
400
600
800
1000
1200
1400

FIGURE 48.6

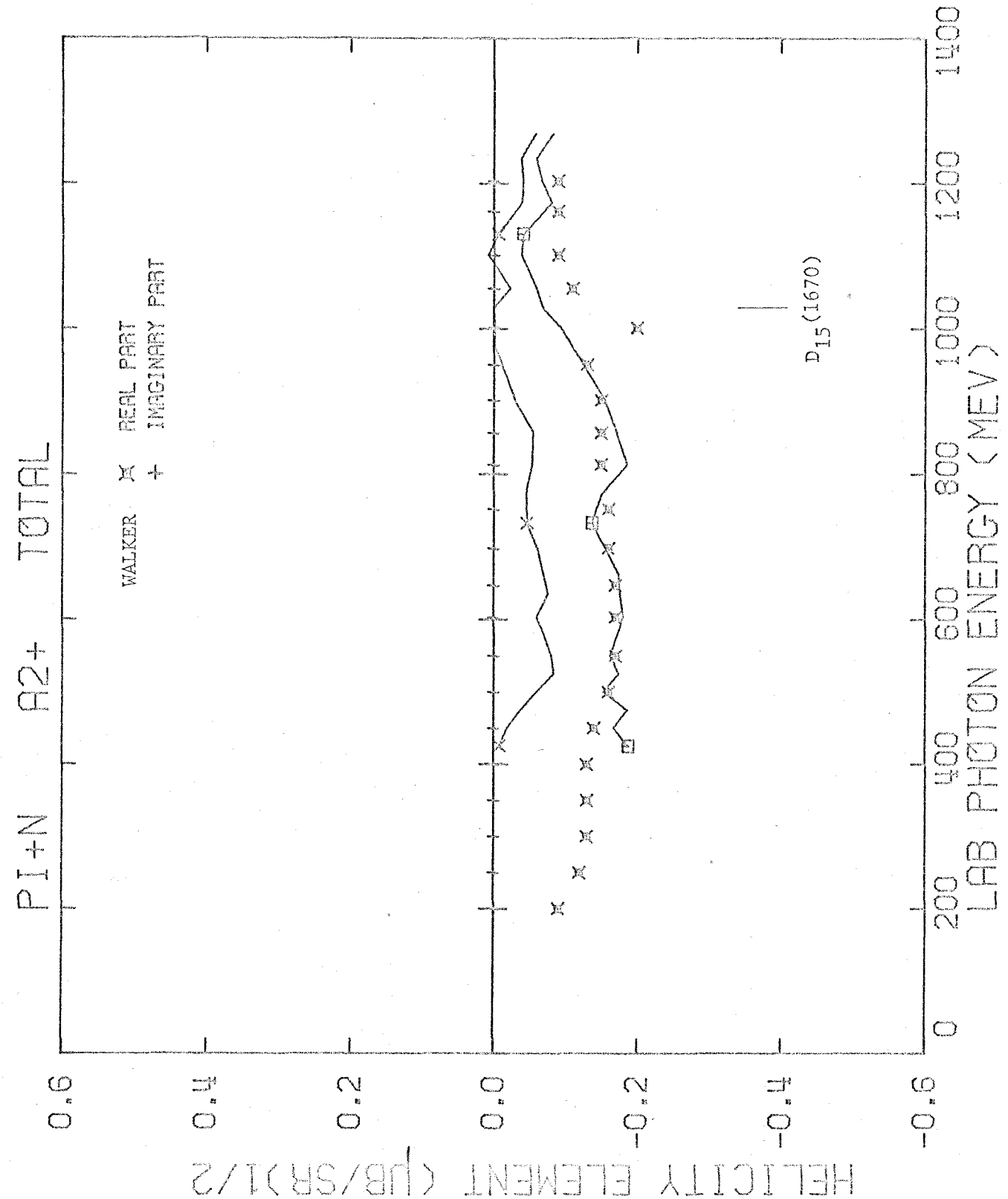
PI+N A2+ TOTAL
WALKER X REAL PART
+ IMAGINARY PART
$D_{15}(1670)$
HELICITY ELEMENT (UB/SR)1/2
LAB PHOTON ENERGY (MEV)
0.6
0.4
0.2
0.0
-0.2
-0.4
-0.6
0
200
400
600
800
1000
1200
1400

FIGURE 48.7

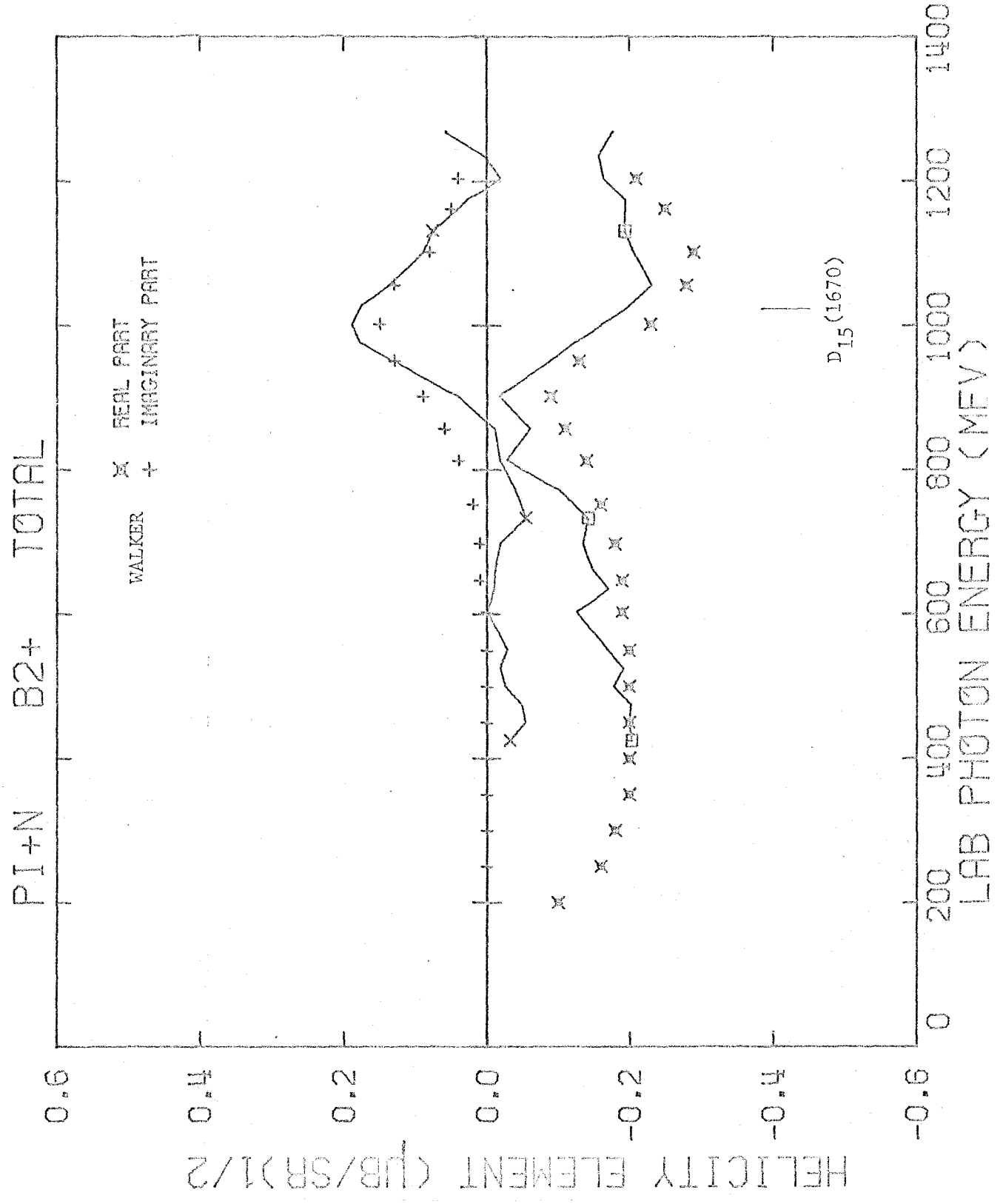
PI+N B2+ TOTAL
WALKER
REAL PART
IMAGINARY PART
$D_{15}(1670)$
HELICITY ELEMENT (UB/SR)1/2
LAB PHOTON ENERGY (MEV)
0.6
0.4
0.2
0.0
-0.2
-0.4
-0.6
0
200
400
600
800
1000
1200
1400

FIGURE 48.8

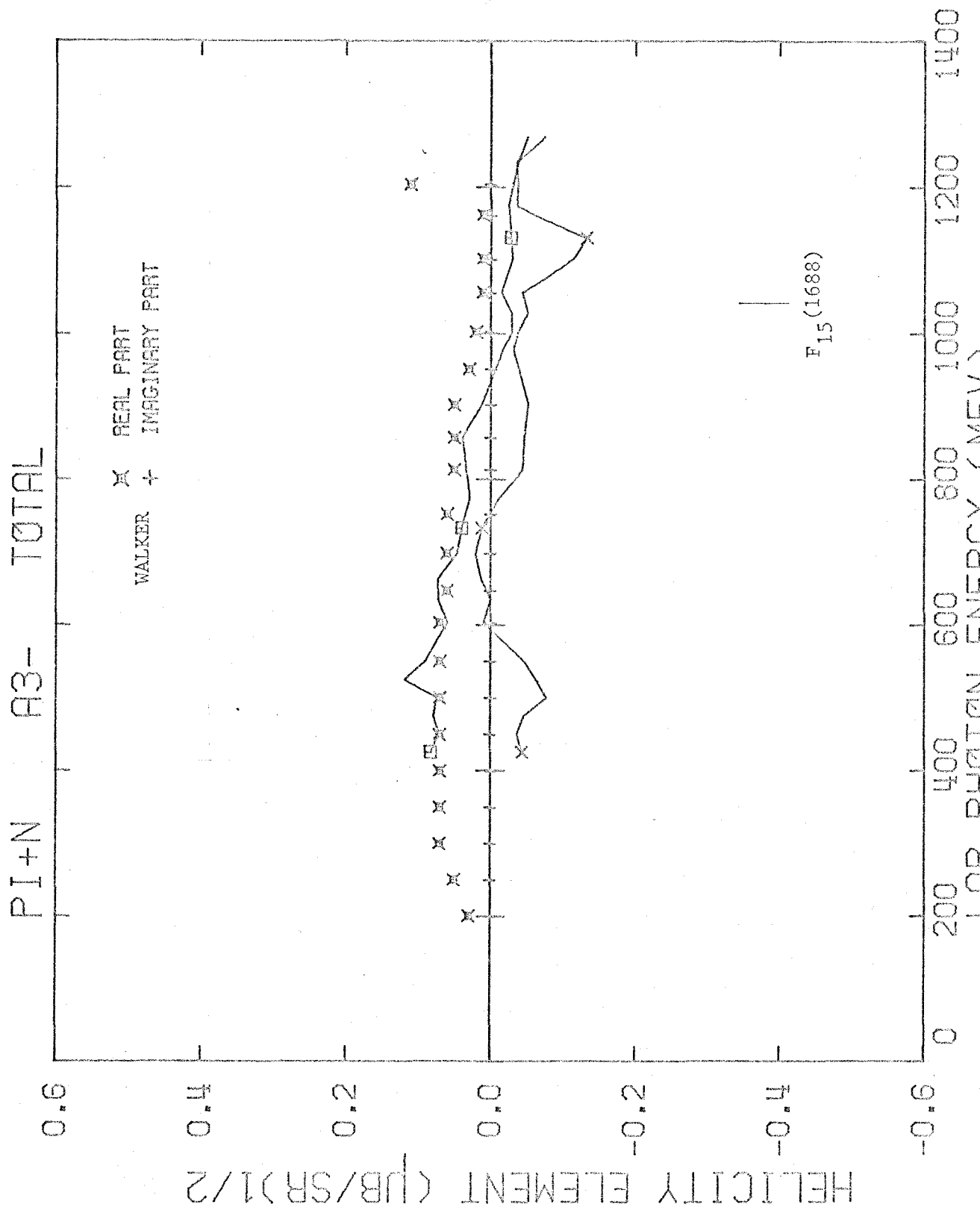
PI+N A3- TOTAL
WALKER
X REAL PART
+ IMAGINARY PART
$F_{15}(1688)$
HELICITY ELEMENT (UB/SR)1/2
0.6
0.4
0.2
0.0
-0.2
-0.4
-0.6
LAB PHOTON ENERGY (MEV)
0
200
400
600
800
1000
1200
1400

FIGURE 48.9

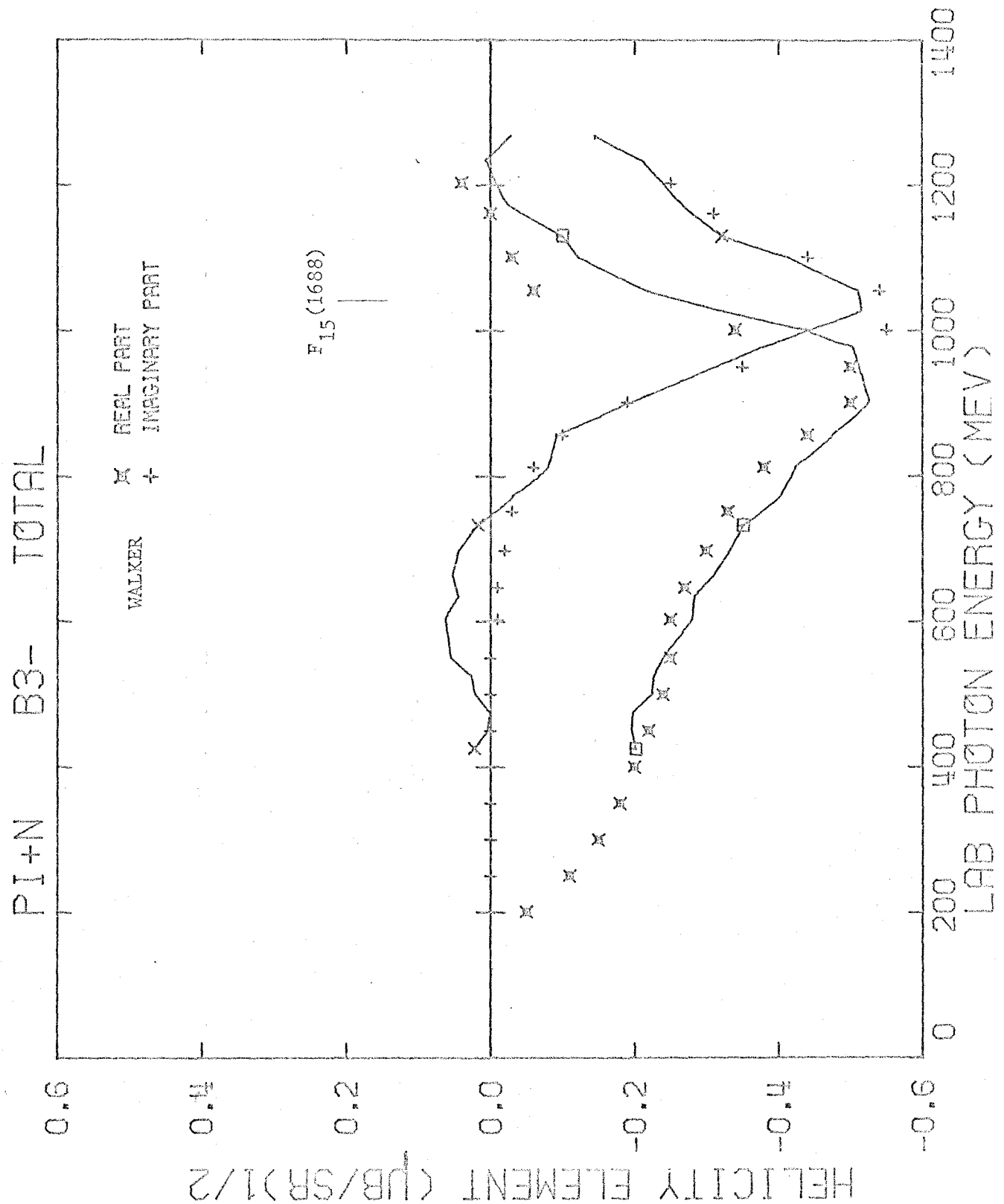
PI+N B3- TOTAL
WALKER
REAL PART
IMAGINARY PART
$F_{15}(1688)$
HELICITY ELEMENT (UB/SR)1/2
LAB PHOTON ENERGY (MEV)
0.6
0.4
0.2
0.0
-0.2
-0.4
-0.6
0
200
400
600
800
1000
1200
1400

FIGURE 48.10

REFERENCES

1. L. A. Copley, G. Karl, and E. Obryk, Nuc. Phys. B13, 303 (1969)

2. R. P. Feynman, M. Kislinger, and F. Ravndal, Phys. Rev. D3, 2706 (1971)

3. R. L. Walker, Phys. Rev. 182, 1729 (1969)

4. G. Fischer, H. Fischer, M. Heuel, G. von Holtey, G. Knop, J. Stumpfig, Nuc. Phys. B16, 119 (1970)

5. C. Betourne, J. C. Bizot, J. Perez-Y-Jorba, D. Treille, and W. Schmidt, Phys. Rev. 172, 1343 (1968)

6. S. D. Ecklund and R. L. Walker, Phys. Rev. 159, 1195 (1967)

7. Henry A. Thiessen, Phys. Rev. 155, 1488 (1967)

8. G. Fischer, H. Fischer, G. von Holtey, H. Kampgen, G. Knop, P. Schulz, W. Wessels, W. Braunschweig, H. Genzel, and R. Wedemeyer, Nuc. Phys. B16, 93 (1970)

9. F. B. Wolverton, Ph.D. Thesis, California Institute of Technology, 1968

10. M. Beneventano, L. Paoluzi, F. Sebastiani, M. Severi, and M. Grilli, Nuovo Cimento 54A, 468 (1968)

11. T. Fujii, H. Okuno, S. Orito, H. Sasaki, T. Nozaki, F. Takasaki, K. Takikawa, K. Amako, I. Endo, K. Yoshida, M. Higuchi, M. Sato, Y. Sumi, Phys. Rev. Lett. 26, 1672 (1971)

12. Y. Hemmi, T. Inagaki, Y. Inagaki, A. Maki, K. Miyaki, T. Nakamura, N. Tamura, J. Tsukamoto, N. Yamashita, S. Yasumi, H. Itoh, S. Kobayashi, and H. Yoshida, Paper 184 submitted to 1971 International Symposium on Electron and Photon Interactions at High Energies,

13. P. S. L. Booth et al., Abstract 37 submitted to 1971 International Symposium on Electron and Photon Interactions at High Energies,

14. R. Morand, E. F. Erickson, J. P. Pahin, and M. G. Croissiaux, Phys. Rev. 180, 1229 (1969)

15. J. R. Holt,

16. G. L. Cassiday, H. Fischer, A. Ito, E. C. Loh, and J. Rutherfoord, Phys. Rev. Lett. 21, 933 (1968)

17. B. Delcourt, J. LeFrancois, G. Parrour, J. P. Perez-Y-Jorba, and G. Sauvage, Phys. Lett. 29B, 70 (1969)

18. M. Grilli, P. Spillantini, F. Soso, M. Nigro, E. Schiavuta, and V. Valente, Nuovo Cimento 54A, 890 (1968)

19. U. Hahn, H. Heinrichs, and W. Wallraff, Bonn Preprint PI 1-143, August 1971

20. J. Alspector, D. Fox, C. Nelson, D. Luckey, L. Osborne, Z. Bar-Yam, J. de Pagter, J. Dowd, W. Kern, G. Tarnopolsky, and S. Matin, Paper 249 submitted to 1971 International Symposium on Electron and Photon Interactions at High Energies,

21. R. L. Walker, in International Symposium on Electron and Photon Interactions at High Energies, Liverpool, England, 1969, edited by D. W. Braben and R. E. Rand (Daresbury Nuclear Physics Laboratory, Daresbury, Lancashire, England, 1970)

22. M. N. Prentice, R. Railton, J. G. Rutherglen, K. M. Smith, G. R. Brookes, P. J. Bussey, F. H. Combley, G. H. Eaton, W. Galbraith, and J. E. Shaw, Paper 248 submitted to 1971 International Symposium on Electron and Photon Interactions at High Energies,

23. P. Blum, P. Brinckman, R. Brockmann, P. Lutter, W. Mohr, P. Feller, M. Minatti, H. Piel, W. Niehaus, and D. Trines, Bonn Preprint PI 1-105 (1970)

24. E. D. Bloom, C. A. Heusch, C. Y. Prescott, and L. S. Rochester, Phys. Rev. Lett. 19, 671 (1967)

25. S. Cheng, Ph.D. Thesis, California Institute of Technology, 1970

26. G. Bologna, F. L. Fabbri, P. Spillantini, and V. Valente, Frascati Report LNF-70/39 (1970)

27. Y. P. Antufyev, L. Agranovich, V. B. Ganenko, V. G. Gorbenko, Y. V. Zhebrovsky, L. Y. Kolesnikov, V. S. Kuzmenko, I. I. Miroshnichenko, P. V. Sorokin, A. L. Rubashkin, and V. F. Chechetenko, Kharkov Preprint (1970)

28. K. H. Althoff, P. Feller, H. Herr, W. Hoffmann, V. Kadansky, D. Menze, U. Opara, F. J. Schittko, W. Schulz, W. J. Schwille, Bonn Preprint PI 1-139, July 1971

29. J. T. Beale, S. D. Ecklund, and R. L. Walker, Caltech Report CTSL-42, CALT-68-108, November 1966. For a more up to date data compilation, see P. Spillantini and V. Valente, CERN Report CERN/HERA 70-1 June 1970.

30. R. G. Moorhouse and W. A. Rankin, Nuc. Phys. B23, 181 (1970)

31. A. Proia and F. Sebastiani, Nuovo Cimento Lett. 3, 483 (1970)

32. W. A. Rankin, Daresbury Preprint and Abstract 50 submitted to 1971 International Symposium on Electron and Photon Interactions at High Energies,

33. R. C. E. Devenish, D. H. Lyth, and W. A. Rankin, Daresbury Preprint (1971)

34. Matthew Sands, J. G. Teasdale, and Robert L. Walker, Phys. Rev. 95, 592 (1954)

35. M. Beneventano, G. Bernardini, G. Stoppini, and L. Tau, Nuovo Cimento 10, 1109 (1958)

36. Gerry Neugebauer, Walter Wales, and R. L. Walker, Phys. Rev. 119, 1726 (1960)

37. E. Lodi-Rizzini, G. C. Mantovani, A. Piazzoli, L. Fiore, G. Gialanella, V. Rossi, A. Piazza, G. Susinno, F. Carbonara, M. Napolitano, and R. Rinzivillo, Nuovo Cimento Lett. 3, 697 (1970)

38. H. G. Hilpert, P. Lauscher, M. Matziolis, H. Schnackers, H. Weber, A. Meyer, A. Pose, K. Bockmann, U. Idschok, K. Muller, E. Paul, E. Propach, H. Butenschon, H. Kubeck, D. Luke, H. Seebeck, H. Spitzer, F. Storim, S. Brandt, O. Braun, P. Steffen, J. Stiewe, P. Schlamp, J. Weigl, K. Wilkinson, Nuc. Phys. B8, 535 (1968)

39. M. Beneventano, F. de Notaristefani, P. Monacelli, L. Paoluzi, F. Sebastiani, M. Severi, Nuovo Cimento Lett. 1, 113 (1969)

40. A. Ito, R.Loe, E. C. Loh, A. Ramanauskas, D. Ritchie, W. Schmidt, Phys. Rev. Lett. 24, 687 (1970)

41. P. A. Berardo, R. P. Haddock, B. M. K. Nefkens, L. J. Verhey, M. E. Zeller, A. S. L. Parsons, and P. Truoel, Phys. Rev. Lett. 24, 419 (1970) and Phys. Rev. Lett. 26, 201 (1971)

42. M. Beneventano, S. D'Angelo, F. de Notaristefani, P. Monacelli, L. Paoluzi, F. Sebastiani, M. Severi, and B. Stella, Nuovo Cimento Lett. 3, 840 (1970)

43. William J. Metcalf, private communication

44. Patrick L. Walden, Ph.D. Thesis, California Institute of Technology, 1972

45. G. E. Chew and H. W. Lewis, Phys. Rev. 84, 779 (1951)

46. Robert G. Sachs, Chap. 3, Nuclear Theory, Addison-Wesley, Cambridge, 1953

47. R. J. Glauber, Phys. Rev. 100, 242 (1955)

48. D. O. Caldwell, V. B. Elings, W. P. Hesse, G. E. Jahn, R. J. Morrison, F. V. Murphy, D. E. Yount, Phys. Rev. Lett. 23, 1256 (1969)

49. W. Hitzeroth, Nuovo Cimento 60A, 467 (1969)

50. H. A. Thiessen, Ph.D. Thesis, California Institute of Technology, 1967

51. G. F. Chew, M. L. Goldberger, F. E. Low, Y. Nambu, Phys. Rev. 106, 1345 (1957)

52. P. E. Scheffler and P. L. Walden, Phys. Rev. Lett. 24, 952(1970)

53. K. Kondo, T. Nishikawa, T. Suzuki, K. Takikawa, H. Yoshida, Y. Kimura, M. Kobayashi, Journal Phys. Soc. Japan 29, 13 (1970)

54. F. F. Liu and S. Vitale, Phys. Rev. 144, 1093 (1966)

55. E. Hilger, H. J. Roegler, L. M. Simons, M. Tonutti, Bonn Preprint PI 1-103, July 1970

56. B. Musgrave, proceedings of conference on Phenomenology in Particle Physics, California Institute of Technology, Pasadena, California, 1971, edited by C. B. Chiu, G. C. Fox, A. J. G. Hey, California Institute of Technology

57. R. L. Anderson and R. Prepost, Phys. Rev. Lett. 23, 46 (1969)

58. Robert R. Wilson, Nuc. Inst. 1, 101 (1957)

59. R. Gomez, J. Pine, and A. Silverman, Nuc. Inst. and Meth. 24, 429 (1963)

60. Henry A. Thiessen and Jerome Pine, Caltech Synchrotron Lab (CTSL) Internal Report No. 22, CALT 68-76, May 1966

61. F. Wolverton, CTSL Internal Report No. 36, 1968

62. H. A. Thiessen, CTSL Internal Report No. 27, CALT-68-96, 1968

63. M. Jacob and G. C. Wick, Annals of Physics 7, 404 (1959)

64. Philip R. Bevington, Data Reduction and Error Analysis for the Physical Sciences, McGraw-Hill, New York, 1969, Paperback, Chapter 11.